Phase Transitions and Fluctuations in Block Copolymer–Based Soft Materials

A DISSERTATION
SUBMITTED TO THE FACULTY OF
UNIVERSITY OF MINNESOTA
BY

Timothy M. Gillard

IN PARTIAL FULFILLMENT OF THE REQUIREMENTS
FOR THE DEGREE OF
DOCTOR OF PHILOSOPHY

Frank S. Bates

September 2015

Acknowledgements

Graduate school, while certainly challenging and at times quite stressful, has been an incredibly rewarding and enjoyable experience. I owe this to the many exceptional people I have had the pleasure of learning from, working alongside, and interacting with throughout my time at the University of Minnesota. I will try not to forget anyone…

First, I must thank my advisor, Professor Frank Bates. Your enthusiasm for research is contagious. The experience of "hunting for quasicwystals" with you at Argonne (on your birthday) is far and away the most fun I have ever had collecting data! I have done my best to absorb as much as I can of what it means to be a scientist from you over the years and cannot possibly thank you enough.

I can't imagine a better environment to be a graduate student than the Polymer Group at the University of Minnesota. The collaborative culture that pervades the Polymer Group has made my time in graduate school infinitely more gratifying as I have been able to learn from and share my knowledge and accomplishments (and occasional failures) with a host of official and unofficial collaborators. Virtually this entire thesis is the result of collaborative work in one way or another and I am happy to thank the many people that have made it all possible. Sangwoo Lee was a patient and thoughtful mentor when I was starting out in the Bates group, always available to answer questions or demonstrate a technique. I am glad this mentorship grew into a dear friendship and a

I would also like to thank my many friends who have made my life outside the lab in Minnesota so enjoyable and full of memorable first year study sessions, coffee breaks, lunches, happy hours, camping trips, bike rides, softball games, ski trips, concerts, get togethers, road trips, and nights out.

Finally, I must thank Colleen and my family for their unconditional love and support. I would be nothing without them.

Dedication

For Colleen and my parents.

Abstract

Block polymers have sustained the interest of both academic and industrial researchers for decades as the preeminent uniquely tunable self-assembling soft materials, finding practical utility in a diverse array of existing commercial products and emerging technologies. This thesis describes an experimental investigation of a class of materials we call short diblock copolymers—block polymers that self–assemble into ordered mesophases even at low molecular weight as a result of high thermodynamic incompatibility between the constituent blocks. The low molecular weight of short diblock copolymers enables accessing the ever-smaller features sizes required by applications such as nanolithography. However, the behavior of short diblock copolymers is dominated by fluctuations and consequently is not well described by the classical mean-field theoretical framework used to understand block polymer phase behavior. This thesis involves the synthesis of a series of model short diblock copolymers and detailed characterization of their thermodynamics and dynamics using a variety of experimental tools including small-angle scattering, rheology, and thermal analysis techniques. The phase behavior is documented, including the discovery of an ordered phase with dodecagonal quasicrystalline symmetry. Taking advantage of opportunities afforded by the low molecular weight of short diblock copolymers, an expansion of the experimental toolkit for block polymer characterization was achieved through the adaptation and application of relaxation calorimetry in conjunction with the development of new approaches for exploiting established tools like differential scanning calorimetry. These tools provide new insight into the central role of composition fluctuations on the order–disorder phase transition in block polymers. In addition, the unusually comprehensive set of experimental characterization data for a single volumetrically symmetric short diblock copolymer is compared to the predictions of the recently developed renormalized one-loop theory and simulation results.

Table of Contents

List of Tables

List of Figures

xv

Chapter 1:

Introduction

1.1 Motivation

Block polymers have sustained the interest of both academic and industrial researchers for decades as the preeminent uniquely tunable self-assembling soft materials.[1–6] A polymer is a large chain-like molecule that is formed by linking a series of identical chemical repeat units (monomers) by covalent bonds. A block polymer is formed when two or more polymer chains, called blocks, with different constituent monomer units are covalently linked together, the simplest manifestation being a linear diblock copolymer (. . .-A-A-A-B-B-B-. . .) shown in Figure 1.1. As a result of unfavorable interactions between the unlike monomer units, block polymers can undergo a phase transition, called the order–disorder transition (ODT), between a disordered phase in which the A and B blocks tend to mix and an ordered phase in which the A and B blocks spatially segregate into separate domains with a characteristic size on the molecular length scale (5-100 nm), a process called microphase separation. These domains can form a variety of intricate periodic patterns in space. The phase behavior of block polymers is largely universal, meaning it is insensitive to the chemical details of

the monomers used and depends only on a small number of parameters that can be controlled during polymer synthesis.
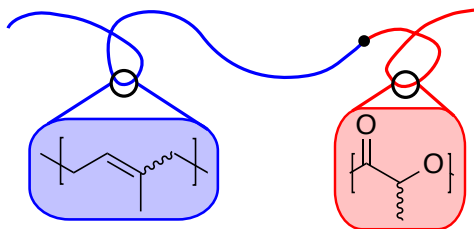
Figure 1.1 Illustration of a linear diblock copolymer.

The universal phase behavior of block polymers provides a framework for rational materials design. Precise control during block polymer synthesis (i.e., judicious choice of the monomer units employed, block molecular weights, and molecular architecture) enables tailoring of block chemical and physical properties, morphology, characteristic length scale, and dynamics. Such exquisite control of properties has led to block polymers being utilized in a diverse array of existing commercial products such as thermoplastic elastomers, adhesives, and surfactants,[7] as well as enabling applications in a variety of emerging technologies[6,8,9] including next-generation lithographic materials,[10] batteries,[11] and drug delivery.[12] A fundamental understanding of block polymer self-assembly is a critical prerequisite for materials design and use in future applications. In addition, the same unique ability to tune the properties that has led to their utility in numerous applications make block polymers excellent model systems for fundamental investigations addressing a diverse array of scientific questions in the field of condensed matter. Consequently, the thermodynamics of block polymer–based soft materials in the bulk, solutions, and blends have been the subject of continued intense experimental and theoretical study.[4,13,14]

The work described in this thesis uses an experimental approach to expand the current fundamental understanding of block polymer self-assembly to a class of materials we call "short" diblock copolymers, which fall outside the current framework used to

interpret block polymer thermodynamics.[15] Short diblock copolymers are block polymers that form ordered nanostructures even at very low molecular weight. In order to overcome the additional configurational entropy that accompanies a reduction in molecular weight and opposes the formation of ordered structures, the monomer units of the different blocks must be selected to be thermodynamically highly incompatible and thus chemically dissimilar. Our interest in short diblock copolymers is motivated by both fundamental and practical considerations. Short diblock copolymers represent a significant departure from the region of validity of the theoretical framework used to understand the thermodynamics of block copolymer self-assembly, which is formulated in the infinite or very high molecular weight limit.[14,16,17] The behavior of short diblock copolymers is influenced by fluctuations, phenomena not properly addressed in the classic statistical mechanical theories of block polymer thermodynamics that become increasingly important as molecular weight is reduced.[17] Therefore, studying short diblock copolymers provides an opportunity to build on the established knowledge of decades of work on block polymer materials and expand this understanding into the range of parameter space where fluctuations dominate.

While the work described in this thesis is of a fundamental nature and therefore does not target any specific application, two broad trends inform our practical interest in short block copolymers. These stem from the low molecular weight and high block incompatibility that characterize short diblock copolymers. First, many emerging applications of block polymers require control of structure at ever decreasing nanoscale dimensions, most notably the directed self-assembly of block polymers for next generation lithographic patterning of microelectronic devices.[8,10,18] Accessing smaller features from self-assembled block polymers is achieved by decreasing the dimensions of the polymer molecules through a reduction in molecular weight. Thus, our interest in studying low molecular weight block polymers is motivated by a desire to understand the physics of self-assembly required to achieve smaller and smaller characteristic features sizes via block polymers. The molecular weight of a block polymer cannot be reduced to achieve arbitrarily small features. Eventually, such low molecular weight "block

polymers" will begin to more closely resemble self-assembling small molecules like lyotropic and thermotropic liquid crystals (as the degree of polymerization approaches 1), which order based on entirely different microscopic physics.[19–21] We are interested in exploring the boundary between block polymer-like behavior and that of self-assembling small molecules, and thus probe the lower limit of feature sizes achievable with block polymers.

Advances in synthetic chemistry continually expand the palette of available monomer units that can be combined into block polymers.[3] Constituent blocks that impart desired functionality are often accompanied by thermodynamic incompatibility. Of particular interest is the development of sustainable polymers derived from renewable feedstock (often natural or biological),[22–24] which tend to have chemical structures containing a much higher proportion of heteroatoms than traditional petroleum based hydrocarbon polymer materials. Incorporation of sustainable blocks into block polymers that also contain more traditional hydrocarbon blocks (e.g., in poly(1,4-isoprene-*b*-DL-lactide), the model materials used throughout this thesis), results in high incompatibility. Thus, knowledge derived from fundamental studies of the thermodynamics of short diblock copolymers is directly relevant for materials design to address future applications requiring small features sizes or that incorporate diverse chemical constituents (e.g., to impart sustainability or achieve a desired functionality).

In the remainder of this chapter, an overview of the current framework used to understand block polymer thermodynamics is presented followed by an outline of the major results of the work described in this thesis.

1.2 Background

1.2.1 *Phase transitions and fluctuations*[*]

Prior to a discussion of the thermodynamics of block polymers, it is useful to introduce several general concepts relating to phase transitions, in particular fluctuations,

---

[*] This information in this subsection is condensed largely from textbooks by Chaikin and Lubensky[120] and Sethna[235] and a review by Stanley.[236]

which will be important throughout the work described in this thesis. Phase transitions, changes between different states of order in matter, are common experiences in daily life, for example the transformations of liquid water to ice or water vapor as temperature is changed. Phase transitions separate states (phases) with vastly different properties. The transformation between different phases of water is accompanied by a discontinuous change in certain properties (e.g., density) that result from changes in the organization of the molecules at microscopic length scales. This discontinuous change in properties is the defining feature of a *discontinuous* or *first-order* phase transition, one of two general classes of phase transitions illustrated in Figure 1.2. First-order transitions are accompanied by a *latent heat*, a characteristic amount of energy that is absorbed or released at the transition temperature during the phase transformation, and typically proceed by a nucleation and growth mechanism. More exotic phase transitions occur when changes in different types of microscopic order are possible. For example, a ferromagnetic material will lose its net magnetization at zero magnetic field if heated above a certain temperature called the Curie temperature, above which the material behaves as a paramagnet. In this case, the property of interest (magnetization) changes continuously through the phase transition, exhibiting no abrupt change at the transition. This is an example of a *continuous* or *second-order* phase transition, often called a critical point, the second general class of phase transitions. These occur without a latent heat, but instead may be accompanied by *fluctuations* near the transition. Fluctuations are transient spatial heterogeneities of the properties of a material that arise from random thermal motion within the material.

At any equilibrium phase transition, the free energy of the two phases is equal. However, thermodynamic derivatives of free energy can exhibit discontinuities or other non-analytical behavior at phase transitions. The lowest order of the derivative of the free energy that is discontinuous is the basis for the classical Ehrenfest classification scheme for phase transitions. Therefore, discontinuities in the first derivative of the free energy (e.g., entropy, enthalpy, volume, density, etc.) define first-order transitions while discontinuities in the second derivatives (e.g., heat capacity, compressibility, etc.) with

continuous first derivatives define second-order phase transitions, as illustrated for enthalpy and heat capacity in Figure 1.2. While the nomenclature of this classification scheme is commonly employed (i.e., first- and second-order transitions), so-called second-order transitions often do not exhibit discontinuities in the second derivatives of the free energy, but instead exhibit other non-analytical behavior at a critical point such as divergence to infinite values. Therefore, phase transitions are more precisely classified as discontinuous, characterized by a jump in properties and a latent heat, or continuous, which lack a latent heat. In this thesis, both nomenclatures are used interchangeably.
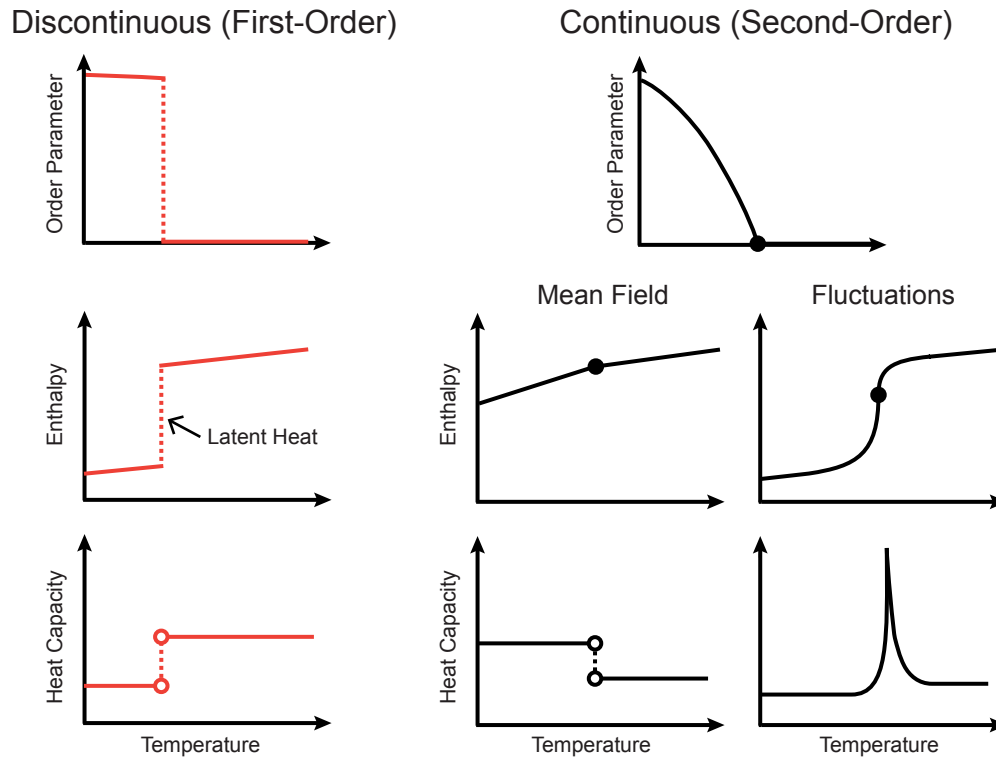
Figure 1.2 Illustration of the two general classes of phase transitions. For continuous phase transitions, the failure of mean-field theory to properly account for fluctuation effects near the critical point, particularly in the heat capacity, is shown. The heat capacity is not defined precisely at a phase transition (shown as open circles) and would appear infinite. Inspired by a similar figure in Thoen et al.[25]

A deep understanding of critical phenomena, the study of behavior near a critical point (i.e., a continuous or second-order phase transition), and the concept of universality

was a major achievement of physics in the 20th century. Regardless of the specific material and type of microscopic order that changes at a phase transition, certain measurable properties display universal behavior near continuous transitions characteristic of one of a small number of categories, called universality classes. Specifically, the evolution of properties like the heat capacity exhibit power law divergence as the critical point is approached with characteristic critical exponents shared by all systems in a specific universality class. Systems with vastly different microscopic physics (e.g., the ferromagnet discussed above, boiling a pure liquid at its critical pressure, and the phase separation of an immiscible blend of two homopolymers at the critical composition) exhibit equivalent behavior when analyzed in the appropriate framework, as they belong to the same universality class (i.e., 3D Ising). In this framework, the free energy of the system is recast as a function of a quantity called the order parameter. The order parameter reflects the microscopic order of the system that changes at a phase transition. It is defined at any point in space (i.e., it is a field) and can be a scalar, vector, or more complicated quantity. For a given system, the choice of order parameter is not always obvious. In the case of the ferromagnet above, the order parameter is net magnetization; in the boiling of a liquid at the critical pressure, a quantity related to density is the appropriate order parameter; and in phase separation of immiscible liquids, departure of the local composition from the average composition is a suitable choice of order parameter. The different universality classes stem from differences in the underlying symmetry breaking of the order parameter at the phase transition.

The qualitative thermodynamic behavior near phase transitions can be described by so-called mean-field theory, a theoretical approach in which the intractable many-body interactions of the individual microscopic components of the system (e.g., spins, polymer molecules) are coarse-grained by treating each component as interacting with the average of all the other components. This approach ignores local correlations in the system (i.e., when the local properties differ from the average properties). Despite this, generic mean-field approaches (i.e., the Landau theory of phase transitions) capture many

of the features relating to phase transitions, including the existence of continuous and discontinuous phase transitions and the divergence of specific quantities near a continuous phase transition (i.e., the order parameter, susceptibility, correlations length). Mean-field theory predicts a single set of critical exponents that do not agree with experiments. This is a result of the profound influence of fluctuations (correlations) near continuous phase transitions, which are not treated appropriately in mean-field theory. For example, mean-field theory predicts a simple jump in heat capacity at the critical point when divergence of the heat capacity is observed in many experimental systems, as illustrated in Figure 1.2. More sophisticated theoretical approaches beyond mean-field theory (i.e., renormalization group theories) allow proper treatment of fluctuations as a continuous phase transition is approached. These methods allow calculation of the critical exponents for different microscopic models and have been found to agree with experimental critical exponents for many systems.

Fluctuations are transient spatial heterogeneities of the properties of a material driven by random thermal motion. Fluctuations herald the imminent continuous phase transition as a critical point is approached, with the characteristic size of the fluctuations (the correlation length) diverging at the transition. This is the mechanism for undergoing a continuous phase transition. In the case of the ferromagnetic material, at high temperature thermal motions randomize the spins and there is no net magnetization at zero magnetic field. As temperature is reduced approaching the critical point, the propensity of neighboring spins to align in the same direction leads to fluctuations in the local order parameter (magnetization) over small length scales. There are small regions (fluctuations) that form spontaneously and exhibit a net magnetization. In general, fluctuations have a characteristic size, the correlation length, and amplitude, the local value of the order parameter. Above the critical temperature, there are an equal amount of spin up and spin down fluctuations and hence no net magnetization at large length scales. At the critical point, the correlation length of the fluctuations diverges, leading to a net magnetization at all length scales (as if the entire sample is within a single fluctuation), though the amplitude is differentially small. On further cooling, the amplitude grows and

net magnetization increases. This mechanism contrasts with the nucleation and growth that occurs in a discontinuous phase transition. Fluctuations profoundly influence the phase behavior of block polymers and become increasingly important as molecular weight is reduced.

1.2.2 Multicomponent polymer systems

The long chain-like nature of polymer molecules makes them particularly amendable to mean-field theory.[26–28] The large spatial extent of polymer molecules leads to interactions being averaged over many contacts with neighboring molecules. The classic mean-field Flory–Huggins theory is very successful in describing the thermodynamics of mixtures of unlike polymers. In Flory–Huggins theory,[26,27] the free energy of mixing polymers of type A and B with volumetric degrees of polymerization N_A and N_B, respectively, is given by

$$\frac{\Delta G}{k_B T} = \frac{\phi_A}{N_A}\ln\phi_A + \frac{\phi_B}{N_B}\ln\phi_B + \phi_A\phi_B\chi_{AB} \qquad 1.1$$

where ϕ_A and ϕ_B are the volume fractions of each polymer in the mixture ($\phi_A + \phi_B = 1$), χ_{AB} is the segment–segment interaction parameter, k_B is the Boltzmann constant, and T is temperature. The first two terms represent the center-of-mass configurational entropy of mixing, which favors mixing and is inversely proportional to the polymer degrees of polymerization. The last term is the enthalpy of mixing resulting from contacts between monomers of types A and B, the magnitude of which is captured by the parameter χ_{AB}. For typical molecular weights, the entropy of mixing is small due to the inverse dependence on N. Even a very small positive value of χ_{AB} is sufficient to drive macroscopic phase separation of unlike polymers.

The magnitude of χ_{AB} is determined by the chemical structure of the repeat units. Within the context of Flory–Huggins lattice theory, χ_{AB} is a strictly enthalpic quantity and is the energy in units of $k_B T$ of the difference in interaction energy of an A-B monomer contact and the average of A-A and B-B contacts (i.e., the exchange energy). For cases in which van der Waals forces are the only important interactions, χ_{AB} is inversely proportional to temperature and always positive (i.e., unlike A-B contacts are

unfavorable). In practice, χ_{AB} is not a directly measurable quantity and must be calculated by fitting experimental results to a particular theoretical prediction. An empirical form $\chi_{AB} = \alpha/T + \beta$, where α and β are constants, is often assumed to subsume non-idealities into the effective $\chi_{AB}(T)$ function, where β accounts for the excess (non-combinatorial) entropy of mixing. In these cases, the quality of the extracted $\chi_{AB}(T)$ will obviously depend on the accuracy of the applied theory. In the absence of experimental data, χ_{AB} can be approximated based on the associated solubility parameters (δ_i): $\chi_{AB} = (V/RT)(\delta_A - \delta_B)^2$ where V is the repeat unit molar volume and R is the gas constant. Heating a polymer mixture generally reduces χ_{AB}. Figure 1.3 shows the solubility parameters for several common polymer repeat units, emphasizing that large χ_{AB} result when there are large chemical differences between the different polymer repeat units. In all cases, the magnitude of χ_{AB} depends on the reference volume used to define the monomer unit.
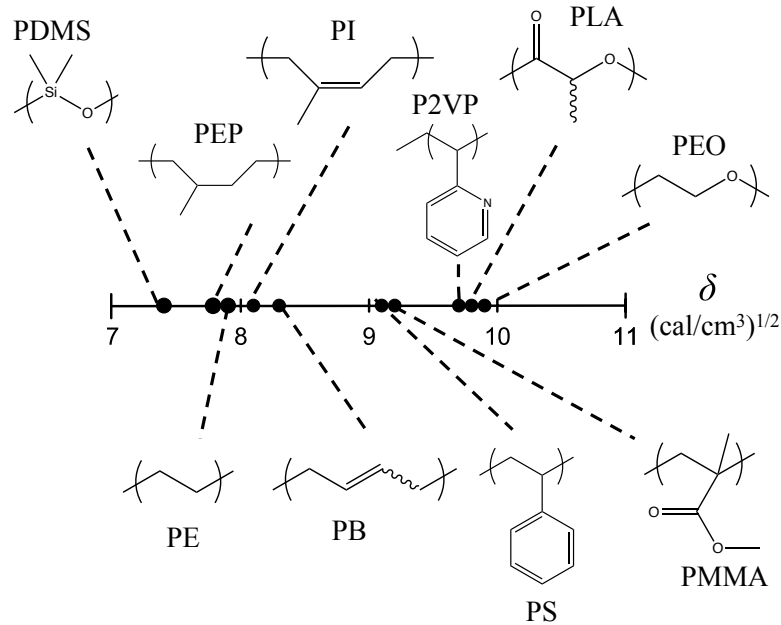
Figure 1.3 Solubility parameters of common polymers. Poly(dimethyl siloxane) (PDMS), poly(ethylene-*alt*-propylene) (PEP), polyethylene (PE), poly(1,4-isoprene) (PI), poly(1,4-butadiene) (PB), polystyrene (PS), poly(methyl methacrylate) (PMMA), poly(2-vinyl pyridine) (P2VP), poly(DL-lactide) (PLA), and poly(ethylene oxide) (PEO).[27,29–31]

For volumetrically symmetric polymer blends ($N_A = N_B = N$), Flory–Huggins theory predicts the phase behavior summarized in Figure 1.4. A mean-field critical point is predicted at $\chi N = 2$ and $\phi_A = 0.5$. The segregation strength χN is a dimensionless measure of the relative importance of enthalpy ($\sim \chi$) and combinatorial entropy ($\sim 1/N$). At low χN (high T), entropy dominates and the polymers mix. At high χN (low T), enthalpy dominates and macrophase separation occur. Mean-field theory describes the thermodynamics in all but a small region of this phase diagram near the critical point where non-mean field fluctuations become important and crossover to 3D Ising critical behavior has been measured.[28,32] The region in χ near the critical point where fluctuations are important is proportional to N^{-1} and therefore shrinks with increasing molecular weight. In the limit of infinite molecular weight, mean-field theory becomes exact.
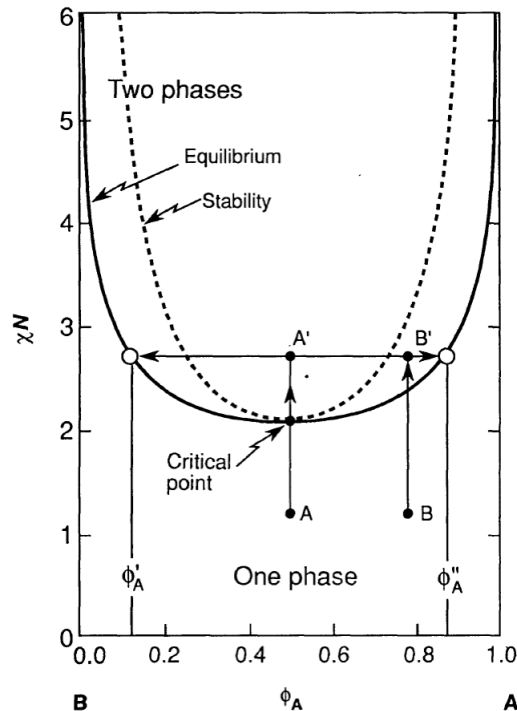
Figure 1.4 Phase diagram of symmetric binary homopolymer blends. From Bates, F. S. *Science* **1991**, *251*, 898–905. Reprinted with permission from AAS.[26]

1.2.3   *Thermodynamics of high molecular weight block polymers*

A block polymer is formed when two or more polymer chains, called blocks, with different constituent monomer units are covalently linked together. An endless variety of block polymers can be envisioned by combining different numbers of blocks in different sequences and architectures,[3] the simplest being the AB diblock copolymer (...-A-A-A-B-B-B-...) shown in Figure 1.1. The single covalent bond linking the A and B blocks profoundly influences the thermodynamics. Macroscopic phase separation to reduce unfavorable contacts between the thermodynamically incompatible A and B type monomer units is not possible. Instead, a delicate interplay is established between the enthalpic drive to separate the A and B blocks and the entropic penalty incurred when the polymer chain stretches to separate the blocks. This tradeoff leads to self-assembly into a variety of ordered mesophases in a process called microphase separation. As with the homopolymer blends, mean-field theoretical tools, specifically self-consistent mean-field

theory of a standard Gaussian chain model (SCFT), have been successful in describing much of the physics associated with block polymer self-assembly and phase behavior.[2,14,16,33–38]

In a seminal publication,[16] Leibler calculated the phase portrait for AB diblock copolymers in the mean-field limit near the order–disorder transition (ODT) phase boundary (in the so-called weak segregation limit applicable at small values of χN). Leibler predicted that in the mean-field (infinite N) limit, the phase behavior of AB diblock copolymers depends on only two coarse-grained parameters: the composition f_A (the volume fraction of the A-block) and the segregation strength χN. The composition, $f_A = N_A/(N_A + N_B)$, primarily controls the geometry of the ordered mesophase formed, while the segregation strength χN dictates the strength of the effective repulsion between the blocks and thus the ODT phase boundary. We note that heating a block copolymer melt generally reduces χN as χ_{AB} is typically inversely proportional to temperature. Leibler's initial mean-field phase portrait has been refined by other theorists, notably Matsen and co-workers,[37,39–43] and these advances in theoretical methodology, amplified by ever greater computational resources, has resulted in the well established SCFT that is in routine use today. A recent SCFT phase portrait is reproduced in Figure 1.5 illustrating the conditions required to form the various equilibrium mesophases including the disordered phase (DIS), a body-centered cubic arrangement of nearly-spherical point-particles (BCC), hexagonally packed cylinders (HEX), lamellae (LAM), and the bicontinuous gyroid morphology (GYR).
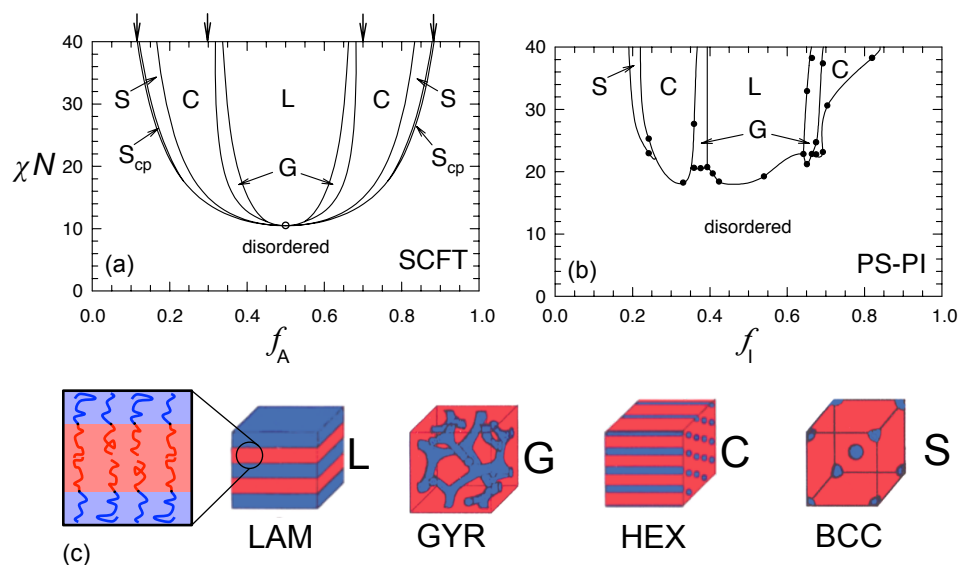
Figure 1.5 Theoretical and experimental diblock copolymer phase portraits. SCFT phase portrait (a), experimental polystyrene-*b*-polyisoprene (PS-PI) phase portrait (b), and illustrations of the most common ordered block polymer mesophases (c). In (a), the regions labeled S_{cp} are where a close packing of point-particles is the equilibrium phase and the arrows across the top indicate order–order phase boundaries calculated from asymptotic theories in the limit of infinite χN (the so-called strong segregation limit). Adapted with permission from various sources.[33,37] Copyright IOP Publishing. All rights reserved.

SCFT has been remarkably successful in capturing the general features of experimentally documented diblock copolymer phase behavior (as well the phase behavior of other types of inhomogeneous polymers), accounting for the various equilibrium ordered phases that occur in diblock copolymer and the approximate location of the order–order phase boundaries, as shown in Figure 1.5.[2,5,14,37,38] SCFT has become an indispensible tool in understanding block polymer phase behavior. Notable results include Leibler's initial prediction of BCC symmetry for asymmetric diblocks[16] that was later confirmed[44] and is now ubiquitous, aiding in identifying the GYR phase as the appropriate equilibrium bicontinuous morphology,[45] and the prediction by Tyler and Morse[42] of a new equilibrium network morphology that was later confirmed in experiments.[46] SCFT has also been used to study the influence of various molecular non-idealities, such as dispersity and statistical segment length asymmetry, on the phase

behavior of block polymers.[34,36,47] In addition, recent simulations suggest SCFT is remarkably accurate within the ordered phase.[48] As a result, the conceptual framework established by SCFT, specifically the universal χN versus f_A phase portrait, is generally used to interpret experimental block polymer phase behavior and in materials design.

Despite the success of SCFT at describing the ordered phases, mean-field theory fails spectacularly near the order–disorder phase boundary. This is a result of the importance of non-mean-field fluctuations in (primarily) the disordered phase, which SCFT, a mean-field theoretical tool, does not consider. SCFT fails to capture the topology of the experimental phase portrait (Figure 1.5b) near the ODT phase boundary, predicting all order–order and order–disorder phase boundaries meet at a mean-field critical point at $(\chi N)_{ODT} = 10.5$ and $f = \frac{1}{2}$, illustrated with the open circle in Figure 1.5. This continuous (second-order) phase transition is illustrated in Figure 1.6. The mean-field uniform and homogeneous disordered state (Figure 1.6a) is predicted to give way to an ordered lamellar phase with a differentially small amplitude of the composition profile (Figure 1.6b). This amplitude then grows as χN is increased, for example by decreasing the temperature. This type of ODT does not occur in real diblock copolymers of finite molecular weight. Fluctuations destroy the mean-field critical point and the ODT is instead a fluctuation-induced weakly first-order transition at all compositions. The influence of fluctuations is discussed in more detail in section 1.2.4.

In addition to calculating the phase portrait in the mean-field limit, Leibler also calculated the structure factor for a diblock copolymer at the level of the random phase approximation (RPA) that has proved useful for interpreting and analyzing experimental scattering data.[16] This structure factor produces a broad peak at intermediate values of q, the momentum transfer vector, even at $\chi = 0$. This peak does not result from segregation of the blocks, but rather from the "correlation hole" effect resulting from the connectivity of the blocks. The intensity of the peak diverges at the mean-field spinodal, leading to a linear dependence of the inverse of the peak intensity on inverse temperature (i.e., χ) as the spinodal is approached. Such linear divergence is characteristic of mean-field theory predictions. Plotting experimental data in this form can be used to judge if mean-field

theory (i.e., the RPA structure factor) is appropriate for interpretation of experimental data.
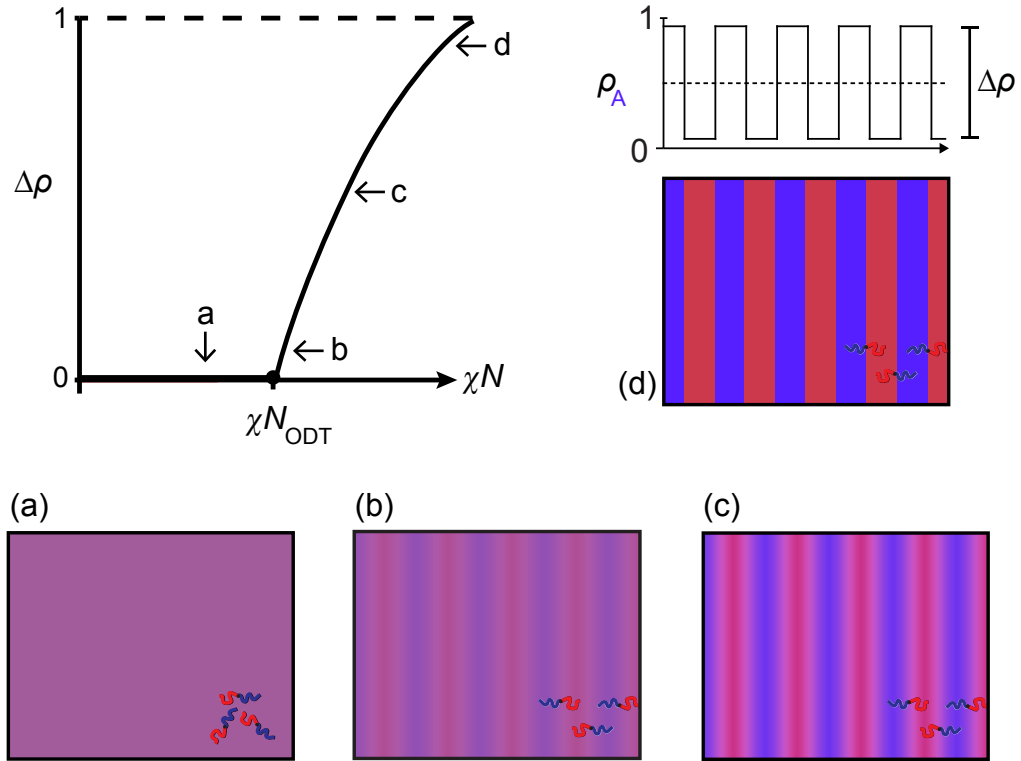
Figure 1.6 Illustration of the order–disorder transition predicted by mean-field theory for symmetric diblock copolymers. (a) through (d) illustrate the evolution of the state of segregation as χN increases at the points indicated. The meaning of the quantity $\Delta\rho$, the amplitude of the composition profile, is indicated in (d).

1.2.4   Fluctuation effects in block polymers

Following a seminal publication by Brazovskii,[49] Frederickson and Helfand proposed a correction to Leibler's theory in an attempt to account for the effects of fluctuations at finite N and bring theoretical prediction more in line with experimental fact.[17] The disordered state in the vicinity of the ODT is not simply homogeneous as depicted in Figure 1.6a and considered by SCFT, but is instead characterized by thermally induced local composition fluctuations. Unlike the examples discussed in

section 1.2.1, the characteristic length scale of these composition fluctuations cannot exceed the size of the polymer molecules (i.e., the radius of gyration) owing to the connectivity of the blocks. Instead of increasing in characteristic size, the amplitude of the fluctuations increases as χN is raised, producing a degree of disordered, dynamically rearranging microphase segregation at values of χN well below the transition to the ordered phase. The instantaneous structure of the fluctuating disorder state is thought to resemble the patterns observed during spinodal decomposition of immiscible liquids but with a characteristic length scale appropriate for the block polymer (i.e., the radius of gyration).[50] In the Fredrickson–Helfand (FH) theory, composition fluctuations are found to break the second-order character of the ODT for symmetric diblocks resulting in a discontinuous, fluctuation induced weakly first-order phase transition, illustrated in Figure 1.7. The theory predicts a discontinuous (N dependent) change in the local composition profile at the ODT coincident with the fluctuating disordered state transforming to the ordered lamellar morphology.
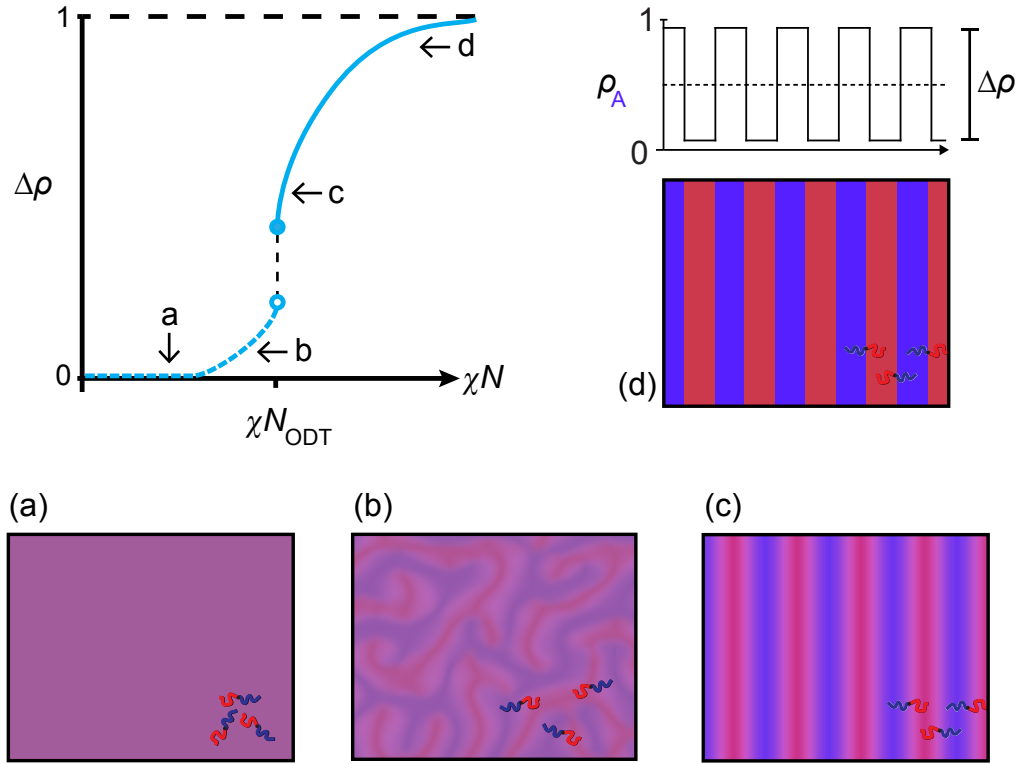
Figure 1.7 Illustration of the order–disorder transition predicted by the FH theory for symmetric diblock copolymers. (a) through (d) illustrate the evolution of the state of segregation as χN increases at the points indicated. In the fluctuating disordered state (b), $\Delta \rho$ is meant to illustrate the instantaneous amplitude of the concentration fluctuations.

In the FH theory, the thermodynamic state of a diblock copolymer depends on a third parameter in addition to χN and f, which determines the influence of fluctuations. This additional parameter is the invariant degree of polymerization $\bar{N} \equiv N b^6 / v_o^2$, where b is the statistical segment length and v_o is the reference volume used to define N and b. Unlike N, the value of $\bar{N}$ does not depend on the choice of monomer reference volume. $\bar{N}$ is a measure of the extent of overlap between chains in the melt (it is equivalent to the square of the ratio of the pervaded volume of a chain, $(N^{1/2}b)^3$, to the occupied volume of the chain, Nv_o). At high $\bar{N}$, each chain interacts with a large number of neighboring chains, averaging interactions and leading to more mean-field-like behavior. In the limit

of infinite $\bar{N}$, the FH theory reduces to the SCFT prediction. However, as $\bar{N}$ is reduced, fluctuations becoming increasingly important.

In FH theory, fluctuations stabilize the disordered phase and effectively cut off the bottom of the SCFT phase portrait, shifting the ODT phase boundary to higher values of $(\chi N)_{\mathrm{ODT}}$. The magnitude of this shift increases with decreasing N. An example of a fluctuation corrected theoretical phase portrait is shown in Figure 1.8, in which Hamley and Podneks[51] have extended the original FH theory to include the GYR phase. For a symmetric ($f_A = 0.5$) diblock, FH theory predicts that the ODT occurs at a value of

$$(\chi N)_{\mathrm{ODT}} = 10.5 + 41.0\,\bar{N}^{-1/3} \qquad\qquad 1.2$$

The FH theory phase portrait is in much better qualitative agreement with experiments (e.g., Figure 1.5b), where the disordered phase and the various ordered phases make direct contact at a first-order transition, including for symmetric diblock copolymers.
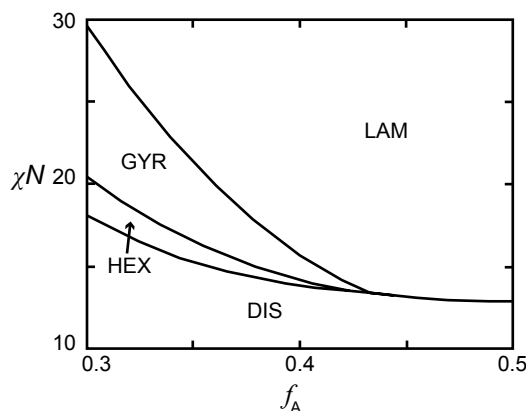
Figure 1.8 Fluctuation corrected theoretical phase portrait. Phase portrait for $\bar{N}$ of 500. Adapted with permissions from Hamley, I. W.; Podneks, V. E. *Macromolecules* **1997**, *30*, 3701–3703. Copyright 1997 American Chemical Society.[51]

The FH theory is successful at capturing certain qualitative features of the phase behavior of real diblock copolymers near the ODT, including the topology of the phase portrait. However, the FH theory represents a correction to Leibler's mean-field theory aimed at revealing the primary effects of fluctuations on block polymer phase behavior and therefore contains several approximations that limit the applicability to nearly

symmetric block polymers over a fairly narrow range of segregation strengths and chain lengths. It is only strictly valid at values of $\bar{N}$ approaching 10^9 and is therefore not quantitatively accurate for realizable experimental polymers.[17,48,51] Variations and improvements of the original FH theory have been reported,[52–58] and all find that the thermodynamic state of a diblock copolymer depends only on the variables of the FH theory (f, χN, and $\bar{N}$), though none have yet gained traction in the field and found to be useful for interpretation of experimental results for polymers of typical molecular weights. Therefore, there is a lack of a comprehensive theory of block copolymer phase behavior at all but the highest molecular weights. The short diblock copolymers studied here fall well outside the range of validity of any quantitative theory. They provide an opportunity to build an experimental data set useful for validation of future theories, with the possibility of revealing qualitatively different behavior than the high molecular weight analogues.

Recently, Morse and co-workers[48,56,57,59–61] have made developments in simulation methodology and advances in a renormalized one-loop (ROL) theory of correlations in the disordered phase, an improvement beyond the RPA that similarly yields a prediction for the structure factor, that have enabled comparison of simulations with theoretical predictions and experimental measurements. Such comparisons are challenging owing to ambiguities involved with the proper evaluation of the parameter dependence of χ (i.e., temperature dependence in experiments and control parameter dependence in simulations). A collaboration with Morse and co-workers in which such a comparison is attempted is the subject of Chapter 7.

Although no comprehensive theory exists for the influence of fluctuations on the behavior of block copolymers of typical experimental molecular weights, the manifestations of fluctuations have been measured using a variety of techniques[62–67] including small-angle X-ray and neutron scattering (SAXS and SANS),[50,68–73] transmission electron microscopy (TEM),[74–76] and rheology.[77–79] Figure 1.9 shows representative examples of evidence of fluctuations deduced from rheology experiments, where fluctuations cause a failure of time–temperature superposition of the dynamics

near the ODT (Figure 1.9a), and SANS experiments, where failure of the RPA theory is evident as upward curvature in the plot of inverse peak intensity versus inverse temperature (Figure 1.9b).
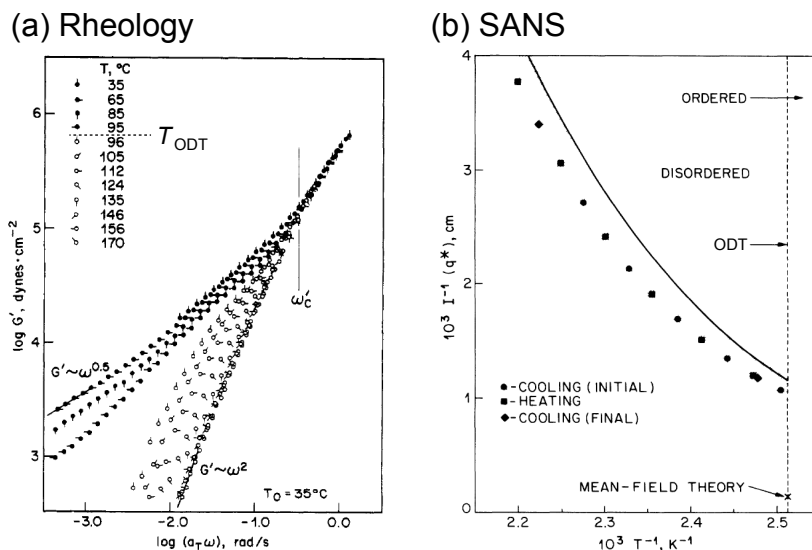
Figure 1.9 Experimental evidence of fluctuations. Fluctuations result in a failure of time–temperature superposition near the ODT in rheology experiments, shown in (a), and cause upward curvature when the inverse of the scattering peak intensity is plotted as a function of inverse temperature, as shown for small-angle neutron scattering (SANS) experiments in (b). (a) Adapted with permission from Rosedale, J.; Bates, F. S. *Macromolecules* **1990**, *23*, 2329–2338. Copyright 1990 American Chemical Society.[78] (b) Adapted with permission from Bates, F. S.; Rosedale, J. H.; Fredrickson, G. H.; Glinka, C. J. *Phys. Rev. Lett.* **1988**, *61*, 2229–2232. Copyright 1988 American Physical Society.[72]

With a few notable exceptions,[80–86] the thermodynamics associated with the ODT in general, and the effects of fluctuations specifically, have been studied using indirect experimental techniques, such as the rheology and SANS experiments summarized in Figure 1.9. Direct, model independent thermodynamic measurements of the influence of fluctuations on block polymers by differential scanning calorimetry (DSC) and relaxation calorimetry are a major achievements of the work described in Chapters 3 and 6 of this thesis.

1.3 Overview

This thesis involves the synthesis and detailed thermodynamic characterization of a series of model short diblock copolymers using a variety of experimental tools, including SAXS, SANS, rheology, and thermal analysis techniques. The overarching theme of the work is to take advantage of opportunities afforded by short diblock copolymers to expand understanding of block polymer thermodynamics and dynamics. This has resulted in the discovery of new behavior, including quasicrystalline order (Chapter 4), and led to an expansion of the experimental toolkit for block polymer characterization, with the adaptation and application of relaxation calorimetry (Chapter 6) in conjunction with new approaches for exploiting established tools like DSC (Chapter 3).

The model materials selected for study throughout this thesis are a series of poly(1,4-isoprene-*b*-DL-lactide) (IL) diblock copolymers. These polymers were chosen based on the large segment–segment interaction parameter χ_{IL} (i.e., polyisoprene and polylactide have very different solubility parameters and lie far apart in Figure 1.3). This enables experimentally accessible order–disorder transition temperatures, T_{ODT}s, (i.e., $T_{g,I} < T_{g,L} < T_{ODT} < T_{deg}$, where $T_{g,I}$ and $T_{g,L}$ are the I and L block glass transition temperatures and T_{deg} is the temperature at the onset of polymer degradation) for IL diblocks of low molecular weight ($M_n \approx 2$–6 kg/mol). IL diblocks cover a regime where fluctuations are expected to (and indeed do) dominate the phase behavior and where existing theories provide minimal guidance. Low molecular weight combined with the low block T_gs result in polymers that have fast molecular dynamics, which allow these materials to respond rapidly to changes in the state of the system (e.g., changes in temperature), thus overcoming kinetic limitations that plague most experimental studies. This work has relied on thermal characterization tools such as DSC and relaxation calorimetry and precise small-angle X-ray and neutron scattering techniques (SAXS and SANS). In addition, the IL diblocks were chosen to build upon recent work in the group in which Lee et al.[87,88] discovered a new equilibrium phase in an IL diblock copolymer, the Frank–Kasper σ phase.

In Chapter 2, the synthesis of model IL diblock copolymers is detailed and the experimental approaches used through the remainder of the thesis are outlined. Methods used for molecular, thermodynamic, dynamic, and structural characterizations are reviewed.

Chapter 3 presents a detailed experimental investigation of the influence of fluctuations on the order–disorder transition in IL diblock copolymers, the result of a collaboration with Sangwoo Lee.[15] In this work, the IL phase portrait is experimentally mapped and $\chi_{IL}(T)$ is estimated. The primary conclusion of this work is that the ODT in short diblock copolymers is found to proceed as a pattern transition, as illustrated in Figure 1.10 for symmetric diblock copolymers, with no change in the local composition profile normal to the I/L interface occurring at the ODT. The fluctuating disordered phase is characterized by large amplitude fluctuations that transforms into the static ordered mesophases at the ODT without additional demixing of the blocks. In symmetric diblock copolymers, this involves a rearrangement of the I/L interface from the cocontinuous disordered phase characterized by negative Gauss curvature to the ordered LAM phase with flat interfaces. This is accompanied by a reduction in interfacial area resulting in small but measurable latent heats. In asymmetric diblock copolymers, fluctuations manifest as micelle-like particles that order onto a BCC lattice at the ODT. This does not require any change in the I/L interface and consequently, exceedingly small latent heats are measured by DSC. These conclusions are further supported by SAXS experiments near the ODT.
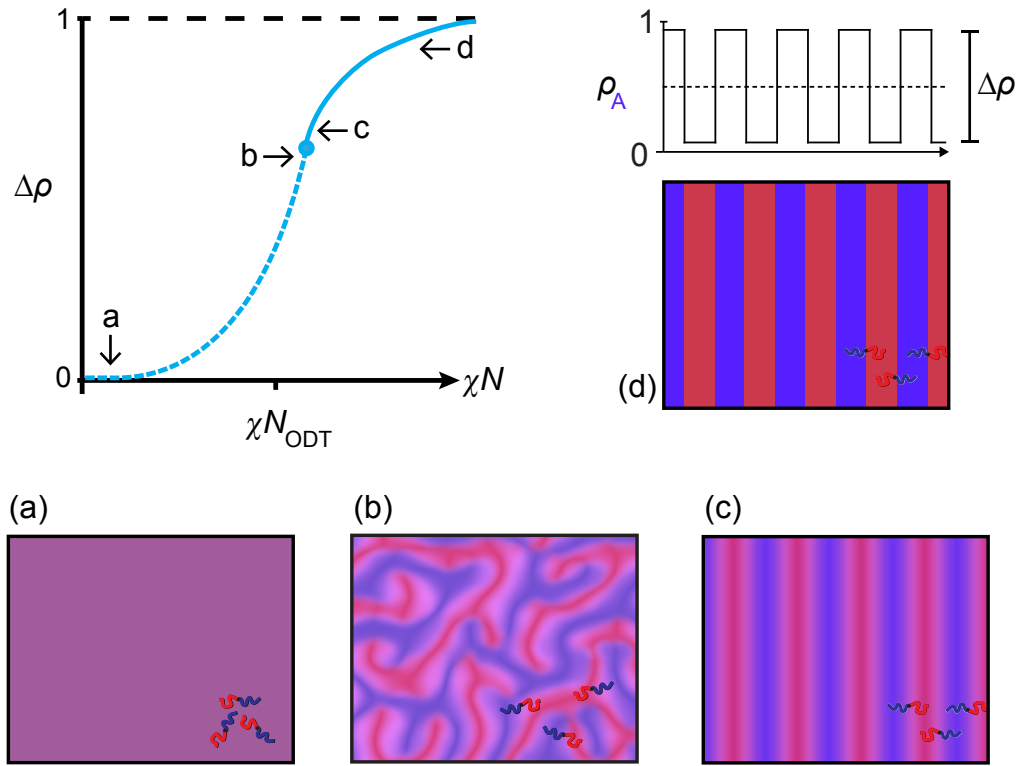
Figure 1.10 Illustration of the order–disorder transition in short diblock copolymers. (a) through (d) illustrate the evolution of the state of segregation as χN increases at the points indicated. In the fluctuating disordered state (b), $\Delta\rho$ is meant to illustrate the instantaneous amplitude of the concentration fluctuations.

In Chapter 4, the discovery of a phase with quasicrystalline long-range order in an IL diblock copolymer is presented. A dodecagonal quasicystalline (DQC) phase is found to be a long-lived metastable state that forms from the supercooled disordered phase after a rapid deep quench from above T_{ODT} into the region of equilibrium stability of the σ phase. Extensive SAXS and rheology experiments conclusively establish the topology of the equilibrium phase portrait where the σ and DQC phases form. An interesting kinetic phenomenon is also documented. The disordered state formed upon quenching from above T_{ODT} goes through a transition from a supercooled metastable liquid state to a nonequilibrium disordered solid state over a narrow range in temperatures, analogous to a

glass transition. The relationship between this interesting quenched disordered state and the formation of the DQC is explored.

The phase behavior of a series of additional IL polymers over a range of f_L and N near the reported σ phase is presented in Chapter 5. The discoveries detailed in Chapter 4 were a serendipitous result of the project summarized in Chapter 5. The main result of the work of Chapter 5 is the establishment of the range in composition f_L over which the σ phase is an equilibrium phase. Studying the σ phase presents significant experimental challenges owing to kinetic limitations that exist even in the very low molecular weight IL diblock copolymers. Consequently, the results presented in Chapter 5 are not comprehensive and, in isolation, are not conclusive. However, taken together with Chapter 4, they provide a reasonably complete picture of the phase portrait for asymmetric IL diblock copolymers. A primary outcome of the effort described in Chapter 5 was an evolution of the synthetic technique, sample preparation, processing, and experiment design that enabled the discoveries of Chapter 4.

In Chapter 6, a thermal analysis technique popular in the hard materials community, relaxation calorimetry, is adapted for measurements of the equilibrium heat capacity of a symmetric IL diblock copolymer near the ODT.[89] Precise measurements of the latent heat and temperature dependence of the heat capacity near the ODT do not reveal evidence of pretransitional divergence of the heat capacity but do indicate a finite width of the transition. The finite width of the ODT is rationalized to be due to dispersity in the IL diblock copolymer through the use of simple model.

Chapter 7 summarizes a collaboration[90] with the theoretical and computational research group of Prof. Dave Morse, in which the detailed thermal measurements of the ODT described in Chapters 3 and 6 are combined with SAXS and SANS measurements to compare the behavior of a symmetric IL diblock copolymer with the universal behavior documented in simulations.[48,59] This comparison is enabled by the ROL theory of correlations in the disordered state of diblock copolymers, which is used to systematically estimate χ in both experiments and simulations.[48,56,57,59–61]

In the appendices that follow the body of this thesis, the result of an additional highly collaborative project with other researchers in the research groups of Prof. Frank Bates and Prof. Tim Lodge are presented in the form of manuscript reproductions.[91,92] This project has studied a second class of block polymer–based soft materials (in addition to short diblock copolymers) in which fluctuation effects play a central role—ternary blends of an AB diblock copolymer with the constituent A and B homopolymers. These blends span the divide in parameter space between the phase behavior of pure (symmetric) diblock copolymers and that of binary homopolymers blends (summarized in in Figure 1.4). Microphase separation of symmetric diblock copolymers and macroscopic phase separation of binary homopolymer blends belong to different universality classes (Brazovskii versus 3D Ising) and are influenced by fluctuations differently. Mean-field theory predicts that the diblock copolymer-like (characterized by microphase separation and an ODT) and homopolymer blend-like (characterized by macroscopic phase separation) regions of phase diagram meet at an isotropic Lifshitz multicritical point. In practice, fluctuations destroy this higher-order critical point and a region of stability of a technologically interesting polymeric bicontinuous microemulsion phase separates the regions of microphase separation and macroscopic phase separation, the so-called microemulsion channel.[93] The polymeric bicontinuous microemulsion is a fluctuation stabilized equilibrium disordered phase with co-continuous A and B domains separated by an A/B interface. The collaborative project, of which the manuscripts reproduced in the appendices represent only a portion of the work, explores the role of fluctuations throughout the ternary blend parameter space.

Chapter 2:

Polymer Synthesis and Characterization Methodology

2.1 Polymer Synthesis

To synthesize model polymers with precise control over architecture, molecular weight, and composition, living[94] polymerization techniques are employed. An ideal living polymerization is chain growth in which unwanted termination and chain transfer reactions do not occur. If initiation is fast relative to propagation and the polymerization is allowed to achieve 100% conversion, the number average molecular weight, M_n, can be controlled simply through the ratio of the mass of monomer to the number of moles of initiator used. Chain end functionality can be selected by judicious choice of terminating reaction(s) and initiating species. Block polymers can be synthesized through a variety of strategies, such as by sequential addition of monomers or by taking advantage of end group functionality (e.g., through coupling reactions or reinitiation and polymerization of an additional block(s)).[27]

In an ideal living polymerization with instantaneous initiation, a Poisson distribution of chain lengths is predicted, resulting in a dispersity $Đ$ (PDI) of

$$\text{PDI} = \frac{M_w}{M_n} = 1 + \frac{N_n}{(1+N_n)^2} \approx 1 + \frac{1}{N_n}$$
                                                                                        2.1

where M_w and N_n are the weight average molecular weight and the (number) average number of chemical repeat units in the polymer chain, respectively.[27] Therefore, living polymerizations result in a relatively narrow distribution of chain lengths and dispersities considerably less than 1.10 are routine.

In the work described in this thesis, poly(1,4-isoprene-*b*-DL-lactide) (IL) diblock copolymers were synthesized by the two step scheme illustrated in Figure 2.1.[95] End functional ω-hyroxyl poly(1,4-isoprene) (PI-OH) was first synthesized by anionic polymerization, which was subsequently used as a macroinitiator for the aluminum catalyzed ring opening polymerization of the poly(DL-lactide) (PLA) block. This two-step synthetic scheme allows for the preparation of large batches of polyisoprene, which can then be used to synthesize a series of IL diblocks with equivalent polyisoprene-block molecular weights. This is a convenient approach for producing materials to map phase behavior. While the anionic polymerization of PI-OH closely approximates an ideal living polymerization, the polymerization of the PLA block is slightly less well controlled.[96] Consequently, the dispersities of the PLA blocks, while still quite low, are typically higher than that of the polyisoprene blocks. Pertinent details regarding each polymerization are summarized in the following sections.
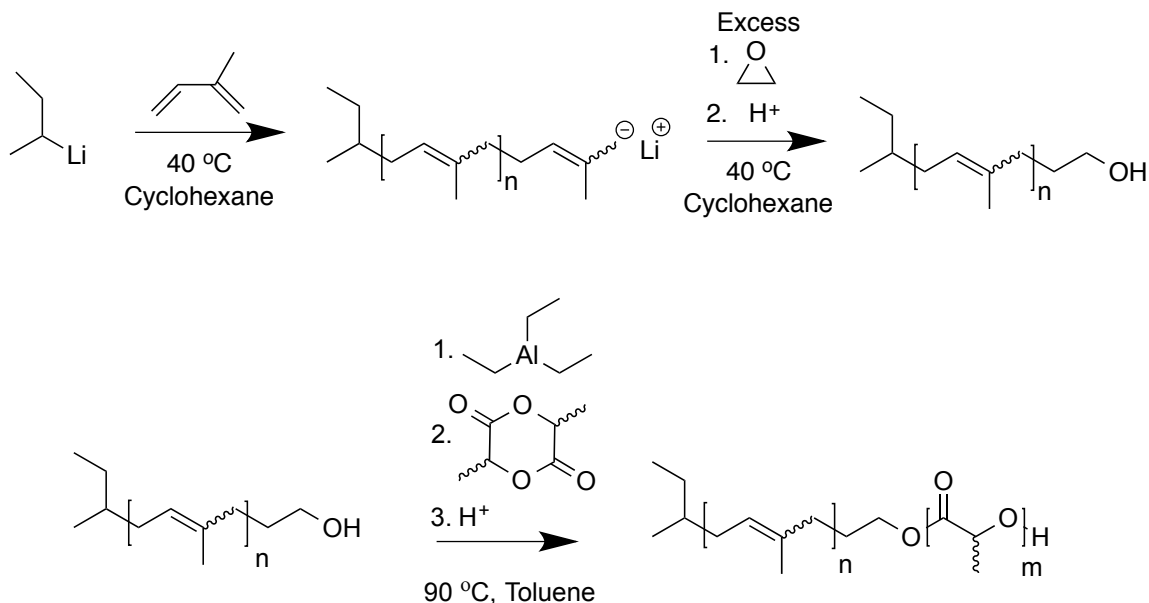
Figure 2.1 Synthesis scheme of the IL diblock copolymers.

2.1.1 *ω-hydroxyl poly(1,4-isoprene) synthesis*

The anionic polymerization of isoprene was accomplished with a lithium counterion in non-polar solvent (i.e., cyclohexane) to achieve a microstructure with high cis-1,4 content.[97] After complete consumption of monomer, the living polyisoprenyl lithium is end-functionalized with a hydroxyl group by reaction with an excess of ethylene oxide prior to termination with methanol. This results in the addition of a single ethylene oxide repeat unit as the covalent character of the oxygen-lithium bond precludes subsequent polymerization of ethylene oxide monomer. Anionic polymerization was accomplished in an argon atmosphere using rigorously purified reagents and solvent to ensure an environment free of oxygen and protic impurities that can cause unwanted termination reactions.

CAUTION: *ANIONIC POLYMERIZATIONS PRESENT MANY HAZARDS AND SHOULD ONLY BE PERFORMED BY PROPERLY TRAINED RESEARCHERS FOLLOWING ESTABLISHED STANDARD OPERATING PROCEDURES UTILIZING APPROPRIATE PERSONAL PROTECTIVE EQUIPMENT AND ENGINEERING CONTROLS. HAZARDS INCLUDE PRESSURIZED GLASSWARE, SOURCES OF*

VACUUM, CRYOGENIC LIQUIDS, POTENTIAL ASPHYXIANTS, FLAMMABLE LIQUIDS, PYROPHORIC LIQUIDS, TOXIC CHEMICALS, HANDLING VOLATILE LIQUIDS IN SEALED GLASS CONTAINERS, SHARPS, ETC. WORKING WITH ETHYLENE OXIDE MONOMER IS PARTICULARLY HAZARDOUS. ETHYLENE OXIDE IS AN EXTREMELY FLAMMABLE, TOXIC, CARCINOGENIC, AND HIGHLY REACTIVE MONOMER WITH A BOILING POINT BELOW AMBIENT TEMPERATURE (B.P. ≈ 10 °C AT 1 ATM). WHEN HANDLED AS A LIQUID IN A SEALED CONTAINER, IT MUST NEVER BE ALLOWED TO WARM UP AS BOILING CAN LEAD TO PRESSURE BUILD UP AND EXPLOSIONS.

Argon gas (high purity grade) was purified by passing through an OMI-2 purifier tube upstream of the Schlenk line. Cyclohexane solvent was degassed by sparging with argon before passing through two columns packed with activated alumina and an oxygen scavenging copper catalyst, respectively, in a custom built solvent purification system prior to use.[98] *sec*-butyllitium (*sec*-BuLi) initiator solutions (approximately 1.3 M in cyclohexane) were used as received (Sigma-Aldrich or Acros Organics). Isoprene and ethylene oxide monomers were degassed by at least three freeze-pump-thaw cycles prior to purification by twice stirring over *n*-butyllithium (*n*-BuLi) at 0 °C for approximately 30 minutes. Methanol used for termination was degassed by sparging with argon gas, several freeze-pump-thaw cycles, or a combination of both methods. The *n*-BuLi purification agent was received as a 2.5 M solution in hexanes (Sigma-Aldrich) and was dried on a vacuum line to remove solvent prior to use. Solvents were used as received for precipitation and other work up procedures.

Modular custom glassware designed specifically for anionic polymerization was used throughout. For isoprene polymerization, a multi-port glass reactor was constructed to contain a Teflon coated magnetic stir bar; a glass thermocouple well deep enough to be submerged when solvent is charged to the reactor; a glass manifold allowing connections to a vacuum/argon Schlenk line and a pressure gauge, along with a port sealed with two stacked rubber septa to allow small additions to the reactor (e.g., initiator, terminating agent); and an airlock designed to allow large addition (e.g., monomer, solvent). In some

cases, a flask containing the purified cyclohexane solvent was also directly connected to the reactor. All connections and ports are sealed with Teflon (e.g., stopcocks, ferrules). Reactor size was chosen to be approximately half full when charged with solvent to ensure ample volume of headspace to allow safe addition of ethylene oxide monomer. After assembly, the reactor was evacuated to baseline pressure (< 0.1 torr) and backfilled with purified argon gas at least five times to remove air. During at least one of the evacuation steps, the reactor was flamed to dry the glass surfaces of adsorbed moisture. Polymerization reactions were performed with the reactor sealed under a static positive argon atmosphere (~2 psig).

In a typical polymerization, approximately 1L of purified cyclohexane solvent is added to the dried reactor and brought to 40 °C using a temperature controlled water bath. Isoprene (~40–100 g) is purified and collected in a flask and attached to the reactor via the airlock. The precise amount of purified monomer is determined gravimetrically by weighing the evacuated flask prior to addition of monomer and again after the monomer is added. Once the amount of monomer is known, the correct volume of *sec*-BuLi initiator required for the targeted molecular weight is collected in a gas tight syringe equipped with a needle at least 12 inches long within a glove box. The initiator is carefully added to the reactor through the rubber septa and stirred with the solvent for several minutes. This allows any remaining protic impurities to react with the initiator prior to adding the monomer, preventing unwanted chain termination. When targeting low molecular weights, substantial volumes of initiator may be required and an appropriately sized syringe must be used. When handling pyrophoric materials such as *sec*-BuLi, syringes should never be filled more than half full in order to prevent accidents caused by inadvertently pulling the plunger out of the syringe body. When targeting the lowest molecular weights, a cannula transfer of the initiator to the reactor directly from the bottle is often safer than handling large volumes of *sec*-BuLi in a syringe. In this case, the mass of initiator added is determined gravimetrically and the amount of monomer required to achieve the desired molecular weight is calculated and purified.

When targeting low molecular weights, a high concentration of propagating species is present in the reactor. Extra caution must be exercised to maintain control over temperature and pressure within the reactor during monomer addition and termination to prevent extremely hazardous runaway reactions. A large volume water bath must be used and it is critical that the thermocouple well be submerged in the solvent to accurately report the temperature of the reaction media. Monomer should not be added in a single addition, but instead introduced in small aliquots. A small increase in temperature is often observed upon monomer addition and sufficient time should be allowed for the reactor to equilibrate at 40 °C again prior to adding the next monomer aliquot. After all monomer is added, the reaction is allowed to proceed for at least 4 hours and usually overnight to reach complete conversion.

To end-cap the polyisoprenyl lithium, at least a three-times molar excess of purified ethylene oxide monomer is added to the reactor through the airlock. To prevent large rises in temperature and pressure in the reactor when the lowest molecular weights were targeted, the reactor was cooled to room temperature prior to ethylene oxide addition. This reduced the baseline pressure within the reactor due to a reduction in the cyclohexane solvent vapor pressure and slows the rate of the end capping reaction. The purified ethylene oxide liquid at 0 °C is added in small amounts to prevent over pressurization and large increases in temperature of the reactor as the ethylene oxide boils, slowly dissolves in the solvent, and reacts with the polyisoprenyl lithium chains. The reaction is then terminated by the addition of degassed methanol to the reactor by a cannula transfer.

The resulting polymer is purified by precipitation in methanol. The low molecular weight liquid PI-OH often takes many days to settled and consolidate at the bottom of the beakers used for precipitation. Excess solvent is decanted off and the PI-OH is dried by rotary evaporation of the remaining solvent followed by stirring under dynamic vacuum for several days. When very low molecular weights were targeted, lithium salts sometimes precipitated in the cyclohexane reaction mixture after termination. In these cases, the reaction mixture was filtered through a glass frit prior to precipitation.

2.1.2   Polylactide block addition

Polylactide block addition was accomplished by the ring opening polymerization of DL-lactide in toluene using PI-OH as a macroinitiator. While there are many synthetic options available, triethyl aluminum was used as a catalyst based on the narrow molecular weights that can be achieved and the ease with which the catalyst can be deactivated and removed from the resulting polymer.[31,95,96,99] To prevent unwanted transesterification and depolymerization side reactions, the polymerization of the PLA block is stopped prior to complete conversion of monomer. Because the polymerization kinetics are complicated,[96] trial and error is practiced to achieve the desired PLA block molecular weights.

Triethyl aluminum solutions were used as received (1 M solution in hexanes or heptanes, Sigma-Aldrich). DL-lactide monomer was used as received (Purac biomaterials) since purity was sufficient as indicted by test polymerizations. Toluene solvent was purified in a similar manner as described above for cyclohexane.[98]

Lactide polymerizations were carried out in thick walled glass pressure vessels with Teflon caps since the volatile toluene solvent is heated near the boiling point (B.P. = 111 °C) when the reaction vessel is sealed during polymerizations. In a typical polymerization, a large Teflon coated stir bar is placed in a 500 mL thick walled glass pressure vessel with the desired amount of PI-OH (~3–10 g) dissolved in a small amount (10–20 mL) of toluene solvent. As a final purification step for the polymer, the toluene is boiled away at 70 °C while stirring under dynamic vacuum prior to cooling to room temperature and drying under dynamic vacuum overnight. The sealed pressure vessel (under static vacuum) is introduced into an argon atmosphere glovebox where the desired quantity of purified toluene solvent is first added to the reactor (DL-lactide concentrations of approximately 0.5 M were generally used). Next, the triethyl aluminum catalyst is added and allowed to react with the PI-OH for approximately 10 minutes prior to adding the DL-lactide monomer (conversion of 60 to 80% was typically assumed). The molar ratio of PI-OH to aluminum was maintained at approximately 2:1.[96] In general, the initiation reaction of PI-OH with triethyl aluminum and the propagation reaction do not

occur to a significant extent at room temperature.[95,96] The reactor is then sealed, removed from the glovebox, and placed in an oil bath at 90 °C to start the polymerization. The reaction is not allowed to go to completion and is quenched to room temperature after approximately 2 hours. The reactor is then vented and the catalyst is deactivated by the addition of a mixture of water and tetrahydrofuran.

The IL polymer is recovered by precipitation in methanol. After removing the bulk of the methanol by decanting, the polymer is purified to remove remaining salts and unreacted DL-lactide by two additional precipitations in methanol. Prior to the second precipitations, the polymer is dissolved in dichloromethane (which is a very poor solvent for the remaining aluminum salts) and filtering through a glass frit funnel, which retains the majority of the salts. After the final precipitation, the polymer is freeze dried from a concentrated benzene solution at least once.

2.2 Proton Nuclear Magnetic Resonance Spectroscopy

Proton nuclear magnetic spectroscopy (^{1}H NMR) is a technique routinely used to characterize the molecular parameters of polymers. Specifically, NMR is used to determine the molecular weight of synthesized PI-OH polymers by end group analysis and the composition of IL diblock copolymers.

^{1}H NMR is a spectroscopy technique that measures differences in the local magnetic properties of protons (i.e., the nuclei of ^{1}H atoms) in a sample that arise from subtle difference of the local chemical environment of the ^{1}H nuclei, leading to signals being measured at different chemical shifts. The signal at a given chemical shift is also sensitive to the number of nuclei that occupy a particular local chemical environment. This allows reasonably accurate (± 5%) determination of the molecular weight and composition of a polymer by comparing the magnitude of a characteristic signals from the polymer end groups and chemical repeat units of a block polymer.

Typical ^{1}H NMR spectra collected from a PI-OH (I-61) polymer and an IL (IL-61-18) synthesized from it are shown in Figure 2.2. The high 1,4 content of the PI-OH is

evident in the I-61 spectra (92% 1,4; 8% 3,4). The (number) average number of isoprene repeat units, n_I, is calculated as

$$n_I = \frac{I_b + I_c/2}{I_d/2}$$

2.2

where I_i is the integrated peak intensity of peak i. M_n can then be calculated by multiplying n_I by the isoprene repeat unit molecular weight and adding the contributions due to the end groups. The low molecular weights of the IL polymers require explicit accounting for the end group contributions to the molecular weight (and composition), which are generally taken to be negligible at higher molecular weights.
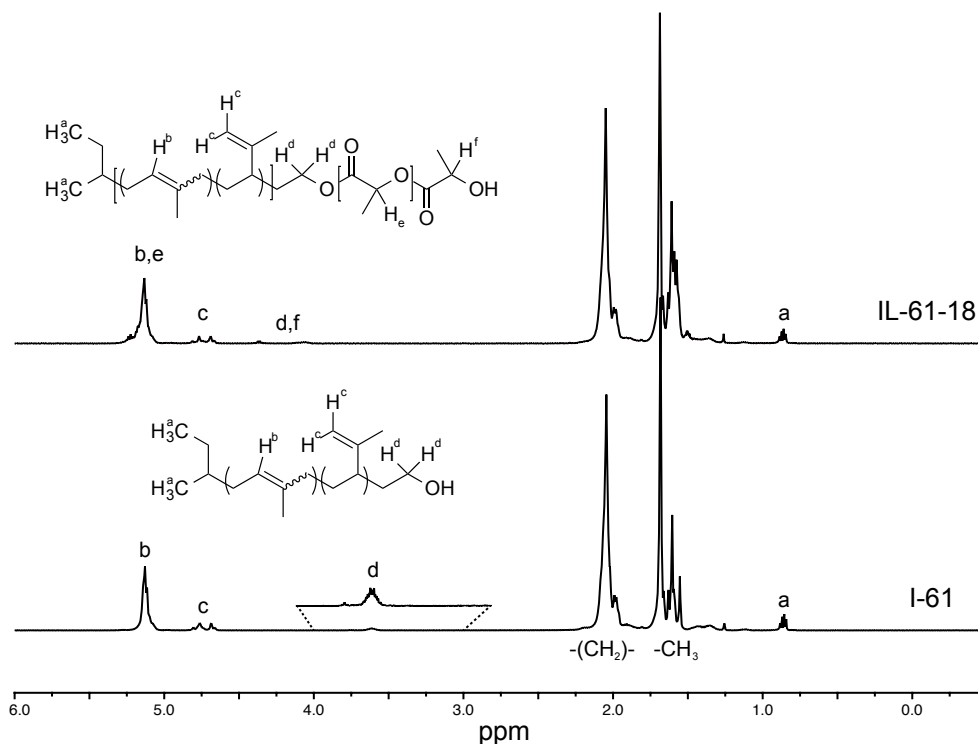
Figure 2.2 Representative ^{1}H NMR spectra of PI-OH and IL polymers.
The protons associated with each characteristic peak are labeled in the respective chemical structures. The peaks in the fingerprint region (1 to 3 ppm) arise from the reaming methylene -(CH$_2$)- and methyl -CH$_3$ groups. Peak *d* in I-61 is also shown with an expanded scale. Spectra were collected from d-chloroform solutions. See Chapter 5 for details regarding the polymers I-61 and IL-61-18 for which spectra are shown.

The calculation of molecular weight and composition of an IL diblock is complicated by the overlap of peaks *b* and *e*. I_b in the diblock is determined by the product of I_b/I_c measured in the PI-OH parent and I_c measured in the diblock. I_e is then simply I_{b+e} measured in the diblock minus the calculated I_b. The number ratio of lactide to isoprene repeat units, $x_{L/I}$, can then be calculated

$$x_{L/I} = \frac{I_e}{I_b + I_c/2}$$ 2.3

This ratio does not include the terminal lactide repeat unit that gives rise to peak *f*, which is often not clearly resolved in the spectra. To accurately calculate the volume fraction of lactide in the diblock, f_L, this repeat unit must be accounted for. To proceed, the molecular weight of the isoprene block is presumed to be that measured for the parent PI-OH, which allows calculation of the total number of lactide repeat units as ($n_I \times x_{L/I} +$ 1). The total M_n and f_L can then be calculated. Calculations of molecular parameters by end group analysis from NMR measurements is generally accurate to within $\pm$ 5%.

When stored for long periods of time, *sec*-BuLi initiator solutions partially deactivates through decomposition reactions mediated by contaminants. This results in the presence of some lithium salts in the *sec*-BuLi solution that do not have a detrimental influence on anionic polymerization. In some polymerization that contained a high concentration of inactive lithium salts (i.e., large volumes of initiator solution used that had an effective concentration less than the as received concentration), some splitting of the peak associated with the *d* protons in Figure 2.2 was documented. This was hypothesized to be due to a change in the relative proportions of the stereochemistry of the terminal isoprene unit, particularly of the lowest molecular weight species. This hypothesis is supported by the fact that the unusual satellite peaks could not be removed by washing or extensive drying, did not affect subsequent lactide block addition, and the species responsible for the satellite peaks elute last from an alumina column and had a lower average molecular weight than the parent material. In addition, the satellite peaks shift downfield largely in concert with peak *d* after the addition of the lactide block, supporting the hypothesis that the satellite peaks come from the same terminal ethylene

oxide units as peak *d*. The concentration of lithium salts are known to influence the stereochemistry of isoprene homopolymerization with a lithium counter ion and it is not unreasonable for the end-capping reaction (which sets the stereochemistry of the terminal isoprene unit) to be sensitive to salt concentrations as well.[97] The satellite peaks mostly occurred in very low molecular weight polyisoprene synthesized to target symmetric compositions that required large volumes of initiator for work not covered in this thesis.

Regardless of the cause, the thermodynamic behavior of the IL diblock copolymers was not influenced by the presence or absence of these satellite peaks. In some cases the satellite peaks overlapped with peak *c* in the diblocks, necessitating an alternative strategy for calculating composition. Since the polylactide block contains no methylene protons, $n_{I/L}$ can be determined by comparing the relative integrations of the methylene and methyl peaks in the fingerprint region of the parent and diblock spectra, thus allowing calculation of f_L and M_n. Both methods used to calculate molecular parameters agree within the 5% uncertainty of the measurements. The method based on the fingerprint region has the advantage of comparing a much larger absolute signal, but these signals are more susceptible to influence from trace solvent impurities. Therefore, the method based on peaks *b* and *e* was preferred and materials requiring the fingerprint method were subjected to extensive drying prior to analysis.

2.3   Size Exclusion Chromatography

Size exclusion chromatography (SEC), also called gel permeation chromatography (GPC), is a routine tool for polymer molecular weight characterization. While NMR methods were used to estimate molecular weights of the PI-OH and IL polymers in this thesis, end group analysis only allows calculation of M_n. To measure the breadth of the molecular weight distribution, SEC was used. SEC is a chromatography technique that separates polymer molecules in solution based on their hydrodynamic radii. Large molecules cannot explore the majority of the pore structure of the packing material in an SEC column and elute at shorter times than smaller molecules. Detection is accomplished most commonly by a differential refractometer that measures changes in

the refractive index (RI) of the eluting solution, providing a signal proportional to polymer concentration as a function of time or elution volume (time × flow rate).[27] To determine the molecular weight distribution from the raw data requires knowledge of the molecular weight as a function of elution time for the polymer of interest through prior calibration by standards of known molecular weight. Since the separation mechanism of SEC is by size in solution (and not molecular weight directly), a molecular weight versus elution time calibration curve is specific to particular polymer. In a strategy termed universal calibration, the molecular weight of polymers of different types can be determined from a single calibration curve (most commonly polystyrene) using tabulated Mark–Houwink parameters. This approach is based on determining the molecular weight of a polymer that is the same size in solution as the calibrant polymer of known molecular weight through their intrinsic viscosities. An alternative detection scheme complements RI detection and uses light scattering to directly measure M_w of the solute as a function of time.
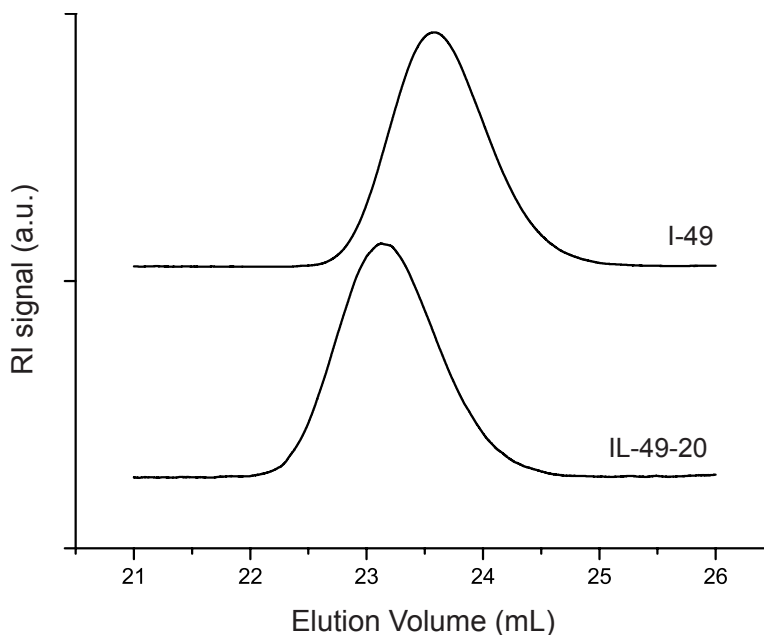
Figure 2.3 Representative SEC chromatograms for PI-OH and IL polymers. See Chapter 5 for details regarding the I-49 and IL-49-20 polymers. Curves shifted vertically for clarity.

In the work reported in this thesis, RI detection calibrated with polystyrene standards is used exclusively. Molecular weights and dispersities were calculated for PI-OH and IL polymers using the Mark–Houwink parameters for polyisoprene (and the calibrant polystyrene) at the appropriate experimental conditions. Instrument smearing results in a minimum resolvable dispersity that is often much higher (1.04 to 1.08) than the anticipated dispersities for ideal living polymerizations (eq 2.1). Therefore, reported dispersities are best understood as an upper bound for the true dispersity of a sample. In addition, two SEC instruments were used to measure dispersities, with tetrahydrofuran and chloroform mobile phases. The tetrahydrofuran instrument has a lower minimum resolvable dispersity. Therefore, values from different instruments should not be directly compared. Figure 2.3 shows representative SEC chromatograms of a PI-OH polymer (I-49) and a diblock synthesized from it (IL-49-20). The IL-49-20 diblock elutes at a lower elution volume (shorter time) than the parent I-49 material since it has a higher molecular weight. These measurements were conducted using a chloroform mobile phase.

2.4   Differential Scanning Calorimetry

Differential scanning calorimetry (DSC) is a thermal analysis technique used to identify thermal transitions in polymers. A DSC instrument measures the difference in heat flow required to heat a sample at the same prescribed rate as a reference. Polymer samples are encapsulated in aluminum DSC pans, with an empty DSC pan used as the reference. The resulting signal is heat flow as a function of temperature (or time). Glass transitions show up as step changes in the heat flow curve while first-order phase transitions, such as crystal melting or the order–disorder transition (ODT), show up as peaks. An example of DSC data from an IL diblock in which the glass transition temperatures T_gs of both block as well as the order–disorder transition temperature T_{ODT} are clearly evident is shown in Figure 2.4. The T_gs are identified as the point at half the width of the step change in heat flow. The latent heat of the ODT can be determined by integrating the corresponding peak in the heat flow curve, see Chapter 3 for details.

Since the measured signal is the heat flow, which increases with increasing heating rate, fast heating rates give better signal to noise. A typical heating rate for determination of T_gs is 10 or 20 °C/min. When designing DSC experiments, the sample is usually first heated above all thermal transitions to remove any processing history, cooled below any suspected thermal transitions, then finally heated through the desired temperature range. Desired quantities are determined from the data recorded during the second heating. To ensure reliable data and flat baselines, changes in heating rate (e.g., going from cooling to heating) must be done sufficiently far from the thermal features of interest to allow the instrument to have time to reach a steady state.

The data shown in Figure 2.4 are unusual in that most DSC experiments conducted on IL diblocks were designed with much more limited temperature ranges to either measure T_gs or the ODT, not both. While the data in Figure 2.4 provides a nice example of the features that can be measured in DSC experiments, it also illustrates possible pitfalls. The DSC used to measure the data in Figure 2.4 was in need of cleaning or calibration, as the zero heat flow baseline is not correct. The heat flow should increase with increasing temperature to reflect the increasing heat capacity of the polymer sample

as it is heated. The seemingly flat signal at high temperature and negative slope of the data at the lowest temperatures suggests the heat flow data is not quantitatively accurate, though the data is certainly of sufficient quality to identify the approximate locations of the block T_gs.
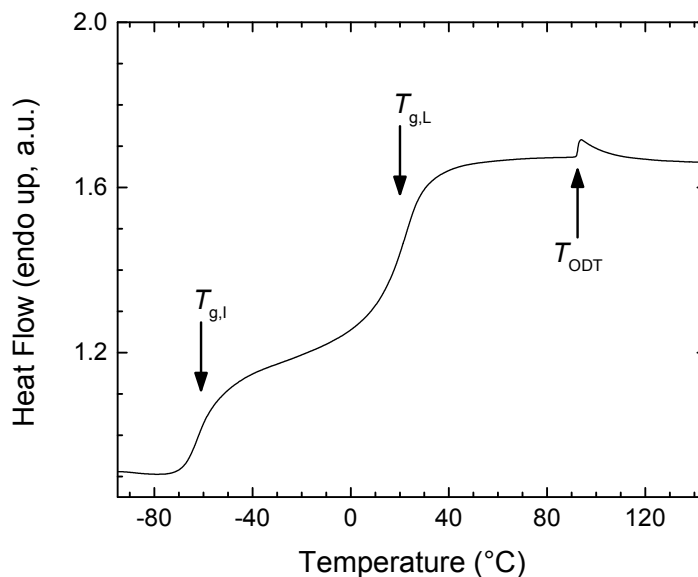
Figure 2.4 Representative DSC data of an IL diblock copolymer. DSC data from the sample IL-1 (see Chapter 3 for details).

2.5 Dynamic Mechanical Spectroscopy

Dynamic mechanical spectroscopy (DMS) or rheology is a technique used to probe the physical properties of viscoelastic polymer materials. In a purely elastic solid, shear stress σ is proportional to the applied strain γ, while in a purely viscous liquid, σ is instead proportional to the time derivative of γ (i.e., the strain rate $\dot{\gamma}$). The proportionality constants are the modulus G and the viscosity η, respectively. As a result, if an oscillating sinusoidal strain is applied $\gamma = \gamma_o\sin(\omega t)$ at a frequency ω, in an elastic solid the sinusoidal stress response of the material will be in phase with the applied strain $\sigma = G\gamma_o\sin(\omega t)$, while the stress response of a viscous liquid will be out of phase with the

applied strain $\sigma = \eta\omega\gamma_o\cos(\omega t)$ (and in phase with the strain rate). A viscoelastic material exhibits a response intermediate to these two limits. This intermediate response can be decomposed into the sum of an in-phase and out-of-phase component

$$\frac{\sigma(t)}{\gamma_o} = G^* = G'\sin(\omega t) + G''\cos(\omega t) \qquad\qquad 2.4$$

where G' and G'' are the shear storage and loss moduli, respectively. The response will, in general, be a function of the applied frequency. DMS experiments are designed to probe the frequency dependent mechanical properties of polymer melts.

The large chain-like structure of polymers molecules leads to a broad spectrum of relaxation times and consequently viscoelastic mechanical properties. In homopolymers, the spectrum of relaxation times result from processes that occur at different length scales. A monomer segment will relax very quickly after being perturbed (e.g., by an applied stress), while a segment of the chain containing many monomer units will take longer to relax, and a collection of interpenetrating entangled chains will require orders of magnitude more time to relax than the monomer unit. As a result, DMS experiments that measure mechanical properties at different frequencies are probing relaxation processes at different length and time scales ($\approx \omega^{-1}$).

The viscoelastic response of a block polymer is sensitive to the detailed state of mesoscopic order present. In particular, the mechanical properties of a disordered block polymer are that of a viscoelastic liquid, while the various ordered phases, as a result of broken symmetry, respond like a soft viscoelastic solid. Therefore, DMS experiments provide a convenient experimental tool for identifying the T_{ODT} as the temperature at which an abrupt change in properties occurs on heating.

Care must be taken to remain in the linear regime when performing DMS experiments. In the linear regime, the measured viscoelastic properties are not a function of the applied strain and the properties reflect the response of the underlying structure of the sample. If too large a strain is used, the structure of the sample will be changed by the applied strain and the measured properties will be strain dependent. This is the non-linear regime.

Interpreting the viscoelastic properties of block polymers is often not straightforward. Measured properties can result from relaxations occurring at length scales ranging from individual monomers to the grain structure of the mesoscopic ordered phases. Each contribution can vary with temperature and frequency differently. The phase behavior of block polymers involves structure at large length scales relative to a single chain. Therefore, the low frequency response of block polymers is often of the most utility for inferring phase behavior. Care must be taken when designing an experiment to select frequencies low enough to be sensitive to changes in the state of mesoscopic order (as opposed to measuring single chain relaxations). DMS is capable of detecting subtle changes in the relaxation response of block polymer melts that result from order–order transitions and composition fluctuations.

If all relaxation times have the same temperature dependence, time–temperature superposition (tTS) is a useful approach to analyzing viscoelastic data. The frequency dependence of G' and G'' measured at different temperatures can be shifted along the frequency axis by factors $a_T(T)$ relative to data at a reference temperature T_r to create a master curve. The principle being applied is one of corresponding states, meaning a measurement at one frequency (time) and temperature is equivalent to a measurement made at a higher temperature and higher frequency (shorter time). The master curve represents the relaxation response that would be measured at the reference temperature for a range of reduced frequencies ωa_T that spans many orders of magnitude beyond what is experimentally accessible at any given temperature. The shift factors applied at each temperature $a_T(T)$ are often found fit to the Williams–Landel–Ferry (WLF) equation

$$\log(a_T) = -\frac{C_1(T - T_r)}{C_2 + (T - T_r)}$$ 2.5

where C_1 and C_2 are the WLF parameters.[27]

2.6   Small-Angle X-ray and Neutron Scattering

Small-angle X-ray and neutron scattering (SAXS and SANS) are valuable tools for studying the structure of block polymer melts. Synchrotron SAXS is the primary

method used to identify the symmetry of the ordered phases reported in this thesis, while SANS is used in Chapter 7 as a complement to SAXS to obtain absolute intensity scattering data in the disordered phase. The underlying principle of both techniques is that when a plane wave propagates through a material it can interact and be scattered by the constituents of the material, resulting in a spherical wave emanating from each individual scattering site. The intensity measured at distant detector is the result of the interference of all of the scattered waves. The spatial variation of scattered intensity, the scattering pattern, contains information about the spatial arrangement of the scatterers in the material. It turns out the coherent elastic scattering pattern represents a Fourier transform of the pair correlation function of scatterers. X-ray scattering experiments are sensitive to variations in the electron density of materials while neutron scattering experiments are sensitive to the scattering length density that arises from interactions of the neutrons with the nuclei present in a material.[100–102]

A scattering experiment measures the scattered intensity of a wave of a particular wavelength as a function of position relative to the incident beam. These experimental details can be subsumed into a convenient parameter $\mathbf{q}$ the scattering or momentum transfer vector

$$|\mathbf{q}| = q = \frac{4\pi}{\lambda}\sin\left(\frac{\theta}{2}\right)$$ 2.6

where λ is the wavelength of the incident wave and θ is the scattering angle, the angle between the scattered an incident beams as shown in Figure 2.5a. The quantity q has units of inverse length and sets the characteristic length scale probed in a particular scattering experiment. In both SAXS and SANS, the wavelengths (typical λ are 0.729 and 6 Å for SAXS and SANS, respectively) and the small scattering angles result in a range of q values of approximately 10^{-3} to 10^{-1} Å^{-1} probing length scales in the range of one to hundreds of nanometers, ideal for studying the structure of self-assembled block polymers.

Of primary interest in most of the work in this thesis is the Bragg scattering arising from the long-rang order in the various mesophases formed by block copolymers.

For the ordered phases that can be described by a unit cell in 1- (LAM), 2- (HEX), 3-(BCC, σ phase, A15, GYR), and higher (DQC) dimensions, the coherent scattering from planes of particles gives rise to sharp Bragg diffraction peaks at particular values of q given by the Bragg condition

$$q_{hkl} = 2\pi/d_{hkl}$$

$$2.7^*$$

where d_{hkl} is the interplanar spacing of corresponding to the plane identified with Miller indicies h, k, and l.

For the 1-D LAM phase, there is only one Miller index and the interplanar spacing is given by

$$\frac{1}{d_{LAM}} = \sqrt{\frac{h^2}{a^2}}$$

$$2.8$$

where a is the lattice parameter equal to the primary domain spacing ($h = 1$). In general, all values of h are allowed resulting in peaks at integer multiples of the q-value of the primary scattering peak q^* ($= 2\pi/a$). For precise volumetric symmetry, only odd Bragg peaks are realized.[103]

For the 2-D HEX phase, there are two Miller indices (hk) and the interplanar spacing is given by

$$\frac{1}{d_{HEX}} = \sqrt{\frac{h^2 + k^2 + hk}{a^2}}$$

$$2.9$$

where a is the lattice parameter of the hexagonal unit cell equal to the primary domain spacing of the (10) reflection (at $q = q^*$). For the hexagonally packed cylinders ($P6/mm$), all combinations of h and k are allowed by the symmetry resulting in peaks at $(q/q^*)^2 = 1$, 3, 4, 7, 9, …

For the cubic 3D phases (BCC, A15, GYR), there are three Miller indices (hkl) and the interplanar spacing is given by

---

* This equation is applicable for 1-, 2-, and 3-D periodic structures. See Chapter 4 for dodecagonal quasicrystal (DQC) indexing, which is done in 5-D.

$$\frac{1}{d_{\text{CUB}}} = \sqrt{\frac{h^2 + k^2 + l^2}{a^2}} \qquad\qquad 2.10$$

where a is the lattice parameter of the cubic unit cell. The reflection conditions and relative peak ratio for phases of interest in this thesis, including the cubic phases, are summarized in Table 2.1.

Table 2.1 Summary of allowed Bragg reflections for typical block polymer phases.

Symmetry	Reflection Conditions	Allowed Reflections	Relative Peak Positions
LAM	All allowed	(1), (2), (3), (4), …	1, 2, 3, 4
HEX ($P6/mm$)	All allowed	(10), (11), (20), (21), (30) …	1, √3, √4, √7, √9, …
BCC ($Im\overline{3}m$)	$h + k + l =$ odd	(110), (200), (211), (220), (310), (222), (321), …	1, √2, √3, √4, √5, √6, √7 …
A15 ($Pm\overline{3}n$)	If 00l or hhl: $l = 2n$ all other allowed	(110), (200), (210), (211), (220), (310), …	√2, √4, √5, √6, √8, √10 …
GYR ($Ia\overline{3}d$)	Complex	(211), (220), (321), (400), (420), (332), …	√6, √8, √14, √16, √20, √22 …
σ phase ($P4_2/mnm$)	If $h0l$ or $0hl$: $h + l = 2n$ If $h00$ or $00l$: $h,l = 2n$ all other allowed	(110), (200), (101), (210), (111), (220), …	n/a

For the tetragonal σ phase, there are three Miller indices (*hkl*) and the interplanar spacing is given by

$$\frac{1}{d_{\text{TET}}} = \sqrt{\frac{h^2 + k^2}{a^2} + \frac{l^2}{c^2}} \qquad\qquad 2.11$$

where a and c are the lattice parameters of the tetragonal unit cell. The reflection conditions are given in Table 2.1. Since the tetragonal unit cell has two lattice parameters, the peaks do not appear at fixed relative q values as the a/c ratio can vary. See Chapter 4 for a more complete set of allowed reflections and which of those are typically observed.
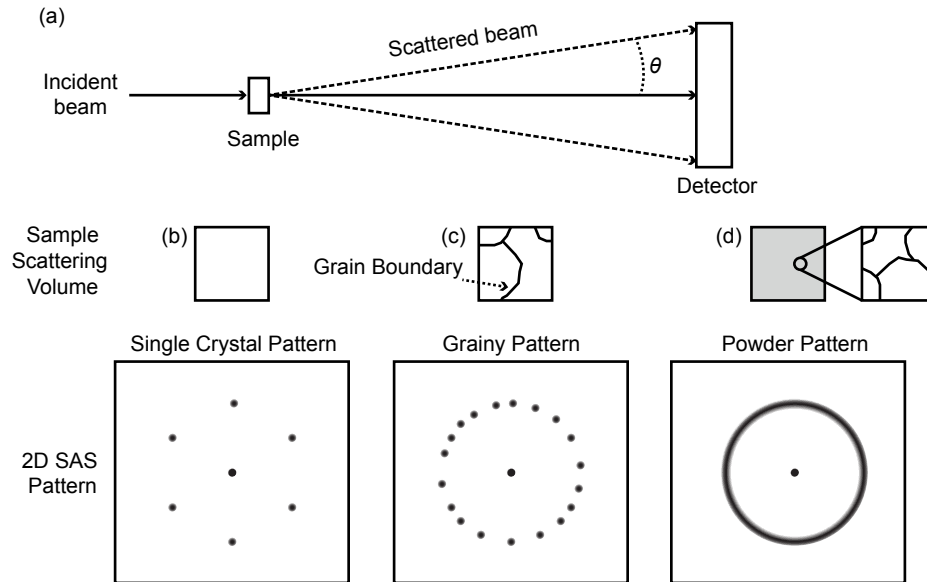
Figure 2.5 Illustration of the small-angle scattering geometry and types of 2D scattering patterns. (a) Small-angle scattering (SAS) geometry of the experiments in this thesis. Sample size, sample-to-detector distance, and scattering angle are not drawn to scale. (b) through (d) show illustrations of how the size of the grains in a sample relative to the illuminated scattering volume influences the 2D scattering patterns obtained.

Each set of *hkl* planes represents a point in the reciprocal lattice of a crystal structure, where $\mathbf{q}_{hkl}$ is now a vector pointing to the lattice point. Points in the reciprocal lattice that satisfy the vector equivalent of eq 2.7 for a particular scattering geometry give rise to peaks in the scattering pattern. For a single crystal, this only occurs for specific orientations of the crystal relative to the incident beam. Therefore, the scattering pattern depends on the orientation of the single crystal. Each *hkl* plane gives rise to a spot in the 2D scattering pattern corresponding to a point in the reciprocal lattice. In high symmetry directions (e.g., along rotational axes), the symmetry of the reciprocal lattice is revealed in the arrangement of the spots in the 2D scattering pattern, as shown in Figure 2.5b for a hypothetical single crystal along a 6-fold axis.

In a polycrystalline sample, the qualitative appearance of the 2D scattering pattern depends on the characteristic grain size of the structure relative to the volume of the sample illuminated by the incident beam, as shown in Figure 2.5b, c, and d. If grain size

is very large relative to the scattering volume, the 2D pattern will resemble that of a single crystal (Figure 2.5b). If on the other hand the scattering volume contains a very large number of grains of all possible orientations, a so-called powder pattern is produced, a name that refers to the particular case of collecting X-ray diffraction data from a finely ground powder of a (atomic) crystalline material. In this case, uniform rings of intensity are measured at scalar values of q_{hkl} that do not depend on the orientation of the sample (Figure 2.5d). This is a result of the large number of grains, which average over all orientations of the reciprocal lattice causing all possible "spots" to occur simultaneously, thus forming rings in a process called powder averaging. In this case, it is often more convenient to average the 2D data over all azimuthal angles in the 2D pattern to obtain a 1D scattering pattern of intensity versus q. If all possible orientations are equally represented in the scattering volume, in addition to the peak positions, the relative intensities of the peaks in the 1D scattering pattern will be characteristic of the structure present.

However, if a small number of grains are present in the scattering volume, scattering patterns with rings of spots are observed, as shown in Figure 2.5c. In this case, each grain contributes to the scattering pattern producing discrete spots but there are not a sufficient number of grains to average the spots into uniform intensity rings. In this case, the relative intensity of the peaks in the 1D scattering pattern will not necessarily be those of the characteristic powder pattern. The intensities may depend on the orientation of the sample as different collections of grains are rotated to satisfy the Bragg condition. In addition, if the grains within the scattering volume share a preferred orientation, called a texture, which could result from crystal growth or processing, proper powder averaging will not occur. Again, the relative intensities of the peaks will not necessarily be those characteristic of the powder pattern. Experimental examples of 2D SAXS patterns of the types illustrated in Figure 2.5c and d are shown in Figure 2.6a and b, respectively.
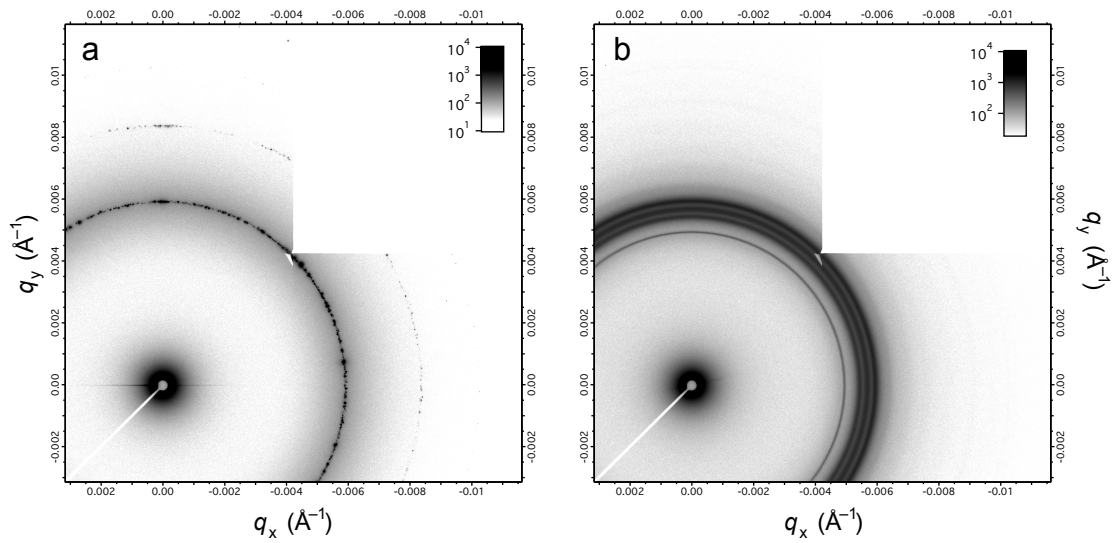
Figure 2.6 Example 2D SAXS patterns. (a) IL-5.1 at 55 °C after 3 minutes of annealing following a quench from above T_{ODT} that exhibits a grainy BCC 2D diffraction pattern. (b) IL-5.1 at 25 °C after 77 days of annealing following a quench from above T_{ODT} that exhibits a DQC phase uniform intensity powder rings. The portion of the detector in the upper right quadrant was not functioning when the data were collected and appears white.

Chapter 3:

Fluctuations, Order and Disorder in Short Diblock Copolymers [*],[†]

3.1 Introduction

Block polymers have fascinated researchers for decades, combining a host of interesting scientific questions with commercial relevance.[1–3,5] Many new and exciting applications require ever decreasing nanoscale dimensions (e.g., lithographic patterning of microelectronic materials),[10,18] which has drawn us into exploring the thermodynamic behavior of block copolymers (BCP's) characterized by large Flory–Huggins segment–segment interaction parameters (χ's). Because the state of segregation of a block copolymer depends on the compound variable χN, where N is the overall degree of polymerization, large values of χ produce ordered nanostructures (often referred to as microphase separation) even at relatively low values of N.[16] Our interest in such high χ, low N materials is twofold. First, as a practical matter we wish to understand the lower

---

limit of the range of characteristic dimensions, and the associated physical properties, which can be accessed using BCPs. However, mean-field treatments of BCP phase behavior are typically formulated in the limit of infinitely large N, i.e., infinitesimally small χ. As N is reduced from this limit composition fluctuations are expected to become increasingly important. A second objective is to expand our fundamental understanding of the thermodynamic behavior of this class of materials under circumstances where the assumptions inherent in the accepted theoretical framework used to describe BCP self-assembly[16,17] would be expected to fail.

In the mean-field limit, Leibler predicted that AB diblock copolymer phase behavior depends on two parameters: the volume fraction f of block A and the combined parameter χN.[2,16,33–36] The composition, f, which is determined by the degree of polymerization of each block (and to a lesser extent the repeat unit densities), primarily controls the geometry of the ordered microphase separated structures, while χN dictates the strength of segregation between the blocks. For systems governed by van der Waals interactions, χ is proportional to the inverse of temperature: $\chi = \alpha / T + \beta$ where α and β are empirically determined constants and T is the temperature. The magnitude of χ is determined by the chemical structure of the repeat units, which can be approximated (in the absence of specific interactions such as hydrogen bonding) based on the associated solubility parameters (δ_i): $\chi = (V/RT)(\delta_A - \delta_B)^2$ where V is the repeat unit molar volume and R is the gas constant. Thus, heating a block copolymer melt generally reduces χN. Leibler showed that within mean-field theory the phase transition from a state of disorder to order, known as the order–disorder transition (ODT), occurs at a critical point: $(\chi N)_{ODT}$ = 10.5 for symmetric (f = 1/2) block copolymers. At this continuous, second-order, phase transition, the homogeneous disordered state gives way to an ordered lamellar phase with a composition profile of differential amplitude. This amplitude then grows as χN is increased, for example by decreasing the temperature.

Following a seminal publication by Brazovskii,[49] Frederickson and Helfand proposed a correction to Leibler's theory to account for the effects of fluctuations at finite N.[17] In this theory, the disordered state in the vicinity of the ODT is no longer

homogeneous, but is instead characterized by thermally induced local composition fluctuations with a characteristic length scale on the order of the radius of gyration of the polymer chain. The amplitude of these fluctuations increases as χN is raised, producing a degree of disordered microphase segregation at values of χN well below the transition to the ordered phase. These fluctuations stabilize the disordered phase and shift the value of $(\chi N)_{ODT}$ to a value greater than 10.5, the magnitude of which increases with decreasing N. Composition fluctuations break the second-order character of the ODT for symmetric diblocks resulting in a discontinuous, fluctuation induced weakly first-order phase transition. The theory predicts a small discontinuous change in the local composition profile at the ODT coincident with the fluctuating disordered state transforming to the ordered lamellar morphology. Although only strictly valid at values of N approaching 10^9 and not considered quantitatively accurate, the Fredrickson-Helfand theory has been remarkably successful at capturing certain qualitative features of the phase behavior of real BCP materials including the topology of the diblock copolymer phase diagram and the presence of fluctuations near the ODT. In this work, we explore the ODT and phase behavior of BCP materials characterized by unusually small molecular weights, $N < 100$, which is well outside the limits where the fluctuation theory is expected to be applicable.

With a few notable exceptions,[80–86] the thermodynamics associated with the ODT in general, and the effects of fluctuations specifically, have been studied using indirect experimental techniques, e.g., rheology and small-angle scattering.[73,78] In this report, we present experimental results obtained with a series of high χ, low N poly(1,4-isoprene-b-DL-lactide) (IL) diblock copolymers in which direct calorimetric measurement of the ODT was possible. This system was chosen based on the large difference in solubility parameters between poly(isoprene) (PI; $\delta_{PI} = 16.6$ J$^{1/2}$/cm$^{3/2}$) and poly(DL-lactide) (PLA; $\delta_{PLA} = 19.7$ J$^{1/2}$/cm$^{3/2}$).[30,31] The thermodynamic properties near the ODT were systematically explored using a combination of small-angle X-ray scattering (SAXS), dynamic mechanical spectroscopy (DMS), and differential scanning calorimetry (DSC) experiments, including direct thermal measurements of the ODT for samples that span the primary diblock copolymer morphologies, including ordered lamellae, cylinders, and

spheres. $\chi(T)$ was estimated and the phase behavior for this system was characterized near the order to disorder transition phase boundary and mapped on a phase portrait.

3.2 Experimental Section

3.2.1 *Materials and molecular characterizations*

A detailed synthetic scheme for the preparation of IL diblock copolymers is described elsewhere[95] (see Chapter 2). Briefly, ω-hydroxyl poly(1,4-isoprene) (PI-OH) was prepared by anionic polymerization of isoprene and used as a macroinitiator for the ring-opening polymerization of lactide monomer using a triethyl aluminum catalyst yielding poly(1,4-isoprene-*b*-DL-lactide) (IL). The molecular weights and block compositions of IL polymers were determined by ^{1}H nuclear magnetic resonance (NMR) spectroscopy experiments (Varian VI-500), and dispersities ($Đ = M_w/M_n$) were determined by size exclusion chromatography (SEC) using chloroform as the mobile phase.

3.2.2 *Dynamic mechanical spectroscopy (DMS)*

Order–disorder and order-order transition temperatures (T_{ODT} and T_{OOT}, respectively) of each IL diblock copolymer were measured using dynamic mechanical spectroscopy (DMS) experiments conducted with a Rheometrics ARES strain controlled mechanical spectrometer.[73] The IL diblock copolymers were loaded between 25 mm parallel plates, disordered by heating above the T_{ODT}, cooled, and heated at a rate of 0.1 °C/min while measuring the isochronal ($\omega = 0.1$ rad/s) linear dynamic shear storage (G') and loss (G'') moduli. The T_{ODT}'s were obtained from the final heating step and were taken as the temperature at which G' shows a precipitous drop to a liquid-like response. T_{OOT}'s were associated with rapid changes in G' that separated non-terminal (soft solid) viscoelastic states.

3.2.3 *Differential scanning calorimetry (DSC)*

A TA Instrument Q1000 differential scanning calorimeter (DSC) was used to measure the glass transition temperatures (T_g) of the PI and PLA blocks. Samples (~ 10

mg) were placed in hermetically sealed aluminum pans, heated to 200 °C, cooled to -100 °C, and heated to 200 °C again at a rate of 10 °C/min. The T_g values were determined using the final heating results.

Many DSC thermograms of the IL diblock copolymers showed distinct thermal features on cooling and heating with onset temperatures corresponding with the T_{ODT}'s of the materials. This phenomenon was further examined in select IL diblock copolymers using a TA Instruments Discovery DSC. In these experiments, samples (10–20 mg) in aluminum Tzero hermetic DSC pans were equilibrated at a temperature 50–75 °C above the T_{ODT}, cooled at a specified rate through the ODT to 0 °C (-20 °C in the case of IL-15), and then heated through the ODT to the initial equilibration temperature. For selected samples, an annealing step at a temperature approximately 20 °C below T_{ODT} was employed between the initial cooling and the final heating steps. The latent enthalpy of the ODT phase transition, ΔH_{ODT}, was determined from the DSC thermograms using TA Instruments Trios software. Thermal degradation was not observed by SEC analysis of the samples after DSC experiments.

3.2.4 Small-angle X-ray scattering (SAXS)

The phase behavior of the IL diblock copolymers was investigated using small-angle X-ray scattering experiments (SAXS) conducted at DND-CAT (beamline 5-ID-D) at the Advanced Photon Source (APS) located at Argonne National Laboratory (Argonne, IL). The sample-to-detector distances employed for the experiments were 3.97, 4.03, 4.63, or 5.5 m and the X-ray wavelength, λ, was 0.729 Å. Scattering data were collected with a Mar area CCD detector, and azimuthally integrated to the one-dimensional form of intensity, I, versus scattering momentum transfer vector, $q = 4\pi\lambda^{-1}\sin(\theta/2)$, where θ is the scattering angle. For isothermal experiments, the samples were placed in aluminum DSC pans and the temperature was controlled using a Linkam DSC stage cooled with liquid nitrogen and maintained under an inert (helium or nitrogen) atmosphere. The samples were first heated above the T_{ODT} then cooled to various target temperatures and held for 2 minutes before data collection, unless otherwise specified. Temperature changes were implemented at a rate of approximately 100 °C/min.

Dynamic temperature ramp SAXS experiments were also conducted on select samples to mimic the DSC measurements used to evaluate the ODT. In these experiments, samples were placed in 1.5 mm nominal diameter quartz capillaries (Charles Supper Company) and the temperature was controlled using a modified Linkam HFS91 hot stage. The samples were equilibrated at a temperature above the T_{ODT} (150 °C, 160 °C, and 100 °C for IL-1, IL-14, and IL-15 samples, respectively), cooled at a controlled ramp rate to a temperature well below T_{ODT} (30 °C, 40 °C, and 0 °C for IL-1, IL-14, and IL-15 respectively), held at the lowest temperature for 2 to 10 minutes, and finally heated at a controlled ramp rate to the original equilibration temperature above the T_{ODT}. Scattering patterns were collected *in situ* in intervals of 10 °C while the temperature was ramped. Analogous experiments were conducted over a narrower temperature range in the vicinity of the T_{ODT} (85 - 100 °C, and 120 - 140 °C for IL-1 and IL-14 respectively) with scattering patterns collected every 1 °C. The scattering invariant, Q_{rel}, was calculated by numerically integrating the intensity data (see eq 3.4) over the range of q that was experimentally accessible (approximately $0.02 - 0.26$ Å^{-1}) after subtracting a background intensity obtained from an empty capillary. The principle scattering peak of the one-dimensional SAXS patterns were fit to Lorentzian (ordered states) or quadratic (disordered state) functions for precise extraction of q^* values.

3.3 Results

A series of 16 IL diblock copolymers was synthesized from 5 PI-OH precursors with a wide range of PLA block volume fractions, $0.17 \leq f_L \leq 0.76$ (Table 3.1). The T_{ODT}'s of these samples, obtained from DMS and DSC experiments, fall within an experimentally feasible temperature window (< 200 °C) except IL-16 (see below). The order–disorder transitions were confirmed and ordered morphologies identified with isothermal synchrotron SAXS experiments. Five characteristic SAXS patterns provide definitive phase assignments as listed in Table 3.2 (representative examples shown in Figure 3.1): disorder – DIS, the Frank–Kasper sigma phase - σ (IL-15), body-centered

cubic spheres - BCC (IL-15, 24), hexagonally packed cylinders - HEX (IL-5, 9, 12, 13, 14, and 16), and lamellae - LAM (IL-1, 2, 3, 6, 7, 8, 10).

Table 3.1 Molecular characterization data for IL diblock copolymers.[*]

Polymer	$M_{n,I}$ [a]	$M_{n,L}$ [a]	M_n [a]	N [b]	f_L [c]	$Đ$ [d]	$T_{g,L}$ (°C) [e]
I-1	1,130	-	1,130	19	-	1.06	-
I-2	1,350	-	1,350	23	-	1.06	-
I-3	1,720	-	1,720	29	-	1.07	-
I-4	2,810	-	2,810	47	-	1.06	-
I-5	3,880	-	3,880	65	-	1.07	-
IL-1	1,130	1,620	2,750	39	0.51	1.12	20
IL-2	1,350	2,200	3,550	49	0.54	1.09	22
IL-3	1,720	2,810	4,530	63	0.54	1.09	29
IL-5	1,130	4,260	5,390	71	0.73	1.08	29
IL-6	1,130	3,140	4,270	57	0.67	1.08	28
IL-7	1,350	2,340	3,690	51	0.56	1.11	21
IL-8	1,350	3,030	4,380	59	0.62	1.13	35
IL-9	1,130	4,930	6,060	79	0.76	1.08	35
IL-10	1,720	2,360	4,080	57	0.50	1.11	24
IL-11	1,720	1,620	3,340	48	0.40	1.10	11
IL-12	2,810	1,190	4,000	62	0.23	1.11	5
IL-13	2,810	1,320	4,130	63	0.25	1.13	11
IL-14	2,810	1,770	4,580	69	0.31	1.15	15
IL-15	2,810	1,080	3,890	60	0.22	1.12	5
IL-16	2,810	2,220	5,030	74	0.36	1.04	32
IL-24	3,880	1,090	4,970	79	0.17	1.08	4

(a) Number-average molecular weight in g/mol based on ^{1}H NMR. (b) Volumetric degree of polymerization based on reported[30,104] homopolymer densities at 25 °C (0.9 and 1.25 g/cm^{3} for I and L, respectively) and a reference volume of 110 Å[3] (c) Volume fraction of L block based on reported homopolymer densities at 25 °C and ^{1}H NMR. (d) From RI-SEC with a chloroform mobile phase. (e) Glass transition temperature from DSC.

---

[*] Polymers, with the exception of I-5 and IL-24, were synthesized by Sangwoo Lee.
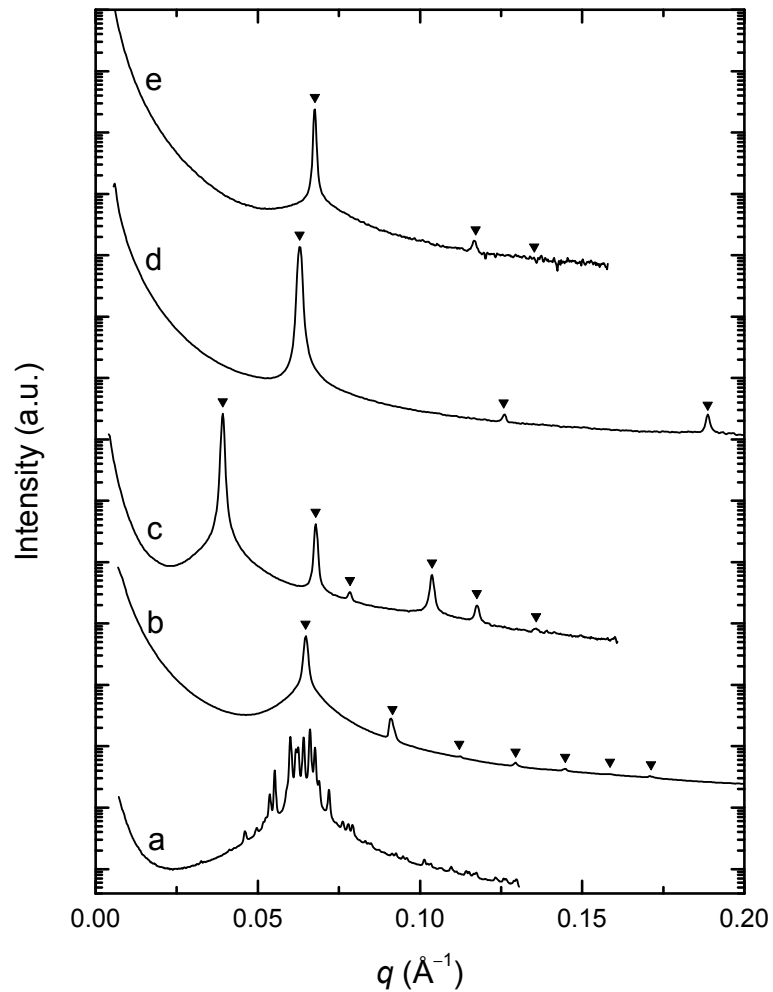
Figure 3.1 SAXS with varying composition. Isothermal Synchrotron SAXS patterns obtained from the IL diblock copolymers.[*] (a) σ phase identified with IL-15 (f_L = 0.22) after 26 days aging at room temperature. (b) BCC phase identified with IL-15 (f_L = 0.22) after 30 minutes annealing at 40 °C. The relative peak positions of BCC phase, q/q^* = √1, √2, √3, √4, √5, √6, √7 are marked by inverse triangles where q^* is the primary peak. (c) HEX phase identified with IL-16 (f_L = 0.36) at 200 °C with q/q^* = √1, √3, √4, √7, √9, √12. (d) LAM phase identified with IL-10 (f_L = 0.50) at 50 °C with q/q^* = √1, √4, √9 (e) HEX phase identified with IL-5 (f_L = 0.73) at 90 °C with q/q^* = √1, √3, √4.

---

[*] Isothermal SAXS data collected by Sangwoo Lee.

Table 3.2 Phase behavior of IL diblock copolymers.[*]

Polymer	Phase(s) and Phase Transition Temperature (°C)	q^* (Å^{-1}) (Temperature in °C, Phase)
IL-1[a]	LAM – 93(96) – DIS	0.0736 (50, LAM)
IL-2[a]	LAM – 110(114) – DIS	0.0699 (50, LAM)
IL-3[a]	LAM – 153(157) – DIS	0.0604 (50, LAM)
IL-5	HEX – 95(98) – DIS	0.0676 (90, HEX)
IL-6	LAM – 77 – DIS	0.0658 (50, LAM)
IL-7[a]	LAM – 111(112) – DIS	0.0685 (50, LAM)
IL-8	LAM – 110 – DIS	0.0615 (50, LAM)
IL-9	HEX – 97 – DIS	0.0590 (25, HEX)
IL-10[a]	LAM – 146(147) – DIS	0.0628 (50, LAM)
IL-11	LAM – 98 – DIS	0.0697 (50, LAM)
IL-12	HEX – 65 – DIS	0.0674 (50, HEX)
IL-13	HEX –105(105) – DIS	0.0605 (25, HEX)
IL-14	HEX – 130(132) – DIS	0.0595 (57, HEX)
IL-15	σ Phase – 27 – BCC – 50(51) – DIS	0.0648 (40, BCC)
IL-16	HEX – 200 < DIS	0.0392 (200, HEX)
IL-24	BCC – 76 – DIS	0.0664 (45,BCC)

[a]Polymers used for determining χ_{IL}. [b]$T_{ODT,}$ and T_{OOT} were measured by DMS. Values listed in parenthesis were determined by DSC. [c]Principal peak positions (q^*) determined by SAXS patterns at the temperature and phase indicated in the parenthesis.

In addition to the typical rheological method used to identify the T_{ODT} (taken as the temperature at which a precipitous drop in G' is observed upon slow heating from the ordered state), many IL diblock copolymer samples showed a weak but distinct thermal signature of the ODT in DSC experiments. The details of this thermal signature were found to be strongly dependent on the ordered phase morphology. Representative DMS and DSC data used to identify T_{ODT}s for IL copolymers that form LAM, HEX, and ordered spheres (BCC and/or σ) are shown in Figure 3.2. Peaks are visible in the DSC

thermograms with onset temperatures that coincide closely with the rheological signatures of the ODT. We attribute these endothermic peaks to the latent heat associated with the order–disorder transition, and take the onset of this temperature response as the T_{ODT}. We accepted the T_{ODT}s obtained from DMS measurements as the equilibrium values due to the much slower heating rate and more quantitative signatures compared to the DSC measurements. A detailed analysis of the DSC results is presented below.
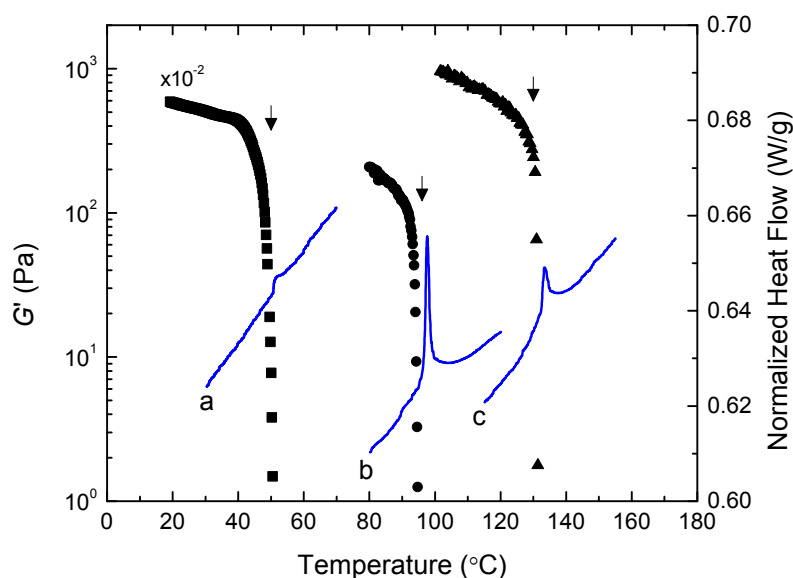
Figure 3.2 Determination of T_{ODT}. Isochronal (0.1 rad/s) dynamic shear storage modulus, G', (filled symbols) and DSC thermograms (lines) obtained from IL-1 (curve b, filled circles), IL-14 (curve c, filled triangles), and IL-15 (curve a, filled squares) while heating at 0.1 (DMS) and 20 °C/min (DSC). The DSC thermogram of IL-15 (curve a) was obtained after a 1 hour isothermal annealing step at 40 °C. The temperature at which a precipitous drop in G' is observed is regarded as the T_{ODT} and are marked with arrows. For clear presentation, DMS data for IL-15 (filled squares) and DSC data for IL-14 (curve c) have been shifted vertically by the factors of 10^{-2} and –0.6 W/g, respectively.

We have estimated $\chi_{IL}(T)$ using the T_{ODT}s determined for the symmetric and nearly symmetric ($f_L \approx 0.5$) IL polymers (IL-1, 2, 3, 7 and 10) based on mean-field theory, assuming $(\chi N)_{ODT} = 10.5$.[16] The degree of polymerization N was determined using a segment reference volume, $v = 110$ Å^3, approximately the geometric average for PI and

PLA. A linear function of the form $\chi_{\text{IL}} = \alpha / T + \beta$ was extracted from the T_{ODT}s and the result is plotted in Figure 3.3, yielding:

$$\chi_{IL}^{110} = \frac{(230 \pm 60 \text{ K})}{T} - (0.38 \pm 0.14) \qquad\qquad 3.1$$
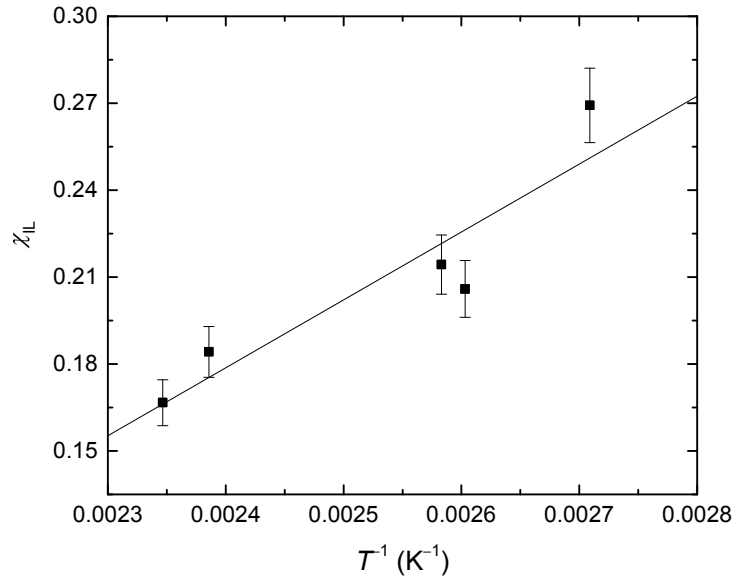
Figure 3.3 IL diblock copolymer interaction parameter χ_{IL} as a function of temperature T. The values of χ_{IL} were calculated based on the mean-field order–disorder criterion, $(\chi N)_{\text{ODT}} = 10.5$ and the T_{ODT}'s of IL-1, 2, 3, 7, and 10 determined using DMS.[*]

DSC thermograms obtained upon cooling and heating at various temperature ramp rates from representative LAM (IL-1), HEX (IL-14), and BCC (IL-15) forming IL samples are shown in Figure 3.4. The qualitative and quantitative features of the thermal response at the ODT are strongly dependent on the ordered phase morphology. Although the thermal signature of the ODT was weak for all samples, the LAM samples exhibited the strongest features comparatively. For LAM samples, peaks we attribute to the ODT were clearly visible for the disorder-to-order transition on cooling and the order-to-disorder transition on heating at all temperature ramp rates tested, as shown for IL-1 in

[*] DMS measurements and determination of $\chi(T)$ performed by Sangwoo Lee.

Figure 3.4a. HEX samples also showed clearly distinguished ODT peaks in the thermograms on cooling and heating at all temperature ramp rates, though they were substantially weaker than those observed from LAM samples, as shown for IL-14 in Figure 3.4b. The thermal signature of the ODT for BCC samples was only observed on heating and only after annealing the sample at temperatures below the T_{ODT} for a minimum of 30 min. The signature was so weak it was almost outside the resolution of the DSC instrument and could only be reliably distinguished from baseline noise at high heating rates of 20 °C/min, as shown for IL-15 in Figure 3.4c. Surprisingly, the temperature difference between the order-to-disorder transition temperature observed on heating (T_m) and disorder-to-order transition temperature observed on cooling (T_c) for the LAM and HEX forming samples was small, less than 5 °C even at the relatively fast temperature ramp rate of 20 °C/min, and became negligible as the heating and cooling rates were decreased. The HEX samples (IL-13, 14, and 5) produced slightly greater temperature differences between T_m and T_c, approximately 2–5 °C at 20 °C/min compared to 1–2 °C for LAM at the same heating/cooling rate.

The nature of the order–disorder transition was also probed with SAXS experiments. Use of the synchrotron X-ray source enabled rapid data acquisition (ca. 5 seconds per frame) while changing the temperature at the same rates as was done with the DSC (see Figure 3.4). Selected SAXS patterns collected while cooling and heating through the ODT of IL-1 at 10 °C/min temperatures are shown in Figure 3.5. Ordering and disordering occurs within the 1 °C resolution of these experiments consistent with the DSC results. These results show that nucleation and growth of the LAM-forming samples is remarkably fast, consistent with our conclusion that the heat of the DIS-LAM transition recorded by DSC (see below) reflects an equilibrium value. Similar results were obtained upon cooling and heating IL-14 (Figure 3.6), leading to the same assessment regarding the DIS-HEX transition.
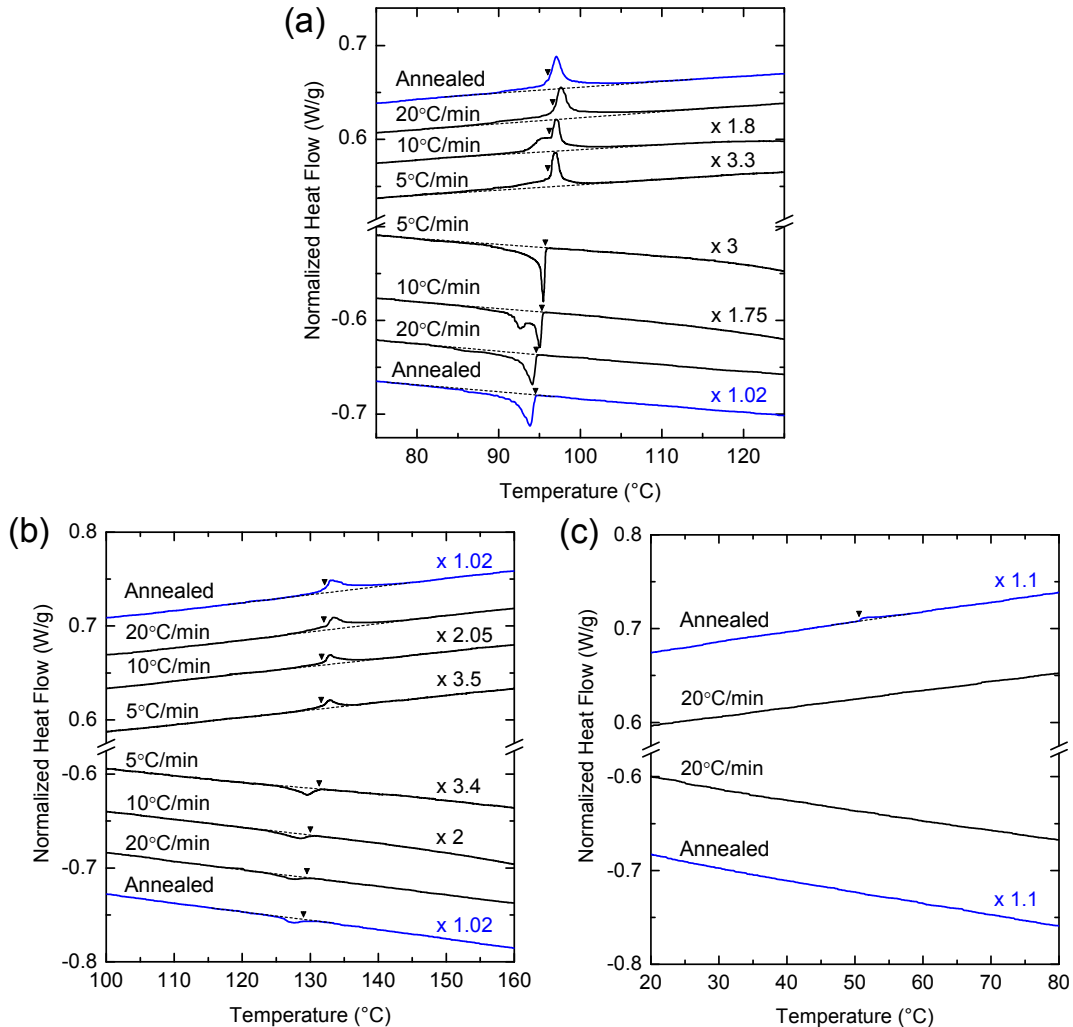
Figure 3.4 Differential scanning calorimetry measurements of the ODT. DSC thermograms obtained on cooling (below vertical axis break) and heating (above vertical axis break) at various temperature ramp rates obtained from (A) LAM forming IL-1 , (B) HEX forming IL-14, (C) BCC forming IL-15. Blue curves labeled "Annealed" were cooled and heated at 20 °C/min with an additional 1 hour annealing step (performed at 70 °C, 110 °C, and 40 °C for samples IL-1, IL-14, and IL-15, respectively) between the initial cooling and final heating steps shown. Onset temperatures are marked with triangles and the dotted lines indicate baselines used in calculations of ΔH_{ODT}. Curves have been scaled by the factors indicated to allow the data for different temperature ramp rates to be clearly presented on a single set of axes.
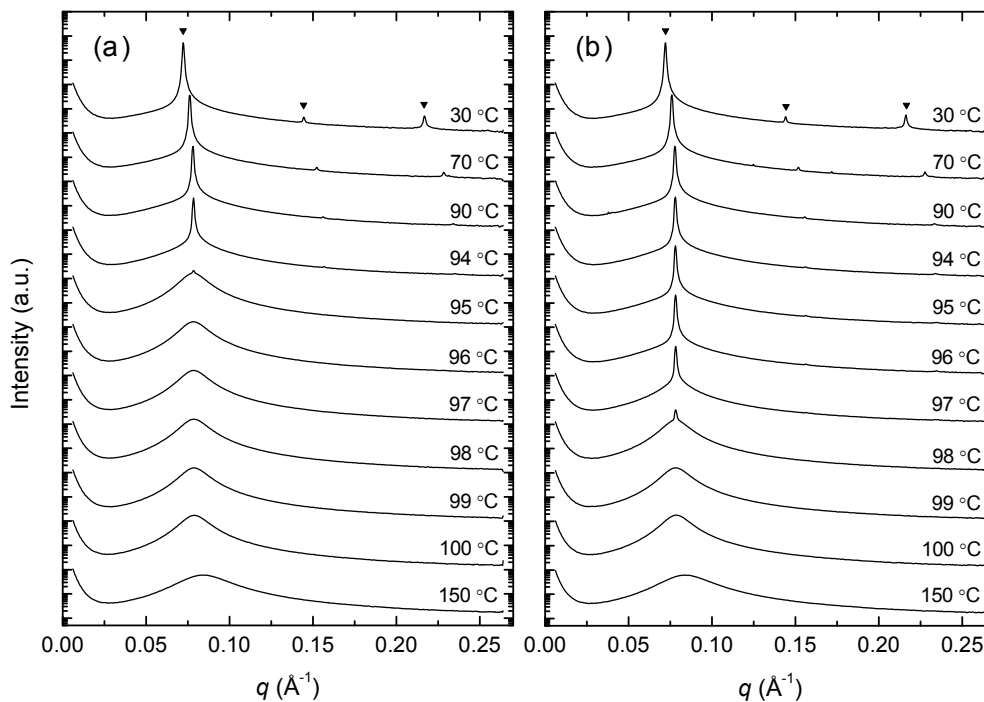
Figure 3.5 Temperature dependent SAXS for LAM forming sample IL-1. Selected scattering patterns of LAM forming IL-1 obtained at the temperatures indicated *in situ* during dynamic temperature ramp SAXS experiments while (A) cooling and (B) heating at 10 °C/min. Triangles above the 30 °C curves mark the first several allowed Bragg reflections at relative peak positions of $q/q^* = 1, 2, 3$. Data from separate temperature ramps in which data was collected at 10 °C and 1 °C temperature intervals have been combined to clearly show the transition between order and disorder. The curves have been shifted vertically for clarity.
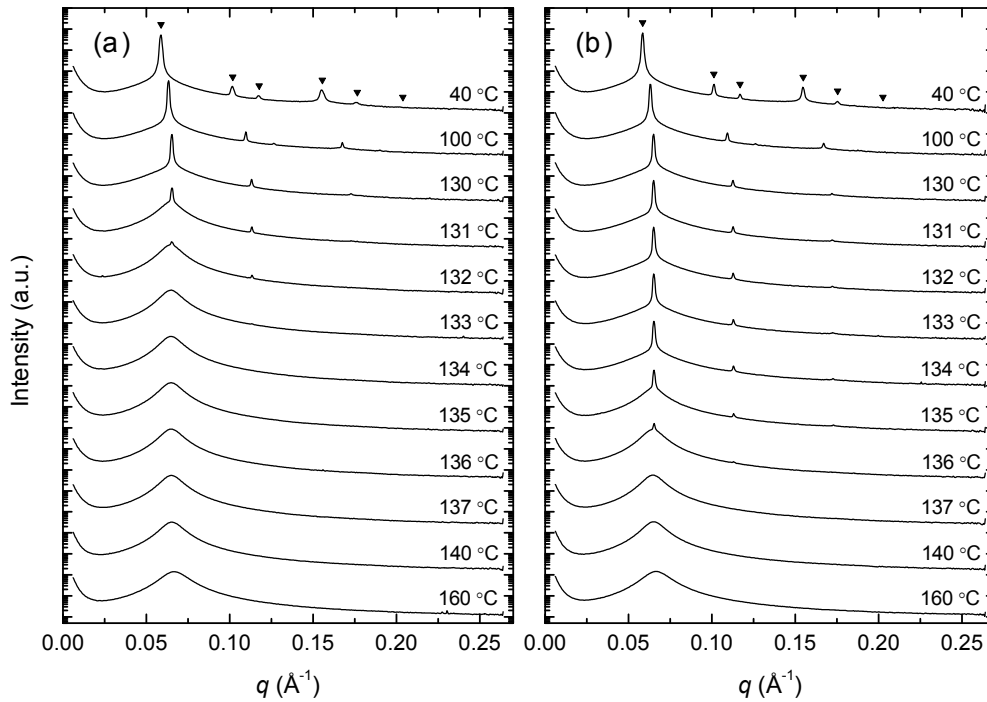
Figure 3.6 Temperature dependent SAXS for HEX forming sample IL-14. Selected scattering patterns of HEX forming IL-14 obtained at the temperatures indicated *in situ* during dynamic temperature ramp SAXS experiments while (A) cooling and (B) heating at 10 °C/min. Triangles above the 40 °C curves mark the first several allowed Bragg reflections at relative peak positions of $q/q^* = \sqrt{1}, \sqrt{3}, \sqrt{4}, \sqrt{7}, \sqrt{9}, \sqrt{12}$. Data from separate temperature ramps in which data was collected at 10 °C and 1 °C temperature intervals have been combined to clearly show the transition between order and disorder. The curves have been shifted vertically for clarity.

The behavior of the sphere-forming specimens contrasts sharply with that documented with the LAM and HEX based materials, as illustrated in Figure 3.7 for IL-15. Cooling at 20 °C/min from 100 °C (T_{ODT} + 50 °C) to 0 °C (T_{ODT} − 50 °C), fails to induce ordering, resulting in a SAXS pattern that contains a broad principal peak at $q^* \approx$ 0.065 Å^{-1} and a weak bump at $q \approx 0.16$ Å^{-1}. We attribute these features to a liquid-like arrangement of spherical (micelle-like) aggregates.[105–108] As shown in a previous publication, annealing IL-15 for 30 minutes at 40 °C following cooling from the

disordered state leads to the development of BCC crystalline order (see Figure 3.1b).[87] These results are consistent with the DSC data found in Figure 3.4c.
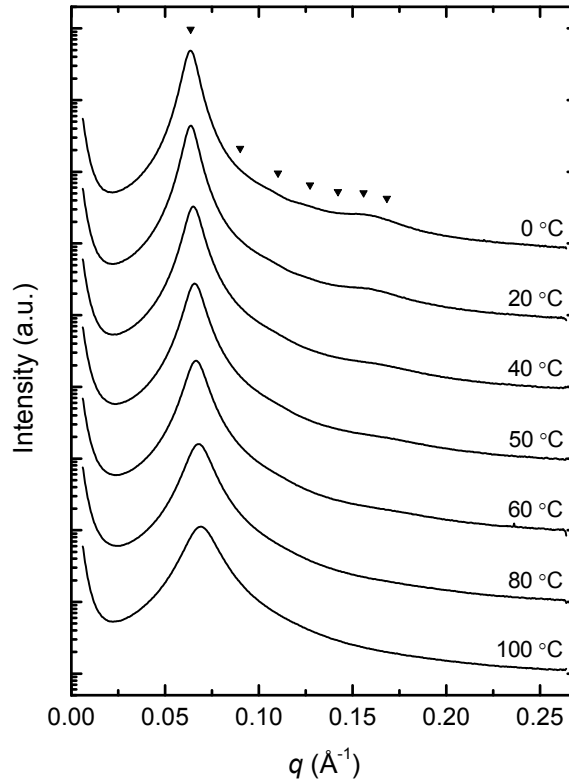
Figure 3.7 Temperature dependent SAXS for BCC forming sample IL-15. Selected scattering patterns of BCC forming IL-15 obtained at the temperatures indicated *in situ* during dynamic temperature ramp SAXS experiments while cooling at 20 °C/min. Triangles above the 0 °C curve mark the first several allowed Bragg reflections at relative peak positions of $q/q^* = \sqrt{1}, \sqrt{2}, \sqrt{3}, \sqrt{4}, \sqrt{5}, \sqrt{6}, \sqrt{7}$. The curves have been shifted vertically for clarity.

Values for ΔH_{ODT}, the latent enthalpy of transition, were calculated from the DSC thermograms by integration of the endothermic (heating) and exothermic (cooling) peaks associated with the ODT. Latent enthalpies of the order-to-disorder transition, ΔH_m, and the disorder-to-order transition, ΔH_c, are listed in Table 3.3. For all the LAM-forming specimens ΔH_m (0.31 - 0.37 J/g) was independent of the thermal history (i.e., cooling/heating rate and annealing time) and we believe this result represents an

equilibrium value referred to as ΔH_{ODT}. However, the values of ΔH_{c} obtained for IL-1 (0.25 - 0.33 J/g) are actually slightly smaller than ΔH_{m}, where the quantitative difference decreases with decreasing cooling/heating rate. This result suggests some degree of (time-dependent) refinement of the ordered LAM phase (e.g., coarsening of the polydomain morphology) following ordering.

Table 3.3 Calculated enthalpies of transition for select IL diblock copolymers.

	LAM		HEX			BCC[f]	
Sample	**IL-1**	**IL-2**	**IL-5**	**IL-13**	**IL-14**	**IL-15**	**IL-24**
Experiment	ΔH_{m} $(\Delta H_{\mathrm{c.}})$, (J/g)		ΔH_{m} $(\Delta H_{\mathrm{c.}})$, (J/g)			ΔH_{m} $(\Delta H_{\mathrm{c.}})$, (J/g)	
20 °C/min w/ anneal	0.33 [a,e] (0.25) [e]				0.17 [b] (0.05)	0.02 [c] (-)	0.01 [d] (-)
20 °C/min	0.36 [e] (0.25) [e]	0.37[e]	0.06	0.21	0.18 (0.03)	-	-
10 °C/min	0.31[e] (0.29) [e]	0.31[e]	0.06	0.08	0.11 [e] (0.07) [e]	-	-
5 °C/min	0.32 [e] (0.33) [e]	0.32[e]	0.05	0.08	0.07 (0.08)	-	-
ΔH_{max} [g]	2.0	1.8	1.0	1.6	1.5	1.9	1.5

All experimental ΔH_{m} values were calculated from the final heating step of the experiments while ΔH_{c} values, shown in parentheses, were calculated from the initial cooling step. [a]Annealed for 60 minutes at 70 °C between initial cooling step and final heating step. [b]Annealed for 60 minutes at 110 °C between initial cooling step and final heating step. [c]Annealed for 60 minutes at 40 °C between initial cooling step and final heating step. [d]Annealed for 30 minutes at 55 °C between initial cooling step and final heating step. [e]Average of values from multiple (2-4) experimental runs. [f]Distinguishable peaks were only observed on heating and only in samples that were annealed prior to the final heating step. [g]Estimated from eq 3.2.

The cylinder-forming (HEX) specimens also displayed measureable ΔH_{m} and ΔH_{c} as listed in Table 3.3. Similar values of ΔH_{m} were extracted from IL-14 approximately independent of the thermal history. (There was a slight dependence of ΔH_{m} with heating rate, i.e., larger values were obtained with faster experimental heating rates. We believe this minor difference can be attributed to systematic error associated with the limits of resolution of the DSC instrument). However, the magnitude of ΔH_{c} for IL-14 is 2- to 5-

times smaller than ΔH_m in sharp contrast to the behavior of LAM-forming IL-1. Other HEX samples (i.e., IL-5 and IL-13) showed similar results.

The BCC forming IL-15 and IL-24 also produced a (barely) measureable ΔH_m, but only at the fastest heating rate (20 °C/min) and after annealing for at least 30 minutes, i.e., the time required to transform the supercooled melt into a polycrystalline BCC material.[87] The measured value of ΔH_m was not sensitive to the annealing times longer than 30 minutes. Although the absolute value of ΔH_m measured for IL-15 and IL-24 is subject to a large absolute error (ca. ± 50%), the difference in magnitude relative to the LAM (IL-1, IL-2) and HEX (IL-5, IL-13, IL-14) is very significant.

Interestingly, IL-1 displays a second thermal transition at temperatures below the primary peak (marked by stars in Figure 3.4a) in DSC traces recorded at intermediate temperature ramp rates. Similar results were obtained with other LAM-forming samples (IL-2 and IL-3; not shown), but not with any of the HEX or BCC-forming materials. The size of this secondary peak appears to depend on the heating/cooling rate; expression of this feature at any heating rate is contingent on an intermediate cooling rate and is most pronounced at 10 °C/min. Nevertheless, the overall integrated ΔH_{ODT} values are essentially independent of this feature. We do not know the origins of this behavior but note that there is no evidence of multiple structural features in the corresponding SAXS patterns (Figure 3.5).

3.4 Discussion

Our determination of $\chi_{IL}(T)$ is based on the assumption that the symmetric ($f_L \approx$ ½) IL diblock copolymers conform with mean-field theory, i.e. $(\chi N)_{ODT} = 10.5$.[16,109] However, the absolute $(\chi N)_{ODT}$ values for the IL diblock copolymers must be somewhat higher than those determined based on mean-field theory due to local composition fluctuations, which are known to suppress T_{ODT}. Recent molecular simulations by Matsen and co-workers[110] and Morse and co-workers[48,59] indicate that $(\chi N)_{ODT} \approx 20–40$ for N values close to those considered in this work. Therefore, we expect the true value of χ_{IL} at a given temperature (e.g., one that also would account for the phase behavior of binary

blends of PI and PLA homopolymers)[17] is substantially higher, perhaps 4 times as great, as what is determined by eq 3.1. Even so, the magnitude of the interaction parameter between PI and PLA was found to be quite large, greater than that for most hydrocarbon based block copolymers.[111,112] For example, with the common segment volume (110 Å^3) used in this work, polystyrene (PS) and PI are characterized at 140 °C by χ_{SI}(140 °C) = 0.07, compared to χ_{IL}(140 °C) = 0.18, i.e. approximately 2.5 times larger.[33] A larger χ parameter dictates a smaller molecular weight for polymers with experimentally accessible T_{ODT}s, leading to behavior near the ODT that is expected to be strongly influenced by large amplitude composition fluctuations in both the disordered and ordered states.

The IL diblock phase portrait constructed using eq 3.1 and Table 3.2 is presented in Figure 3.8. The overall features of the phase portrait are very similar to those of relatively weakly-segregated systems, i.e., for much larger N.[33,113,114] Compared to the ideal theoretical phase portrait (assuming a conformationally symmetric system with perfect uniformity of chain length), the order-order phase boundaries are shifted toward slightly higher PLA compositions.[16,109] For a minority of PLA, the HEX-LAM phase boundary is located at f_L, (HEX-LAM) = 0.38 ± 0.02 while at higher PLA content, f_L, (HEX-LAM) = 0.70 ± 0.02; in the strong segregation limit theory anticipates $f_A \cong 0.32$ and 0.68, respectively for symmetric diblock copolymers.[41,109] Asymmetrically placed phase boundaries can be attributed to differences in block dispersities ($Đ = M_w/M_n > 1$) and conformational asymmetry.[34–36,115] Although the dispersities of the PLA blocks are slightly higher than those of the PI counterparts (this can be deduced from the somewhat larger IL diblock copolymer dispersities compared to the PI values, see Table 3.1), we do not believe the modest shifts in the IL phase portrait can be attributed to these minor differences. Most likely, the locations of the phase boundaries reflect conformational asymmetry between PI and PLA: the ratio of statistical segment lengths, a, at a common reference volume at 140 °C is $a_{PLA}/a_{PI} \approx 1.2$.[116,117] Several experimental studies of diblock copolymer phase behavior have correlated a shift of the phase boundaries toward higher fractions of the blocks with the larger statistical segment length, which are

consistent with the current findings and supported by self-consistent mean-field theory (SCFT).[34]
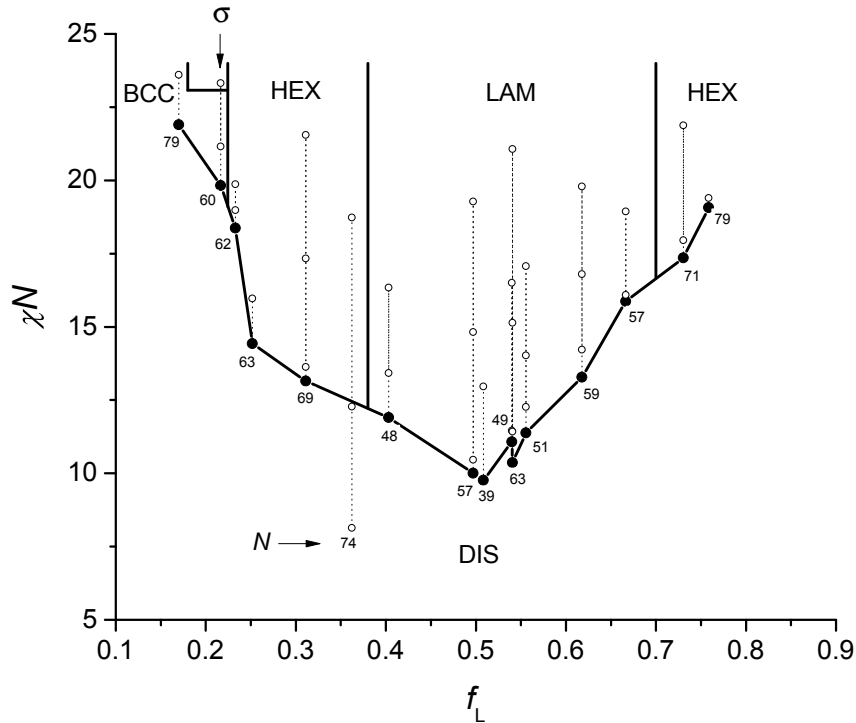
Figure 3.8 Experimental phase portrait for IL diblock copolymers.
The phase space points examined by SAXS are marked by white dots ($\circ$) and $(\chi N)_{ODT}$ identified by DMS based on the mean-field theory are marked by black dots ($\bullet$). Below or near the $(\chi N)_{ODT}$ points, degrees of polymerization N are identified. Data points obtained from each sample are connected with dashed lines ($\cdots$) and the interpolated phase boundaries are marked by solid lines ($-$).

Along with the classical ordered phases (LAM, HEX, BCC), the IL phase portrait contains the recently discovered Frank–Kasper σ phase,[87] located at large values of χN between the BCC and HEX regions. This is consistent with the relative placement of the analogous phase in thermotropic dendritic liquid crystals.[118,119] See Chapters 4 and 5 for a detailed study of the phase behavior of IL diblock copolymers in the region of the phase portrait near IL-15, including the discovery of a long lived metastable dodecagonal

quasicrystal phase. The appearance of the Frank–Kasper σ phase on the L-rich side of the IL phase portrait between the BCC and HEX phases is consistent with recent SCFT results for conformationally asymmetric diblock copolymers motivated by the discovery of the σ phase in IL diblock copolymers.[43] These SCFT calculations predict an opening of a window of stability of Frank–Kasper phases between the BCC and HEX phases on the side of the phase portrait rich in the block with the smaller statistical segment length (i.e., the isoprene rich side of the phase portrait in the IL system), analogous to what is observed in the IL system here.[43] It seems statistical segment length asymmetry plays an important role in the thermodynamics of short diblock copolymers.

The IL-16 ($f_L = 0.36$ and $N = 74$) is unusual in that an ordered HEX phase persists well below the order–disorder phase boundary interpolated from neighboring samples (IL-14 and IL-11), and did not display any signature of an order–disorder transition by DMS and SAXS experiments up to 250 °C (data is not shown). IL-16 has a PLA block, on average, just 5 lactide repeat units longer than IL-14 ($f_L = 0.31$, $N = 69$). These compounds were polymerized using the same polyisoprene precursor (I-4), yet resulted in very different $(\chi N)_{ODT}$ values. Surprisingly IL-11 ($f_L = 0.40$, $N = 48$) showed $(\chi N)_{ODT} = 11.9$, seemingly consistent with the overall order–disorder transition behavior exhibited by the complete set of IL diblock copolymers. We do not understand the origins of this anomaly. However, it may be another consequence of fluctuation effects, which introduce an additional N dependence to $(\chi N)_{ODT}$.[16,17]

The ODT must be accompanied by thermal effects that, in principle, should be amenable to characterization using calorimetric techniques. However, due a miniscule latent heat of transition ($\Delta H_{ODT} \sim \chi \sim N^{-1}$) such techniques have been of limited use with BCPs, even those with moderately low molecular weight. Although relatively rare, there have been several previous reports identifying the ODT by differential scanning calorimetry (DSC).[80–82,84–86] Nevertheless we are unaware of any systematic studies of such thermal features, i.e., measurements of ΔH_{ODT} over a wide range of compositions covering three distinct morphologies as reported in this work.

A striking feature of Figure 3.4a and Figure 3.4b is the almost negligible differences between T_m and T_c for the LAM and HEX forming specimens; $T_m - T_c \approx 0$ when the heating/cooling rate was lowered from 20 to 5 °C/min. We believe this lack of hysteresis is a manifestation of composition fluctuations, and the resulting weakly first-order character of the associated phase transitions. Strong first-order phase transitions generally are governed by substantial free-energy barriers to nucleation leading to significant supercooling (superheating) as is well-documented with water and other simple compounds during condensation (evaporation) and crystallization (melting).[120]

Another feature that implicates composition fluctuations is the magnitude and strong composition (i.e., ordered-state symmetry) dependence of ΔH_{ODT}, ranging from 0.36 J/g for IL-1 (LAM) to 0.02 J/g for IL-15 (BCC) (see Table 3.3). These ΔH_{ODT} values are very small, several orders of magnitude lower than those associated with the crystallization of polymer chains; for example, the heat of fusion for PLA is 93 J/g.[121] In an effort to gain a better appreciation for the magnitude of these ΔH_{ODT} values we consider two simples models, illustrated schematically for the DIS-LAM transition in Figure 3.9.
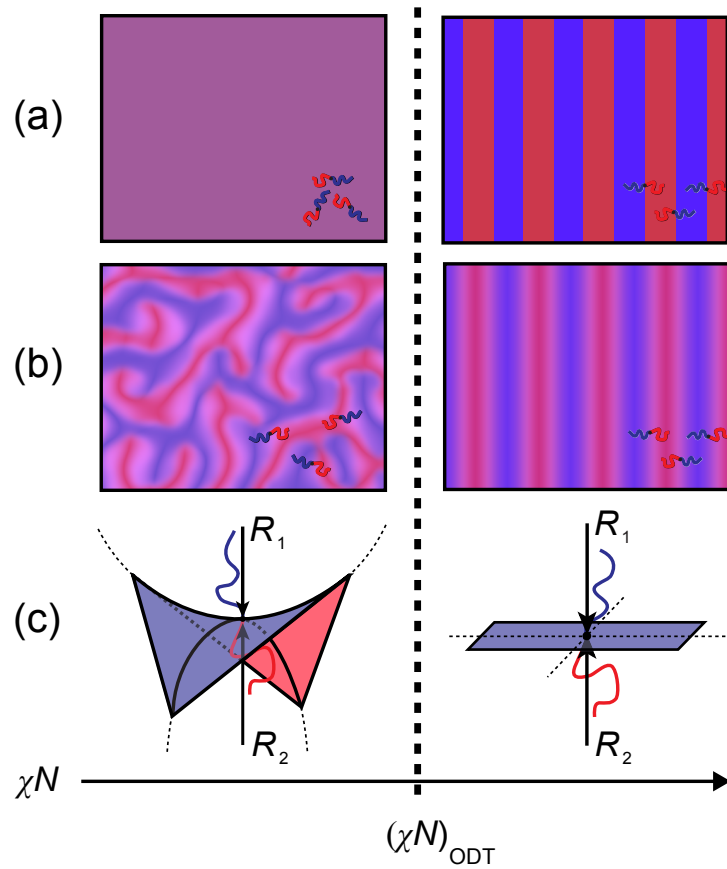
Figure 3.9 Schematic illustrations of order and disorder in LAM forming diblock copolymers. (a) Formation of a LAM phase with pure domains and sharp interfaces from a homogeneous disordered phase resulting in the maximum possible enthalpy of transition, as estimated in eq 3.2. (b) Formation of a LAM phase from a fluctuating disordered phase. (c) Illustration of the curvature of the interface separating the domains for the situation depicted in (b) in which $R_1 = -R_2 \approx R_g$ in the disordered state and $R_1 = R_2 \approx \infty$ in the LAM phase.

The maximum possible change in enthalpy for the order–disorder transition can be estimated as:

$$\Delta H_{max} = \frac{RT_{ODT} f_L (1 - f_L) \chi_{ODT} N}{M_n} - \frac{\Sigma \gamma_{IL}}{\rho} \qquad 3.2$$

The first term on the right-hand side of eq 3.2 accounts for the difference in enthalpy between homogeneously mixed and completely separated (i.e., strongly segregated) PI

and PLA segments, where R is the gas constant.[83] The second term deals with contact between segments at domain interfaces, where $\gamma_{IL} \approx (kT/a^2)\sqrt{\chi/6}$ is the interfacial tension[122] (k is Boltzmann's constant and a is the statistical segment length)[2] and Σ is the interfacial area per unit volume; e.g., $\Sigma_{LAM} = 2/D = q*/\pi$ for the LAM morphology. Assuming $a \approx 0.63$ nm (the average of a_{PI} and a_{PLA} using a common 110 Å[3] segment reference volume), a density of 1 g/cm^{3}, and taking $q*$ from the SAXS results, yields estimated average values of ΔH_{max} for the LAM (2.0 J/g), HEX (1.5 J/g) and BCC (1.9 J/g) forming compounds (Table 3.3). These estimates are much larger than the experimentally determined heats of transition.

Alternatively, we can imagine that the transition from disorder to order involves almost no change in the local composition profile (i.e., the first term in eq 3.2 disappears) as depicted in Figure 3.9b. In this limit, a symmetric fluctuating bicontinuous disordered phase features domains with finite concentrations of PI and PLA divided by hyperbolic interfaces characterized by zero mean curvature ($H = [c_1 + c_2]/2 = 0$, where $c_1 = 1/R_1$ and $c_2 = 1/R_2$), negative Gauss curvature ($K = c_1 c_2 < 0$) and no spontaneous curvature ($c_o = 0$).[50,123] Virtually complete loss of higher-order diffraction, for example extinction of $I(3q*)$, as T approaches T_{ODT} (Figure 3.5) suggests that the LAM composition profile at the transition is essentially sinusoidal. Transition to a lamellar morphology produces flat interfaces with $H = 0$, $K = 0$ and $c_o = 0$. Assuming there is no change in the local (instantaneous) composition profile, the heat of transition will reflect only the change in the topology of the interface separating the domains,

$$\Delta H_{fluc} = \frac{\gamma_{AB}}{\rho}(\Sigma_{DIS} - \Sigma_{LAM}) \qquad 3.3$$

where Σ_{DIS} is the interfacial area per unit volume of the disordered phase. The disordered fluctuating state for LAM-forming diblock copolymers ($f_L = 1/2$) is believed to be bicontinuous, similar to the structure observed during the late stages of spinodal decomposition,[14,50] hence $\Sigma_{DIS} \approx 0.5q*$.[123] Setting $q* = 0.078$ Å[-1] (Figure 3.5) yields $\Delta H_{fluc} \approx 0.37$ J/g. This result is remarkably consistent with the value measured for IL-1

(Table 3.3). Although both estimates of ΔH_{ODT} (eqs 3.2 and 3.3) are relatively crude constructions (most seriously due to the mean-field assumption implicit in calculating χ), they lead us to favor the interpretation represented by Figure 3.9b and Figure 3.9c, i.e., a weakly first-order pattern transition that exchanges interfacial area for configurational entropy.

The SAXS data collected during temperature ramp experiments through the ODT further support our speculation that the ODT for LAM samples occurs with almost no change in the local composition profile. The total integrated scattering intensity (i.e., the total scattering power of a sample) known as the Porod invariant, Q, can be obtained by integrating the scattered intensity, $I(q)$, over all of reciprocal space. For an isotropic sample,[100,124]

$$Q = \frac{1}{2\pi^2} \int_{q=0}^{\infty} q^2 I(q) \, dq \qquad\qquad 3.4$$

The invariant reflects the extent of scattering length density inhomogeneity in a sample, which in the case of BCPs is directly linked to the local composition profile. For an ideal two-phase system consisting of regions of constant but differing scattering length densities separated by sharp boundaries (e.g., the LAM model in Figure 3.9a), the invariant calculated by eq 3.4 (with $I(q)$ in absolute intensity) reduces to,

$$Q_{\mathrm{ideal}} = (\Delta\rho)^2 \phi_1 \phi_2 \qquad\qquad 3.5$$

where ϕ_1 and ϕ_2 are the volume fractions of the two phases and $\Delta\rho$ is the difference in scattering length density between the two regions. Q_{ideal} does not depend on how the two regions are arranged in space, hence the term invariant. SAXS data reported here were acquired on a relative intensity scale, hence the absolute magnitude of the invariant, and the associated composition profile, cannot be determined. The temperature dependence of the *relative* invariant, Q_{rel}, was calculated by integrating the background corrected intensity over $0.02 \leq q \leq 0.26$ Å^{-1}; this q range captures the entire measureable intensity

in excess of the background scattering as illustrated in inset (b) of Figure 3.10 for IL-1.[*] The temperature dependence of Q_{rel} determined for IL-1 while heating and cooling at 10 °C/min is shown in Figure 3.10. Q_{rel} decreases approximately linearly with increasing temperature consistent with a graduate reduction in the degree of segregation between the PI and PLA blocks. Most significantly, Q_{rel} changes by less than 2 % at the ODT consistent with little if any change in the local composition profile at the LAM-DIS transition in agreement with the case depicted in Figure 3.9b.

Remarkably, the LAM-DIS transition is accompanied by almost no change in $q^*(T)$ (Figure 3.11a), consistent with earlier studies based on higher molecular weight symmetric diblock copolymers.[50,71,73] As shown in the inset to Figure 3.10a q^* jumps by just 0.2% (i.e., < 0.02 nm) at the ODT. Nevertheless, individual chains are stretched considerably beyond the theoretical mean-field values at the ODT;[16] for IL-1 the periodic spacing, $D^* = 2\pi/q^* = 8$ nm (Figure 3.5), is more than 50% greater than $D_{MF}^* = (2\pi/1.95)R_g = 5.1$ nm, where $R_g = a(N/6)^{1/2}$. Apparently, loss of negative Gauss curvature does not influence local molecular packing constraints reinforcing the notion that the LAM-DIS transition rearranges the global interfacial curvature without significantly affecting the local composition density profile, H or c_o. These results leave open the possibility that $\Delta q^* \to 0$ at the ODT under precisely symmetric conditions (i.e., an AB diblock copolymer with $f_A = \frac{1}{2}$, $Đ = 1$ and $a_A/a_B = 1$); note that the small diffraction peaks at $2q^*$ in Figure 3.5 demonstrate that IL-1 is slightly off of volumetric symmetry.

---

[*] We note that for an ideal polymer melt (i.e., an ideal random Gaussian coil), the intensity as q approaches ∞ decays as q^{-2} and thus, the invariant integral is mathematically unbounded.[237] From a practical standpoint, the q^{-2} decay does not persist to arbitrarily high q for a real polymer chain, being limited by the finite size of the monomer units, and real experimental data is often dominated by background contributions at high q. In the calculations here of Q_{rel} over a finite q range, the effect is simply a constant background contribution to Q_{rel} in both the LAM and DIS phases that has no influence on the subsequent interpretation and conclusions.
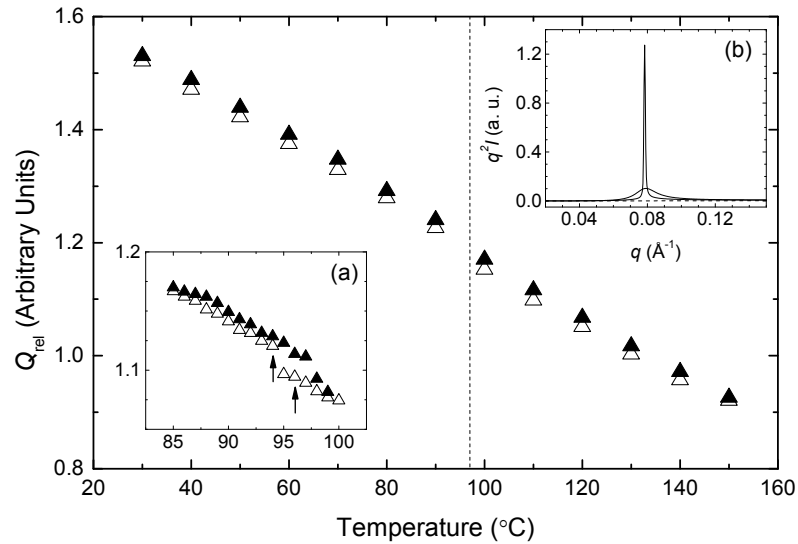
Figure 3.10 SAXS Invariant near the ODT for sample IL-1. Temperature dependence of the relative SAXS invariant, Q_{rel}, for LAM forming IL-1 calculated from temperature ramp SAXS experiments conducted at 10 °C/min on heating (filled symbols) and cooling (open symbols) at 10 °C/min. The vertical dotted line indicates the location of the ODT. Inset (a) shows data collected over a narrower temperature range in the vicinity of T_{ODT} on heating (filled symbols) and cooling (open symbols). Inset (b) shows SAXS patterns collected on cooling corresponding to the data points indicated by arrows in inset (a) at 96 °C (DIS, broad peak) and 94 °C (LAM, sharp peak) displayed as q^2I (related to the integrand of eq 3.4) as a function of q. The empty capillary data, which is subtracted from the experimental data prior to calculation of Q_{rel}, is shown as a dashed curve.
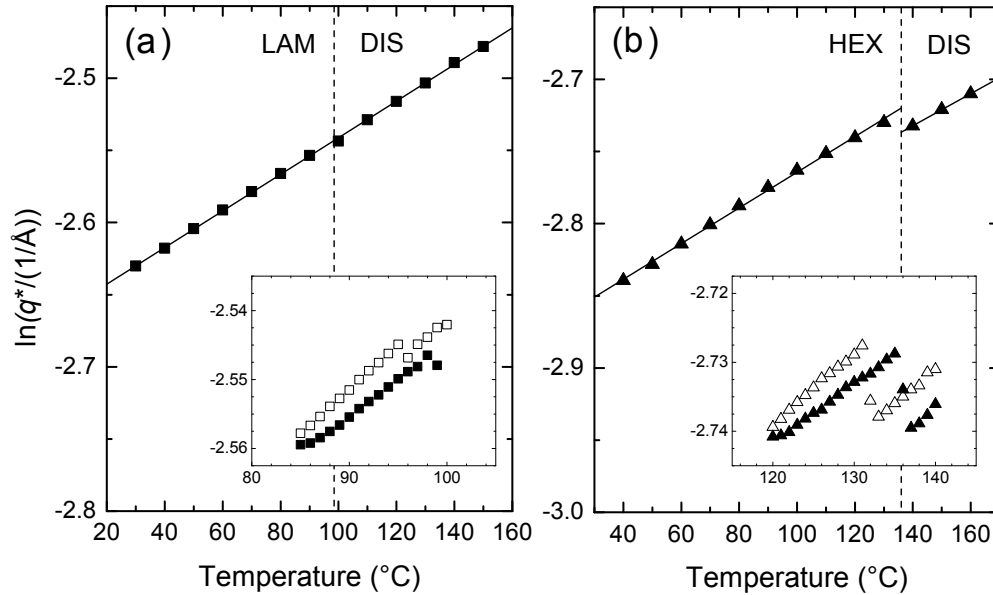
Figure 3.11 Temperature dependence of q^* near T_{ODT}. (a) LAM forming IL-1 and (b) HEX forming IL-14 extracted from temperature ramp SAXS experiments conducted at 10 °C/min on heating. Solid lines are linear fits to the data and dashed vertical lines indicate the locations of the ODTs. Insets show data collected over a narrower temperature range in the vicinity of T_{ODT} on heating (filled symbols) and cooling (open symbols) at 10 °C/min.

Taken together, the SAXS, DMS and DSC results demonstrate that symmetric diblock copolymers belong to the Brazovskii universality class of fluctuation-induced weakly first-order phase transitions even in the limit of very low N. Reducing the composition to $f_L = 0.31$ (sample IL-14) changes the nature of the ODT. As shown in Figure 3.11b, q^* exhibits a small (ca. 1%) but distinct discontinuity at the DIS-HEX transition, which we associate with qualitative differences in the interfacial properties of the ordered ($H \neq 0$, $K = 0$ and $c_o \neq 0$ for a cylindrical morphology) and fluctuating disordered states. A modestly asymmetric composition likely narrows the difference between the fluctuating disordered and ordered morphologies, driving down ΔH_{ODT}, relative to the symmetric ($f_L = \frac{1}{2}$) case (Table 3.3).
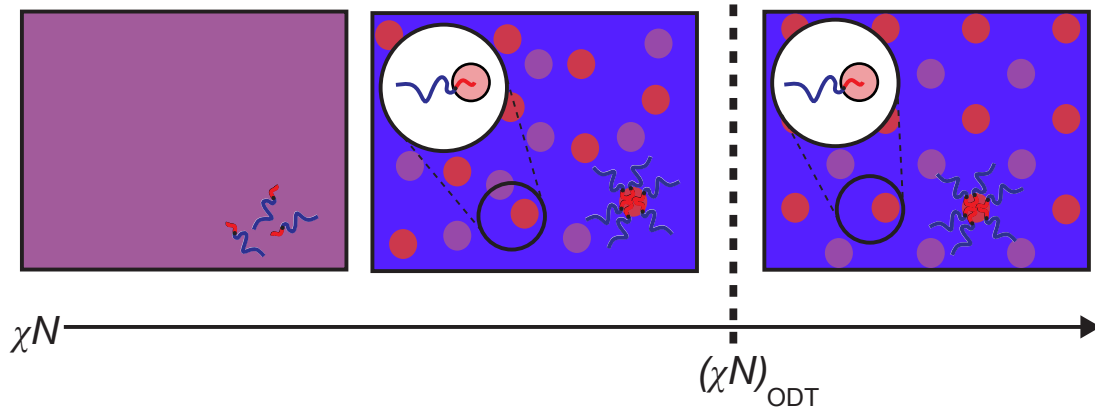
Figure 3.12 Schematic illustration of order and disorder in point particle (sphere) forming diblock copolymers. At low χN (high temperature for a fixed N sample) a homogeneous and isotropic disordered phase exists (left panel). As χN increases (temperature decreases) to approach the ODT, composition fluctuations result in a disordered phase that contains micelles (middle panel). At the ODT, the micelles order on a BCC lattice with minimal change to the interface between the blue and red domains (right panel).

More dramatic thermodynamic and structural differences were obtained with $f_L = 0.22$, where the ordered state morphology is a BCC arrangement of nearly spherical ($H \neq 0$, $K = 0$ and $c_o \neq 0$) point particles. In this limit ΔH_{ODT} practically disappears (Table 3.3) and the rate of ordering drops by orders of magnitude, i.e. 30 minutes at 40 °C (BCC) and more than a day at 25 °C (σ phase).[87] We believe these changes can be explained based on the structure of the disordered state as depicted in Figure 3.12. As the temperature approaches T_{ODT} asymmetric composition fluctuations will be manifested as discrete micelles as anticipated theoretically by Semenov[125] in the limit $f \to 0$. The presence of micelles in the disordered state has been demonstrated using a variety of experimental techniques including DMS, SAXS, small-angle neutron scattering, transmission electron microscopy, and x-ray photon correlation spectroscopy.[67,106,107,126,127] Since the disordered and solid (crystalline) phases are characterized by the same domain morphology no change in interfacial topology occurs during ordering, i.e. $\Sigma_{DIS} \cong \Sigma_{BCC}$

with essentially constant $H \neq 0$, and $c_o \neq 0$ and $K = 0$. We believe this explains the drastic reduction in ΔH_{ODT}.

Assuming the small bump that appears at high q in the SAXS patterns in Figure 3.7 corresponds to the first maximum in the spherical form factor ($qR = 5.76$) we estimate a micelle core radius of $R = 3.5$ nm. Combined with the BCC lattice spacing of $a = 13.7$ nm extracted from Figure 3.1b yields a volume fraction of spheres at the ODT of $f_{spheres} \approx 0.14$. This value is less than f_L suggesting that a portion of the PLA blocks remain dissolved in the PI matrix. This may help to explain the existence of the σ phase by analogy with the multiplicity of ordered spherical states predicted by Semenov[125] near the ODT in the asymmetric limit $f \rightarrow 0$.

3.5 Conclusions

This report describes the thermodynamic behavior of a series of model high χ and low N poly(1,4-isoprene-b-DL-lactide) block copolymers (BCPs) near the order–disorder transition (ODT). The measured structural and thermal characteristics of the ODT, particularly the magnitude of ΔH_{ODT} and the strong dependence of ΔH_{ODT} on ordered phase morphology, provide direct evidence that supports an interpretation of the ODT in BCPs as a weakly first-order phase transition dominated by the effects of local composition fluctuations. Weakly first-order, fluctuation-driven phase transitions are known to occur in many physical systems,[128] ranging from technologically important materials (e.g., isotropic-nematic[129] and nematic-smectic[130,131] transitions in liquid crystals, certain types of superconductors[132] and magnetic alloys[133]) to more exotic forms of condensed matter (e.g., Bose-Einstein condensation of ultracold atoms[134]). Block polymers offer convenient experimental systems for studying this fascinating class of phase transitions while providing access to industrially relevant nanostructured materials. An added dividend of the work reported here is direct contact with computer simulations, potentially exact analogues of our experimental system, made feasible by the reduced molecular size.[48,59,110,135] See Chapter 7 for a direct comparison of simulations and experimental data from the IL-1 polymer.[90]

Chapter 4:

Dodecagonal Quasicrystalline Order in a Diblock Copolymer Melt

4.1 Introduction

The initially controversial discovery of what has come to be called quasicrystalline[136] order in rapidly cooled Al-Mn alloys by Shechtman et al. in 1984[137] heralded a paradigm shift in the understanding of condensed matter, expanding the concept of order beyond traditional, periodic crystals. Quasicrystals (QCs) are structures that have long-range order but are not periodic. That is, QCs exhibit sharp, essentially discrete diffraction spots in scattering experiments (what is now accepted as a condition for long-range order)[138] but their structures lack translational symmetries and therefore cannot be reduced to a finite volume unit cell that can be tiled to fill space like traditional (periodic) crystal structures. Since QCs are not periodic, they can exhibit scattering patterns with rotational symmetries that are not compatible with periodic order (e.g., 5-, 8-, 10-, 12-fold rotational symmetries). Different QCs are often categorized by their rotational symmetries. Since the initial discovery of icosahedral QCs (QCs with

scattering patterns with the point group symmetry of an icosahedron, $m\overline{3}\overline{5}$) in Al-Mn alloys,[137] a continually expanding variety of QCs have been identified in a diverse array of hard[137,139] and soft[140–147] materials, including in some natural minerals.[148–150] These discoveries have led to considerable interest from researchers across many disciplines (physicists, mathematicians, chemists, engineers, etc.) to understand and utilize these fascinating materials.[*]

In 2004, Zeng et al.[143] first discovered quasicrystalline order in a soft material, wedge-shaped dendrimer molecules that in the undiluted melt self-assemble into approximately spherical aggregates that order on a quasicrystalline lattice. This discovery indicated that QCs are a universal structural motif across length scales ranging from atomic to supramolecular dimensions. The soft QC discovered in the wedge-shaped dendrimers was a dodecagonal quasicrystal (DQC), a QC with 12-fold rotational symmetry, identified through careful X-ray scattering measurements from a sample prepared to contain a single quasicrystalline grain. Illustrations of the structures of DQCs and closely related periodic phases are shown in Figure 4.1. The single grain two-dimensional X-ray scattering patterns showed the characteristic 12-fold rotational symmetry of the DQC and closely matched the predicted scattering pattern from the structural model of the DQC shown in Figure 4.1c.[143]

DQCs are 2-dimensional or axially symmetric quasicrystals, meaning the structure is aperiodic in the x–y plane perpendicular to the 12-fold axis but periodic along the z-direction of the 12-fold axis. The structural model of the DQC in Figure 4.1c is generated from an aperiodic tiling of the x–y plane with square and equilateral triangle tiles that are "decorated" with particles at particular positions within the tile in the x–y plane and at particular periodic elevations in the z-direction. In this tiling pattern, there is one type of square tile and two types of equilateral triangular tiles (identified with filled and empty circles in Figure 4.1c).

---

[*] For an interesting first hand account of the history of quasicrystals, see the article by Steinhardt.[238]
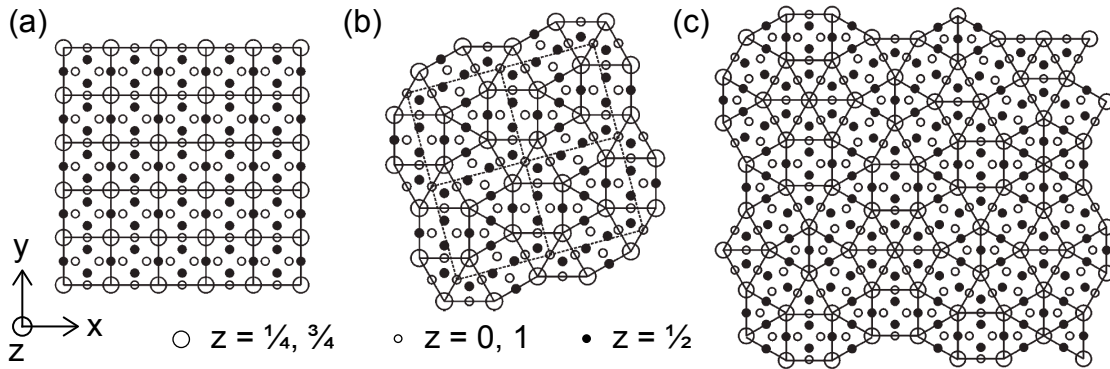
Figure 4.1 Particle packing in the dodecagonal quasicrystal and closely related Frank–Kasper phases. The structure of these phases can be generated by tessellation of the x–y plane using square and equilateral triangles that are "decorated" with particles at particular positions in the z-direction. (a) The cubic A15 phase generated from a tessellation using only identical square tiles. (b) The tetragonal σ phase generated from a periodic tessellation of the same square tile as the A15 phase along with two equilateral triangle tiles (2:1 triangle to square ratio). (c) The dodecagonal quasicrystal generated from an *aperiodic* tiling using the same tiles as the σ phase ($4/3^{1/2}$:1 ($\approx$ 2.31) triangle to square ratio). Positions in the z-direction are given in fractions of the z-direction period. Adapted by permission Macmillan Publishers Ltd: Zeng, X. et al. *Nature* **2004**, *428*, 157–160. Copyright 2004.[143]

The DQC is structurally related to a class of periodic, large unit cell crystal structures called Frank–Kasper phases.[151,152] These crystal structures contain only tetrahedral interstitial holes and are consequently also called tetrahedrally or topologically close-packed structures. They were first considered by Frank and Kasper in the 1950s to explain the complex, low symmetry crystal structures of intermetallic alloys based on sphere packing arguments.[151,152] Two Frank–Kasper phases that have been reported in soft materials are shown in Figure 4.1.[87,118,141,147,153–158] The so-called A15 phase (space group 223, $Pm\overline{3}n$) shown in Figure 4.1a is a cubic structure that can be constructed by tiling the x–y plane with square tiles, while the σ phase (space group 136, $P4_2/mnm$) shown in Figure 4.1b is a tetragonal structure constructed from a *periodic* tiling of the x–y plane using the same square and triangle tiles employed in the DQC model. Frank–Kasper phases compete with the structurally related DQC for stability in soft materials, with the σ phase and A15 phase often appearing near the DQC in

parameter space. Indeed, the dendrimer DQC has been reported to occur over a range of temperatures adjacent to regions of stability of the A15 and σ phases, depending on the details of the molecular architecture.[141,143,147] The Frank–Kasper phases are often viewed as periodic approximants to the DQC as they are closely related structures that have large, but finite volume unit cells.

Several examples of DQCs have been reported in various categories of soft materials in relatively complex multi-component systems, including binary mixtures of ligand coated nanoparticles,[146] mesoporous silica derived from concentrated solutions of surfactant micelles,[145] concentrated micellar solutions of diblock copolymers,[142] and in polymer blends containing ABC-type miktoarm star polymers.[140] QCs are rare in single component systems. To the best of our knowledge, the DQC state has only been documented in the wedge-shaped dendrimers described above[141,143,147] and a linear poly(styrene-*b*-isoprene-*b*-styrene-*b*-ethylene oxide) (SISO) tetrablock terpolymer.[144] Here, we report the discovery of a DQC phase in a one component poly(1,4-isoprene-*b*-DL-lactide) (IL) linear diblock copolymer melt, the simplest system to exhibit a DQC phase to date. This chapter describes the experiments that led to the identification of the DQC phase, an extensive characterization of the kinetics of ordering of the DQC and related phases, and an evaluation of the stability of the DQC phase. Much like the case for the wedge shaped dendrimers,[143] the DQC phase is found in parameter space near, and competes for stability with, the Frank–Kasper σ phase, also recently discovered in a IL diblock copolymer melt by Lee et al.[87] The DQC phase is found to be a long-lived metastable state that nucleates and grows from the supercooled disordered state and transforms into the equilibrium Frank–Kasper σ phase over sufficiently longer times.

4.2 Experimental Section

4.2.1 Material
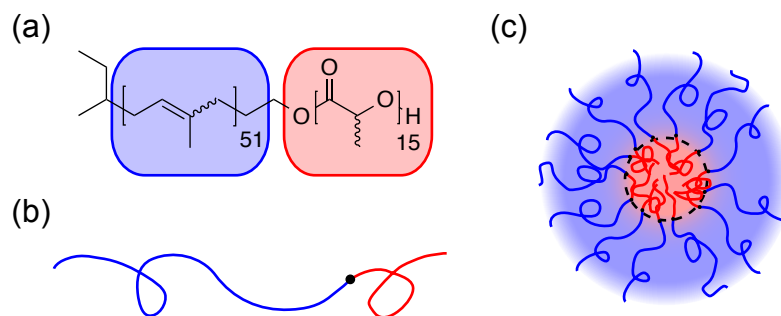
Figure 4.2 Molecular and supramolecular structure of the IL polymer designated IL-5.1. (a) molecular structure of IL-5.1. Schematic illustrations of (b) an asymmetric IL diblock copolymer molecule and (c) a single self-assembled nearly spherical micelle-like point particle.

The experiments described in this chapter were conducted on a compositionally asymmetric IL diblock copolymer material designated IL-5.1. The molecular structure is shown in Figure 4.2. Synthesis and molecular characterization of this polymer are described in Chapter 2. Pertinent molecular parameters for IL-5.1 are summarized in Table 4.1. For a complete description of the thermodynamics of IL diblock copolymers see Lee et al.[15] and Chapters 3 and 5. It is important to note that IL-5.1 has an overall molecular weight and composition f_L slightly larger and slightly smaller, respectively, than the polymer IL-15 recently shown to form the Frank–Kasper σ phase (M_n = 3890 and f_L = 0.22).[87,88] To improve stability of this polymer, the material was extensively dried by twice freeze-drying from a concentrated benzene solution with a small amount (≤ 0.5 wt. %) of antioxidant stabilizer (butylated hydroxytoluene, BHT) added to the polymer during the second freeze-drying step. Small amounts of BHT do not measurably influence the phase behavior of block polymer melts.[159]

Table 4.1 Molecular characterization data for IL-5.1.

Polymer	$M_{n,I}$[a]	$M_{n,L}$[a]	M_n[a]	N[b]	f_L[c]	$Đ$[d]	$T_{g,I}$[e]	$T_{g,L}$[e]	T_{ODT}[f]
IL-5.1	3540	1070	4600	72.5	0.18	1.06	−63 °C	0 °C	66 °C

(a) Number-average molecular weight in g/mol based on ^{1}H NMR. (b) Volumetric degree of polymerization based on reported[30,104] homopolymer densities at 25 °C (0.9 and 1.25 g/cm^3 for I and L, respectively) and a reference volume of 110 Å^3 (c) Volume fraction of L block based on reported homopolymer densities at 25 °C and ^{1}H NMR. (d) From RI-SEC with a tetrahydrofuran mobile phase. (e) Glass transition temperature from DSC. (f) Order–disorder transition temperature from DMS.

4.2.2 Small-angle X-ray scattering (SAXS)

SAXS experiments were conducted on the DND-CAT 5-ID-D beamline at the Advanced Photon Source (Argonne National Laboratory).[160] Experiments utilized a sample-to-detector distance of 8500 mm and an X-ray wavelength of $\lambda = 0.729$ Å. 2D scattering patterns were collected with a Rayonix area CCD detector. All SAXS patterns were integrated to obtain 1D plots of intensity (in arbitrary units) versus q. Temperature was controlled with a modified Linkam HFS91 hot stage. IL-5.1 samples were loaded in 1.5 mm nominal diameter quartz capillaries (Charles Supper Company) and inspected visually to ensure the X-ray beam illuminated a portion of the capillary filled with polymer material. For experiments conducted at elevated temperatures the capillaries were sealed with epoxy to limit exposure to atmospheric oxygen.[161] Unsealed capillary samples that were annealed for extended periods of time at room temperature ($\approx$ 25 °C) were placed in airtight screw cap vials that were flushed with argon gas prior to closure. Selected capillary samples were analyzed by SEC following SAXS experiments to confirm the absence of polymer degradation; no evidence of degradation was found in any of the samples tested.

To load the polymer samples into capillary tubes, polymer is placed in the top of a capillary tube with care taken to avoid completely blocking the opening. The capillary is then placed into a glass culture tube to protect it during handling. The culture tube is placed into a vacuum oven maintained at a temperature above T_{ODT}. Rapid evacuation

occurs prior to heating, which facilitates flow of the polymer down the capillary. In the hot vacuum oven, the polymer material disorders into a low viscosity polymer melt. The vacuum oven is then backfilled with air, which forces the polymer partially down the capillary tube. While the capillary is still above T_{ODT}, the glass culture tube (with capillary) is placed in a centrifuge and spun (3300 rpm) for about 30 seconds, which forces the polymer to the bottom of the capillary. Finally, the sample is annealed in the disordered phase in the vacuum oven to remove any residual air and to consolidate the sample in a stress-free state.

Typical SAXS experiments described in this chapter involve equilibrating the sample in the disordered phase, quenching the sample to a desired temperature below T_{ODT}, and annealing the sample at the desired temperature while occasionally collecting SAXS patterns. For annealing at room temperature (25 °C), samples were disordered in a vacuum oven and rapidly quenched to room temperature by removing the capillaries from the vacuum oven and immediately quenching the capillary tube in a beaker of room temperature water. Quenching from high temperature ($T > T_{ODT}$) to a desired temperature below T_{ODT} was accomplished by manually moving the capillary tube from the vacuum oven or Linkam heating stage into a temperature controlled copper heating block maintained at the target temperature. To collect SAXS patterns following annealing in the copper block, the capillary was quickly moved from the heating block into the Linkam stage preset to the measurement temperature.

4.2.3 *Dynamic mechanical spectroscopy (DMS)*

DMS experiments were performed on a TA Instruments ARES-G2 strain controlled dynamic mechanical spectrometer using the 8 mm stainless steel parallel plate geometry with a gap of approximately 1 mm for most experiments. The 25 mm stainless steel parallel plate geometry was used to collect data used for time–temperature superposition in order to increase torque during measurements in the disordered phase. Temperature was controlled using the forced convection oven attachment. An inert nitrogen purge gas was used to prevent oxidative degradation of the IL-5.1 sample. All

experiments were conducted in the linear viscoelastic regime, as confirmed by strain sweep measurements at selected temperatures.

4.3   Results and Analysis

In this section, results from SAXS and DMS experiments on the IL-5.1 polymer will be presented. First, the thermal properties of the IL-5.1 polymer are summarized. Next, all phases that were observed in the material as a function of temperature are identified, including the experimental evidence supporting the identification of the DQC phase in this material. Then, the kinetics of ordering of IL-5.1 are presented as a function of temperature and ordered phase morphology in an attempt to gain insight into the mechanism of formation of the DQC in diblock polymers. Finally, the results from experiments designed to determine the phases that represent the thermodynamic equilibrium states as a function of temperature are presented.

4.3.1   Thermal properties of IL-5.1

The order–disorder transition (ODT) temperature, T_{ODT} of IL-5.1 is 66 °C as measured by DMS experiments on slow (0.1 °C/min) heating as presented in Figure 4.3. The ODT is evident as the precipitous drop in the linear shear storage (G′) and loss (G″) moduli at 66 °C as the material transitions from an ordered (liquid crystalline) soft solid state to a disordered material with a liquid-like viscoelastic response. In the disordered phase, the experimental frequency (ω) range is well below the frequency for crossover to terminal behavior (G′ $\sim \omega^2$, G″ $\sim \omega^1$) and there was insufficient torque to reliably measure the viscoelastic properties (i.e., confirm liquid-like terminal scaling of the moduli). Nevertheless, the ODT is clearly evident.
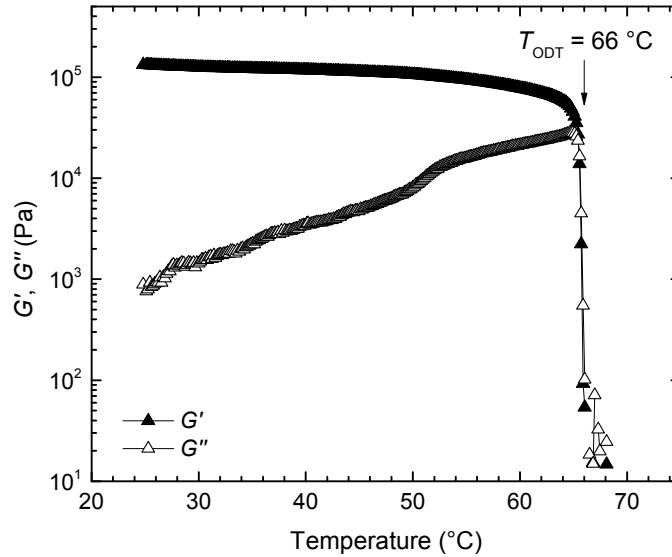
Figure 4.3 Measurement of the order–disorder transition temperature of IL-5.1 by DMS. Linear (0.5%) isochronal (0.1 rad/s) dynamic shear storage (G', filled symbols) and loss (G'', open symbols) moduli measured on heating at 0.1 °C/min. Prior to measurement, the sample was cooled from the disordered state at 0.1 °C/min to 25 °C and held isothermal for approximately 45 min. The ODT is evident as the precipitous drop in modulus at 66 °C. The broad feature in the loss modulus near 50 °C suggests an order–order transition may be present.

In addition to the ODT, there is a subtle feature in the G'' data, a broad stepwise increase in G'' beginning around 50 °C that suggests an order–order transition (OOT) may be present in this temperature range. A similar but much more subtle feature suggestive of an order–order transition was observed in experiments upon slow (0.1 °C/min) cooling (analogous to that reported by Lee[162] in a sample that formed the σ phase). However, this feature measured on cooling could not be reliably distinguished from instrument-induced artifacts and the data are not presented here.
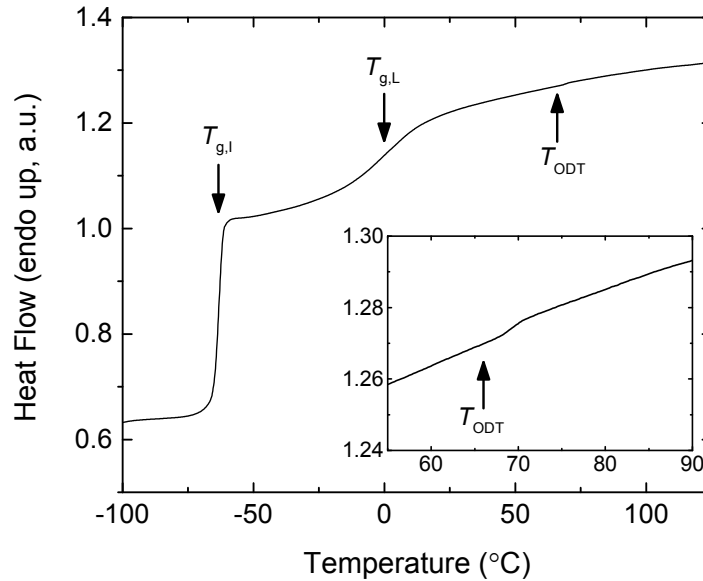
Figure 4.4 DSC measurements of thermal transitions in IL-5.1.Measurements were collected on heating at 10 °C/minute. T_gs and the T_{ODT} are indicated with arrows. The inset shows an expanded view of the data near T_{ODT}.

Glass transition temperatures, T_gs, of the constituent blocks of IL-5.1 were determined by differential scanning calorimetry (DSC) experiments. A specimen was equilibrated at a temperature above T_{ODT} to erase any thermal history prior to cooling and heating through any thermal transitions at a prescribed rate. DSC data collected during heating at 10 °C/min, after cooling at the same rate, are shown in Figure 4.4. The glass transitions of the poly(1,4-isoprene) and poly(DL-lactide) blocks are clearly evident as stepwise increases in the measured heat flow; T_gs are identified as the point associated with half the stepwise increase in heat flow. A weak signature of the ODT is also evident in the DSC data as a small peak in heat flow with an onset consistent with the T_{ODT} measured by DMS but at a slightly higher temperature, owing to the much faster rate of heating. If cooled below the highest block T_g (i.e. $T_{g,L} \approx 0$ °C), the material will partially vitrify into a kinetically frozen non-equilibrium state and is no longer able to evolve toward equilibrium over experimental timescales.

4.3.2   *Order and disorder in IL-5.1*

A series of experiments were conducted to determine the stable ordered phases present in IL-5.1. Specimens were disordered ($T > T_{ODT}$) and then rapidly (≥ 30 °C/min) cooled to a series of temperatures below T_{ODT} and annealed for a sufficient time to allow the material to order completely. Figure 4.5 shows the synchrotron SAXS patterns obtained after adequate annealing at various temperatures. Annealing times were selected based on the ordering kinetics from SAXS and DMS experiments described in section 4.3.3.

At 70 °C, a single broad peak characteristic of the disordered (DIS) phase is evident (curve d in Figure 4.5). It is important to note that this result is not due to correlation hole scattering from a molecularly mixed uniform (mean-field like) disordered state. Near T_{ODT} the disordered phase is characterized by thermally driven large amplitude composition fluctuations (see Chapter 3 for a detailed treatment of the ODT). In compositionally asymmetric diblock copolymers, these composition fluctuations manifest as relatively long-lived but dynamically active micelle-like aggregates (see Figure 4.2c) with a liquid-like spatial arrangement.[15,67,88,106,127] When cooled below the ODT, these micelle-like point particles spontaneously order resulting in a soft solid that produces the elastic signature evident in DMS experiments (see Figure 4.3). Heating above T_{ODT} reduces the amplitude and concentration of the fluctuating micelles and a point of complete "evaporation" occurs at $T \gg T_{ODT}$.[127]
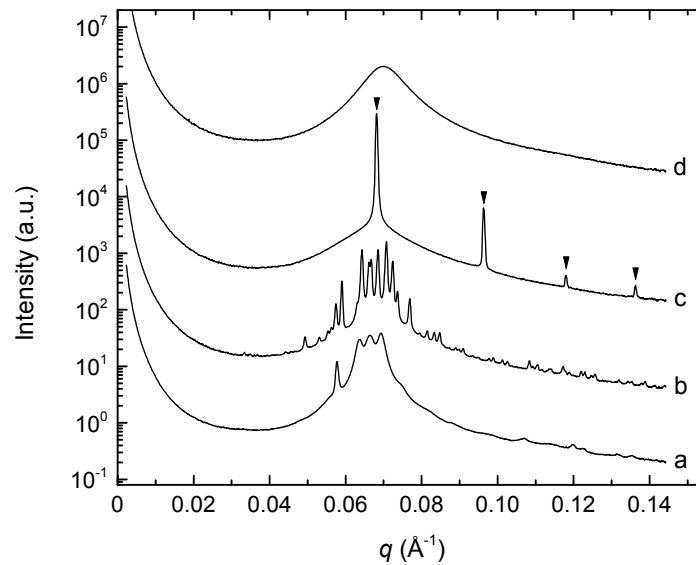
Figure 4.5 Representative SAXS patterns of the phases observed in IL-5.1. SAXS patterns collected (a) after 49 days of annealing at 25 °C following a rapid quench from above T_{ODT} exhibiting a pattern consistent with DQC symmetry, (b) after 260 minutes of annealing at 40 °C following a rapid quench from above T_{ODT} exhibiting a pattern consistent with the Frank–Kasper σ phase, (c) after 20 minutes of annealing at 45 °C following a rapid quench from above T_{ODT} exhibiting a pattern consistent with the BCC phase (allowed BCC Bragg peaks, $(q/q^*)^2 = 1, 2, 3, 4, \ldots$, are marked with arrows), and (d) after 1 minute of annealing at 70 °C exhibiting a pattern consistent with the DIS phase. Curves have been shifted vertically for clarity.
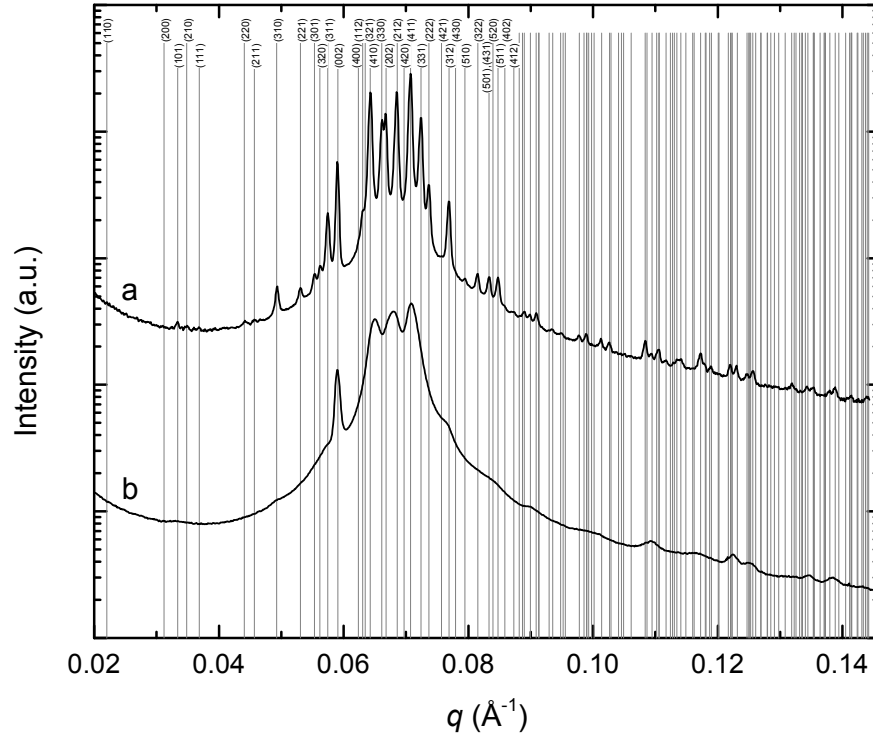
Figure 4.6 Indexing the IL-5.1 SAXS pattern collected at 40 °C confirming the σ phase. Curve (a) is the SAXS pattern collected after 260 minutes of annealing at 40 °C following a rapid quench from above T_{ODT} exhibiting a pattern consistent with the Frank–Kasper σ phase. The q values of all allowed Bragg reflections of the σ phase ($P4_2/mnm$) with lattice parameters a and c of 413 and 213 Å in the experimental q range are show as vertical gray lines. Miller indices of the low q planes are shown. For comparison, curve (b) is the SAXS pattern collected after 150 days of annealing at 25 °C following a rapid quench from above T_{ODT} exhibiting a pattern consistent with DQC symmetry. The q data of curve (b) have been rescaled by a common factor (≈ 1.025) to position the (00002) peak of the DQC at the same q value as the (002) peak in curve (a) to facilitate comparison with the allowed Bragg reflections of the σ phase.

When IL-5.1 is annealed at temperatures from just below T_{ODT} to about 45 °C, the material orders into a body-centered cubic (BCC) phase, where the nearly spherical micelle-like domains (with cores rich in the poly(DL-lactide) (PLA) block and coronas rich in the poly(1,4-isoprene) (PI) block) are arranged with one particle per lattice site.

The BCC structure generates a unique SAXS pattern shown in curve c in Figure 4.5 with Bragg diffraction peaks at positions relative to the primary (lowest q) scattering peak, q^*, of $(q/q^*)^2 = 1, 2, 3, 4, 5, 6, 7, \ldots$. However, when IL-5.1 is annealed at the slightly lower temperature of 40 °C, the ordered phase that forms at long times is the Frank–Kasper σ phase. The σ phase was recently discovered in a closely related IL diblock copolymer designated IL-15 (and a SISO tetrablock terpolymer) by Lee and co-workers.[87,88] In the σ phase, the particles are arranged in a large tetragonal crystal structure, 30 per unit cell as illustrated in Figure 4.1b, resulting in a distinctive SAXS pattern with a large number of closely spaced Bragg diffraction peaks as shown in Figure 4.5b. As demonstrated in Figure 4.6, the peaks in the scattering pattern collected at 40 °C can be indexed to space group $P4_2/mnm$ with lattice parameters a and c of 413 and 213 Å. In addition, the relative intensities of the Bragg peaks are consistent with those observed in IL-15, conclusively establishing the σ phase as the proper symmetry assignment for the IL-5.1 material ordered at 40 °C.

When IL-5.1 is annealed at temperatures at or below 35 °C, a different scattering pattern emerges at intermediate times, shown for 25 °C in Figure 4.5a. This diffraction pattern contains a sharp peak coincident with the (002) reflection associated with the σ phase (see Figure 4.6) and a triplet of closely spaced peaks at slightly higher q (the q axis of the 25 °C data has been normalized with respect to the (002) reflection by a factor of 1.025 as justified in section 4.3.4). To the best of our knowledge, this pattern has not been reported previously in diblock copolymer melts. We believe this 1-D (powder) scattering pattern derives from the DQC phase, which forms as a long-lived metastable structure at low ordering temperatures within the region of stability of the equilibrium σ phase in IL-5.1. Evidence suggests that the DQC phase, while stable during annealing for many hours at 35 °C and many weeks at 25 °C, is eventually consumed by nucleation and growth of the equilibrium σ phase (see sections 4.3.3 and 4.3.4 for details). The justification for the assignment of DQC symmetry to the powder SAXS pattern of curve a in Figure 4.5 is presented in the remainder of this section.

It is clear from the comparison of the σ phase scattering pattern with that collected at 25 °C (Figure 4.6) that the 25 °C data do not arise simply from an intermediate state during the nucleation and growth of the σ phase, that is this pattern constitutes a qualitatively different and long-lived ordered phase symmetry. In curve b in Figure 4.6, the scattering pattern collected at 25 °C is shown overlaid with the σ phase indexing for the data collected at 40 °C. From this construction, it is clear that the closely spaced triplet of peaks in the pattern collected at 25 °C, specifically the intermediate q peak, cannot be indexed with the allowed reflections of the σ phase (we note that the rescaling of the q axis used to construct Figure 4.6 does not influence the ability to index the pattern and that no choice of σ phase lattice parameters can fit the four strongest reflections in the 25 °C pattern). However, some of the very weak and diffuse undulations and shoulders in the 25 °C scattering pattern do correlate to strong peaks in the σ phase scattering pattern, the implications of which will be considered further in subsequent discussion.

The SAXS pattern collected at 25 °C is remarkably similar to the powder X-ray scattering patterns obtained by Zeng et al.[143] from supramolecular dendrimers, as shown in Figure 4.7; the q axes have been rescaled such that the sharp peak at low q in the dendrimer DQC pattern is coincident with the corresponding peak in the pattern collected from IL-5.1. For the dendrimer materials, the DQC phase was definitively identified based on additional 12-fold rotationally symmetric single domain (2D) X-ray scattering patterns reproduced in Figure 4.8.[143] The similarity of the powder X-ray scattering patterns in Figure 4.7 leads us to conclude that IL-5.1 has the same structure as that of the DQC reported in the wedge-shaped dendrimers and we tentatively assign the IL-5.1 SAXS pattern collected at 25 °C to a DQC phase.
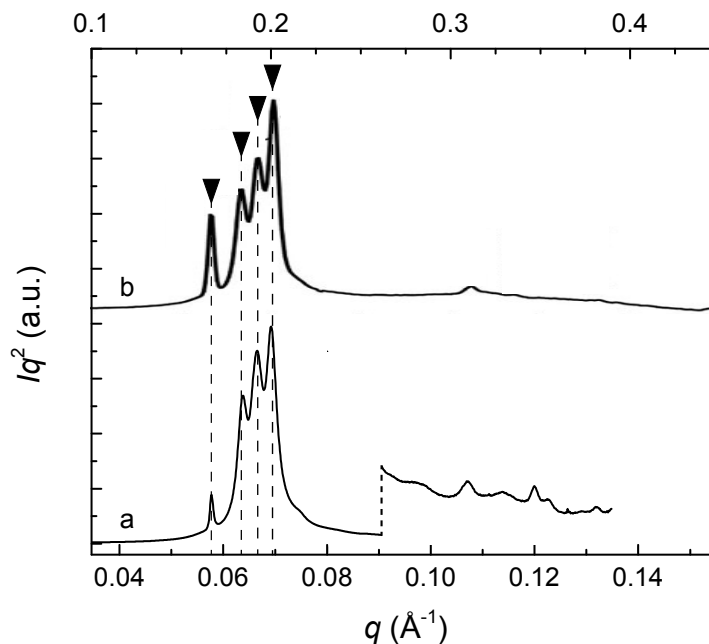
Figure 4.7 Comparison of the powder diffraction pattern of IL-5.1 at 25 °C with the DQC reported in supramolecular dendrimers. The powder SAXS pattern of IL-5.1 after annealing at 25 °C for 12 days following a rapid quench from the disordered phase (a, bottom q axis) is compared with the powder X-ray diffraction pattern of a supramolecular dendrimer that exhibits dodecagonal quasicrystalline order collected at 70 °C reported by Zeng et al.[143] (b, top q axis). Arrows and dashed lines indicate the positions of the most intense peaks in the dendrimer scattering pattern. For clarity, the curves have been shifted vertically and the intensity of the high q data of (a) has been magnified. Adapted by permission Macmillan Publishers Ltd: Zeng, X. et al. *Nature* **2004**, *428*, 157–160. Copyright 2004.[143]
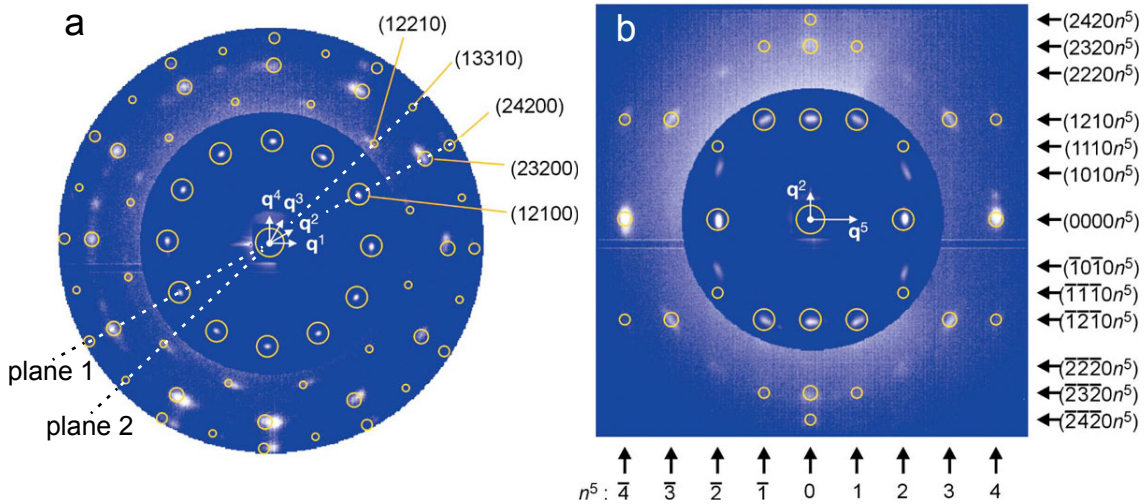
Figure 4.8 2D X-ray scattering patterns reported for the DQC phase in dendrimers. X-ray scattering patterns (a) along the 12-fold axis and (b) of plane 1 in (a). Intensities of the outer diffraction peaks are scaled up by a factor of 100. Simulated diffraction patterns of the structure in Figure 4.1c are superimposed (circles; area is proportional to log(amplitude)). Adapted by permission Macmillan Publishers Ltd: Zeng, X. et al. *Nature* **2004**, *428*, 157–160. Copyright 2004.[143]

Based on this DQC assignment, we have explored indexing the peaks in the IL-5.1 SAXS pattern collected at 25 °C according to the 5-dimensional indexing scheme used by Zeng et al.[143] Quasicrystal lattices, while aperiodic in the spatial dimensions that are actually occupied, can be viewed as incommensurate projections of certain higher-dimensional periodic structures into the lower 1-, 2-, and 3-dimensional quasicrystals found in nature. This is directly analogous to how an aperiodic Fibonacci sequence (a 1D quasicrystal) can be generated by a projection of a square lattice onto a line (1D) drawn at an irrational angle (related to the golden ratio $(1 + 5^{1/2})/2 \approx 1.618$) to the lattice vectors of the 2D lattice.[163] In the case of the DQC, a 5D reciprocal lattice is used to index the scattering pattern. For the experimentally accessible "real" 3D reciprocal space in which scattering data is actually collected, four reciprocal lattice basis vectors, q_1–q_4, lie in the plane perpendicular to the 12-fold axis pointing from the origin and each separated in the plane by 30° (see Figure 4.8). A single reciprocal lattice basis vector q_5 points in the direction of the 12-fold axis. Each reciprocal lattice basis vector has a corresponding

lattice parameter, a_1–a_4 being related to the edge length of the square-triangle tiling pattern in the *x*–*y* plane in Figure 4.1c, all taken to be equal in magnitude, and a_5 related to the domain spacing in the periodic dimension (*z*-direction in Figure 4.1c).[143]

Indexing is presented in Figure 4.9 based on an analysis of the single domain 2D scattering patterns reported by Zeng et al. [143] In Figure 4.9, the calculated *q* values of the planes derived from the 2D data are marked with solid vertical lines. While not perfect, this indexing is equivalent to the indexing reported by Zeng et al., capturing the approximate positions of most of the observed peaks.[143] Significantly, the relative position of the strong (10102) peak in IL-5.1 is at higher *q* than the predicted peak position. This discrepancy also exists in the dendrimer DQCs at temperatures near the ODT.[141,143] Although, the position of this peak appears to shift to lower *q* at temperatures far below T_{ODT} and becomes better aligned with the predicted position at room temperature, where the reported single domain X-ray scattering experiments were conducted.

Indexing of the powder SAXS pattern of IL-5.1 at 25 °C is improved significantly by including reflections in addition to those used by Zeng et al. for the supramolecular dendrimers. Additional reflections were chosen rationally such that they lie in one of the two families of planes in the 3D reciprocal space that exhibit 2-fold symmetry in the scattering pattern from an ideal, single domain sample, based on reported DQC scattering patterns. [143,164] Examples of these planes are labeled as plane 1 and 2 in Figure 4.8a. Positions of the reflections associated with these additional planes are marked with dashed lines in Figure 4.9. This improved indexing scheme accounts for all of the strong peaks observed in the IL-5.1 SAXS pattern and correctly captures the position of the four strongest peaks at low *q*. Based on this indexing scheme, the sharp peak at low *q* corresponds to the (00002) peak, which is due to the periodic stacking in the direction parallel to the 12-fold axis (the *z* direction in Figure 4.1), directly analogous to the (002) peak of the σ phase related to the stacking in the direction of the lattice parameter *c* (again, the *z* direction in Figure 4.1), justifying the rescaling approach used in Figure 4.6. The magnitudes of the reciprocal lattice basis vectors extracted from the DQC indexing

are consistent with expectation. The equivalent edge length of the square-triangle tiling (214 Å) and the z direction periodicity (218 Å) are nearly equal and slightly larger than the equivalent values determined for the σ phase at 40 °C, consistent with the expected increase in chain stretching upon a reduction in temperature. The success of indexing the IL-5.1 SAXS pattern shown in Figure 4.9 provides additional support for the identification of the DQC phase in IL-5.1.
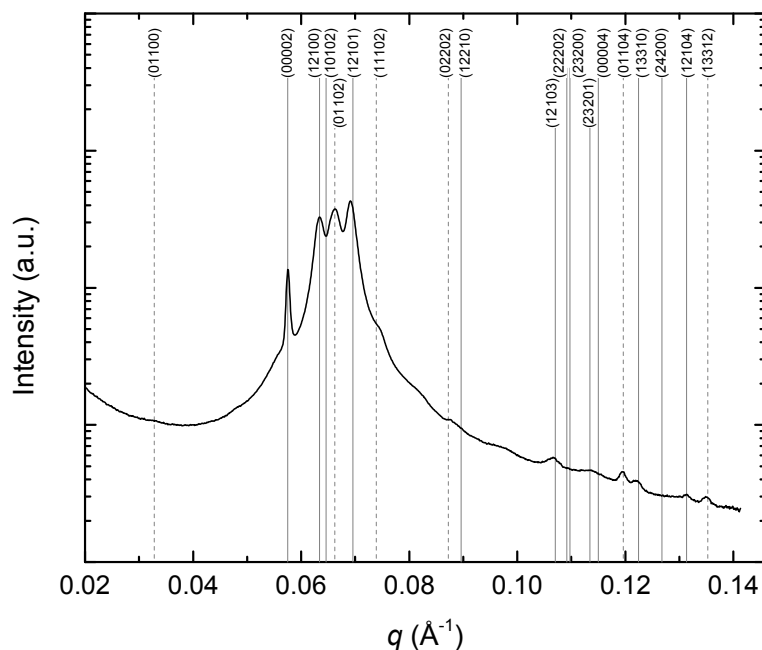
Figure 4.9 Indexing the IL-5.1 SAXS pattern collected at 25 °C according to the 5-dimensional indexing scheme for the DQC. Experimental SAXS pattern collected after 77 days of annealing at 25 °C following a rapid quench from above T_{ODT}. Vertical gray lines indicate the q values of the planes with the Miller indices indicated with the magnitude of the four reciprocal lattice basis vectors in the 12-fold plane, q_1 through q_4, equal to 0.0170 Å^{-1} (d = 370 Å; corresponding to a edge length of 214 Å in the square–triangle tiling of Figure 4.1) and the magnitude of the reciprocal lattice basis vector perpendicular to the 12-fold plane, q_5, equal to 0.0288 Å^{-1} (d = 218 Å). Vertical solid lines indicate Bragg reflections observed by Zeng et al.[143] in the DQC phase in supramolecular dendrimers while vertical dashed lines indicate additional planes used to index the IL-5.1 SAXS pattern.

Unfortunately, due to the low molecular weight and low T_{g}s of the constituent blocks, accessing real space TEM images of the structure present at 25 °C in IL-5.1 is

challenging and not practical. However, additional support for the identification of the DQC can be gained by comparing powder SAXS patterns obtained from IL-5.1 with similar SAXS patterns recorded from linear SISO multibock polymers that have been shown, based on TEM analysis, to form DQCs.[144]

Linear poly(styrene-*b*-isoprene-*b*-styrene-*b*-ethylene oxide) (SISO) multiblock polymer melts form a wide variety of phases in which the poly(ethylene oxide) block forms the core of nearly spherical point particles that order onto complex crystal and quasicrystal lattices over a broad range of block compositions. Reported ordered phases include BCC, hexagonal packing, A15, and the σ phase.[87,144,165–167] A DQC phase was identified in an SISO polymer designated SISO-2 when annealed at 175 °C based on TEM and SAXS evidence summarized in Figure 4.10.[144] A region of stability of a phase with unusual symmetry was identified between the simple hexagonal packing of particles at low temperature (120 °C) and the σ phase at high temperature (210 °C) based on the (thermoreversible) SAXS patterns obtained at 175 °C, which could not be attributed to any known symmetry. The SAXS patterns at 175 °C (Figure 4.10a) were collected after a relatively short annealing time (~15 minutes) and most likely do not reflect the equilibrium structure, but rather coexistence of the hexagonal and DQC phases. Conclusive identification of DQC symmetry was based on TEM micrographs collected after annealing for 1 day at 175 °C. These TEM micrographs demonstrated a lack of translational symmetry, 12-fold rotational symmetry in the Fourier transform of the image (Figure 4.10b), as well as the presence of 12-fold bond orientational order in real space, deduced from tilted TEM images (Figure 4.10c) that reveal correlated planes of particles every 30° upon rotation. All of these features are characteristic of the DQC phase. The identified DQC phase in SISO-2 competes for stability with the σ phase and forms at temperatures just below a region of equilibrium stability of the σ phase, similar to what is observed for the proposed DQC phase in IL-5.1.
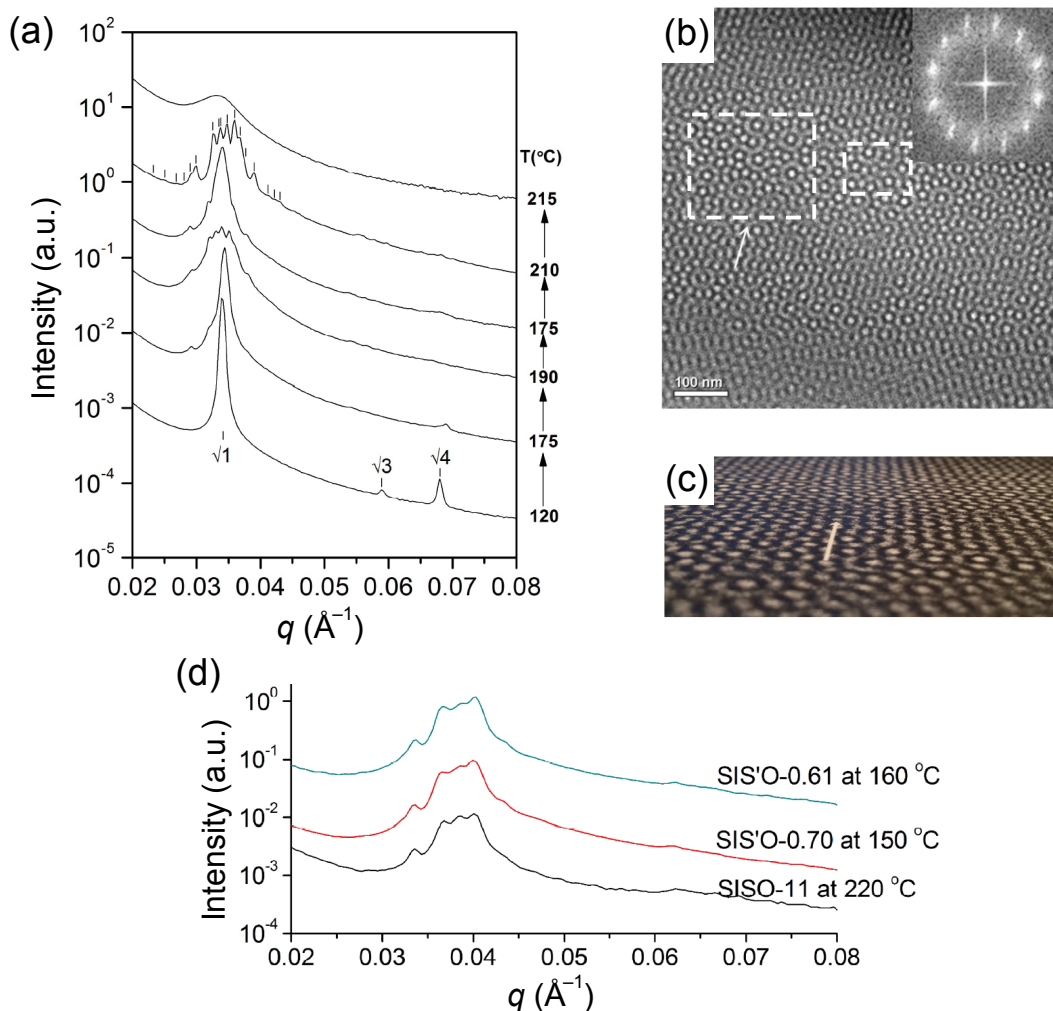
Figure 4.10 Summary of DQC in SISO tetrablock terpolymers.
(a) SAXS patterns of SISO-2 collected sequentially from bottom to top (approximately 15 minutes of annealing at each temperature). Lines above the 210 °C curve indicate allowed reflections of the σ phase. (b) TEM micrograph from samples of SISO-2 annealed at 175 °C for 1 day prior to quenching, sectioning, and staining with OsO_4 exhibiting DQC order (inset shows Fourier transform of the TEM image revealing 12-fold rotational symmetry). (c) A tilted view of the micrograph in (b) revealing orientational order along the direction marked with an arrow in (b) and (c). (d) SAXS patterns of suspected DQC order in SIS′O samples.[167] Adapted with permission from Zhang and Zhang, J.; Bates, F. S. *J. Am. Chem. Soc.* **2012**, *134*, 7636–7639. Copyright 2012 American Chemical Society.[144]

Several SISO polymers, in addition to SISO-2, have produced powder SAXS patterns similar to that shown in Figure 4.9, in close proximity to the occurrence of the σ phase, as shown in Figure 4.10d;[167] the slightly broader line widths are typical of the SISO materials.[87] These data, together with the aforementioned comparison to the dendrimer results, lead to the conclusion that the transient low temperature phase in IL-5.1 is indeed a DQC.

4.3.3 *Kinetics of ordering in IL-5.1*

The discovery of a DQC phase in a simple diblock copolymer provides new opportunities to gain fundamental insight into the physics underlying the formation of quasicrystalline order in soft materials. Block polymers provide excellent model systems for such fundamental investigations due to the highly tunable nature of block polymer materials, in which the physical properties, characteristic length scales, and dynamics can be controlled during synthesis and processing. Moreover, the availability of a wide variety of complementary experimental tools that probe real and reciprocal space, and a wide range of mechanical properties in the time and frequency domains, affords unparalleled access to the structural and dynamical phenomena associated with quasicrystals.

IL-5.1 was designed to have a low overall molecular weight, below the onset of molecular entanglements, and to have block glass transition temperatures (T_gs) below ambient temperatures to ensure fast dynamics at the level of individual chains. These fast dynamics enable the IL-5.1 material to quickly respond to perturbations (i.e. changes in temperature) and approach thermodynamic equilibrium in experimentally accessible timescales. The sub-ambient T_gs of the constituent blocks in IL-5.1 (see Figure 4.4) also allow very long annealing times at room temperature (nominally taken as 25 °C throughout this work), where the material is dynamic and thus can continue to approach equilibrium for many weeks or months without risk of thermally activated oxidative polymer degradation reactions. However, the close proximity of the lactide block T_g to room temperature ($T_{g,L} \approx 0$ °C) results in very strong temperature dependence of the molecular dynamics as $T_{g,L}$ is approached. This provides a convenient way to effectively

tune the dynamics (by changing temperature) facilitating observation of intermediate states during *in situ* experiments, for example by time-resolved X-ray scattering during ordering transitions.

In this section, SAXS and DMS experiments are described that document the kinetics of ordering as well as the evolution of structure during formation of the BCC, σ, and DQC phases as a function of temperature. For these experiments, samples were disordered ($T > T_{ODT}$) and allowed to equilibrate (which occurs within seconds) before being cooled as rapidly as possible ($\geq$ 30 °C/min) to a targeted temperature where the evolution of structure was monitored by SAXS and DMS experiments as a function of time. Synchrotron SAXS experiments conducted at selected temperatures are presented first, followed by DMS measurements performed at a more robust set of temperatures.

For ordering temperatures from just below T_{ODT} to 45 °C, a BCC phase forms in a matter of a few minutes, quickly reaching the point at which the SAXS pattern become invariant upon further annealing. A representative example, obtained at 45 °C, is presented in Figure 4.11. When IL-5.1 is quenched to an ordering temperature of 40 °C, the BCC structure initially nucleates and grows to completion in about 10 minutes before being consumed by the nucleation and growth of the equilibrium σ phase at much longer times over the course of a few hours, as shown in Figure 4.12. This result is consistent with the previously reported mechanism of growth of the σ phase through a metastable BCC intermediate.[87] Specifically, when IL-15, the only diblock copolymer previously shown to form the σ phase,[87] was rapidly quenched from the disordered state ($T > T_{ODT} \approx$ 48 °C) to 40 °C, BCC order was fully established in approximately 30 minutes and remained stable indefinitely at this temperature. When rapidly quenched from the disordered phase to 25 °C, a BCC structure formed initially but transformed by nucleation and growth to the σ phase over the course of approximately 24 hours.
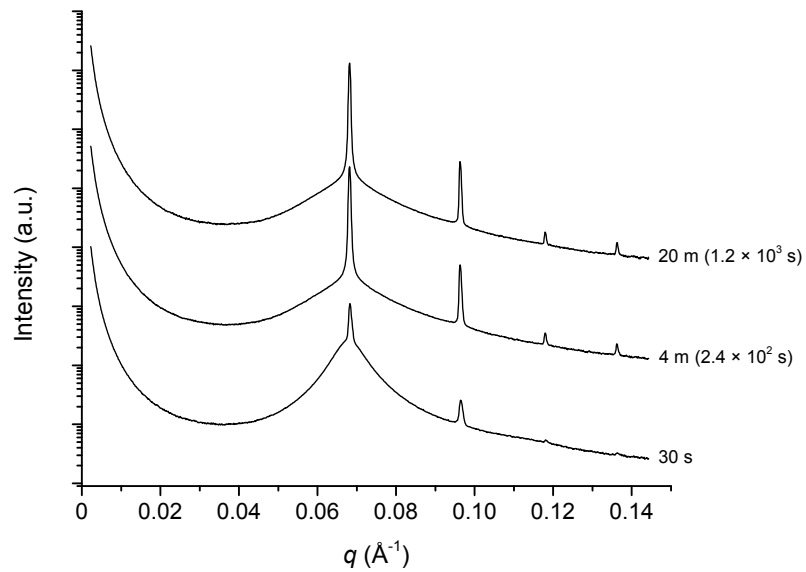
Figure 4.11 Kinetics of ordering of IL-5.1 at 45 °C measured by SAXS. SAXS patterns collected after annealing at 45 °C for the indicated times following a rapid (t < 30 seconds) quench from above T_{ODT}. The SAXS patterns come from time-resolved SAXS experiments on a single sample. The BCC phase nucleates and grows and remains stable at long times. Curves have been shifted vertically for clarity.
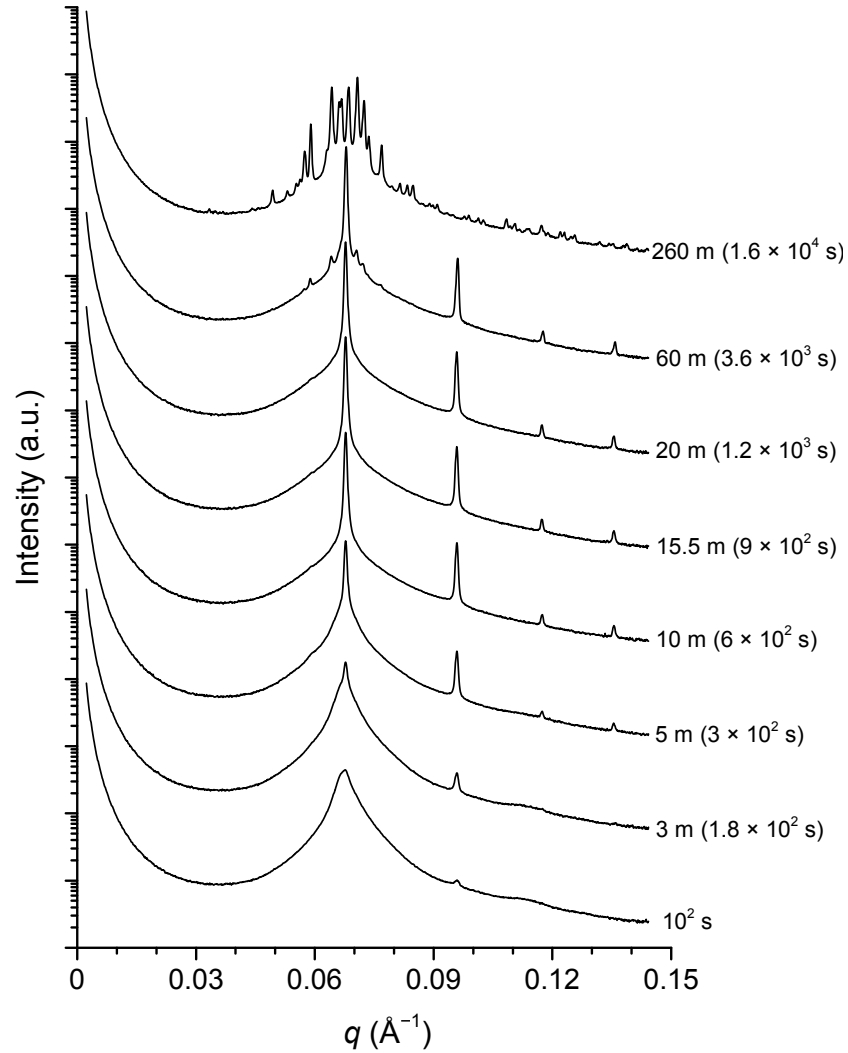
Figure 4.12 Kinetics of ordering of IL-5.1 at 40 °C measured by SAXS. SAXS patterns collected after annealing at 40 °C for the indicated times following a rapid ($t < 1$ minute) quench from above T_{ODT}. The SAXS patterns come from time-resolved SAXS experiments on a single sample. A BCC phase nucleates and grows at short times before being replaced by the nucleation and growth of the σ phase at longer times. Curves have been shifted vertically for clarity.

At 35 °C and 25 °C the DQC phase appears to develop directly from the disordered state, as can be seen in Figure 4.13 and Figure 4.14. After an extended period of metastability, the σ phase begins to nucleate and grow from the DQC phase at long times as evidenced by the SAXS data shown in Figure 4.13. This transition appears to transform certain DQC reflections into specific Bragg peaks associated with the σ phase (see Figure 4.6). Remarkably, the first evidence of nucleation of the σ phase at 25 °C takes more than half a year to appear. Discrete diffraction spots located at q values consistent with the σ phase (slightly displaced from the uniform intensity powder rings associated with the DQC) are seen in the scattering pattern collected after 220 days at room temperature (Figure 4.15). Faint evidence of similar features are barely discernable in the 150 day pattern, but no such features are found in the 119 day pattern.

In the data of Figure 4.13 collected at 35 °C, there is evidence of a small amount of nucleation of a BCC structure at short time, as evidenced by the appearance of the small peak at the $q/q^* = \sqrt{2}$ (marked with an arrow above the 177 minute data in Figure 4.13). However, this BCC structure never grows to a significant extent and this peak disappears after further annealing as the DQC grows. This peak is not evident in the data collected on ordering at 25 °C. The consumption of the small amount of the BCC structure that nucleated during ordering at 35 °C by the DQC phase further demonstrates that the DQC is more stable than the BCC structure at low temperature.

While the evolution of structure upon ordering of the DQC phase is very similar at 35 and 25 °C, the time required for the phase transition changes dramatically over this temperature range. At 35 °C, the material forms a well-ordered DQC structure in several hours, approximately the time required to form a well-ordered σ phase structure at 40 °C. At 25 °C, it takes dramatically longer to establish a well ordered DQC state, taking several days to nucleate and a few weeks to complete the ordering process.
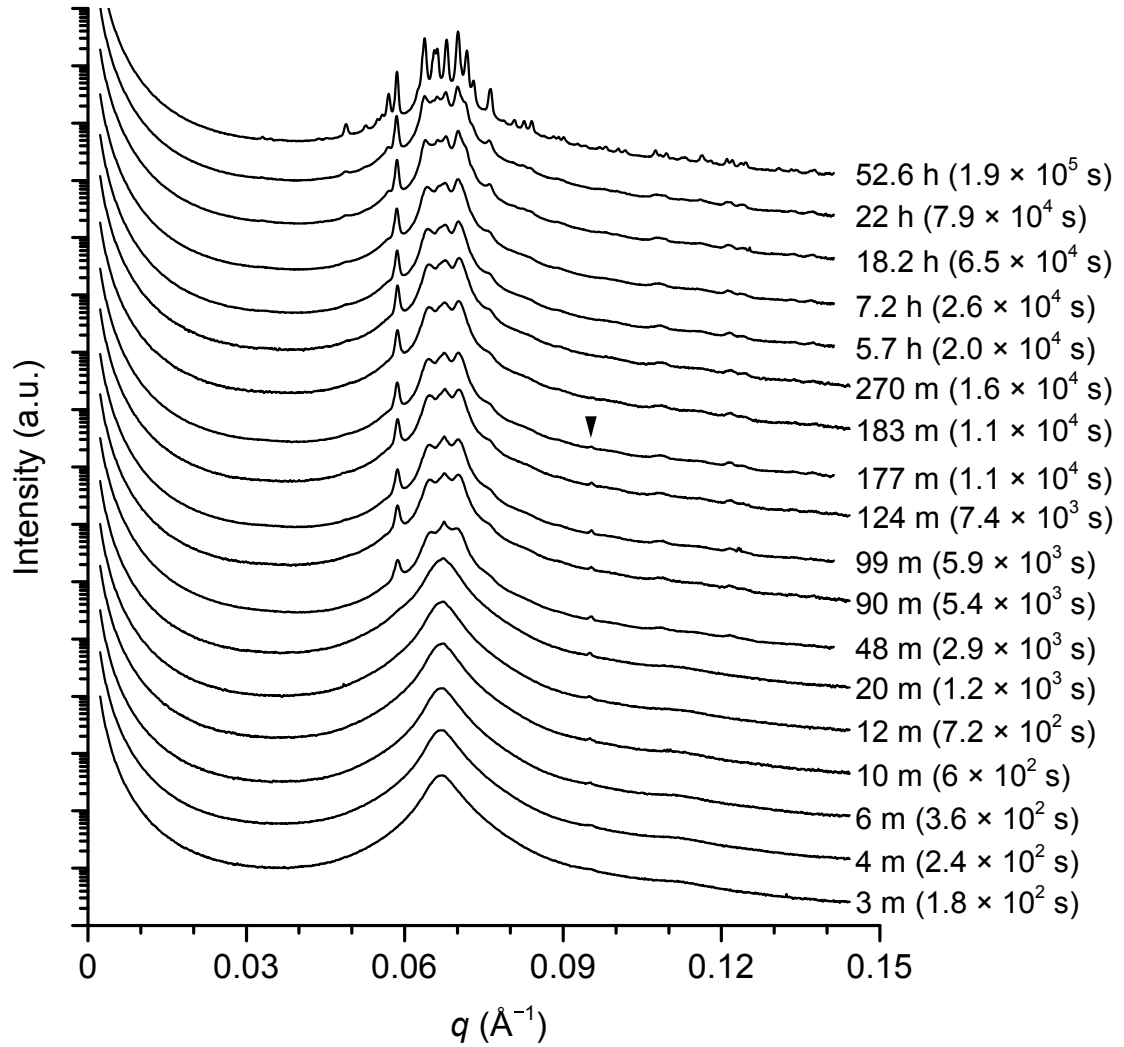
Figure 4.13 Kinetics of ordering of IL-5.1 at 35 °C measured by SAXS. SAXS patterns collected after annealing at 35 °C for the indicated times following a rapid (t < 1 minute) quench from above T_{ODT}. The SAXS patterns come from time-resolved SAXS experiments on three separate samples. The DQC phase grows directly from a quenched disordered phase with LLP. At long times, the σ phase nucleates and grows from the DQC. Curves have been shifted vertically for clarity. The arrow above the 177 minute data indicate the location of the $(q/q^*)^2 = 2$ peak associated with the BCC structure.
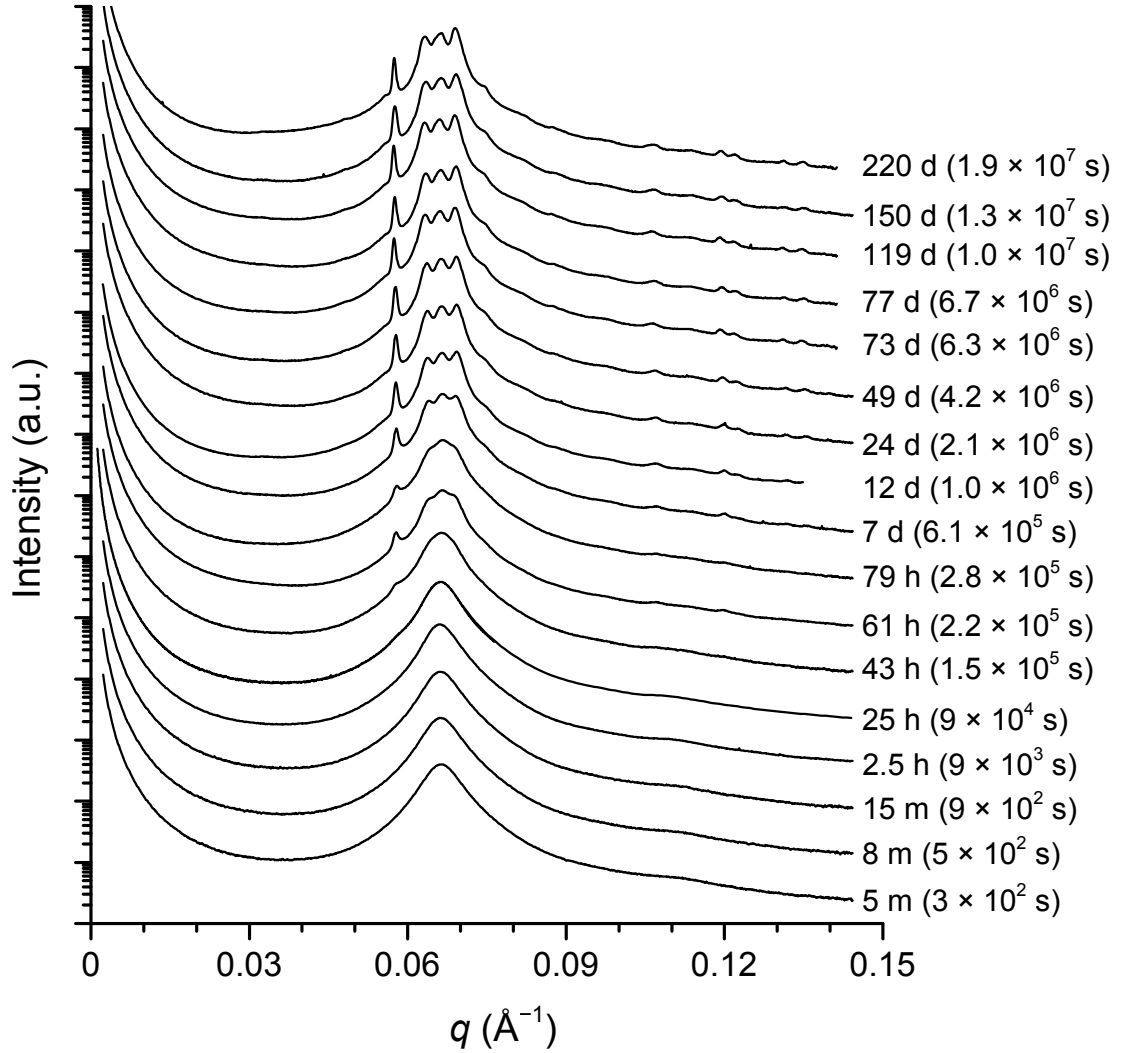
Figure 4.14 Kinetics of ordering of IL-5.1 at 25 °C measured by SAXS. SAXS patterns collected after annealing at 25 °C for the indicated times following a rapid ($t < 10$ seconds) quench from above T_{ODT}. The SAXS patterns come from many samples quenched at different times prior to traveling to the synchrotron X-ray source. The DQC phase grows directly from a quenched disordered phase with LLP. Curves have been shifted vertically for clarity.
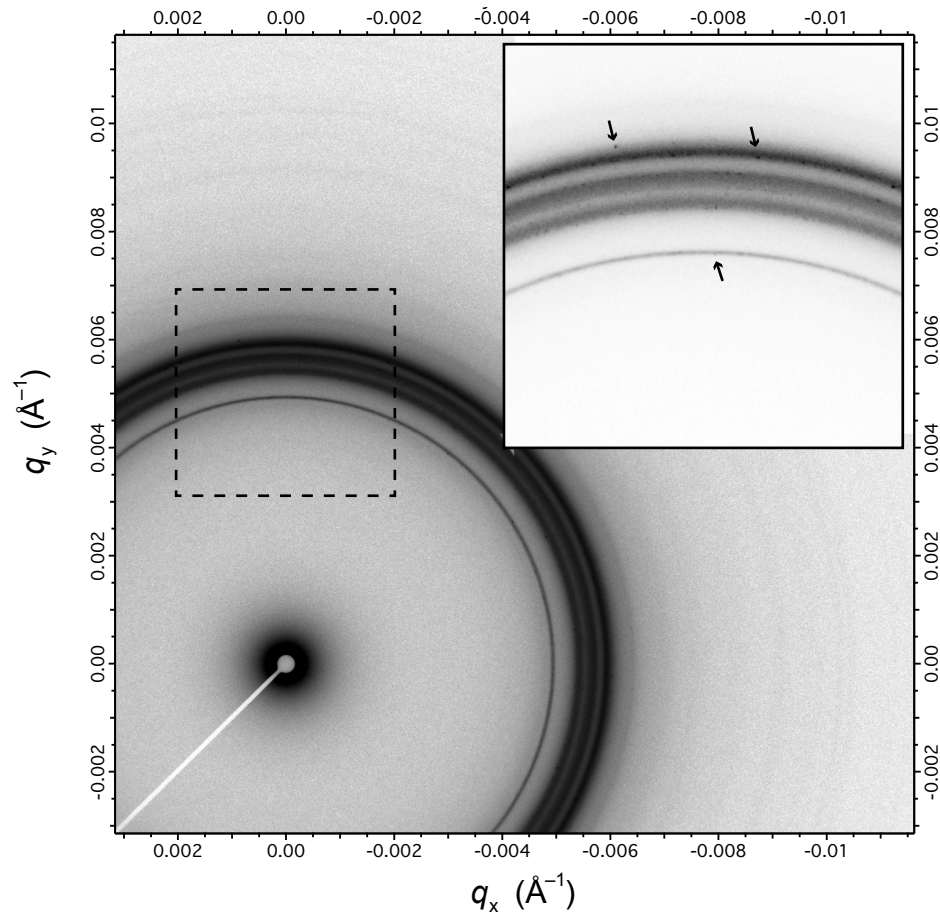
Figure 4.15 Evidence of σ phase nucleation at 25 °C after 220 days of annealing. 2D SAXS pattern collected after annealing at 25 °C for 220 days following a rapid quench from the DIS phase. The main image displays the data with a logarithmic intensity color scale while the inset shows an expanded view of the region outlined with the dashed lines near the highest intensity rings with a linear intensity color scale. Arrows highlight the locations of a few discrete spots associated with scattering from the nucleating σ phase. The small bright areas in the main image near the bottom left corner of the inset are dead pixels in the detector while the lollipop shaped white area emanating from the bottom left corner of the main image is the beamstop.

In addition to SAXS measurements, the evolution of structure and the kinetics of ordering were characterized using DMS experiments. In these experiments, the modulus of the material is monitored as a function of time at a select frequency after quenching to the desired temperature. As the material transforms from a disordered state with liquid-

like behavior to an ordered state with solid-like viscoelastic properties, the isochronal linear elastic shear modulus G' increases then becomes invariant once the material has fully ordered.[88] These experiments are very sensitive to differences in the mechanical properties of the ordered phases as well as the disordered phase. Thus it is possible to document order–order and order–disorder transitions with these experiments.

The results of DMS experiments designed to monitor the kinetics of ordering are summarized in Figure 4.16. The changes in temperature during selected DMS experiments are presented in Figure 4.17. For ordering temperatures in the region of BCC stability very close to T_{ODT} (shallow quenches), nucleation is slow and there is a long incubation period before growth begins (e.g., 65 °C data in Figure 4.16a). Upon nucleation, the modulus smoothly increases to the maximum value and remains constant during further annealing indicating the material is completely ordered. As the ordering temperature decreases in the BCC stability window (quench depth increases), the nucleation rate increases and the time to ordering is reduced. The ordering time reaches a minimum at approximately 55 °C at which temperature the material basically orders by the time the sample equilibrates at the ordering temperature (~ 100 seconds; see Figure 4.17). At lower ordering temperatures (still deeper quenches), the growth of the ordered BCC phase becomes diffusion limited and the times to ordering increases with decreasing temperature. The times to complete ordering of the BCC phase measured by DMS agree well with those measured by SAXS. However, SAXS experiments appear to be more sensitive to the early stages of nucleation and growth, with nucleation detected at shorter times in SAXS experiments than in DMS experiments. It seems SAXS is able to detect the presence of small crystallite grains that are not yet large enough to influence the mechanical properties to a sufficient degree to be detected by DMS. We note that the rheometer gap was not adjusted to account for thermal expansion of the parallel plate fixtures or sample so there may be minor errors in the relative magnitude of the moduli between measurements (the absolute error in G' may be quite large due to the non-ideal geometry at the sample edge). However, this does not affect the changes of G' as a function of time.
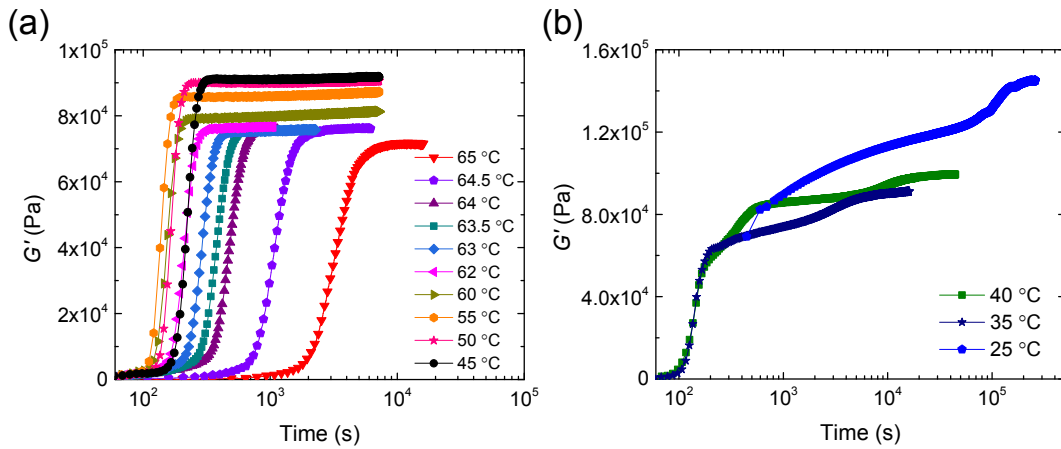
Figure 4.16 DMS measurements of the kinetics of ordering of IL-5.1. The development of elasticity measured via the isothermal linear (0.5 %) isochronal (0.1 rad/s for 25 °C data, 1 rad/s for data at all other ordering temperatures) dynamic shear storage modulus as a function of time. Sample was equilibrated in the disordered phase prior to quenching to the desired ordering temperature. Data collection began upon the initiation of the quench. Stabilization at the desired ordering temperature took approximately 100 s. (a) Ordering temperatures in the BCC stability window. (b) Ordering temperatures at low temperatures where the σ and DQC form. Note the expanded ranges of modulus and time in (b) relative to (a).
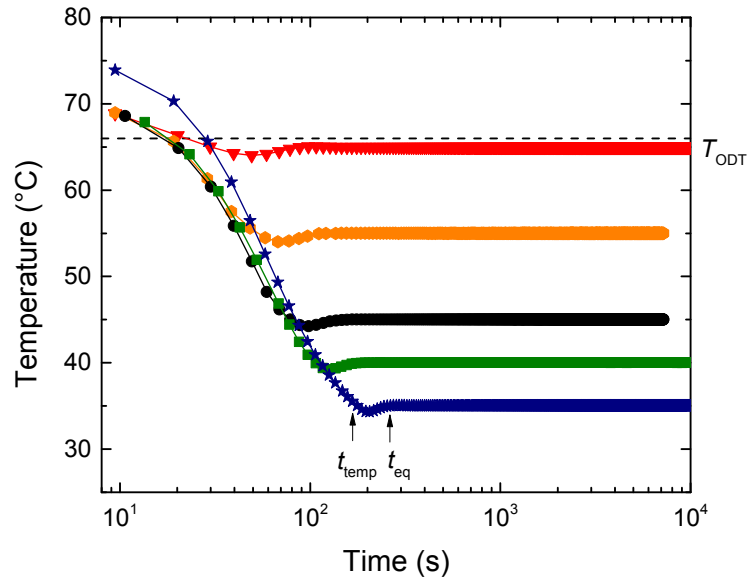
Figure 4.17 Evolution of temperature during DMS experiments. Temperature as a function of time during selected DMS ordering experiments. Data marker and color schemes are consistent with Figure 4.16. Times t_{temp} and t_{eq} are the time the sample first reached the target temperature during cooling and the time required to equilibrate the sample at the target temperature, respectively.

The ordering kinetics as measured by DMS for temperatures at which the σ and DQC phases form are qualitatively different than those observed in the region of stability of the BCC phase, as can be seen in Figure 4.16b. Upon quenching to a temperature below about 42 °C, the sample immediately becomes stiff but with a modulus considerably lower than that measured for the BCC phase at similar temperatures. This stiffening is not accompanied by the development of any ordered structure, as evidenced by the SAXS patterns collected at short times at 40, 35, and 25 °C. After this initial stiffening, the modulus then proceeds to evolve with time. We define the temperature below which the sample immediately becomes stiff (≈ 42 °C) as T_{erg}, the significance of which will be addressed in subsequent discussion.

At 40 °C (in the region of long time stability of the σ phase) the initial stiffening at short times (~ 100 seconds) is followed by two additional increases in the modulus.

From approximately 2 minutes to 10 minutes (1×10^2 to 6×10^2 seconds), the modulus increases and appears to saturate, correlating with the time to nucleate and grow the metastable BCC structure as documented by SAXS experiments (Figure 4.12). Over the next several hours, the nucleation and growth of the equilibrium σ phase is reflected in the DMS experiments as a second stepwise increase in the modulus, again agreeing well with the SAXS experiments.

At temperatures where the DQC phase forms, the modulus evolves in a manner that is qualitatively different than what occurs at 40 °C. After the initial stiffening, the modulus continues to slowly increase as a function of time without any evidence in the SAXS experiments of nucleation, growth, or even any appreciable change in the scattering patterns. Then, when the DQC begins to nucleate, as evidenced by the SAXS measurements, the modulus increases in a stepwise manner and saturates at long times, similar to the growth of the other ordered phases.

The DMS data obtained at 25 °C were collected at a lower frequency ($\omega = 0.1$ rad/s) than the data recorded at the higher temperatures ($\omega = 1$ rad/s). The choice of measurement frequency during an ordering experiment determines the minimum time interval between measurement points (equal to the time required to collect a single data point, which increases with decreasing frequency) and consequently this sets the shortest timescale over which ordering can be measured. A frequency of 1 rad/s was chosen to allow measurement of the fast ordering of the IL-5.1 polymer at most experimental temperatures. A frequency of 0.1 rad/s was chosen to improve sensitivity to relaxations that occur at longer timescales and thus provide a slightly more sensitive probe of the ordering process at 25 °C, at the expense of not acquiring the data at short times. All the solid-like phases exhibit a nearly constant $G'(\omega)$ (i.e., G' is not a strong function of ω) over the experimentally accessible range of ω, except very close to T_{ODT}, as shown in Figure 4.18. Hence, the choice of a lower frequency at 25 °C has a minimal influence on the qualitative nature of the data after the initial stiffening at short times.
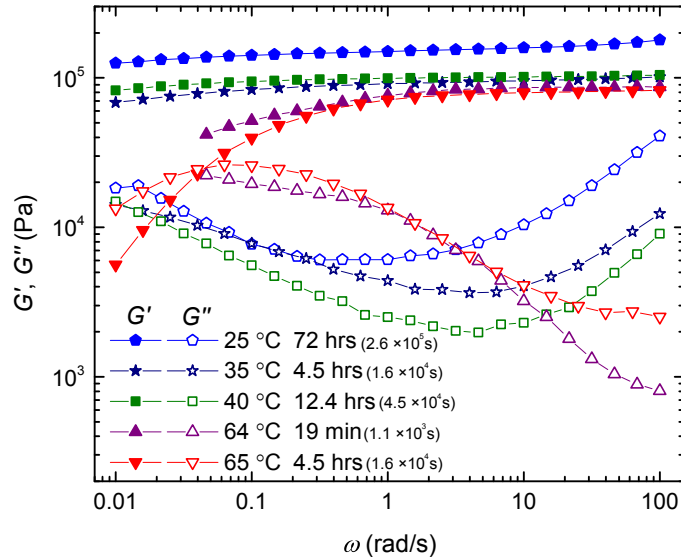
Figure 4.18 Frequency sweeps in the ordered phases at selected temperatures and annealing times. Frequency dependence of the linear (0.5 %) dynamic shear storage (*G′*, filled symbols) and loss (*G″*, open symbols) moduli after ordering at various temperatures and times.

Note that in the DMS experiments shown in Figure 4.16, annealing times at 35 and 25 °C were not long enough to initiate the nucleation and growth of the equilibrium σ phase. To capture this behavior and the related frequency dependences of the moduli during ordering, an additional set of DMS experiments was conducted during ordering at 35 °C. In this sequence of experiments, summarized in Figure 4.19, after quenching from the DIS phase, a series of frequency sweeps were performed, one after another. At longer times, 1 rad/s measurements were inserted between the end of each frequency sweep measurement and the initiation of the next frequency sweep measurement. This experimental protocol allows simultaneous monitoring of the long-time trend in *G′*(1 rad/s) while capturing any changes in the frequency dependence of the moduli during the ordering process. These measurements clarify the evolution of structure from the initial stiffening (10^2 s), through the development of the DQC (step change at 10^3 to 10^4 s), and finally the nucleation and growth of the σ phase (subtle step change at 10^4 to 10^5 s). The

times of the step changes in G' in the DMS experiment, while in general agreement, do not precisely match the phase transformations times documented in SAXS experiments (given above Figure 4.19). This minor discrepancy perhaps results from small differences in the actual sample temperature between experiments (and strong temperature dependence of the dynamics, see Figure 4.22) or differences in the sensitivity of the two techniques. In addition, it is evident that the frequency dependence of the moduli changes only subtly over the course of structural evolution from the stiff, disordered structure that forms initially, through the DQC, and through the eventual formation of the σ phase. The storage modulus (G') is largely independent of frequency, while the loss modulus (G'') exhibits a local minimum that deepens and moves to lower frequency over time as the structure evolves.

The BCC, σ, and metastable DQC phases form through different dynamic pathways and consequently are expected to exhibit qualitatively different mechanical properties as a function of time during ordering. An overlay of representative G'(1 rad/s) curves obtained at 35, 40, and 45 °C, drawn from Figure 4.16 and Figure 4.19 is presented in Figure 4.20 to allow a direct comparison. Noting again that the rheometer gap was not adjusted to account for thermal expansion of the parallel plate fixtures or sample, there may be minor errors in the relative magnitude of the moduli between measurements (the absolute error in G' may be quite large due to the non-ideal geometry at the sample edge). However, this does not affect the changes of G' as a function of time. An expanded view of the data of Figure 4.20 is shown in Figure 4.21, emphasizing the stiffening at short times.
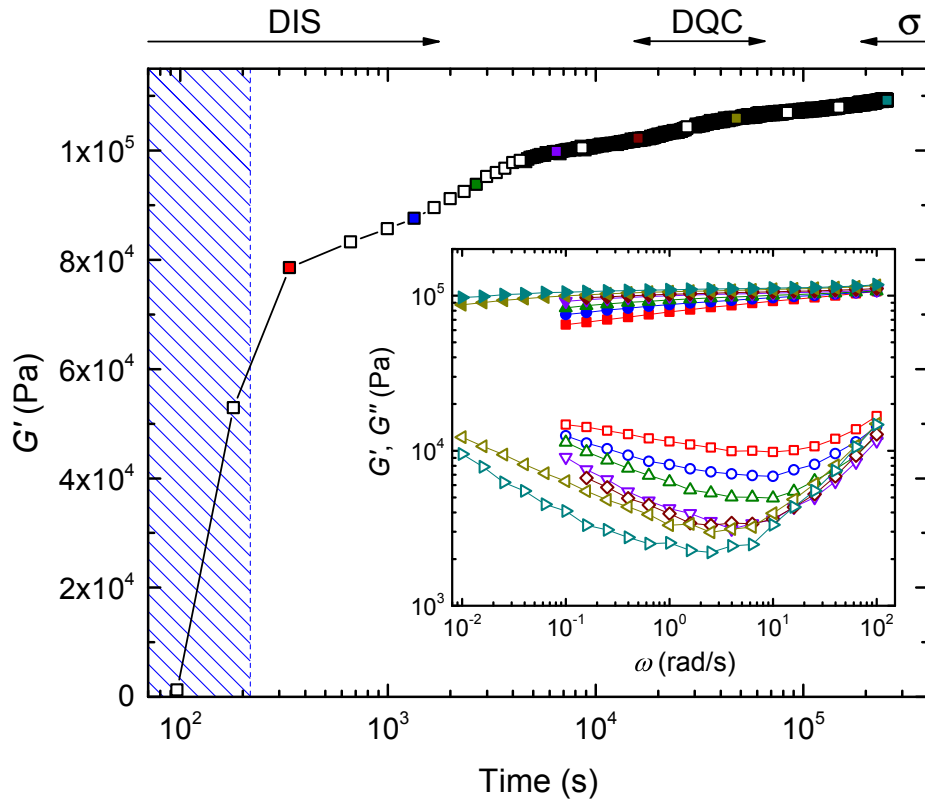
Figure 4.19 DMS measurements of ordering at 35 °C. The development of elasticity measured via the isothermal linear (0.5 %) isochronal (1 rad/s) dynamic shear storage modulus G' as a function of time. Open symbols and symbols filled with colors (not black) were extracted from frequency sweep measurements. Selected frequency sweep measurements are shown in the inset. Colors of the filled data markers in the main panel correspond to the colors of the symbols in the inset frequency sweeps from which they were extracted. In the inset, square, circle, up triangle, down triangle, diamond, left triangle, and right triangle data markers indicate frequency sweeps from progressively longer annealing times, with filled and open symbols indicating G' and G'', respectively. The hatched blue area represents times during cooling prior to equilibration at 35 °C. The ranges in time the pure DIS, DQC, and σ phases were observed in SAXS experiments are indicated along the top axis.
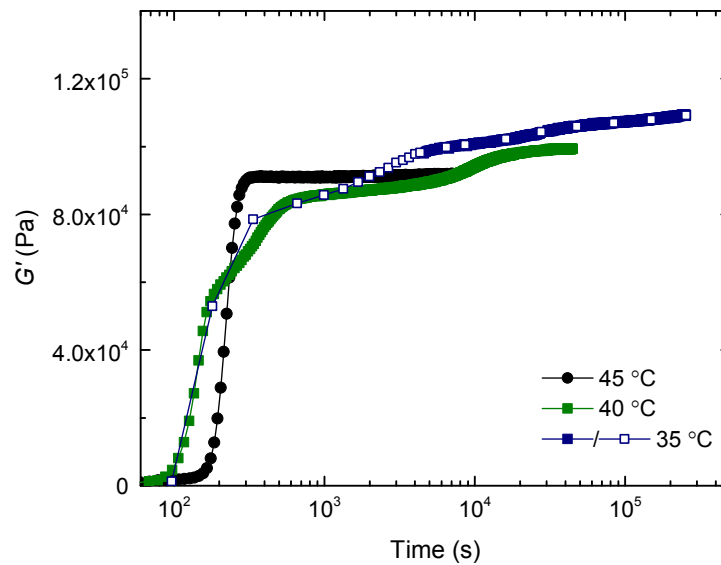
Figure 4.20 Comparison of representative ordering kinetics for the DIS-BCC, DIS-BCC-σ, and DIS-DQC-σ ordering pathways as evidenced by DMS. Isothermal linear (0.5 %) isochronal (1 rad/s) dynamic shear storage modulus G' during the growth at 45 °C (DIS-BCC), 40 °C (DIS-BCC-σ), and 35 °C (DIS-DQC-σ) from Figure 4.16 and Figure 4.19.
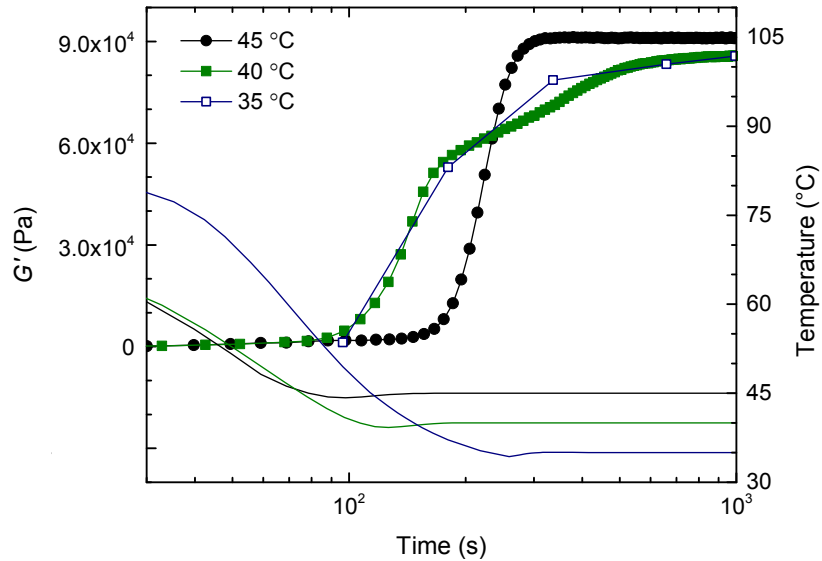
Figure 4.21 Expanded view of the low time data of Figure 4.20. Solid lines indicate temperature as a function of time (right *y*-axis).

The isothermal ordering kinetics of IL-5.1 can be summarized in a time-temperature-transformation (TTT) diagram, as shown in Figure 4.22. The progression from nucleation limited to diffusion limited growth of the BCC phase is clearly evident in the TTT diagram, leading to the classic "nose" shape with a minimum ordering time occurring at an intermediate ordering temperature where both nucleation and growth are facile ($\approx$ 55 °C). At the "nose" ($\approx$ 55 °C), nucleation and growth is rapid with the onset of ordering occurring almost immediately upon equilibration at the target temperature ($t_{eq} \approx$ 120 s). The TTT diagram of Figure 4.22 is similar to the TTT diagram for the IL-15 polymer reported by Lee et al.[88] but with a much broader range of ordering temperatures and times, and a "nose" at roughly one-tenth the time.
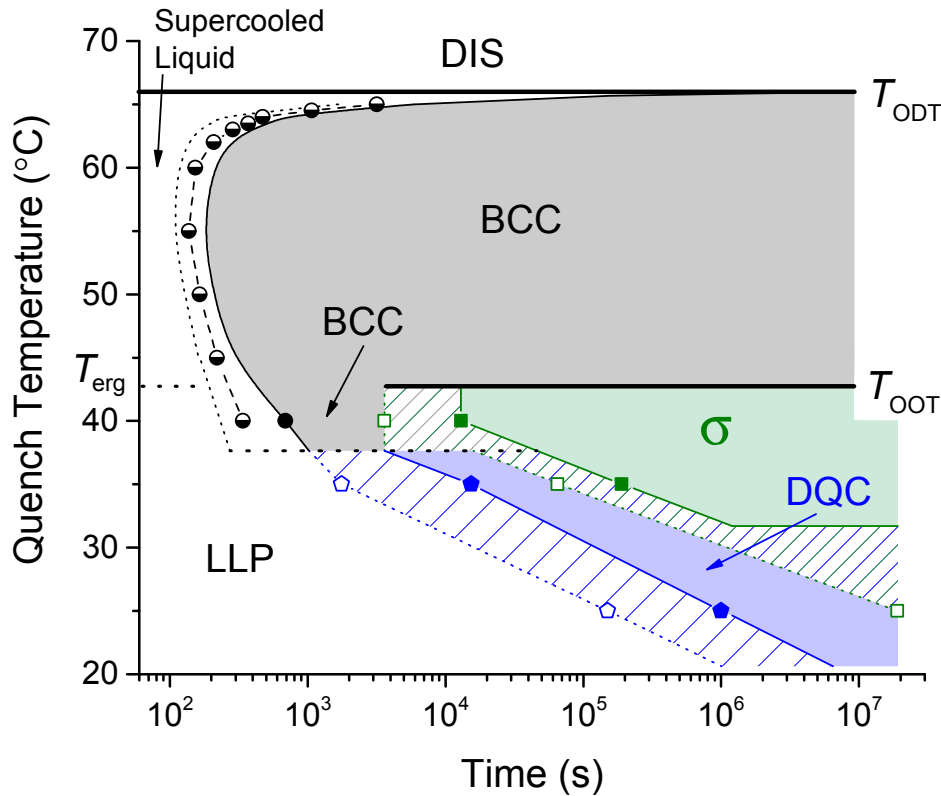
Figure 4.22 Time-temperature-transformation diagram for IL-5.1 summarizing the kinetics of ordering as measured by SAXS and DMS. In the BCC-forming regions (shaded gray), dotted lines, dashed lines and half filled circles, and solid (black) lines indicate achievement of 5, 50, and 95 % of the maximum measured value of G', respectively. In the complex phase region, open symbols and filled symbols indicate the first evidence of nucleation and completion of ordering in SAXS, respectively, with lines connecting these symbols being guides to the eye. Circle (gray shaded area), square (green shaded area), and pentagon (blue shaded area) data markers indicate formation (regions of stability) of BCC, σ, and DQC phases, respectively. Order–disorder and order–order transition temperatures are indicated by thick horizontal solid lines.

The physical state that corresponds to the initial, short time (~100 seconds, see Figure 4.21) stiffening below T_{erg} prior to nucleation of the BCC, σ or DQC phases is intriguing. From the SAXS data, it is clear that this supercooled state is not an ordered phase. These SAXS patterns are characterized by a single peak at $q*$ that, while much broader than a Bragg peak, is somewhat narrower than the single peak observed in the

equilibrium DIS phase above T_{ODT}, consistent with a dense disordered arrangement of the nearly spherical point particles. The glass transition temperatures, T_gs, of both blocks are well below the experimental ordering temperatures, particularly the majority (corona) polyisoprene block, $T_{g,I}$ = −63 °C. Therefore, one might naively expect this disordered arrangement of soft particles to behave like a liquid. Instead, a solid-like response is measured ($G' \approx 10^5$ Pa independent of ω, see Figure 4.19) with the modulus increasing over time. This evolution of modulus is not accompanied by any appreciable change in the measured scattering patterns prior to nucleation of an ordered phase. Lee et al.[88] reported similar behavior in the IL-15 polymer (which forms the σ phase at long times at 25 °C) during experiments in which the sample was quenched to ordering temperature close to the core block (polylactide) T_g. In Figure 4.22, this interesting solid-like but disordered state with no long-range order is designated LLP (liquid-like packing).

The onset of stiffening appears to change abruptly between 40 and 45 °C as shown in Figure 4.21. At 45 °C and above, stiffening is clearly associated with nucleation and growth of the BCC phase from a liquid ($G' < 10^4$ Pa). At 40 °C, the material stiffens ($G' \approx 10^5$ Pa) before the development of any ordered phase. In Figure 4.22, T_{erg} separates the regions where the supercooled disordered state exhibited the mechanical properties of a liquid ($T > T_{erg}$) and a solid designated LLP ($T < T_{erg}$). We return to this issue in the discussion section.

4.3.4 Equilibrium in IL-5.1

In addition to the simple isothermal ordering experiments discussed in section 4.3.3, SAXS and DMS experiments with a variety of thermal profiles were conducted to determine whether the phases identified in the isothermal ordering experiments are equilibrium states. The results of these experiments are described in this section.
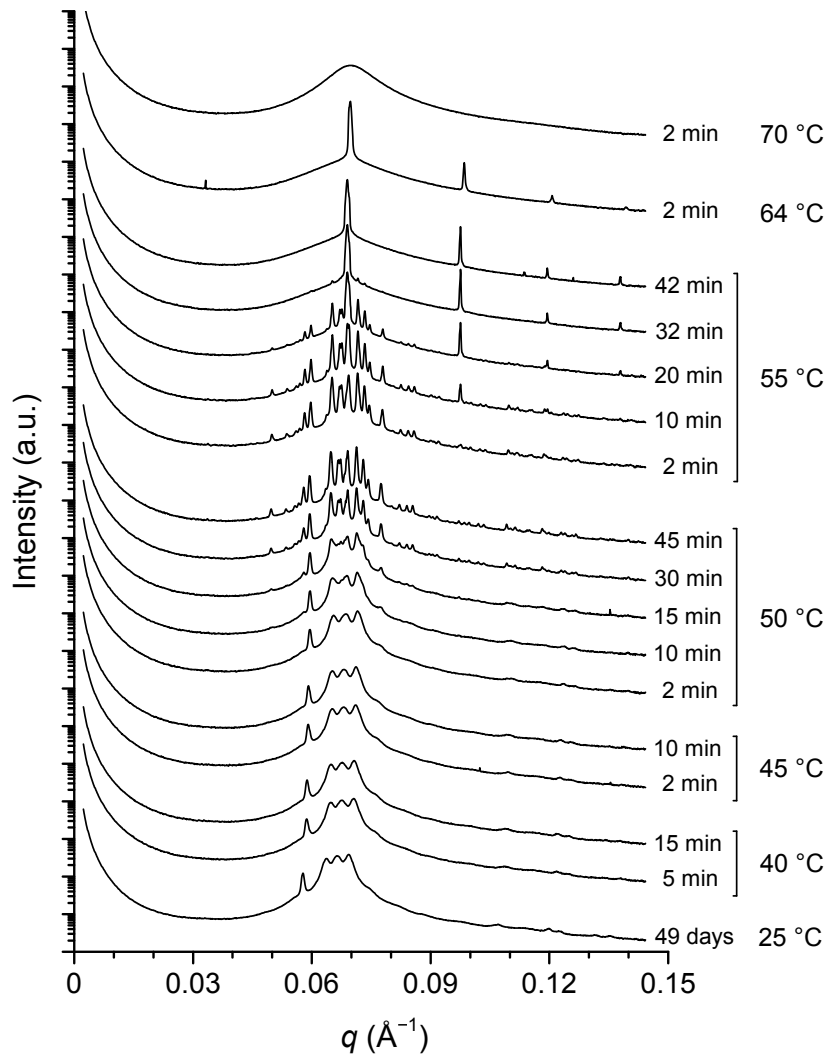
Figure 4.23 SAXS patterns collected upon heating of the DQC phase grown at 25 °C. The DQC grown by annealing at 25 °C for 49 days following a quench from the DIS phase (see Figure 4.14) was heated, stopping to anneal at several temperatures, and the subsequent evolution of structure was monitored by time-resolved SAXS. Heating to each annealing temperature was rapid ($t < 30$ seconds). SAXS patterns were collected sequentially from bottom to top at the temperatures and annealing times at each temperature indicated. Curves have been shifted vertically for clarity.

In the only previously reported sample to form the σ phase (IL-15), ordering at 40 °C led to development of a BCC phase while ordering at 25 °C resulted in the σ phase. However, once the σ phase developed at low temperature, it remained stable upon heating to T_{ODT} (i.e., did not transform to a BCC phase before disordering). Therefore, an open question is whether the BCC or the σ phase is the true equilibrium phase near the ODT. To address this question, IL-5.1 was subjected to a series of heating, cooling, and annealing procedures in order to further elucidate how kinetic restrictions influence access to the equilibrium states.

Figure 4.23 shows the evolution of structure on heating after growing the metastable DQC phase at 25 °C. Upon heating, the DQC phase remains stable for short times at 40 and 45 °C but rapidly nucleates the σ phase at 50 °C and completes the order–order phase transition (OOT) to the σ phase in approximately 30 minutes. Upon further heating to 55 °C, the σ phase transitions to BCC, and this morphology disorders upon heating above T_{ODT}. Figure 4.24 shows the evolution of structure on heating to 50 °C after growing the metastable DQC phase at 35 °C. Here, the sample was annealed for a considerably longer time at 50 °C than the experiment of Figure 4.23, resulting in the sequence of transformations from the DQC phase to the σ phase and then finally to BCC, all in less than four hours. These experiments demonstrate that at temperatures at or above about 50 °C, the BCC phase is formed regardless of the starting morphology (DQC, σ, or DIS), showing conclusively that this is the equilibrium phase near T_{ODT}.
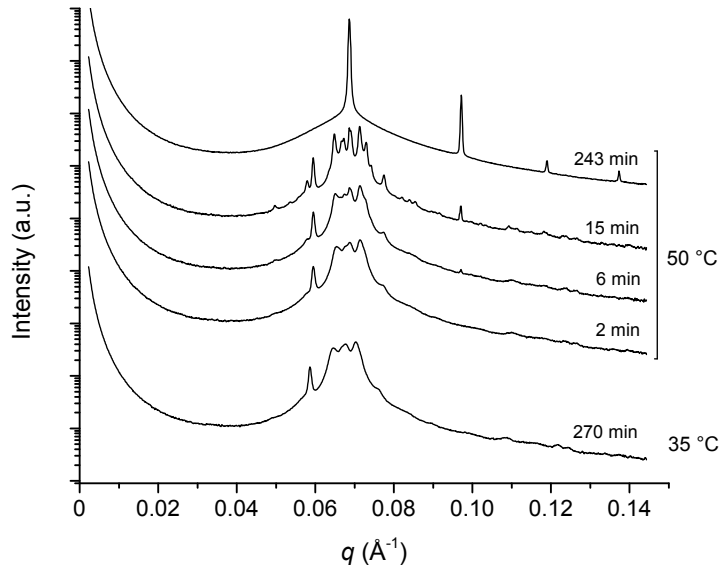
Figure 4.24 SAXS patterns collected upon heating of the DQC phase grown at 35 °C. The DQC grown by annealing at 35 °C for 270 minutes following a quench from the DIS phase (see Figure 4.13) was rapidly (t < 1 minute) heated to 50 °C and the subsequent evolution of structure at 50 °C was monitored by time-resolved SAXS. SAXS patterns were collected sequentially from bottom to top at the temperatures and annealing times at each temperature indicated. Curves have been shifted vertically for clarity.

The equilibrium order–order transition temperature T_{OOT} appears to lie between 40 and 45 °C, as revealed by the isothermal ordering experiments summarized in sections 4.3.2 and 4.3.3. The rate of transition between the BCC and σ phases is different upon cooling versus heating, a type of hysteresis commonly encountered with first-order phase transitions governed by nucleation and growth mechanisms. The OOT can be observed in DMS experiments as well as the SAXS experiments presented above, as shown in Figure 4.3 and Figure 4.25. It is evident in Figure 4.3 as a subtle stepwise increase in the loss modulus on heating beginning at approximately 50 °C. Figure 4.25 displays additional DMS measurements associated with the OOT. After annealing at 25 °C for several days to produce a DQC phase (see Figure 4.16b for ordering kinetics prior to heating) the sample was slowly (0.1 °C/min) heated while monitoring the moduli at 0.1 rad/s (Figure 4.25a). Heating was paused every ~10 °C and the sample was held at a fixed temperature

for approximately 1 hour in order to perform a set of frequency sweep measurements (Figure 4.25b). In Figure 4.25, below T_{OOT} (i.e., at 35 °C; $40 \leq T_{OOT} \leq 45$ °C) the moduli at 0.1 rad/s does not change when heating is arrested to complete the frequency sweep experiments and the heating branches in Figure 4.25a from before and after the frequency sweep measurement line up almost seamlessly. In contrast, above T_{OOT} (i.e., at 45 and 55 °C) the moduli at 0.1 rad/s seem to evolve with time during the frequency sweep measurement and the heating branches before and after the frequency sweep measurements are discontinuous. This evolution of the modulus is consistent with the slow transformation of the DQC phase to the equilibrium BCC phase between T_{OOT} and T_{ODT} measured in SAXS experiments. At 64 °C, the BCC phase is fully formed and the moduli at 0.1 rad/s do not change while heating is arrested, leading to the observed agreement of the heating branches from before and after the frequency sweep experiment at 64 °C. These results dictate using caution when interpreting frequency sweep data obtained under conditions where the morphology is changing.

In addition to the heating experiments described above, a second class of experiments with alternative thermal profiles were conducted to determine the equilibrium phase at temperatures below T_{OOT}. In these experiments, the samples were initially annealed at a higher temperature to grow a BCC or σ phase. The results are summarized in Figure 4.26 and Figure 4.27. These (and past) experiments show that below T_{OOT} the BCC phase transforms directly into the σ phase, which then remains stable with extended periods of annealing. Significantly, once formed, the σ phase has never been observed to change when $T < T_{OOT}$, consistent with the notion that this morphology is the equilibrium state for $T \leq T_{OOT} \approx 42$ °C.

An interesting feature of the kinetics of the experiments summarized in Figure 4.26 and Figure 4.27 is that the nucleation and growth of the σ phase from a BCC structure at both 35 and 25 °C occurs much faster than growth of the σ phase upon direct quenching to the respective ordering temperatures that proceed through the transient DQC structure at intermediate times. Also of note is that the DQC forms from the

quenched disordered state designated LLP faster than the σ phase forms from the preformed BCC structure at both 35 and 25 °C.
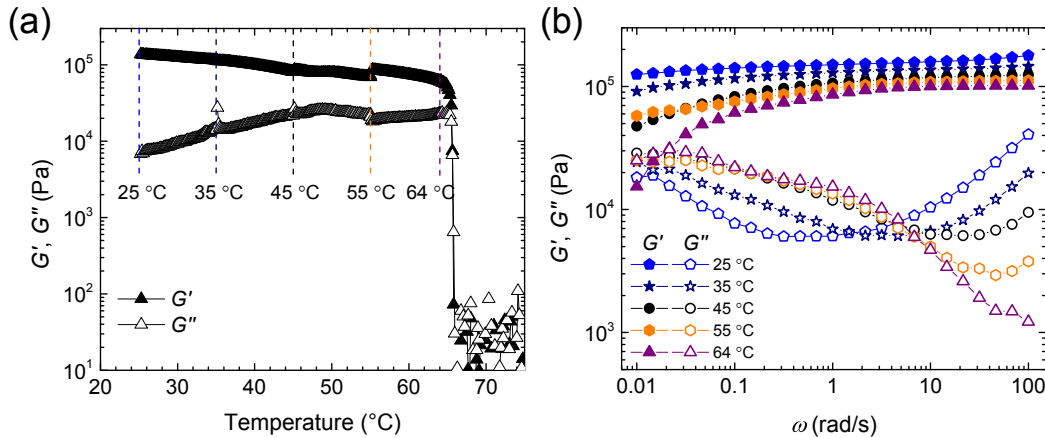
Figure 4.25 DMS of IL-5.1 during heating of the DQC phase. (a) Linear (0.5%) isochronal (0.1 rad/s) dynamic shear storage (G', filled symbols) and loss (G'', open symbols) moduli measured on heating at 0.1 °C/min. Prior to measurement, the sample was rapidly quenched from the disordered state to 25 °C and held isothermal for approximately 72 hours to grow the DQC phase. At selected temperatures indicated with vertical dashed lines in (a) heating was stopped and the linear (0.5 %) frequency dependence of the storage and loss moduli were measured, shown in (b).

If a well ordered phase is grown prior to quenching to low temperatures, the scattering patterns (BCC or σ phase) often show discrete diffraction spots on the 2D area detector, as opposed to the rings of uniform intensity associated with a fine "powder" (Figure 4.28). This indicates that within the illuminated scattering volume (≈ 0.1 mm^3) there are a relatively small number of large grains of the ordered phases. This leads to imperfect powder averaging upon data reduction to the 1D SAXS patterns shown in Figure 4.26 and Figure 4.27 (i.e., sufficient numbers of grains with all possible orientations are not in the illuminated scattering volume). As a consequence, relative peak intensities in the 1D SAXS patterns, which reflect the sum of scattering from all grains intercepted by the X-ray beam, may vary as the X-ray beam is directed at different points along the length of the capillary. This explains the minor variations in the ratio of diffraction peak intensities found in Figure 4.26.
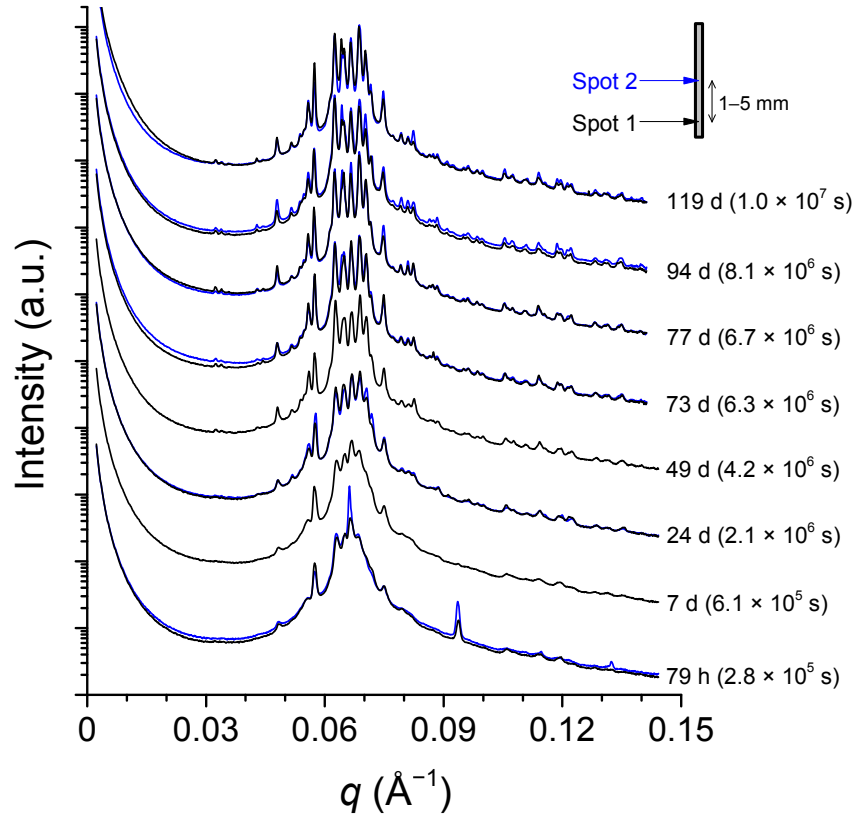
Figure 4.26 Annealing of IL-5.1 at 25 °C following complete growth of the BCC structure at 55 °C. SAXS patterns collected after annealing for the indicated times following a rapid (*t* < 10 seconds) quench from 55 °C. Prior to quenching, the samples were disordered above T_{ODT} and slowly cooled to 55 °C and allowed to anneal for at least 20 minutes to grow a well ordered BCC phase. The SAXS patterns come from many samples quenched at different times prior to traveling to the synchrotron X-ray source. At selected time points, SAXS patterns were collected at multiple locations along the capillary as shown in the schematic in the top right corner (SAXS patterns from additional locations shown as blue curves). The BCC phase is replaced by the growth of the σ phase over time. Curves have been shifted vertically for clarity.
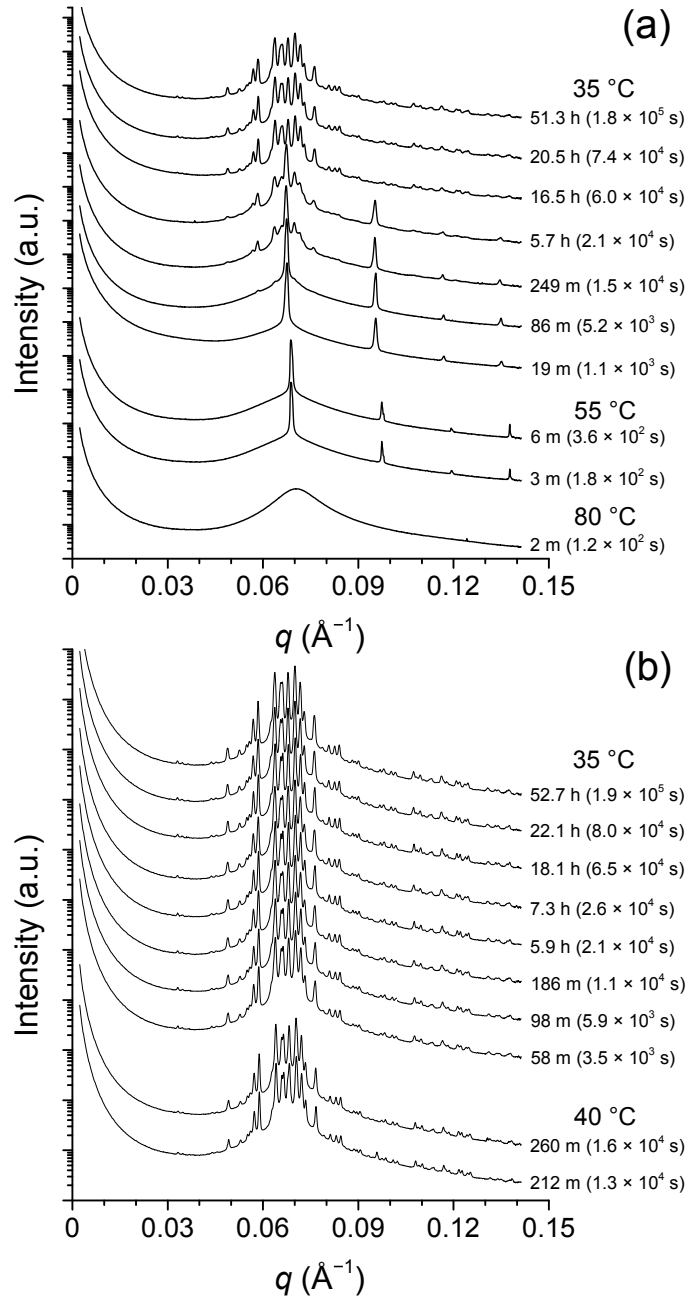
Figure 4.27 Annealing of IL-5.1 at 35 °C after growing the BCC (a) or σ phase (b) structure. SAXS patterns were collected sequentially from bottom to top at the temperatures and annealing times at each temperature indicated. In (b), prior to the first SAXS pattern shown, the sample was disordered above T_{ODT} and rapidly cooled to 40 °C. Curves have been shifted vertically for clarity.
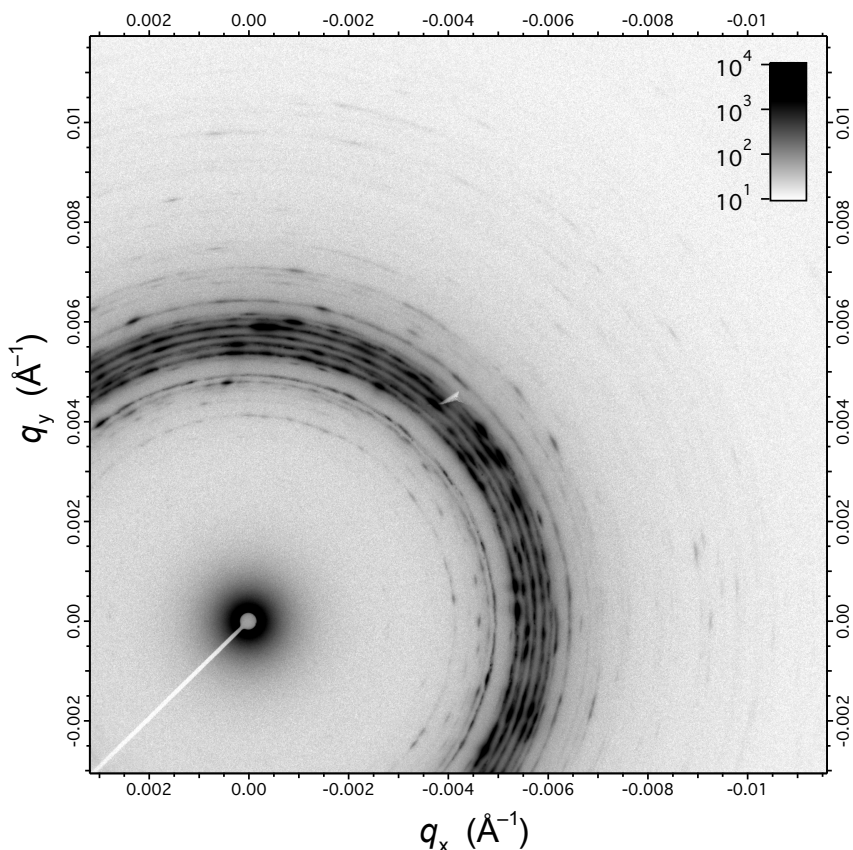
Figure 4.28 2D SAXS pattern corresponding to the 49 day data of Figure 4.26. The scattering pattern exhibits discrete diffraction spots as opposed to rings of uniform intensity.

4.4 Discussion

4.4.1 Discovery of dodecagonal quasicrystalline order in a diblock copolymer melt

In this chapter, detailed SAXS and DMS experiments have been presented that elucidate the discovery of a dodecagonal quasicrystal (DQC) phase in a diblock copolymer melt. The DQC phase was found to be a long-lived metastable structure that forms from a supercooled disordered state upon quenching far below the order–disorder transition temperature. Upon further annealing at temperatures where it forms, the DQC phase eventually transforms into the equilibrium Frank–Kasper σ phase, a closely related periodic quasicrystal approximant. Apparently, the DQC phase only forms from the

supercooled disordered state. This quasicrystal was never found to develop from either the BCC or σ phases.

The detailed structure of the DQC formed in IL-5.1 (i.e., the precise particle positions that make up the square–triangle tiling of the plane orthogonal to the 12-fold axis) cannot be determined from the powder SAXS data. These results do, however, provide some insight into the DQC structure beyond identification of the symmetry. The (00002) peak related to periodic stacking in the direction parallel to the 12-fold axis is much sharper than the triplet of strong peaks, (12100), (01102), and (12101), at slightly higher q associated with the aperiodic plane orthogonal to the 12-fold axis. This suggests the degree of long-range order in the aperiodic plane (x–y in Figure 4.1) is less than in the periodic direction parallel to the 12-fold axis. The arrangement of particles in the aperiodic plane in IL-5.1 likely contains numerous defects such as grain boundaries, dislocations, and disinclinations that have analogues in periodic crystals as well as what is known as phason strain, a type of departure from perfect long-range order that is unique to quasicrystals.[145,168–170] Therefore, the structure illustrated in Figure 4.1c should be viewed as an idealized structure and not as an accurate representation of detailed structure present in the DQC phase of IL-5.1.

The discovery of a DQC phase in the single component IL-5.1 diblock copolymer melt marks only the third experimental single component system to exhibit quasicrystalline order, joining supramolecular wedge-shaped dendrimers[141,143,147] and linear SISO tetrablock terpolymers[144] (quasicrystals have only been reported in multicomponent hard materials such as binary metal alloys).[139] Diblock copolymers are perhaps the simplest of these systems, and the most amenable to statistical mechanical theory.

As a result of the separation in length scale between the individual monomer units and the polymer chain as a whole, flexible diblock copolymers exhibit largely universal phase behavior dependent on a small number of parameters that are easily tuned during polymer synthesis and processing (primarily f_L and χN and to a lesser extent N, $Đ$, and the block statistical segment lengths), and not on the detailed chemistry or structure of the

monomer units.[14,37] The nearly spherical micelle-like point particles that order into the DQC structure are further removed from the individual monomer units, being spontaneously self-assembled aggregates composed of approximately 200 polymer molecules.[88] Therefore, the formation of the DQC phase in diblock copolymers cannot be rationalized based on the detailed shape or chemistry of the individual molecules, complicated interactions between preformed particles, or other such arguments. The underlying reasons for the formation of the DQC in diblock copolymers and other soft materials, as a result, must stem from something more fundamental. Understanding DQC formation in diblock copolymers thus provides an opportunity to gain insight into the workings of nature beyond just the phase behavior of block copolymer melts. In the following sections, key results of the experiments involving IL-5.1 are summarized and interpreted in the context of the current understanding of block copolymer thermodynamics, making broader connections where appropriate.

4.4.2 Equilibrium

At low temperatures (high χN), the equilibrium ordered phase in IL-5.1 appears to be the σ phase. All thermal processing pathways eventually lead to the formation of the σ phase structure at temperatures at or below 40 °C. At temperatures between 45 °C and T_{ODT} (66 °C), the BCC structure forms, either by cooling from the DIS phase or heating from the σ phase. The σ–BCC order–order transition temperature T_{OOT} lies between 40 and 45 °C and above $T_{ODT} = 66$ °C, IL-5.1 disorders.
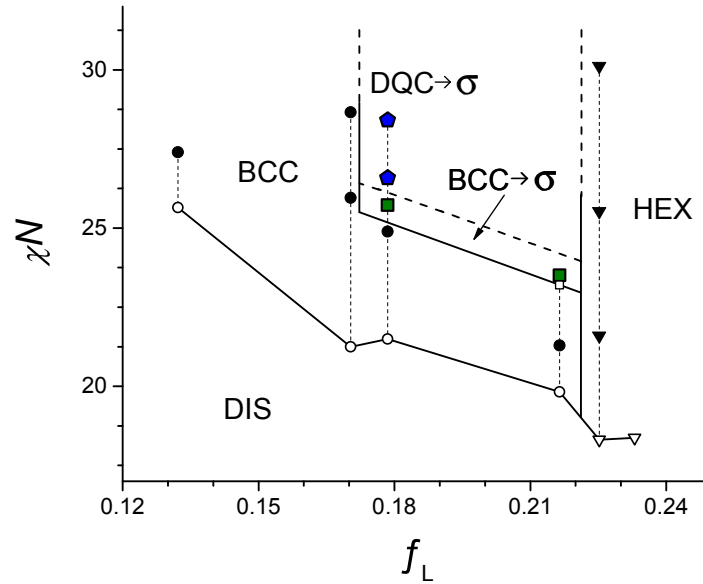
Figure 4.29 Simplified IL phase portrait near IL-5.1. Order–disorder and order–order transitions determined by rheology are marked with open symbols. Points where ordered phase symmetry was determined by SAXS are marked with filled symbols Filled black circles indicate BCC, filled black triangles indicate HEX (hexagonally packed cylinders), filled green squares indicate regions in which the σ phase forms through a short-lived metastable BCC intermediate, and filled blue pentagons indicate regions in which the σ phase forms through a long-lived metastable DQC intermediate. Phase boundaries (solid lines for confirmed and dashed lines for speculative) and the vertical dotted lines connecting data points from the same samples are drawn as guides to the eye.

Based on the reported temperature dependence of the interaction parameter χ for the IL diblock copolymer system ($\chi_{IL}(T) = 230/T - 0.38$) [15] and assuming no composition dependence, a simplified phase portrait can be constructed to summarize the equilibrium phase behavior of IL-5.1 along with other isoprene-rich asymmetric IL diblock copolymers studied, as shown in Figure 4.29. This phase portrait focuses on the documented phase behavior of IL5.1 and IL-15.[87] IL-5.1 is the sample at $f_L = 0.18$ while IL-15 is the sample at $f_L = 0.22$. The complex low symmetry ordered phases (σ phase and DQC) form in a relatively narrow range of composition at high χN that separates the BCC and HEX phases. Presumably the HEX symmetry is associated with hexagonally packed cylinders, although the provocative discovery of a hexagonal phase composed of

point particles in SISO polymers that also form the σ phase[144,166] casts some doubt on this assignment. See Chapter 5 for a more detailed phase portrait including data from additional IL diblock copolymers and the molecular details of the other samples included in Figure 4.29, including the samples that bound the range in f_L over which the complex low symmetry ordered phases form.

Perhaps more interesting than the equilibrium phase behavior of sample IL-5.1 are the different pathways toward equilibrium the sample was found to take, including through the metastable DQC structure. Following quenches to temperatures just below T_{OOT}, the equilibrium σ phase forms from the disordered state through a metastable BCC intermediate (filled green squares in Figure 4.29). However, when the sample is quenched further below T_{OOT}, the equilibrium σ phase instead forms from the quenched disordered state through the DQC phase (filled blue pentagons in Figure 4.29). The intriguing non-equilibrium behavior and the associated kinetics is addressed in section 4.4.3.

Of note, all the SISO tetrablock terpolymers for which scattering patterns consistent with the DQC have been measured (Figure 4.10d) share certain common features with the DQC discovered in IL-5.1. All the structures with the scattering patterns consistent with the DQC (Figure 4.10d) grew from nonequilibrium disordered states (either from a rapidly quenched supercooled DIS phase well below T_{ODT} or upon heating a freeze dried sample).[*] In addition, the DQC structures eventually transformed into the σ phase upon heating and the σ phase structure that formed on heating persists upon subsequent cooling. This suggests that the DQC phase in the SISO polymers of Figure 4.10d may also be a long-lived metastable structure that forms where the σ phase is the equilibrium structure. Perhaps the formation of the DQC phase as a metastable intermediate structure is a universal feature during ordering of the σ phase from a far from equilibrium disordered state (e.g., upon deep quenches into the region of

---

[*] In SISO-2 (Figure 4.10a–c) the (possibly equilibrium) DQC phase identified by TEM seems to form from a phase with hexagonal symmetry. However, a characteristic DQC SAXS pattern was not observed in this material, perhaps due to the previously noted differences in the thermal profiles during SAXS and TEM experiments.

equilibrium stability of the σ phase). In addition, the behavior of IL-5.1 documented in this chapter, in particular the metastability of the DQC phase for months of annealing at room temperature, calls into question the equilibrium stability of other reported soft single component quasicrystals.

From the phase portrait in Figure 4.29, it is clear that the slightly higher molecular weight (and therefore N) and concomitant higher T_{ODT} of the IL-5.1 polymer relative to IL-15 affords experimental access to higher values of χN, deeper in the ordered region of the phase diagram. This expanded experimentally accessible region of the phase diagram facilitated discovery of the DQC in IL-5.1. Further increasing molecular weight (and thus increasing the highest accessible χN) is an interesting avenue for future investigations that may reveal additional related ordered phases (e.g., other Frank–Kasper phases) or perhaps regions in parameter space where the DQC is the equilibrium phase.

With the equilibrium phase behavior of IL-5.1 established, how does the documented behavior fit with current understanding of the formation of the σ phase and related structures in block copolymers? Recent work from Lee, Leighton, and Bates[88] introduced two concepts that rationalize why and how complex low symmetry phases, particularly the σ phase, form in block copolymer melts: sphericity and chain exchange. These important concepts are summarized in the following paragraphs.

In the undiluted melt, asymmetric diblock copolymers self assemble into point particles that form mesoscopic ordered structures (e.g., BCC, σ) with characteristic length scales on the order of the radius of gyration of the overall polymer chain. These structures form as a result of a delicate balance between the enthalpic drive to minimize unfavorable core/corona contacts and the entropic penalty that accompanies stretching the chains to separate the core and corona blocks.[14] All structures (ordered and disordered) exhibit liquid-like packing of chain segments at the monomer length scale that imposes a constraint of uniform density on any structure formed (e.g., no voids between mesoscopic particles). In an isolated micelle-like point particle such as the single particle illustrated in Figure 4.2c, the core/corona interface would prefer to adopt a spherical shape at high segregation strength χN (low temperature) to minimize unfavorable core/corona contacts

and chain stretching, much like asymmetric diblock copolymers in a selective solvent form spherical micelles.[171] However, when the particles order onto the lattice of a particular crystal structure in the undiluted melt they are necessarily distorted from the preferred spherical shape. This distortion results from the fact that each particle must assume the shape imposed by the neighboring particles on the lattice (i.e., the Wigner–Seitz cell or Voronoi polyhedra).[88] In the strong segregation limit ($\chi N \gg 10$), the core/corona interface becomes a sharp step function with minimal interpenetration of the corona blocks between neighboring particles. As a result, each particle must assume the size and shape of the Wigner–Seitz cell of the occupied lattice site.[14] This leads to a competition between the tendency to form spherically symmetric interfaces (i.e., to assume the shape preferred by the isolated particle) and the constraints imposed on the shape of the particles by the lattice symmetry (or local coordination shell in a disordered structure).[88] At high χN (low temperatures), this competition leads to a preference for ordered structures in which the Wigner–Seitz cells of the lattice most closely approximate spheres, that is, have higher sphericity. As χN is reduced (temperature increased), intermixing of the core and corona blocks within a particle as well as among corona blocks of neighboring particles occurs, softening the interfaces and easing somewhat the constraints on shape imposed by the lattice. It is this preference towards ordered structures with more spherical Wigner-Seitz cells (i.e., higher sphericity) as temperature is reduced that is believed to result in the order–order transition from the BCC structure to the Frank–Kasper σ phase on cooling.[88]

All the particles in the BCC structure have an identical coordination environment with a Wigner–Seitz cell that is a truncated octahedron with 14 faces (eight nearest neighbors and 6 next nearest neighbors). In the σ phase, there are five different coordination environments among the 30 particles per unit cell and thus five unique shapes of Wigner–Seitz cells with an average of 13.5 faces.[87,151,152] Importantly, each of the five Wigner–Seitz cells of the Frank–Kasper σ phase structure found in block polymers is of a slightly different volume ranging from 91.0 to 106.5% of the average.[87] The sphericity, as measured by the isoperimetric coefficient ($IQ = 36\pi V^2/S^3$, where V and

S are the volume and surface area, respectively; for a sphere $IQ = 1$), is higher for the average of the five particles of the σ phase ($IQ_σ = 0.7624$) than for the BCC structure ($IQ_{BCC} = 0.7534$).[88] The Wigner–Seitz cells of the σ phase are thus on average more spherical than that of the BCC structure. The reduction of the frustration between the preferred spherical particle shape and the constraints imposed by the lattice symmetry therefore leads to the transition from BCC to the σ phase on cooling.

In order to form the σ phase, the exchange of individual chains between particles must occur to achieve the five different particle volumes of the various lattice sites. While the exchange of an individual chain may be fast, the redistribution of mass between particles to satisfy the requirements of the σ phase structure is apparently quite slow, as evidenced by the difference in timescales at a given temperature measured for the formation of the σ phase and BCC structures (forming the BCC phase does not require a redistribution of mass amongst particles to achieve different sized particles at particular lattice sites as all lattice sites in the BCC structure are equivalent).[87,88] It is fascinating that the ostensibly single component system spontaneously breaks symmetry and forms the optimal distribution of particle sizes to relieve the frustration between sphericity and lattice symmetry by forming the σ phase. This occurs without the need to deliberately prepare or otherwise "build in" pre-determined sizes or shapes of the constituent particles.[146,168,172,173]

The concept of particle sphericity has both a local and global component. Each individual particle has a preference for a local structure that most closely resembles a sphere, however, the perturbations from the preferred spherical structure are imposed by the global structure of the collection of nearby particles (i.e., the lattice symmetry or local coordination shell of nearest and next-nearest neighbors). In forming the σ phase, the block polymer system redistributes mass amongst particles in a way to globally increase the average sphericity, an astounding result.

The results presented in this chapter are entirely consistent with the sphericity concept invoked to describe the appearance of the σ phase in IL-15 and IL-5.1 displays essentially identical equilibrium phase behavior to IL-15. However, the appearance of the

DQC phase in IL-5.1 as a metastable intermediate during ordering of the σ phase raises many interesting questions. Based on the supposition that the sphericity explanation for the stability of the σ phase is correct, it would seem that the σ phase has a higher sphericity than the DQC. While the σ phase has five unique local environments, the precise structure of the DQC is not known in detail. The idealized DQC structure in Figure 4.1c is comprised of the same square and triangle tiles as the σ phase (but in slightly different proportions) that would presumably lead to particles with a similar set of local environments in the DQC and σ phase. From the diffraction data (e.g., Figure 4.5), it is clear that the "grain" size or correlation length of long-range order in the DQC is much smaller than that in the σ phase, particularly in the aperiodic plane, as evidenced by broader line widths of the diffraction peaks of the DQC phase compared to the σ phase. Thus, the real DQC structure likely includes many defects (grain boundaries, dislocations, disinclinations, and phason strain[145,168,169]). Therefore, the precise shapes and sizes of the particles in the DQC are not known and may not be knowable for the quasicrystalline structure, which lacks a finite size unit cell. As a result, the sphericity cannot be calculated *a priori* in analogy to the σ phase. Perhaps the presence of defects leads to low sphericity particles at certain sites, reducing the average sphericity of the structure below the σ phase and leading to the observed DQC–σ order–order transition. It remains an open question if a perfect DQC (i.e., one that gives rise to delta function diffraction peaks) would possess higher sphericity than the σ phase, leaving open the possibility of an equilibrium DQC under certain conditions.

The preference for formation of the DQC over BCC at short times as temperature is reduced suggests that the sphericity of the DQC is higher than the BCC structure, though kinetic factors likely play a role. Particularly intriguing is the apparent consumption of the small amount of the BCC phase that is initially nucleated on the direct quench to 35 °C by the growing DQC (Figure 4.13), which would support the idea that the DQC has higher stability, and therefore sphericity, than the BCC structure at low temperatures. However, in other experiments (Figure 4.27), if BCC was grown prior to quenching to 35 °C, the BCC structure transformed directly into the σ phase and did not

form the DQC. Perhaps nucleation of the DQC from BCC occurs slower than nucleation of the equilibrium σ phase (and hence the σ phase forms directly). An alternative explanation for this apparent contradiction is that the apparent consumption of the BCC by the DQC (Figure 4.13) was in fact simply disordering of the BCC structure during initial nucleation of the σ phase following the initial step on the pathway of the BCC–σ order–order transition proposed by Lee, Leighton, and Bates.[88]

Recent developments in self-consistent mean-field theory (SCFT) calculations of block polymers,[43,174] historically the workhorse theoretical tool for understanding the thermodynamics of block polymers,[37] have allowed consideration of the σ phase as a candidate structure. Shi and co-workers[43] found that in the SCFT framework, the σ phase is a stable equilibrium phase (i.e., has a lower free energy than all other candidate structures considered) in a region of the phase portrait between the BCC and HEX phases for linear diblock copolymers if the statistical segment lengths of the A and B block are sufficiently different. We note that the DQC was not considered as a candidate structure, though common point particle ("sphere") phases such as BCC, cubic (FCC) and hexagonally (HCP) close packing, and the A15 phases were considered. These SCFT results are in qualitative agreement with the findings in the IL system, a topic that is addressed further in Chapter 5.

The formation of a metastable DQC phase from a quenched disordered state under conditions where the σ phase is the equilibrium structure as documented in IL-5.1 is also a feature of a single component computational model in which particles of uniform size interact via a spherically symmetric modified Lennard–Jones interparticle potential (the Dzugotov potential). The Dzugotov potential is designed to suppress the formation of BCC, FCC and HCP crystals.[175–177] There are key differences between the computational model and the experimental IL-5.1 polymer system including the absence of any predefined particle shapes or volumes in the diblock copolymer system and the arbitrarily chosen and complicated interparticle potential of the computational model. A variety of degrees of freedom are available to the experimental system (e.g., mass exchange between particles) that are not available in computational model. Despite these

differences, the similarity of the behavior in the model and IL-5.1 is interesting. The ability to investigate the behavior of the simulation models at the level of the individual particles can perhaps be instructive when considering the ordering pathways of IL-5.1. This topic is taken up again in the discussion of the interesting LLP disordered state below.

4.4.3   The path to equilibrium

As stated above, perhaps more interesting than the equilibrium phase behavior of sample IL-5.1 are the different pathways toward equilibrium the sample was found to take depending on temperature. Upon quenches to temperatures just below T_{OOT}, the equilibrium σ phase forms from the quenched disordered state through a metastable BCC intermediate (filled green squares in Figure 4.29), as was previously documented in IL-15.[87] However, when the sample is quenched further below T_{OOT}, the equilibrium σ phase instead forms from the quenched disordered state through the long-lived metastable DQC phase (filled blue pentagons in Figure 4.29).

The metastable BCC and DQC phases form from the quenched disordered state as the kinetically favored ordered phase (analogous to the kinetic product in a chemical reaction with multiple possible product species). The disorder–order transition and the subsequent order–order transitions are first-order phase transitions that proceed through a nucleation and growth mechanism. The nucleation and growth of the equilibrium σ phase is much slower than the nucleation and growth of the BCC phase near T_{OOT} and the DQC phase well below T_{OOT}. The fast nucleation and growth of the BCC phase relative to the σ phase is easily rationalized as resulting from the necessity to redistribute mass between neighboring particles to achieve the five different particle sizes required by the σ phase structure that does not need to occur to form the BCC structure (in which all lattice sites are identical).[88] The mechanism that leads to formation of the DQC and of the subsequent DQC–σ order–order transition is less clear. Some insight can be gained by comparing the relative rates of different disorder–order and order–order phase transitions under similar conditions.
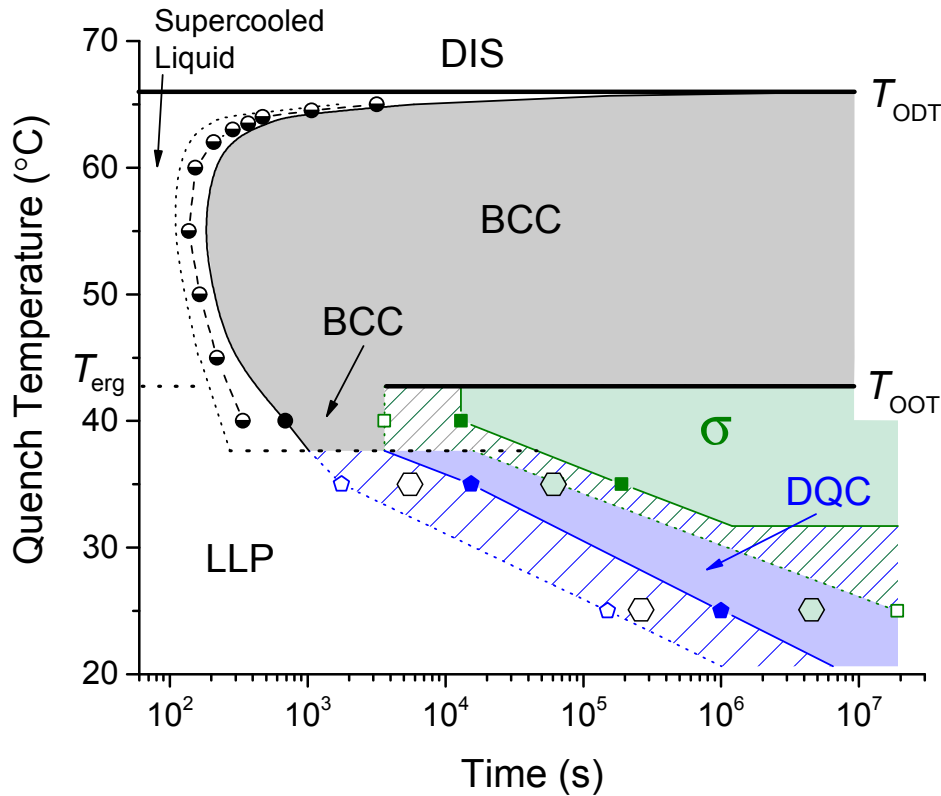
Figure 4.30 Modified time-temperature-transformation diagram for IL-5.1 summarizing the kinetics of ordering as measured by SAXS and DMS. Reproduced from Figure 4.22, see caption for details. Open and green filled hexagons have been added to indicate the times after quenching to 35 and 25 °C at which the first signs of nucleation and the completion of the BCC–σ order–order transition occurred for samples previously annealed at $T_{OOT} < T < T_{ODT}$ to form a BCC structure, as evidenced by SAXS.

The rate of nucleation and growth of the DQC at 35 °C is significantly slower than the nucleation and growth rate of the BCC structure that would be expected at 35 °C based on extrapolation of the measured BCC growth kinetics at higher temperatures (Figure 4.22). The rate of nucleation and growth of the σ phase upon a direct quench to 35 or 25 °C can be compared to the rate of growth when the sample is first annealed at $T_{OOT} < T < T_{ODT}$ to form a BCC structure prior to quenching to 35 or 25 °C (see Figure 4.26 and Figure 4.27). At both temperatures, the σ phase forms much faster from a BCC structure than upon a direct quench from the disordered phase through the DQC

intermediate. However, the formation of the σ phase from the quenched BCC phase is slightly slower than the formation of the DQC from the quenched disordered state, as is shown in the modified TTT diagram of Figure 4.30.

Several conclusions can be drawn from the relative growth rates summarized above. The suppression of BCC formation at short times suggests nucleation or growth (or both) of the BCC phase is inhibited in the quenched disordered state at 35 °C and below. There is some evidence of nucleation of BCC grains at 35 °C at early times in Figure 4.13, suggesting that it may be the inhibition of growth that dominates. The nucleation and growth of the DQC from the quenched disorder state occurs faster than the formation of the σ phase from quenched BCC structure, a process that is known to require a redistribution of mass. An open question is whether the formation of the DQC from the quenched disordered state itself requires a redistribution of mass similar to the formation of the structurally related σ phase. It is our suspicion that chain exchange is indeed required to form the DQC based on the finding of Lee, Leighton, and Bates[88] in which the DQC did not form upon quenching IL-15 from the disordered phase to 0 °C and annealing for 48 days. By quenching to 0 °C, the core block of the point particles vitrifies, preventing chain exchange. No evolution of structure toward the DQC (or σ phase) was documented in IL-15, suggesting chain exchange is required for DQC (and σ phase) formation from the quenched disordered state. Similar experiments over longer times with IL-5.1, a sample known to form the DQC, may prove more conclusive.

The fact that the σ phase forms relatively quickly from a BCC structure as opposed to relatively slow formation from the disordered state through the DQC intermediate suggests that the slow DQC–σ order–order transition does not result exclusively from the time required to redistribute mass among particles since this process must occur for σ phase formation along either pathway. In fact, the distribution of particles sizes present in the DQC is likely to more closely approximate the distribution of particle sizes required by the σ phase structure than the single particle size of the BCC structure and therefore, the transformation to the σ phase from the DQC might be expected to require less redistribution of mass and to occur more quickly.

The structure and dynamics of the non-equilibrium quenched disordered state play an important role in the path taken to equilibrium. Above T_{ODT}, the equilibrium disordered state is known to be fluctuating structured fluid, in which non-mean field composition fluctuations manifest as relatively long-lived micelle-like point particles,[67,106,127] the same particles that eventually order into the various ordered structures upon cooling below T_{ODT}. It is instructive to compare the temperature dependent dynamics of this fluctuating disordered state with the measured bulk ordering dynamics. Such comparisons may provide insight into the salient features of the supercooled disordered state that led to the formation of the DQC phase. Lee, Leighton, and Bates[88] were successful in investigating the dynamics of the disordered state of IL-15 by DMS. Frequency sweep measurements were collected both at equilibrium above T_{ODT} and in the supercooled disordered state at temperatures below T_{ODT}. Below T_{ODT}, frequency sweep measurements were conducted after quenching to the desired temperature in the time before the onset of ordering. The principle of time-temperature superposition (tTS) was applied to the data yielding a master plot. The temperature dependence of the shift factors $a_T(T)$ in the temperature range from 20 to 60 °C was fit to the Williams–Landel–Ferry (WLF) equation $\log(a_T) = -C_1(T - T_{\mathrm{ref}})/(C_2 + T - T_{\mathrm{ref}})$ yielding parameters of C_1 and C_2 of 10.4 and 67.3 °C with $T_{\mathrm{ref}} = 25$ °C.[88] Analogous experiments were conducted with IL-5.1 to quantify the dynamics of the disordered state and allow comparison with IL-15. These experiments are summarized in Figure 4.31 and Figure 4.32.
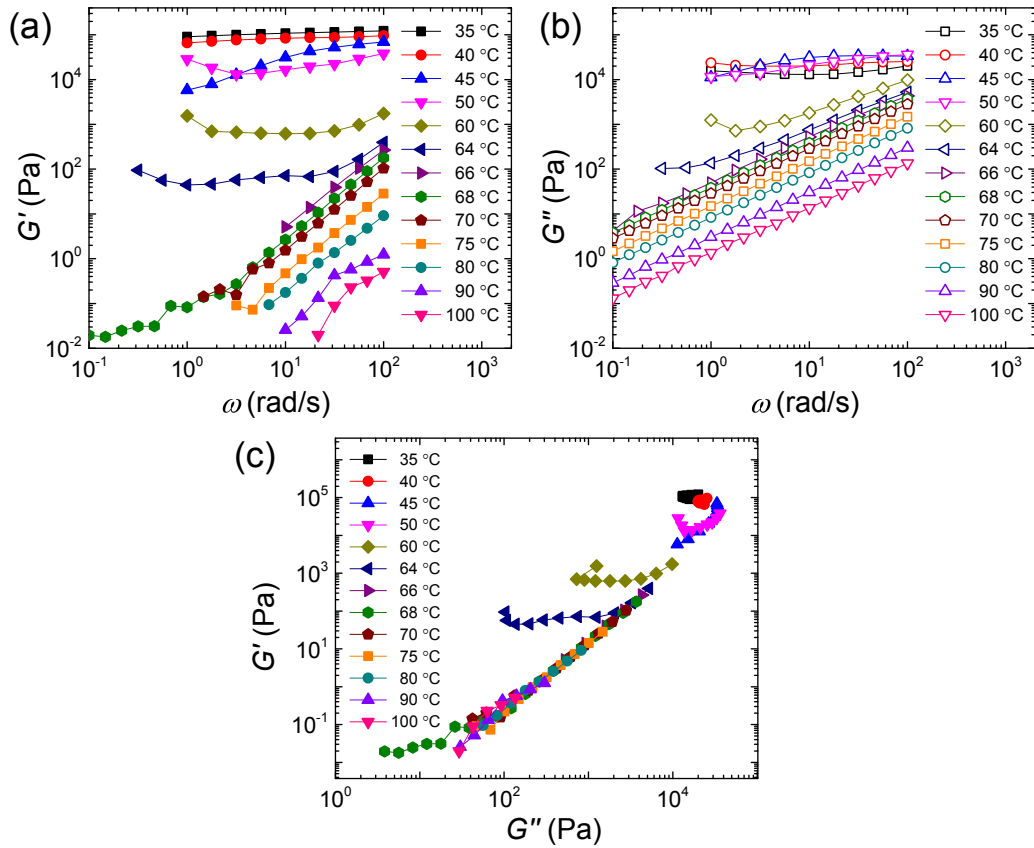
Figure 4.31 Raw DMS data of the disordered state in IL-5.1. Frequency dependence of the raw linear shear storage (a) and loss (b) moduli. (c) Modified Cole–Cole plot of the data in (a) and (b).

Above T_{ODT} (66 °C), frequency sweeps of the equilibrium disordered state exhibited terminal scaling ($G' \sim \omega^2$, $G'' \sim \omega^1$). The accessible experimental frequency range was far below the crossover frequency ω_c, and thus the timescales probed were longer than the longest relaxation time τ_o ($\tau_o \approx \omega_c^{-1}$) of the fluctuating disordered state. Below T_{ODT}, measurements of the moduli of the supercooled disordered state over the full experimental frequency range were not possible as the BCC phase began to grow before the completion of the frequency sweep measurement. This was a particular problem at temperatures near the "nose" of the TTT diagram around 55 °C where BCC ordering is fastest. Frequency sweep measurements were conducted from high to low frequency,

therefore, ordering of the BCC structure is evident in the frequency sweep measurements as an upturn in both moduli with decreasing measurement frequency, as can be seen most prominently in the data collected at 50, 60, and 64 °C. At the lowest temperature (e.g., 40 and 35 °C, $T < T_{erg} \approx 42$ °C), the material stiffens immediately in the curious disordered but solid state previously designated LLP.

To apply the principle of tTS and construct a master plot of the dynamics of the disordered state, it is necessary to omit the data influenced by BCC ordering. To help determine what portions of the data should be expected to superpose and aid in selecting the proper shift factors, a modified Cole-Cole plot was prepared (Figure 4.31c). The Cole-Cole plot involves no arbitrary shifting of the data but does form a master curve if tTS is possible, thus revealing under what conditions tTS is appropriate. From the Cole-Cole plot, it is obvious what ranges of data are influenced by BCC ordering, as these data do not fall on the master curve. Also revealed is that the data in the LLP ($T < T_{erg} \approx 42$ °C) state exhibit thermorheological complexity and should not be expected to superpose, as these data also do not fall on the master curve. Based on the information gleaned from the Cole-Cole plot, the tTS principle was applied to the raw data with a reference temperature of 66 °C (i.e., T_{ODT}) resulting in the master plot of Figure 4.32a. The shift factors used are plotted in Figure 4.32b. A non-linear least squares fitting of the shift factors to the WLF equation yields parameters C_1 and C_2 of 4.58 and 66.6 °C with $T_{ref} =$ 66 °C (solid black curve in Figure 4.32b). Owing to the thermorheological complexity evident in the Cole-Cole plot, shifting of the 40 and 35 °C data was not attempted. Instead, the shifts used for these temperatures in preparing Figure 4.32a were calculated based on the WLF fit. For comparison, the fit to the WLF shift factors of IL-15 (rescaled to have $T_{ref} = 66$ °C, giving C_1 and C_2 of 6.46 and 108 °C) is shown as the dashed red curve in Figure 4.32b. An alternative way to compare the dynamics of the disordered state of IL-15 and IL-5.1 is to calculate the longest relaxation time τ_o as a function of temperature from the master plots and the WLF parameters, as shown in Figure 4.33 for both IL-15 and IL-5.1.
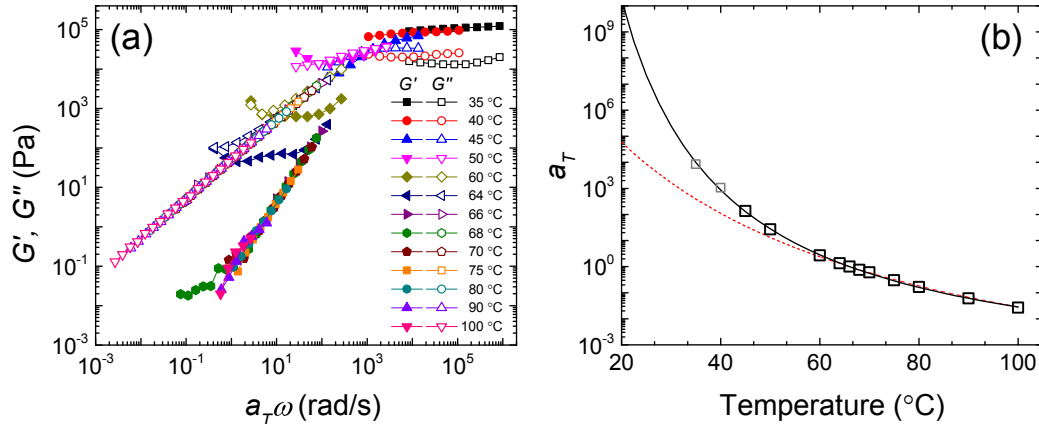
Figure 4.32 Time-temperature superposition of the data IL-5.1 DMS data in the disordered state. (a) Time-temperature superposed master plot with a reference temperature of 66 °C. (b) Shift factors used to superpose the DMS data. Solid line in (b) is a WLF fit with parameters C_1 and C_2 of 4.58 and 66.6 °C, respectively, and T_{ref} of 66 °C. Black data points in (b) were used to determine WLF parameters (gray data points calculated from fit). Dashed red curve in (b) is the fit of the IL-15 WLF shift factors[88] rescaled to have a $T_{ref} = 66$ °C.

There are several processes across various length scales that may contribute to the dynamics of the disordered state as measured by DMS experiments. These include relaxation processes on the level of the micelle-like point particles, such as translation of an intact particle and the formation/dissolution of particles, to individual chain diffusion and segmental relaxations. The temperature dependent dynamics of each of these processes may be influenced by proximity to block glass transitions as well as changes in segregation strength with temperature. While it is not possible to deconvolute these many interrelated contributions to temperature dependent dynamics measured by DMS, comparison of the data for IL-15 and IL-5.1 provides clues as to the dominant factors. Based on comparisons of the dynamics measured in diblocks to the constituent homopolymers,[106] DMS experiments are sensitive to dynamic processes on the scale of the composition fluctuations rather than individual chains in the fluctuating disordered state of asymmetric diblock copolymers. Yet, τ_o (Figure 4.33) is orders of magnitude

faster than the measured ordering times at equivalent temperatures (Figure 4.30). We therefore attribute τ_o to chain diffusion mediated relaxation of the structured disordered phase.[67,88] This is supported by the apparent divergence of τ_o on cooling approaching $T_{g,L}$ and increasing segregation strength.

The difference in the divergence of a_T (and τ_o) on cooling in IL-5.1 and IL-15 implicates segregation strength as an important parameter influencing dynamics in the disordered state. If segmental dynamics, and therefore proximity to T_g, was the primary "clock" dictating dynamics, similar behavior would be expected for both IL-5.1 and IL-15 as the measured values of $T_{g,L}$ are nearly the same. In fact, it might be expected that the divergence of a_T (and τ_o) for IL-5.1 would occur at a slightly lower temperature, given the slightly lower $T_{g,L}$ (0 versus 5 °C), the opposite of what is experimentally measured. Indeed, the measured relaxation times in IL-5.1 diverge at temperatures well above $T_{g,L}$. IL-5.1 is of higher molecular weight than IL-15 and is therefore at a higher segregation strength (χN) at a given temperature. Increasing segregation strength sharpens the core/corona interfaces in the particles, reduces the amount of free chains (i.e., chains not part of a particle), increases the barriers for single chain pullout from a particle,[178] and increases the barriers to various other inter- and intra-particle relaxation processes including particle fusion and evaporation.[179] These factors combine to cause a significant reduction in the rate of relaxation measured by DMS. The large differences in ordering times at equivalent temperatures (e.g., many weeks versus 1 day at 25 °C for IL-5.1 and IL-15 to grow the σ phase) seem to primarily result from segregation strength mediated reductions in dynamics.

The temperature dependence of the dynamics (i.e., a_T) of IL-5.1 and IL-15 become almost equivalent at higher temperatures where, although there are still differences in the segregation strength between IL-5.1 and IL-15 at a given temperature, segregation strength is much lower. This result suggests the influence of segregation strength on dynamics only becomes important at high segregation strength, with other factors acting as the "clock" dictating dynamics at low segregation strength. Although the temperature dependence is the same at low segregation strength for IL-15 and IL-5.1, the

higher molecular weight of IL-5.1 does lead to slightly longer absolute values of τ_os at equivalent temperatures, an effect which also contributes to the differences in measured ordering times between IL-5.1 and IL-15.
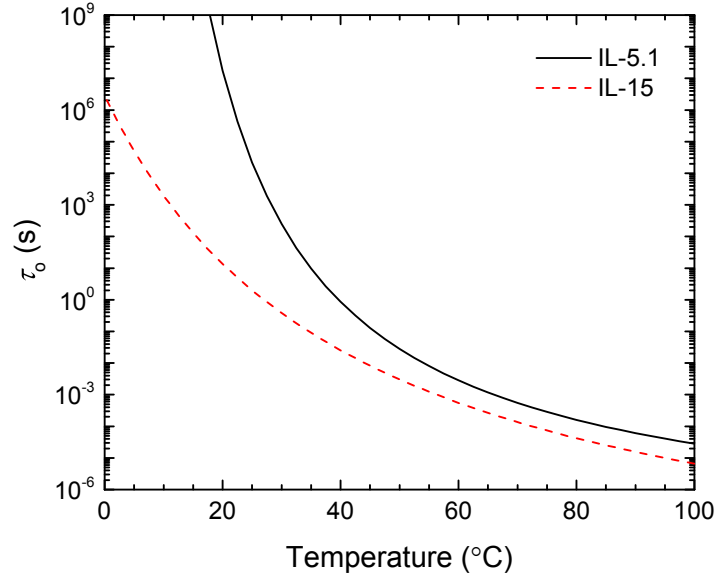
Figure 4.33 Comparison of calculated longest relaxation times τ_o as a function of temperature.

Curiously, while there is a small difference in N between IL-5.1 and IL-15, as a result of the difference in f_L between the samples, the molecular weight of the PLA block is almost exactly the same in IL-5.1 and IL-15 ($N_L \approx 13$ for both materials). This suggests the dynamics of the fluctuating disordered state that influences ordering kinetics in the bulk melt is dictated by χN_{total}, the segregation strength based on the total molecular weight, and not χN_{core}, the segregation strength based on the core block molecular weight ($\chi N_L \approx 5$ at 25 °C for both materials). This result suggests that single chain diffusion (i.e., extraction and exchange of single chains between particles) is not the rate-limiting step in the dynamics measured by DMS or the bulk ordering kinetics in the IL diblocks. This conclusion is based on the fact that chain diffusion in asymmetric block polymer melts containing micelle-like point particles[178] and chain exchange in block polymer micelles

in a selective solvent[180] are known to depend on χN_{core}. Cavicchi and Lodge[179] have hypothesized that the rate limiting step leading to long equilibration times following jumps down in temperature within the ordered BCC phase in higher molecular weight diblock copolymers is not chain diffusion, but rather barriers to particle evaporation or fusion. On cooling deep within the ordered phase, the particle aggregation number (i.e., the number of diblock chains per particle) increases slightly with decreasing temperature, leading to a reduction in the number density of particles. To reduce the number of particles, some particles must be consumed by evaporation or fusion, processes with increasing energy barriers with decreasing segregation strength. This leads to equilibration times much longer than what would be expected based on measured rates of chain diffusion.[179] Perhaps similar unfavorable particle-level processes are responsible for the measured dynamics of the disordered state after deep quenches to high segregation strength.

Upon cooling to higher segregation strengths, a variety of changes are thought to occur in the fluctuating disordered state in asymmetric diblock copolymers. Theory[126,127] and experiments[105,106,108] suggest that the number density of micelle-like point particles in the fluctuating disordered phase increases with decreasing temperatures, reducing the free unimer concentration. The particle aggregation number (i.e., the number of diblock chains per particle) increases slightly with decreasing temperature, as also occurs in the ordered BCC phase.[179] However, the number density of particles cannot increase beyond a certain limit with increasing segregation strength. At high segregation, the number density must saturate as the particles become tightly packed and the unimer concentration approaches zero. At this point, the increasing aggregation number actually results in a drive to *reduce* particle number density on cooling, a reversal of the trend expected at low particle densities. Such effects may explain the measured dynamics of the supercooled disordered phase, as well as the kinetics of ordering for the IL samples and formation of the curious LLP state upon deep quenches below T_{erg} in IL-5.1.

On cooling to higher and higher segregation strengths, the sharpening of the core/corona interface, increased concentration of particles, and reduction in unimer

concentration combine to lock out certain particle-level modes of relaxation, leading to the divergence of relaxation times measured by DMS in IL-5.1 well above $T_{g,L}$. While individual chain exchange remains facile, the "freezing" out of particle-level relaxation modes leads to a lack of available relaxation processes and the particles become "jammed" in analogy to granular materials, colloidal suspensions, foams, and emulsions[181,182] exhibiting essentially solid-like mechanical properties (i.e., frequency independent G') while maintaining a disordered arrangement of particles. The intriguing disordered, yet solid-like state that forms in IL-5.1 upon deep quenches below T_{erg} (designated LLP) may therefore be thought of a kinetically trapped, jammed solid.

At temperatures below the onset of this particle "jamming", the LLP state likely cannot quickly respond to changes in temperature due to the lack of available relaxation processes, resulting in the material falling out of even the local, metastable equilibrium of the supercooled disordered state. Below this temperature, which we have designated T_{erg}, the material ceases to behave like a supercooled liquid in the traditional sense, instead taking on the characteristics of a glass (i.e., a non-equilibrium and non-ergodic disordered solid).[183,184] This falling out of local equilibrium is realized experimentally in the thermorheological complexity of the DMS data collected in IL-5.1 at 40 and 35 °C. Below T_{erg}, the "ergodicity temperature", ergodicity is lost. Therefore, T_{erg} of the supercooled fluctuating disordered state is analogous to T_g in molecular glasses. Obviously, this structure is not a glass at the molecular level, as it exists at temperatures well above the glass transition of all constituent blocks, but rather at the level of the mesoscopic micelle-like point particles. The idea that a microphase separated structure in a block polymer melt can exhibit a dynamic transition much like a glass transition well above the block T_gs is not unprecedented. Zhang and Wang[185] considered this type of glass transition from a theoretical perspective in diblock polymer melts. Using an extension of the Fredrickson-Helfand theory,[17] they identified the appearance of a glass transition on cooling as evidenced by the emergence of broken ergodicity at high segregation strength.

The abrupt change in the mechanical properties of the disordered state is highlighted in Figure 4.21 and Figure 4.34. At 45 °C ($T > T_{erg}$), there is a short induction period between the time the sample requires to equilibrate at the target temperature (t_{eq}) and the onset of stiffening (estimated by extrapolating the steep portion of the G' growth curve to zero modulus), which occurs via the nucleation and growth of the BCC structure. For quenches below T_{erg}, the onset of stiffening occurs prior to t_{eq} (and in some cases even prior to t_{temp}, the time required to first reach the target temperature) and is not a result of the development of an ordered structure.
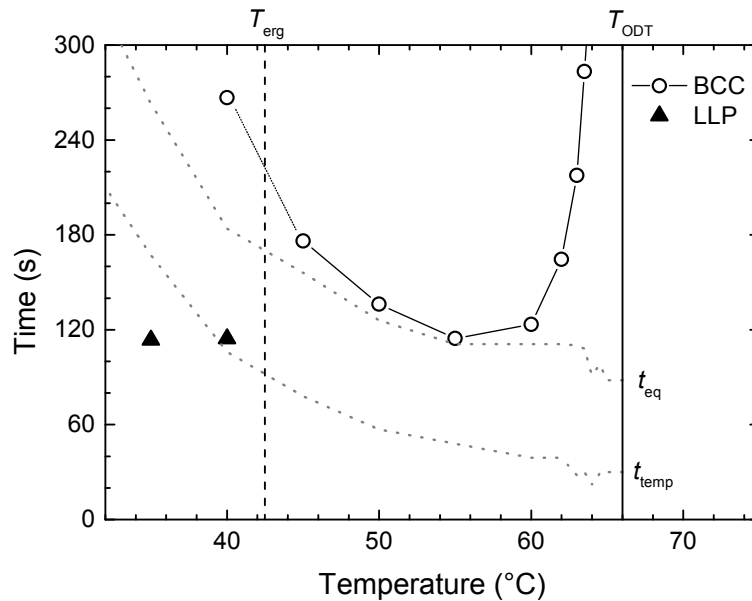
Figure 4.34 Time of the onset of stiffening in IL-5.1 as a function of temperature upon rapid quenches from above T_{ODT}. Dotted lined labeled t_{temp} and t_{eq} are the time the sample first reached the target temperature during cooling and the time required to equilibrate the sample at the target temperature, respectively, examples are shown in Figure 4.17.

Returning to the formation of the DQC in IL-5.1, it seems deep quenches into the soft glass LLP state ($T < T_{erg}$) are necessary for formation of the σ phase through the DQC intermediate. This can be rationalized by considering the kinetically trapped structure of the LLP state and the relaxation mechanisms still available to the LLP state

(i.e., chain exchange). Upon deep quenching, the dense but disordered liquid of particles must pack to fill space (likely with the drive toward sphericity operative). The most efficient packing of a small number of spheres is the tetrahedron. Therefore, polytetrahedral short-range order is a common feature of deeply quenched liquids (e.g., metallic glasses), leading to local coordination environments that resemble icosahedra and the various Frank polyhedra that make up Frank–Kasper phases.[151,152,186–188] It seems that this kinetically trapped glassy structure, in which chain exchange still occurs but other particle-level relaxation modes have been frozen out, prevents nucleation and growth of the BCC structure but enables formation of the DQC phase. Perhaps the local structure in the BCC phase is too dissimilar to the quenched glassy state to be accommodated via a chain exchange mechanism (i.e., one or more particle level relaxation modes such as translation, fusion, evaporation, etc. is required). Meanwhile, we posit that the DQC structure may form through only local rearrangements that can be affected through chain exchange since the DQC structure is composed of a quasiperiodic arrangement of Frank polyhedral, which can accommodate considerable heterogeneity owing to the lack of a periodic unit cell. The DQC represents a conveniently accessible metastable local minimum in the free energy landscape with high sphericity that can form from the quenched disordered state through minimal structural rearrangement. If enough time is provided, the equilibrium σ phase eventually nucleates and grows, either through chain exchange alone or in combination with particle-level relaxation processes that perhaps can occur over the much longer timescales.

The conceptual picture of DQC formation in IL-5.1 outlined above is superficially consistent with the growth mechanism of the DQC phase in simulations of the single component computational model of Keys and Glotzer.[177] They rationalize the formation of the DQC instead of the equilibrium σ phase from a supercooled liquid that exhibits polytetrahedral short-range order based on the idea that more of the locally stable polytetrahedral clusters present in the supercooled liquid can be incorporated into the DQC structure without rearrangement, thus offering the "path of least resistance" to quickly reach a metastable free energy minimum.

We note that at 40 °C, the material stiffens immediately, the condition used to identify the LLP state, but the structural relaxation time estimated by DMS is only about 1 second. It seems that at this temperature, the structure can still relax to a sufficient degree to nucleate and grow the BCC structure before forming the DQC. In addition, the relatively fast transformation to the σ phase upon quenching after growing a BCC structure compared to the formation of the σ phase through the DQC intermediate on direct quenching from the disordered phase can be rationalized. The BCC structure represents an unfavorable arrangement at low temperature leading to destabilization, while the inherent order of the BCC structure serves to select the σ phase as the favorable kinetic as well as thermodynamic structure.

4.5 Concluding Remarks

In this chapter, the discovery of a DQC phase in an undiluted IL diblock copolymer melt is detailed. The DQC was found to form from a quenched disordered state that behaves like a soft glass as a long-lived metastable intermediate on the way to the formation of the equilibrium σ phase. The discovery of the DQC (and soft "glassy" state) in IL diblock copolymers raises more questions than it answers, providing fertile ground for further exploration. It is of note that the formation of the DQC, like the σ phase, forms in the single component IL diblock copolymer spontaneously and without the need to artificially prepare particles of different sizes and shapes.

Both the DQC phase and the quenched glassy or jammed state (LLP) represent interesting discoveries in a simple diblock copolymer that warrant further exploration. Both states have analogues across hard and soft materials, the underlying details of the formation of which represent unanswered questions in condensed matter. [139,181–184,187] The appearance of the "soft glass" and DQC state in the simple and infinitely tunable block polymer model system allows contact with a broad range of interesting questions in fields of structure formation, jamming, and the glass transition. Interestingly, the block copolymer system has additional degrees of freedom not operative in other model systems (i.e., the ability to relax through chain exchange) that can also be turned on or off

though judicious design of the polymer system and experimental conditions (e.g., by quenching below the core block T_g).

Chapter 5:

Phase Behavior of Asymmetric Poly(1,4-isoprene-*b*-DL-lactide) Block Polymers

5.1   Introduction

The discovery of a long-lived metastable dodecagonal quasicrystal (DQC) phase in the IL-5.1 poly(1,4-isoprene-*b*-DL-lactide) (IL) diblock copolymer described in Chapter 4 was a fortuitous outcome of larger study designed to elucidate the phase behavior near the sample IL-15, the only diblock copolymer that had been previously reported to form the Frank–Kasper σ phase.[15,87,88] This larger study was intended to reproduce the σ phase in additional IL samples, reveal any additional ordered phases present, establish the range of parameters over which the σ phase and any other discovered phases form in IL diblock copolymers (i.e., the range of polylactide block volume fraction f_L and volumetric degree of polymerization N), and therefore establish the topology of the phase portrait in the vicinity of IL-15. To that end, a library of IL diblock copolymers was synthesized and their thermodynamics characterized with dynamic mechanical spectroscopy (DMS), differential scanning calorimetry (DSC), and

small-angle X-ray scattering (SAXS) experiments. The results of these experiments are presented in this chapter.

The thermodynamic characterization of the IL diblock copolymers near the σ phase presents considerable experimental challenges due to the slow kinetics of ordering of the σ phase and the presence of competing metastable ordered phases (e.g., body-centered cubic; BCC) often necessitating very long annealing times. The long annealing times required, coupled with the chemically labile nature of both the backbone double bond in the polyisoprene (PI) block and the backbone ester group in the polylactide (PLA) block, makes polymer degradation a significant experimental concern and limits the feasible annealing experiments to relatively low temperatures (e.g., room temperature). The sample IL-5.1 was one of the last polymers synthesized for the work discussed in this chapter and as a result, the detailed characterization of IL-5.1 presented in Chapter 4 benefitted from experience gained during the course of this study. The characterization of the IL samples discussed in this chapter is not as extensive as that of IL-5.1 in Chapter 4 or that reported for IL-15.[15,87,88] Consequently, the results presented in this chapter are not comprehensive and, in isolation, are not conclusive. However, taken together with Chapter 4 and the previous reports for IL-15, a reasonably complete picture of the phase portrait for asymmetric IL diblock copolymers emerges. A primary outcome of the effort described in this chapter was an evolution of the synthetic technique, sample preparation, processing, and experiment design that enabled the discoveries of Chapter 4.

5.2   Experimental Section

5.2.1   Materials and molecular characterizations

The compositionally asymmetric IL diblock copolymers discussed in this chapter were synthesized in the same manner as the materials described in Chapters 3 and 4. A detailed synthetic scheme for the preparation of IL diblock copolymers is described elsewhere[95] (see Chapter 2). Restating briefly, ω-hydroxyl poly(1,4-isoprene) (PI-OH) was prepared by anionic polymerization of isoprene in cyclohexane solvent at 40 °C and

used as a macroinitiator for the ring-opening polymerization of DL-lactide monomer with a triethyl aluminum catalyst. This synthetic procedure yields poly(1,4-isoprene-*b*-DL-lactide) (IL). The molecular weights and block compositions of IL polymers were determined by ^{1}H nuclear magnetic resonance (NMR) spectroscopy experiments (Varian VI-500), and dispersities ($Đ = M_w/M_n$) were determined by size exclusion chromatography (SEC) using either chloroform or tetrahydrofuran as the mobile phase. SEC analysis was also used to detect signs of polymer degradation (e.g., broadening of the molecular weight distribution) during or after selected long term annealing studies. All experiments presented here are believed to be free from the influence of polymer degradation, confirmed either through independent replication of results or by SEC analysis (i.e., no detectable broadening of the molecular weight distribution).

5.2.2   *Dynamic mechanical spectroscopy (DMS)*

The order–disorder transition temperature (T_{ODT}) of each IL diblock copolymer was measured using dynamic mechanical spectroscopy (DMS) experiments conducted with a Rheometrics ARES strain controlled mechanical spectrometer equipped with either the 25 or 8 mm stainless steel parallel plate sample geometry and a forced convection oven using a nitrogen purge gas for precise temperature control.[73] The IL diblock copolymers were loaded on the sample geometry, disordered by heating above T_{ODT}, cooled, and heated at a rate between 1 and 0.1 °C/min while measuring the isochronal ($\omega = 0.1$ rad/s) linear dynamic shear storage (G') and loss (G'') moduli. The T_{ODT}'s were obtained from the final heating step and were taken as the temperature at which G' shows a precipitous drop to a liquid-like response.

5.2.3   *Differential scanning calorimetry (DSC)*

A TA Instrument Q1000 differential scanning calorimeter (DSC) was used to measure the glass transition temperatures (T_g) of the PI and PLA blocks. Samples (~ 10 mg) were placed in hermetically sealed aluminum pans, heated to 200 °C, cooled to −100 °C, and heated to 200 °C again at a rate of 10 °C/min. T_gs were identified using the final heating results. In addition, it was possible to identify T_{ODT} of some samples using DSC.

The first-order order–disorder phase transition leads to a small peak in the heat flow curve, the onset of which is identified as T_{ODT} (see Chapter 3).

5.2.4 Small-angle X-ray scattering (SAXS)

The phase behavior of the IL diblock copolymers was investigated using small-angle X-ray scattering experiments (SAXS) conducted at DND-CAT (beamline 5-ID-D) at the Advanced Photon Source (Argonne National Laboratory; Argonne, IL). The sample-to-detector distances employed for the experiments ranged from 4 to 8.5 m while the X-ray wavelength, λ, was 0.729 Å. Scattering data were collected on a 2D CCD area detector (Mar or Rayonix) and azimuthally integrated to the one-dimensional form of intensity, I, versus scattering momentum transfer vector, $q = 4\pi\lambda^{-1}\sin(\theta/2)$, where θ is the scattering angle. The samples were placed in aluminum TA Instruments hermetic DSC pans (data presented for samples IL-61-18, IL-61-17B, IL-49-20) or Charles Supper Company 1.5 mm nominal diameter quartz capillary tubes (data presented for samples IL-15 (IL-47-22), IL-5.1 (IL-60-18), IL-60-23, IL-61-17A). Temperature was controlled during SAXS experiments using a Linkam DSC stage or a Linkam HFS91 hot stage modified to accept a capillary tube, both cooled with liquid nitrogen to enable fast (≥ 30 °C/min) temperature changes and sub-ambient operation.

5.3 Results and Analysis

To study the phase behavior of IL diblock copolymers near the reported σ phase in sample IL-15 (see Chapter 3) and establish the topology of the phase portrait, a total of 21 IL diblock copolymers were synthesized in addition to those already discussed in Chapter 3. A range of volume fractions of the PLA block in the diblocks, f_{L}, near the reported σ phase and BCC–HEX phase boundary was investigated ($0.12 \leq f_{\text{L}} \leq 0.30$). These additional 21 IL diblock copolymers were synthesized from four PI-OH precursors with volumetric degrees of polymerization N ($v_{\text{ref}} = 110$ Å^3; $T_{\text{ref}} = 25$ °C) ranging from 44 to 61, leading to five homologous series of IL diblock copolymers in which the molecular weight of the polyisoprene block is fixed and f_{L} (and consequently the total molecular weight) is varied, including the series to which the sample IL-15 belongs. The range of

total N and f_L values for the five homologous series of IL diblock copolymers is illustrated in Figure 5.1. The molecular and thermodynamic details of these five series of IL diblock copolymers are summarized in Table 5.1.

For convenience, in this chapter the IL diblock copolymers will be designated with descriptive names of the form IL-XX-YY where "XX" specifies N_I, the volumetric degree of polymerization of the isoprene block, and "YY" specifies the percentage of the total diblock molecular volume that is occupied by the PLA block (i.e, $f_L \times 100$). For example, the polymer designated elsewhere as IL-5.1 with a N_I of 60 and a f_L of 0.18 will be designated in this chapter as IL-60-18. These samples names, along with any other names used for a given polymer material in other works, are given in the first column of Table 5.1.

Order–disorder transition temperatures (T_{ODT}s) were determined from DMS or DSC experiments (see Chapter 3 and 4 for examples). Ordered phase symmetries were determined from SAXS experiments. In a typical SAXS experiment, the polymer sample would be equilibrated in the disordered (DIS) phase ($T > T_{ODT}$) before rapidly ($\geq$ 30 °C/min) cooling the sample to the desired temperature for annealing prior to SAXS data collection. Figure 5.2 provides examples of the characteristic SAXS patterns of the ordered phases identified in the IL samples.
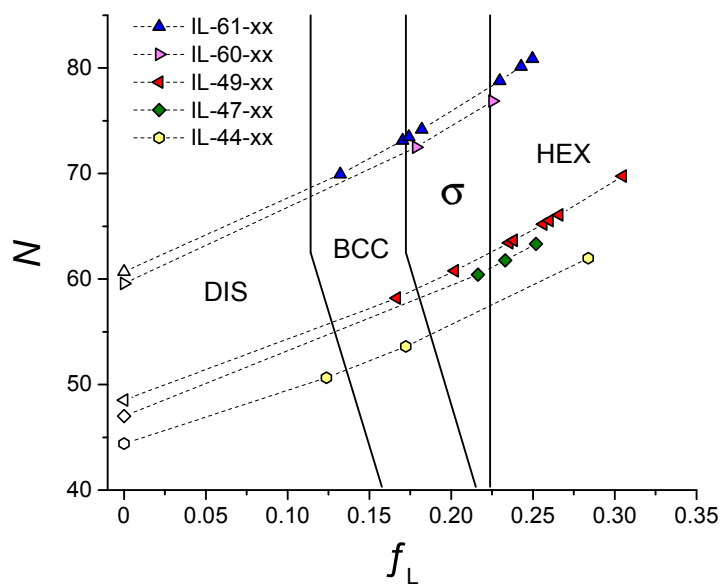
Figure 5.1 Illustration of the five homologous series of IL diblock copolymers investigated in this chapter. Phase boundaries are drawn as guides to the eye and reflect the ordered phases present at the lowest experimental temperature, generally room temperature.

Table 5.1 Summary of asymmetric ILdiblock copolymer characterization data

Polymer	$M_{\text{n,I}}{}^{\text{a}}$	$M_{\text{n,L}}{}^{\text{a}}$	$M_{\text{n}}{}^{\text{a}}$	N^{b}	$f_{\text{L}}{}^{\text{c}}$	$Đ^{\text{d}}$	$T_{\text{g,L}}{}^{\text{f}}$	$T_{\text{ODT}}{}^{\text{g}}$	Phases$^{\text{j}}$
I-44	2640	-	2640	44	-	1.06	-	-	-
IL-44-12	2640	520	3150	51	0.12	1.06	not obs	not obs	DIS
IL-44-17	2640	760	3400	54	0.17	1.07	not obs	6 °C	BCC
IL-44-28	2640	1450	4090	62	0.28	1.06	6 °C	114 °C$^{\text{h}}$	HEX
I-47 (I-4)$^{\text{i}}$	2810	-	2810	47	-	1.06$^{\text{e}}$	-	-	-
IL-47-22 (IL-15)$^{\text{i}}$	2810	1080	3890	60	0.22	1.12$^{\text{e}}$	5 °C	50 °C	BCC/σ
IL-47-23 (IL-12)$^{\text{i}}$	2810	1190	4000	62	0.23	1.11$^{\text{e}}$	5 °C	65 °C	HEX
IL-47-25 (IL-13)$^{\text{i}}$	2810	1320	4130	63	0.25	1.13$^{\text{e}}$	11 °C	105 °C	HEX
I-49	2880	-	2880	49	-	1.09$^{\text{e}}$	-	-	-
IL-49-17	2880	800	3680	58	0.17	1.06	not obs	30 °C	BCC
IL-49-20	2880	1010	3890	61	0.20	1.09$^{\text{e}}$	-4 °C	45 °C	multi
IL-49-24A	2880	1230	4110	63	0.24	1.10$^{\text{e}}$	-2 °C	60 °C	HEX
IL-49-24B	2880	1250	4130	64	0.24	1.10$^{\text{e}}$	-1 °C	75 °C	HEX
IL-49-24C	2880	1250	4130	64	0.24	1.10$^{\text{e}}$	-2 °C	56 °C	HEX
IL-49-26A	2880	1380	4260	65	0.26	1.10$^{\text{e}}$	2 °C	97 °C	HEX
IL-49-26B	2880	1410	4280	66	0.26	1.10$^{\text{e}}$	3 °C	98 °C	HEX
IL-49-27	2880	1450	4330	66	0.27	1.10$^{\text{e}}$	1 °C	101 °C	HEX
IL-49-30	2880	1750	4630	70	0.30	1.10$^{\text{e}}$	6 °C	118 °C	HEX
I-60	3560	-	3560	60	-	1.05	-	-	-
IL-60-18 (IL-5.1)	3560	1070	4600	72	0.18	1.06	0 °C	66 °C	BCC/DQC/σ
IL-60-23	3560	1430	4960	77	0.23	1.07	1 °C	99 °C$^{\text{f}}$	HEX
I-61	3600	-	3600	61	-	1.07$^{\text{e}}$	-	-	-
IL-61-13	3600	760	4370	70	0.13	1.05	not obs	35 °C$^{\text{h}}$	BCC
IL-61-17A	3600	1030	4630	73	0.17(0)	1.05	1 °C	70 °C	BCC
IL-61-17B	3600	1050	4660	73	0.17(4)	1.05	4 °C	76 °C	multi
IL-61-18	3600	1110	4720	74	0.18	1.05	4 °C	78 °C	multi
IL-61-23	3600	1490	5100	79	0.23	1.06	5 °C	131 °C	HEX
IL-61-24	3600	1600	5210	80	0.24	1.06	5 °C	120 °C	HEX
IL-61-25	3600	1670	5270	81	0.25	1.05	13 °C	148 °C	HEX

(a) Number-average molecular weight in g/mol based on ^{1}H NMR. (b) Volumetric degree of polymerization based on reported[30,104] homopolymer densities at 25 °C (0.9 and 1.25 g/cm^3 for I and L, respectively) and a reference volume of 110 Å^3 (c) Volume fraction of L block based on reported homopolymer densities at 25 °C and ^{1}H NMR. (d) From RI-SEC with a tetrahydrofuran mobile phase, unless specified otherwise. (e) From RI-SEC with a chloroform mobile phase. (f) From DSC. (g) From DMS, unless specified otherwise. (h) Estimated from SAXS. (i) Synthesized and characterized by Sangwoo Lee. (j) From SAXS: DIS (disordered), BCC (body-center cubic arrangement of nearly spherical point particles), HEX (hexagonally packed cylinders), σ (Frank–Kasper σ phase structure of nearly spherical point particles), DQC (dodecagonal quasicrystalline arrangement of nearly spherical point particles), multi (multiple phases observed including one of the complex arrangements of nearly spherical point particles such as σ or DQC).
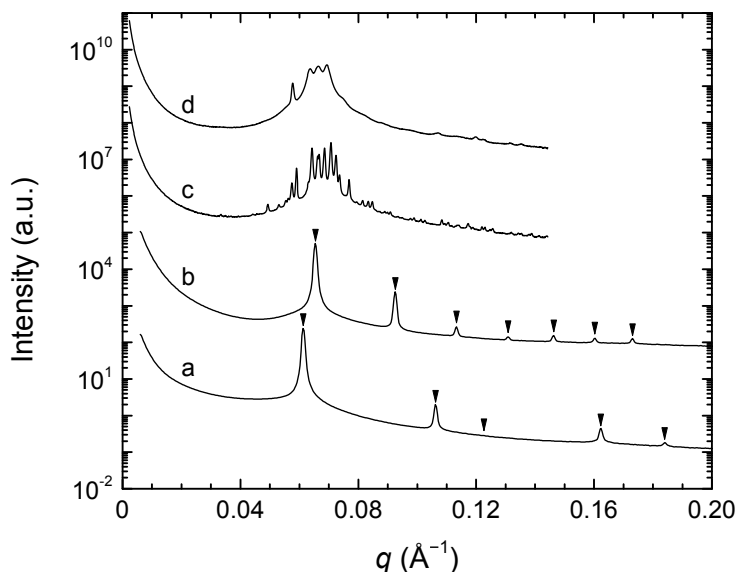
Figure 5.2 Representative SAXS patterns of the ordered phases. (a) IL-61-25 after 2 minutes of annealing at 100 °C consistent with the HEX phase (allowed HEX Bragg peaks, $(q/q^*)^2 = 1, 3, 4, 7, 9,\ldots$, are marked with arrows). (b) IL-61-17A after 4 days of annealing at 25 °C consistent with the BCC phase (allowed BCC Bragg peaks, $(q/q^*)^2 = 1, 2, 3, 4, 5, 6, 7,\ldots$, are marked with arrows). (c) IL-5.1 (IL-60-18) after 260 minutes of annealing at 40 °C consistent with the Frank–Kasper σ phase. (d) IL-5.1 (IL-60-18) after 49 days of annealing at 25 °C consistent with DQC symmetry. Curves have been shifted vertically for clarity.

Using the temperature dependence of the segment–segment interaction parameter χ for the IL system determined in Chapter 3 ($\chi_{IL} = 230/T - 0.38$; $v_{ref} = 110$ Å^3) and assuming no composition dependence, the phase behavior of all the asymmetric IL diblock copolymers of Table 5.1 is summarized on the phase portrait shown in Figure 5.3. The detailed phase behavior of IL-5.1 (IL-60-18) and IL-15 (IL-47-22) has been reported in Chapters 3 and 4 and by Lee and co-workers.[15,87,88] In the remainder of this section, experiments probing the phase behavior of the additional IL polymers that span and bound the region of the phase diagram within which the σ phase appears to be the stable equilibrium phase are detailed. The experiments of these additional samples within the region of stability of the σ phase are not nearly as exhaustive or definitive as those of

IL-5.1 (IL-60-18) and IL-15 (IL-47-22). In many cases, thermodynamic equilibrium is not reached, with only the nucleation of a complex ordered phase (i.e., the σ or DQC phase) captured during the timescale of the experiments. In these cases, the SAXS patterns document coexistence of the complex phase with the metastable BCC phase or the disordered liquid-like packing state (LLP). Experiments in which this coexistence of multiple phases was measured are labeled "multiple" in Figure 5.3.
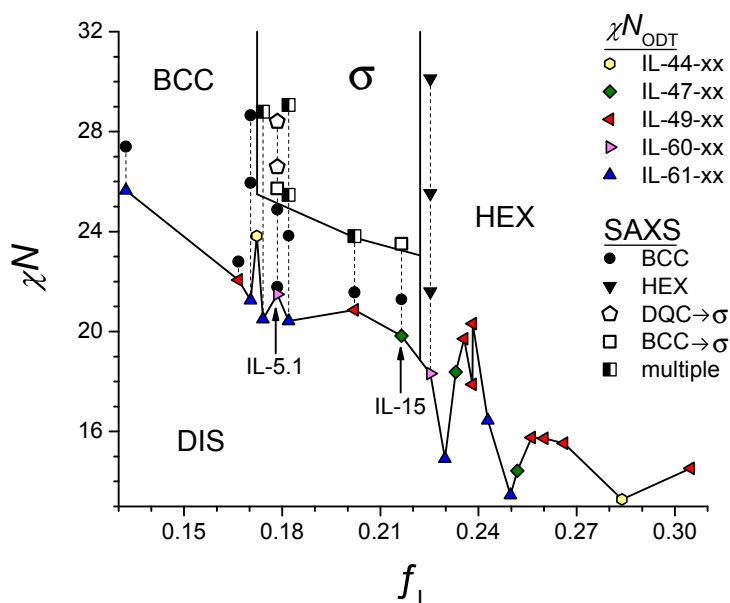
Figure 5.3 Phase portrait summarizing the phase behavior of asymmetric IL diblock copolymers. The order–disorder phase boundary is represented by the colored data markers (the shape and color of the marker indicate N_I of the polymer) connected with solid black lines to guide the eye. Points at which SAXS experiments were conducted are marked with the black and white data markers (shading and shape indicate order phase(s) identified; points for HEX samples not directly adjacent to BCC/σ region omitted). Order–order phase boundaries are draw as guides to the eye (σ–BCC boundary for IL-15 drawn to reflect T_{OOT} determined by DMS[88]).

5.3.1   Experiments with IL-61-18

The sample IL-61-18 has a slightly higher polyisoprene block molecular weight and polylactide composition than IL-5.1 (IL-60-18) and consequently exhibits a higher T_{ODT} of 78 °C but similar phase behavior. At temperatures just below T_{ODT}, IL-61-18

forms a well-ordered BCC phase in a matter of minutes, as shown in Figure 5.4 for ordering at 70 and 50 °C. If the sample is instead quenched from the DIS phase to room temperature (25 °C), ordering is much more sluggish and it appears that the σ phase is the preferred equilibrium ordered phase, though the data are far from conclusive.
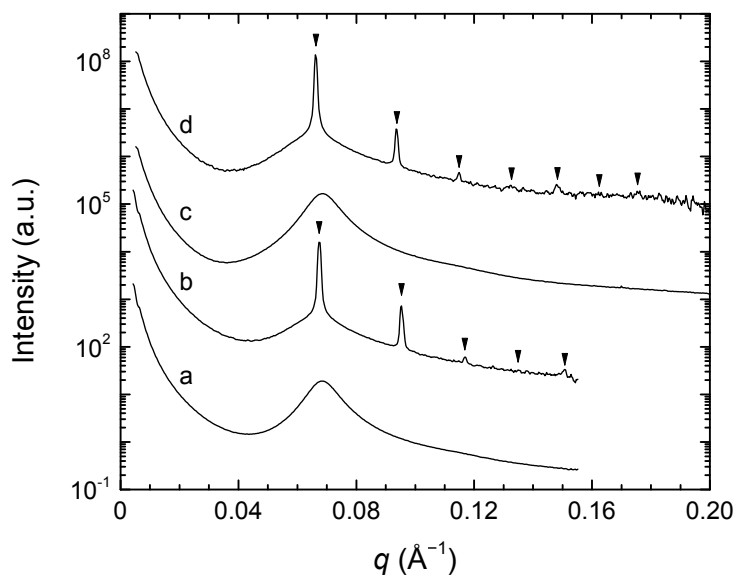
Figure 5.4 Ordering of IL-61-18 in the region of stability of the BCC phase. SAXS patterns of IL-61-18 (a) in the DIS phase at 90 °C and (b) after rapidly cooling to 70 °C and annealing for 3 minutes forming a BCC phase (allowed BCC Bragg peaks, $(q/q^*)^2 = 1, 2, 3, 4, 5,\ldots$, are marked with arrows) and a separate specimen (c) in the DIS phase at 85 °C and (d) after rapidly cooling to 50 °C and annealing for 33 minutes forming a BCC phase (allowed BCC Bragg peaks, $(q/q^*)^2 = 1, 2, 3, 4, 5, 6, 7,\ldots$, are marked with arrows). Samples were contained in DSC pans.

In Figure 5.5 the results of long time annealing experiments at room temperature (nominally taken as 25 °C) are summarized. In these experiments, IL-61-18 samples were prepared in hermetically sealed DSC pans and disordered above T_{ODT} by annealing the DSC pans for 3 minutes in the wells of an aluminum heating block maintained at a temperature well above T_{ODT} of the polymer (approximately 120 °C) using a temperature controlled hot plate. After disordering, the samples were quenched to room temperature

by placing them on a second high mass aluminum block at room temperature (estimated to cool to room temperature in less than 1 minute). The samples were then annealed at room temperature prior to SAXS data collection. To access different annealing times, separate samples were prepared at different times before scheduled synchrotron X-ray beamtime.
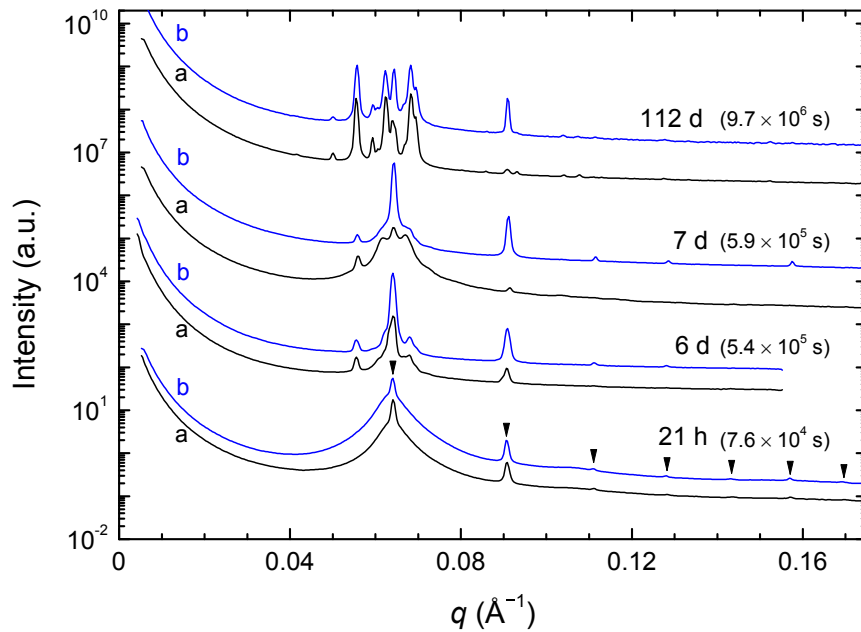
Figure 5.5 Ordering of IL-61-18 at 25 °C. SAXS patterns collected after annealing at room temperature (25 °C) for the times specified following a rapid quench from the DIS phase ($T > T_{ODT}$). For each time point, two different samples in separate DSC pans were prepared and are shown as the curves labeled a (black) and b (blue) at each time point. The data for the different time points come from separately prepared samples with the exception of the 112 day time point, which utilized the same physical samples as the 6 day time point reanalyzed after further annealing. The locations of the allowed reflections for the BCC symmetry $(q/q^*)^2 = 1, 2, 3, 4, 5, 6, 7$ are indicated with arrows.

From the SAXS data in Figure 5.5, at short annealing times (21 hours) the quenched disordered state referred to previously (Chapter 4) as liquid-like packing (LLP) is documented with evidence of nucleation of a BCC structure. At intermediate times (6

to 7 days), the appearance of satellite peaks in the low q region near q^* of the DIS and BCC phases indicate the nucleation of grains of what appears to be the σ and DQC phases. At long times (112 days), what is most likely the σ phase begins to consume the BCC phase, though the resulting 1D SAXS patterns obtained at long times is not the same as the characteristic pattern previously observed for the σ phase, having very different relative peak intensities.

The SAXS pattern of the IL-61-18 samples annealed for 112 days at 25 °C is analyzed in Figure 5.6 and Figure 5.7 and compared to typical SAXS patterns of the σ and DQC phases from samples IL-15 (IL-47-22) and IL-5.1 (IL-60-18), respectively. While the relative intensities differ from those typically observed, all peaks observed in IL-61-18, with the exception of peaks from the remaining BCC phase, can be indexed to the allowed reflections of the σ phase. Note that for clarity only allowed peaks observed in IL-15 (IL-47-22) are explicitly shown in Figure 5.6 and only allowed σ reflections of the form (*hhl*) are shown in Figure 5.7 (see below). The three strong Bragg peaks observed in the SAXS patterns of IL-61-18 are reminiscent of the characteristic SAXS pattern of the cubic A15 phase (space group 223, $Pm\overline{3}n$), a Frank–Kasper phase that has been observed in soft material systems that also form the σ phase.[141,156,157] In addition to being allowed reflections of the σ phase, the three strong peaks in IL-61-18 can be indexed with the allowed reflections of the cubic A15 phase. However, the peaks observed that are consistent with the A15 structure are also allowed reflections of the σ phase and peaks that generally appear in the SAXS patterns of the A15 structure are absent, as shown in Figure 5.7 for the full experimental q range. Therefore, we favor the conclusion that the structure present in IL-61-18 is a mixture of a minority (by volume) BCC being replaced by the growing equilibrium σ phase, much like what was demonstrated in IL-5.1 (IL-60-18) (the causes of the different relative peak intensities measured in IL-61-18 are discussed below). However, the data do not definitively rule out the intriguing possibility that the A15 phase or another phase with as yet unidentified symmetry may be present in these samples.
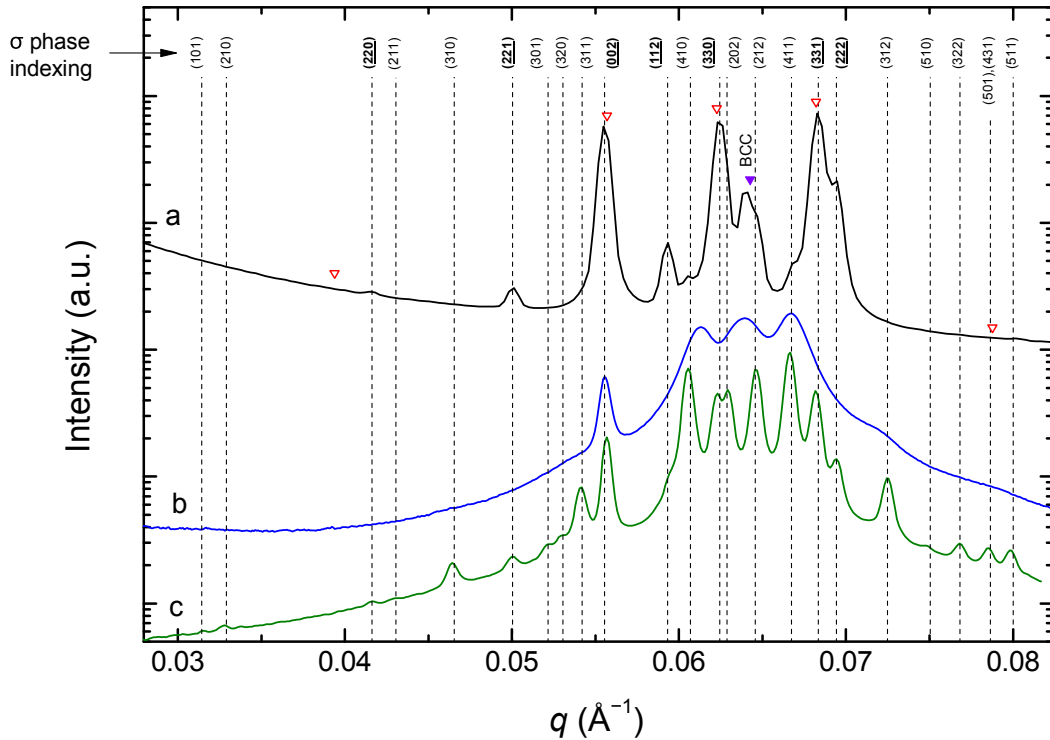
Figure 5.6 Indexing of the IL-61-18 SAXS pattern collected after 112 days of annealing at room temperature (25 °C). (a) IL-61-18 SAXS pattern collected after 112 days of annealing at 25 °C (sample a in Figure 5.5). (b) IL-5.1 (IL-60-18) SAXS pattern collected after 49 days of annealing at 25 °C (q axis rescaled such that the (00002) peak is at the same q value as the (002) peak in curve a). (c) IL-15 (IL-47-22) SAXS pattern collected after 26 days of annealing at 25 °C (q axis rescaled such that the (002) peak is at the same q value as the (002) peak in curve a). Dashed vertical lines show the q values of allowed Bragg reflections for the σ phase with lattice parameters a and c of 427 and 226 Å (for clarity only allowed reflections experimentally observed in IL-15 are shown). $q^* = 0.0641$ Å^{-1} for the coexisting BCC phase is indicated with the labeled filled purple arrow. Unlabeled open red arrows indicate the first 5 allowed reflections of the cubic A15 phase, (110) (200) (210) (211) and (220), with a lattice parameter of 226 Å. Sample (a) was contained in a DSC pan while samples (b) and (c) were contained in capillaries.
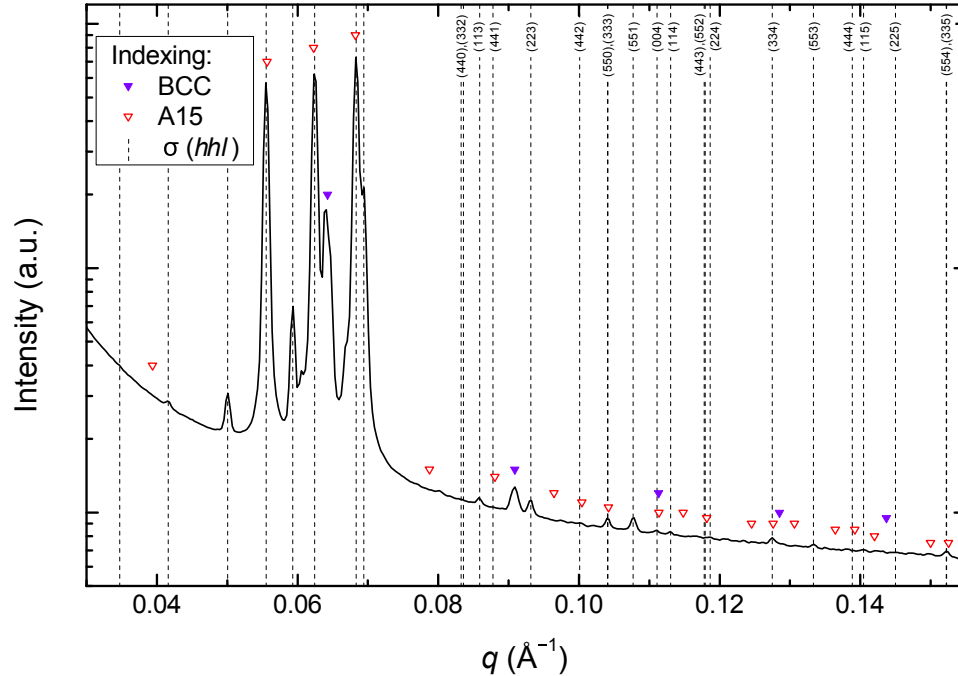
Figure 5.7 Indexing of the IL-61-18 SAXS pattern collected after 112 days of annealing at room temperature (25 °C) over an expanded *q* range. Dashed lines indicate the allowed σ phase reflections of the form (*hhl*). Allowed reflections of the BCC phase are indicated with the filled purple arrows. Open red arrows indicate the allowed reflections of the cubic A15 phase. The sample was contained in a DSC pan.

Although the peak positions for all peaks observed in IL-61-18 after 112 days of annealing are consistent with the σ phase (or the BCC phase that the σ phase is consuming), the relative peak intensities are much different than those typically observed for the σ phase. Curves (b) and (c) in Figure 5.6 are derived from 2D SAXS patterns that exhibit rings of uniform intensity associated with a fine polycrystalline grain structure or a powder, while the 2D SAXS pattern shown in Figure 5.8 associated with curve (a), the IL-61-18 sample annealed for 112 days at 25 °C, exhibits discrete diffraction spots. This indicates that within the illuminated scattering volume of the IL-61-18 sample, there are a relatively small number of large grains of the ordered phases. This leads to imperfect powder averaging upon data reduction to the 1D SAXS patterns (i.e., sufficient numbers

of grains with all possible orientations are not in the illuminated scattering volume). As a consequence, relative peak intensities in the 1D SAXS patterns, which reflect the sum of scattering from all grains intercepted by the X-ray beam, may vary between specimens and as the X-ray beam is directed at different points within a specimen. Imperfect powder averaging can largely account for the variations in the relative diffraction peak intensities in IL-61-18 documented in Figure 5.5. In addition, the cooling method used to quench the IL-61-18 samples, placing the DSC pans on a room temperature aluminum block used as a heat sink, is not particularly well controlled. This perhaps leads to differences in the effective cooling rate between samples, and thus the time at which a given sample has to nucleate and grow BCC during the cooling process. This may lead to different proportions of BCC and σ in the structures observed in SAXS experiments.

Non-idealities in SAXS sample preparations contributed to the documented imperfect powder averaging. The IL-61-18 samples had small effective scattering volumes. When preparing SAXS samples, it is impossible to completely fill the DSC pan. If air is present, when the low molar mass IL polymers are heated above T_{ODT} the low viscosity polymer melt wicks to cover exposed internal aluminum surfaces, as illustrated in Figure 5.9. This leads to coalescence of an air bubble that usually ends up in the center of the DSC pan, the portion of the pan at which the X-ray beam can be aimed. This results in a reduced effective scattering volume occupied by polymer. This effect can be significant if a large portion of the internal volume of the DSC pan is filled with air, leading to only thin layers of polymer material on the internal surfaces of the DSC pan where the X-ray beam can be aimed. The effective scattering volume can be qualitatively evaluated by cutting open the DSC pans after SAXS experiments (e.g., when conducting SEC experiments to rule out degradation of the polymers). Indeed, large bubbles were found when inspecting the DSC pans from the IL-61-18 samples. In addition, the low scattering volume is evident in the SAXS data, resulting in the low intensities of the Bragg peaks relative to the parasitic background scattering near the beamstop. A small effective scattering volume reduces the number of grains illuminated by the X-ray beam leading to imperfect powder averaging.
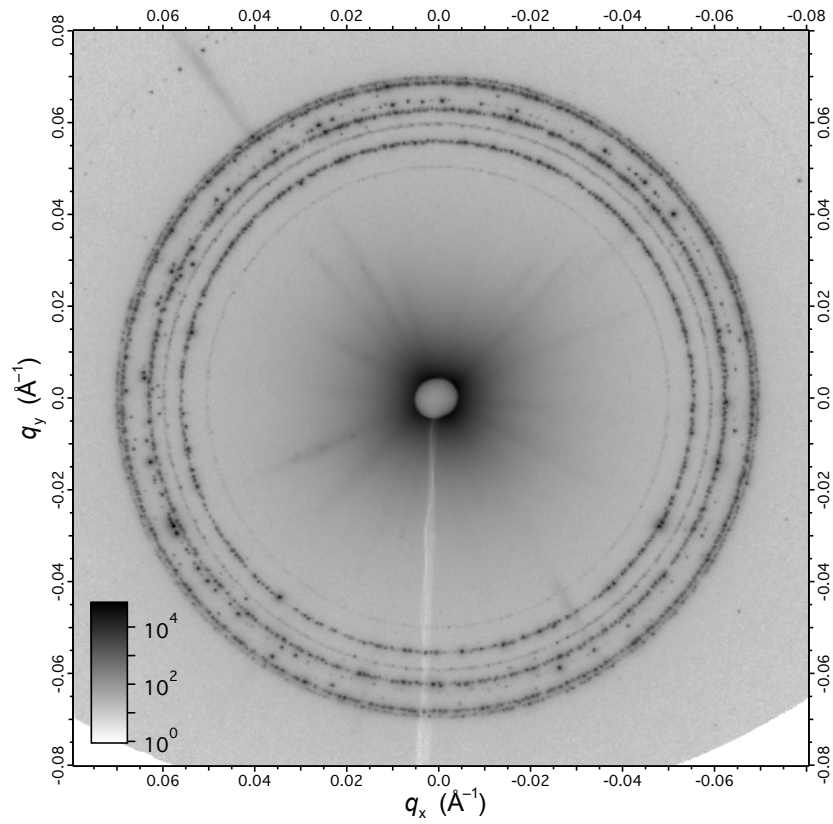
Figure 5.8 Two-dimensional SAXS pattern of the IL-61-18 sample annealed for 112 days at 25 °C. The sample was contained in a DSC pan.
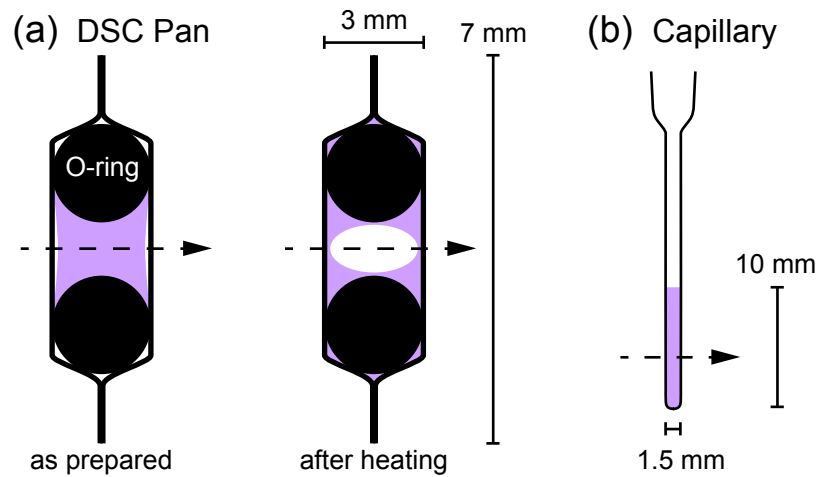
Figure 5.9 Cross section illustrations of DSC and capillary SAXS samples. (a) SAXS sample encapsulated in a DSC pan before and after the first heating, illustrating the reduction in effective scattering volume that often results. (b) SAXS samples prepared in capillaries, which can be visually inspected to ensure the X-ray beam is directed at sufficient polymer material. The dotted arrows indicate the direction of the X-ray beam. Not drawn to scale.

The relative peak intensities measured after long annealing times do not vary randomly between samples as would be expected for imperfect powder averaging if the orientation of the grains were randomly distributed. An analysis of the peak intensities measured in the IL-61-18 sample annealed for 112 days at 25 °C reveals a possible preferred orientation of the grains present, which could account for the similarity of the relative intensities between samples. In Figure 5.6, the labels of the Miller indices of the planes corresponding to peaks that are measured with enhanced or equivalent intensity relative to those measured in IL-15[87] (IL-47-22) and IL-5.1 are bolded and underlined in the upper portion of the figure while the indices of planes not observed or measured with reduced relative intensity are shown in normal type. All planes with equivalent or enhanced intensity are planes of the form (hhl), for example (002) and (330), while none of the absent or reduced intensity planes are of that form. This trend continues over the entire experimental q range, as shown in Figure 5.7. All distinguishable peaks are σ phase (hhl) reflections or BCC peaks. This suggests that grains oriented in the $[1\bar{1}0]$ or equivalent zone axes are overrepresented in the experimental SAXS patterns. The source

of the symmetry breaking that could lead to this preferred direction may be the presence of the aluminum–polymer or air–polymer interfaces, enhanced in importance due the polymer samples wicking into a thin film on the internal surfaces of the DSC pans. These surfaces could provide a different nucleation environment for the σ phase with a preferred orientation of the nucleated grains relative to the surface. In the dendrimer, which on slow cooling formed the single domain DQC that facilitated identification of the 12-fold rotational symmetry, the direction of 12-fold axis (analogous to the [001] direction of the c axis in the σ phase unit cell) was parallel to the capillary used to contain it, an thus parallel to the glass–dendrimer interface.[143][*] If the grains of IL-61-18 indeed have a preferred $[1\bar{1}0]$ orientation, the [001] direction would lie in the plane of the aluminum–polymer interface. This is consistent with a nucleation mechanism that favors the c axis (and equivalent direction in the DQC) pointing along interfaces present in nucleation limited growth conditions. An alternative hypothesis is that the preferred grain orientation is perhaps a residual effect resulting from the polymer flow that occurs during wicking upon initial heating above T_{ODT}, though it is not clear how any orienting effect of the flow would be subsequently translated to the σ phase after cooling.

In Figure 5.10 SAXS data is presented from an experiment in which the IL-61-18 sample annealed for 7 days at room temperature forming a mixture of BCC and DQC was heated through T_{ODT}. Upon heating to 55 °C, the DQC present in the sample transforms into BCC, indicating that the order–order transition (OOT) temperature T_{OOT} lies somewhere between 45 and 55 °C. Given that a BCC phase forms and appears stable at 50 °C (Figure 5.4), the T_{OOT} in IL-61-18 probably actually lies between 45 and 50 °C, though the annealing time at 50 °C was limited to 33 minutes.

---

[*] Unfortunately, the orientation of monodomains relative to the capillary sample containers were not reported for analogous experiments in dendrimers that form the σ phase,[118] preventing a more direct comparison.
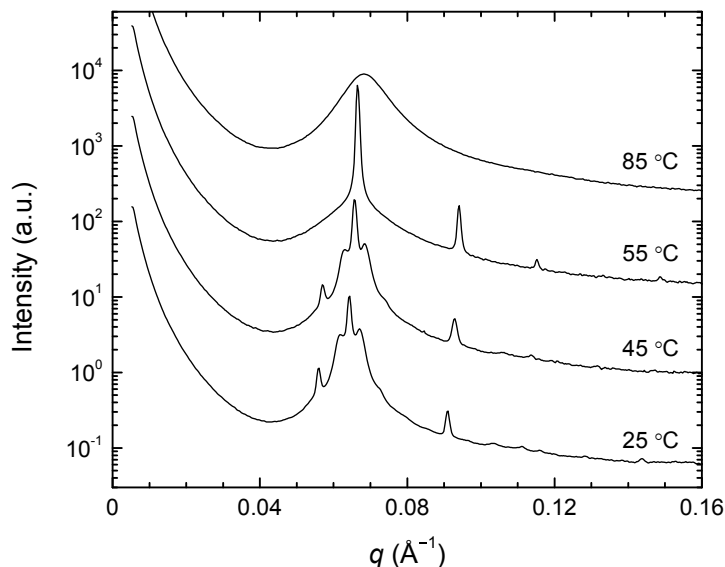
Figure 5.10 SAXS patterns upon heating of the IL-61-18 sample annealed for 7 days at room temperature. Sample a from the 7 day time point in Figure 5.5 was heated and annealed for approximately 2 minutes at the temperatures indicated before SAXS data collection. Data were collected in sequence from bottom to top with rapid (≥ 30 °C/min) heating between annealing temperatures. The sample was contained in a DSC pan.

Taking as a whole, the SAXS data are consistent with the σ phase forming as the stable ordered phase at low temperature in IL-61-18, analogous to what was determined in Chapter 4 for the closely related material IL-5.1 (IL-60-18). The location of the σ/DQC–BCC OOT in IL-61-18 (Figure 5.10) is consistent with the trend of OOTs previously documented in IL-5.1 (IL-60-18) and IL-15 (IL-47-22), as can be seen on the phase portrait of Figure 5.3. Further implications of these data, including why characterizing IL-61-18 proved more challenging than IL-5.1 (IL-60-18) is taken up again in the discussion section.

5.3.2 Experiments with IL-49-20

The sample IL-49-20 has a slightly higher polyisoprene block molecular weight and slightly lower polylactide composition than IL-15 (IL-47-22). IL-49-20 exhibits a T_{ODT} of 45 °C and similar phase behavior to IL-15 (IL-47-22) with BCC forming at temperatures just below T_{ODT} and the σ phase forming at lower temperatures.

Unfortunately, the σ–BCC T_{OOT} is very close to room temperature in IL-49-20 and it seems that normal variations in room temperature are sufficient to transverse T_{OOT} precluding long term annealing to form a well-ordered σ phase in this sample.

Figure 5.11 shows SAXS patterns collected after 19 days of annealing at room temperature (25 °C) following an identical disordering and quenching protocol used for IL-61-18 samples described in section 5.3.1. In the SAXS pattern, a BCC phase is observed coexisting with a nucleating σ phase. The satellite peaks observed near the BCC $q*$ can be indexed to the allowed reflections of the σ phase (see inset of Figure 5.11).
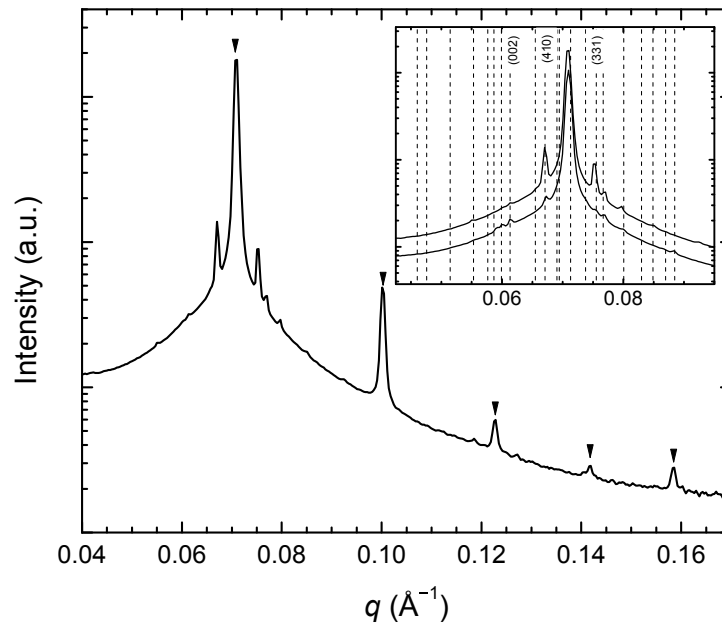
Figure 5.11 SAXS pattern from IL-49-20 annealed at room temperature (25 °C) for 19 days following a rapid quench from above T_{ODT}. Allowed BCC Bragg peaks, $(q/q*)^2 = 1$, 2, 3, 4, 5,…, are marked with arrows ($q* = 0.0707$ Å^{-1}). In inset shows the non-BCC peaks in the SAXS pattern shown in the main panel along with a SAXS pattern collected from the same sample after 18 days of annealing at 25 °C indexed to the allowed reflections of the σ phase with lattice parameters a and c of 386 and 205 Å, respectively (dashed vertical lines). For clarity, only the allowed planes actually observed in IL-15 are shown and only select planes are labeled. The samples were contained in DSC pans.

Based on the ordering kinetics of the closely related IL-15 (IL-47-22) material, 19 days would be expected to be sufficient to form a well ordered σ phase if it was the stable

ordered phase at 25 °C. Instead, in the IL-49-20 sample there is only evidence of the early stages of σ phase nucleation. The reason for this apparent contradiction is revealed by examining the evolution of the SAXS patterns over the next few days of annealing and considering the probable σ–BCC T_{OOT}. The lower curve in the inset of Figure 5.11 shows the same sample from the main panel measured after 1 further day of annealing at room temperature (19 total days), in which the intensities of the σ phase peaks are reduced. Presumably, a different location in the sample was exposed to the X-ray beam, perhaps illuminating different nucleating grains of the σ phase resulting in some variability in relative peak intensities from position to position. However, given the σ–BCC order–order phase boundary interpolated from the IL-61-18, IL-5.1 (IL-60-18), and IL-15 (IL-47-22) samples, room temperature is very close to the order–order phase boundary expected at the f_L of 0.20 in the IL-49-20 sample. Therefore, the variability of intensity of the σ phase peaks may be a result of inadvertently traversing the order–order phase boundary and melting and re-nucleating the σ phase as room temperature varies slightly from day to day. Indeed, Figure 5.12a shows 2D SAXS data from the same sample as Figure 5.11 after 1 additional day of annealing at room temperature (20 total days). In the 2D data, there is evidence of a very small amount of σ phase nucleation (discrete diffraction spots of the σ phase peaks, selected spots indicated by arrows), which was not distinguishable from the background in the reduced 1D data. Upon heating to 40 °C, the σ phase diffraction spots disappear (Figure 5.12b).

Based on the day-to-day variability of the σ phase peak intensities, the fast melting of the σ phase peaks on heating, and the close proximity of room temperature to the interpolated σ–BCC order–order phase boundary, we conclude that the sample has inadvertently traversed the order–order phase boundary causing melting and nucleating of the σ phase as room temperature varies slightly from day-to-day (or by handling the sample in warm hands). Therefore, the true annealing times in the region of stability of the σ phase during the SAXS experiments of Figure 5.11 and Figure 5.12 are likely much less than 18, 19, and 20 days quoted (and perhaps considerably less than 1 day). Nevertheless, the SAXS results still suggest that the σ phase forms at low temperatures.

The results for IL-49-20 are consistent with the results of the samples IL-61-18, IL-5.1 (IL-60-18), and IL-15 (IL-47-22) with regard to the stable phases, measured location of the ODT, and inferred location of the σ–BCC OOT.
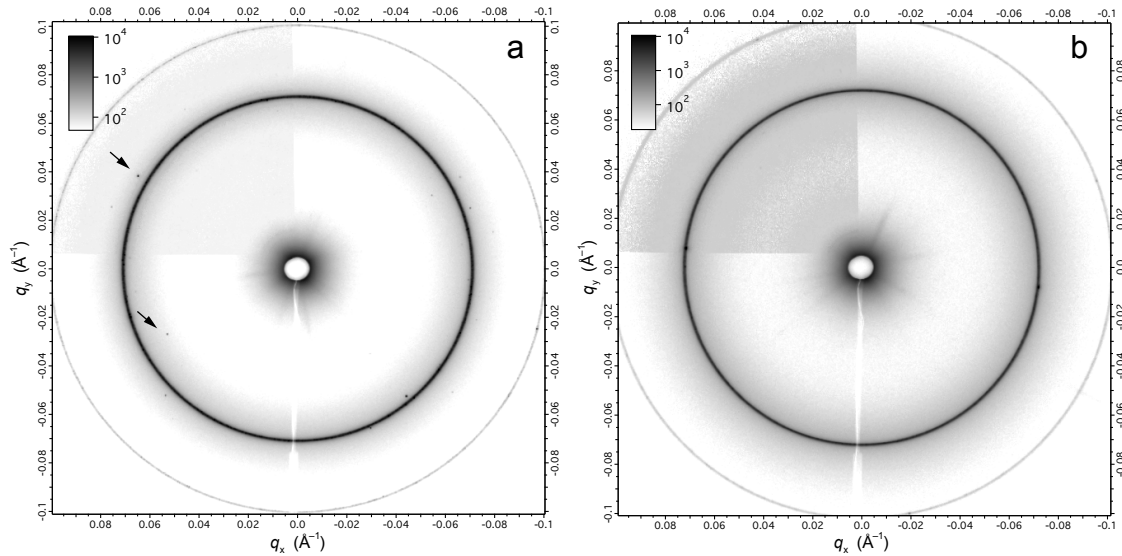
Figure 5.12 Two-dimensional SAXS patterns from the IL-49-20 sample upon heating. IL-49-20 (a) annealed for 20 days at room temperature (25 °C) after a rapid quench from the above T_{ODT} and (b) after heating the sample of (a) from 25 °C to 40 °C and annealing for 8 minutes. Diffractions spots from grains of the σ phase in (a) are visible (selected spots identified with arrows) but disappear in (b) on heating. The different appearance of the upper left quadrant of the SAXS patterns is a result of problems with that region of the detector and not from the sample (data from upper left quadrant was not used during reduction to the 1D SAXS patterns). The sample was contained in a DSC pan.

5.3.3 *Experiments with IL-61-17B*

IL-61-17B is the IL sample with the smallest f_L to show evidence of forming the σ phase at low temperature. IL-61-17B has a slightly smaller polylactide content (and thus total molecular weight) than IL-61-18 and therefore exhibits a T_{ODT} of 76 °C, slightly lower than that of IL-61-18. Annealing for short time just below T_{ODT} leads to formation of a BCC structure. Annealing after quenching from above T_{ODT} to room temperature, as described for sample IL-61-18 in section 5.3.1, leads to nucleation and

growth of the σ phase, as shown in Figure 5.13. After annealing for 6 days at room temperature, coexistence of a BCC structure with the σ phase is evident in the measured SAXS pattern. The satellite peaks near q^* of the BCC structure can be indexed to the allowed reflections of the σ phase, as shown in the inset of Figure 5.13. The extent of nucleation and growth of the σ phase after 6 days in IL-61-17B (Figure 5.13) is similar to that measured in IL-61-18 (Figure 5.5).
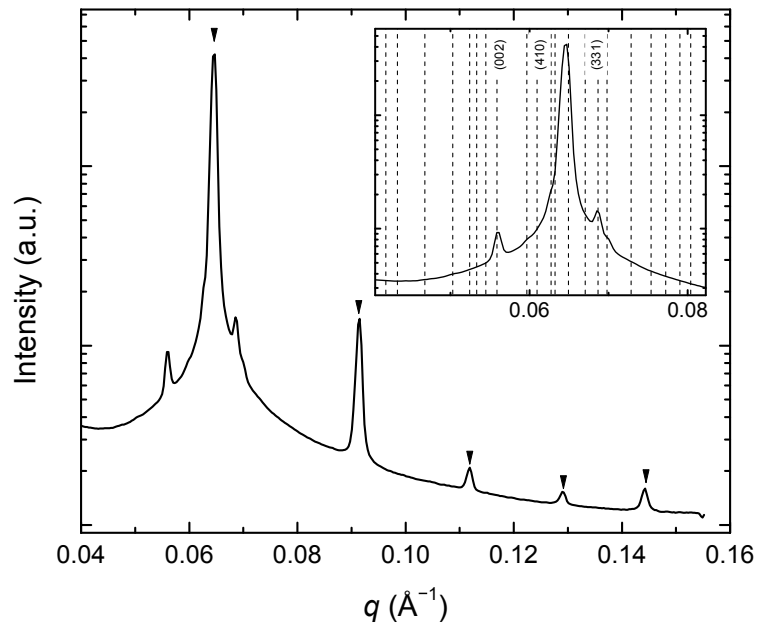
Figure 5.13 SAXS pattern from IL-61-17B annealed at room temperature (25 °C) for 6 days following a rapid quench from above T_{ODT}.
Allowed BCC Bragg peaks, $(q/q^*)^2 = 1, 2, 3, 4, 5,...$, are marked with arrows ($q^* = 0.0646$ Å^{-1}). In inset shows indexing of non-BCC peaks in the SAXS pattern shown in the main panel to the allowed reflections of the σ phase with lattice parameters a and c of 425 and 225 Å, respectively (dashed vertical lines). For clarity, only the allowed planes actually observed in IL-15 are shown and only select planes are labeled. The sample was contained in a DSC pan.

5.3.4   *Experiments with IL-61-17A*

IL-61-17A has a polylactide block molecular weight measured to be just slightly less than IL-61-17B, leading to a nearly identical, but slightly smaller f_L and a T_{ODT} of 70 °C. IL-61-17A is the polymer with the largest calculated f_L that does not show evidence of forming the σ phase at low temperatures. SAXS samples of IL-61-17A were prepared by loading the samples into quartz capillary tubes (Figure 5.9b), equilibrating the samples in the disordered phase by annealing in a vacuum oven well above T_{ODT}, and quenching the samples to room temperature by removing the samples from the vacuum oven and immediately plunging the capillary tube in 25 °C water. This sample preparation and quenching protocol leads to much faster and repeatable cooling and avoids issues with bubbles that occurred when using DSC pans to prepare samples. We note that the sample preparation routine described above in which the sample is loaded in a capillary tube was used for all experiments involving the IL-5.1 (IL-60-18) sample in which the DQC was documented. Samples of IL-61-17A prepared in this way were annealed for various times at room temperature (25 °C) prior to SAXS data collection, as shown in Figure 5.14. After 4 days of annealing at room temperature (following the quenching protocol described above), one sample was heated to 40 °C in a vacuum oven, annealed for 6 day at 40 °C, quenched to room temperature again, and annealed at room temperature for a further 4 days before SAXS data collection.

All samples exhibited a SAXS pattern consistent with a BCC structure with no evidence of nucleation of the σ phase after annealing at room temperature for as long as 23 days. Based on the kinetic of ordering of the closely related IL-5.1 (IL-60-18), IL-61-18, and IL-61-17B sample, 23 days of annealing at room temperature should be more than sufficient to reveal signs of nucleation of the σ phase. Therefore, we conclude that the σ phase is not the stable ordered phase at 25 °C in IL-61-17A.
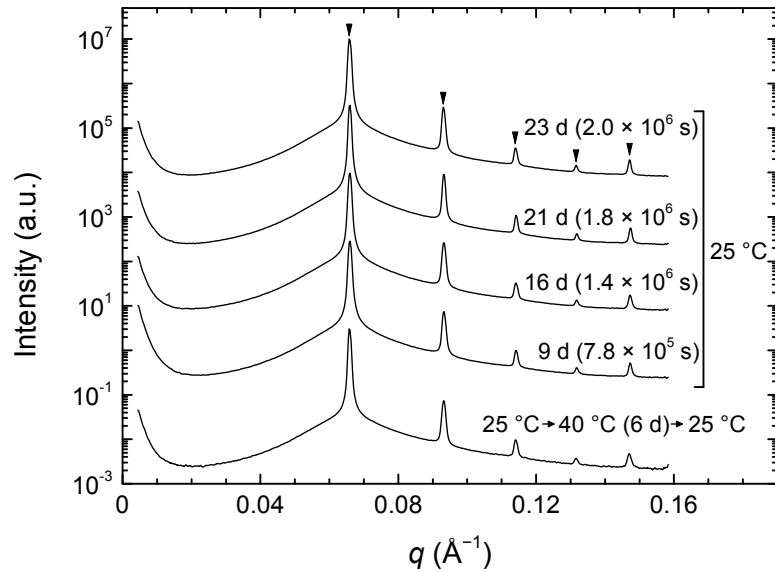
Figure 5.14 SAXS patterns collected during annealing of IL-61-17A at 25 °C. SAXS patterns collected after annealing at room temperature (25 °C) for the times specified after a rapid quench from above T_{ODT}. The data for each time point come from separately prepared samples. The data of the bottom curve was collected from a sample annealed at 25 °C for 4 days after a rapid quench from the DIS phase, heated to 40 °C and annealed for 6 days, then cooled back to 25 °C and annealed for a further 4 days. Allowed BCC Bragg peaks, $(q/q^*)^2 = 1, 2, 3, 4, 5,...$, are marked with arrows ($q^* = 0.0658$ Å^{-1}). The sample was contained in a capillary.

5.3.5 Experiments with IL-60-23

IL-60-23 is the IL sample with the smallest f_L that forms the HEX phase. IL-60-23 forms a well-ordered HEX phase with no evidence of σ phase nucleation when cooled from above T_{ODT} (99 °C) to 75, 50, and 25 °C, as shown in Figure 5.15. The sample annealed at 25 °C was prepared in an identical fashion as described for IL-61-17A. The sample annealed at 50 °C was placed in a vacuum oven heated to 120 °C (in the DIS phase), slowly cooled in the vacuum oven to 50 °C ($\approx$ 30 minutes) and annealed for 22 hours. To transport the sample annealed at 50 °C to the synchrotron X-ray source, the sample was quenched below the polylactide block T_g to 0 °C and stored in a freezer or refrigerator ($T \leq 4$ °C) to prevent evolution of the structure of the sample. This cooling

protocol is known to arrest major changes in the order phases present in the closely related IL-15 (IL-47-22) material.[88] Once at the synchrotron beamline, the sample was quickly reheating to 50 °C immediately prior to SAXS data collection. The sample annealed at 75 °C was heated above T_{ODT} and cooled to 75 °C directly on the beamline ($dT/dt \approx 30$ °C/min). To capture the higher order Bragg peaks at high q, data on the so-called middle-angle X-ray scattering (MAXS)[160] detector collected simultaneously with the SAXS data is included in Figure 5.15 as the dashed curves. Based on the kinetics of ordering of the closely related IL-5.1 (IL-60-18) and IL-15 (IL-47-22) sample, 12 days of annealing at room temperature should be more than sufficient to reveal signs of nucleation of the σ phase. Therefore, we conclude that the σ phase is not a stable ordered phase at 25 °C in IL-60-23.

The experiments with IL-60-23 presented in Figure 5.15 involved annealing a sample at 50 °C and quenching below the below the polylactide block T_g to 0 °C and storing the sample in a freezer or fridge ($T \leq 4$ °C) to prevent evolution of the structure of the sample. This quenching protocol is known to arrest major changes in the order phases present in the closely related IL-15 (IL-47-22) material, since cooling below $T_{g,L}$ stops the exchange of individual chains between PLA domains required to form the σ phase.[88] Interestingly, upon quenching an IL-15 (IL-47-22) sample that had grown a BCC structure below $T_{g,L}$ (where the σ phase is the equilibrium structure) the BCC peaks broadened. Similar results were obtained with IL-5.1 samples, as shown in Figure 5.16. A similar broadening of the HEX peaks in the IL-60-23 sample processed in the same way was not observed. Instead, the broad base of the primary Bragg scattering peak that is typically observed in block polymer melts was suppressed. Quenching below the core block T_g and observing changes in the SAXS patterns may be a way to screen materials for the underlying stability of the σ phase (or other ordered phases) when long time annealing above T_g of the core block is not practical.
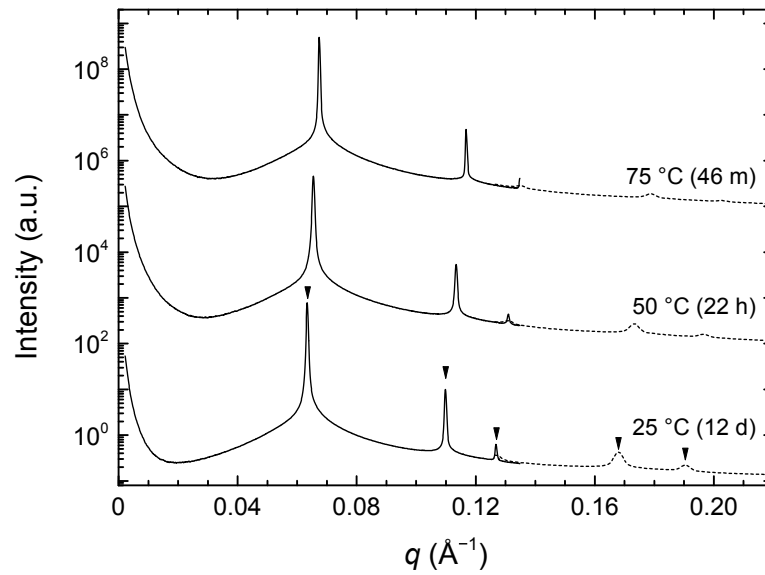
Figure 5.15 SAXS patterns collected during annealing of IL-60-23 at various temperatures. SAXS (solid lines) and MAXS (dashed lines) patterns collected after annealing at the identified temperatures for the times specified after a rapid quench from above T_{ODT}. Allowed HEX Bragg peaks, $(q/q^*)^2 = 1, 3, 4, 7, 9,\ldots$, are marked with arrows. The samples were prepared in capillaries.
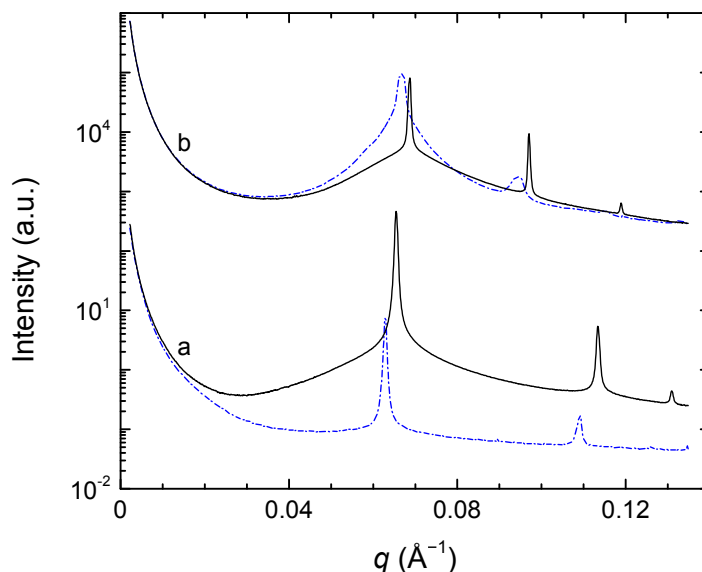
Figure 5.16 Comparison of SAXS patterns after quenching below the polylactide block T_g. Comparison of (a) IL-60-23 SAXS and (b) IL-5.1 (IL-60-18) patterns after rapid cooling from the DIS phase to 50 °C, annealing for 22 hours at 50 °C, and rapid cooling to 0 °C (dashed blue curves; samples stored for 7 days in a freezer below 0 °C and 3 days in a refrigerator below 4 °C prior to data collection) and after reheating to 50 °C (solid black curves). The samples were prepared in capillaries.

5.4 Discussion

The primary objectives of the study reported in this chapter were to (1) reproduce the discovery of the σ phase in additional IL samples, (2) reveal any additional ordered phases present, (3) establish the range of parameters over which the σ phase and other ordered phases form in IL diblock copolymers (i.e., the range of polylactide block volume fraction f_L and volumetric degree of polymerization N), and (4) establish the topology of the phase portrait in the vicinity of IL-15 (IL-47-22). In this section, the key results addressing each of these goals is summarized and put into context.

5.4.1 *Region of stability of the σ phase*

A well-ordered pure σ phase was reproduced in IL-5.1 (IL-60-18), while evidence of nucleation of the σ phase at low temperatures was documented in several additional

samples. These results confirm that the σ phase is a universal feature of the IL diblock copolymer phase portrait and not unique to the sample IL-15 (IL-47-22). All samples studied that in this chapter form ordered phases other than BCC and HEX (e.g., σ phase, DQC) show evidence of eventually forming the σ phase at long times. This suggests that, as previously documented for IL-15 (IL-47-22) and IL-5.1 (IL-60-18), the σ phase is the equilibrium ordered phase at low temperatures in these samples.

Evidence of σ phase formation was found for all IL samples synthesized in the range of f_L from 0.17(4) to 0.22 but not for sample IL-61-17A and IL-60-23. Therefore, the breadth of the stability window of the σ phase in the IL system is $0.17(4) \leq f_L \leq 0.22$, as shown in the phase portrait of Figure 5.3. Within the range of f_L in which the σ phase forms, the line of σ–BCC order–order transitions closely follows the slope of the BCC–DIS order–disorder transitions on the χN versus f_L phase portrait but at higher values of χN.

The sphericity concept invoked to explain the stability of the complex, low symmetry Frank–Kasper σ phase at low temperature[88] (see Chapter 4) is consistent with the topology of the IL phase portrait documented in Figure 5.3. The low symmetry phases are preferred at low temperature since the micelle-like point particle (and the core–corona interface) is able to maintain a shape that more closes approximates the preferred spherical shape within the constraints of the lattice symmetry and uniform density. The enhanced sphericity of the σ phase relative to BCC is facilitated by the redistribution of chains to form slightly different particle sizes (and shapes) in the five different local coordination environments of the particles at the lattice sites in the σ phase crystal structure. As the volume fraction of the particle cores is reduced with reduced f_L, the ability of the core–corona interface to "feel" the confining influence of the lattice site geometry is also reduced, and thus the driving force to form the σ phase is reduced. At a certain volume fraction of the core, the reduction in sphericity of the σ phase structure relative to the BCC phase is apparently not sufficient to overcome the entropic penalty of forming different size particles at particular locations within the structure, at least over experimental temperature range probed. This occurs at $f_L \approx 0.17$ in the IL system.

5.4.2 *Role of conformational asymmetry: comparison with recent SCFT predictions*

The experimental results for the IL system can be compared to resent self-consistent mean-field theory (SCFT) calculations by Shi and co-workers,[43] summarized in the theoretical phase diagrams reproduced in Figure 5.17. Shi and co-workers[43] found that the σ phase becomes a stable equilibrium ordered phase in AB diblock copolymers as the conformational asymmetry, quantified by the parameter $\varepsilon \equiv b_A^2 / b_B^2$ where b_i is the statistical segment length of the i block,[*] is increased. The σ phase first appears in the AB diblock phase diagram at values of ε of 2.25 over a narrow range of f and χN values above the region of stability of BCC. As the values of ε increases, the range in f over which the σ phase is stable grows.

The topology of the phase diagrams from the SCFT calculations are similar to that observed experimentally in the IL system, with a region of stability of BCC separating the σ phase from the DIS phase. Unfortunately, SCFT calculations (being mean-field calculations) fail to account for the dramatic consequences of composition fluctuations that dominate the disordered state near the ODT, and consequently do not accurately predict phase behavior near the ODT. Therefore, SCFT results near the ODT should be viewed with caution, such as the apparent similarity of the topology of the SCFT and experimental phase diagrams. In fact, SCFT calculations predict an intervening BCC window between all ordered phases and the ODT, with the exception of at the LAM–DIS critical point. In practice, fluctuations result in direct transitions between ordered and DIS phases and destroy the mean-field critical point (see Chapters 1 and 3).[14,17] Nevertheless, SCFT is remarkably successful at capturing the general qualitative features of block copolymer phase behavior, especially as χN increases.

---

[*] Note that (1) the statistical segment lengths used in the given definition of ε must be based on the same reference volume and (2) Shi and co-workers use an alternative definition of ε as simply the ratio of statistical segment lengths in their work.
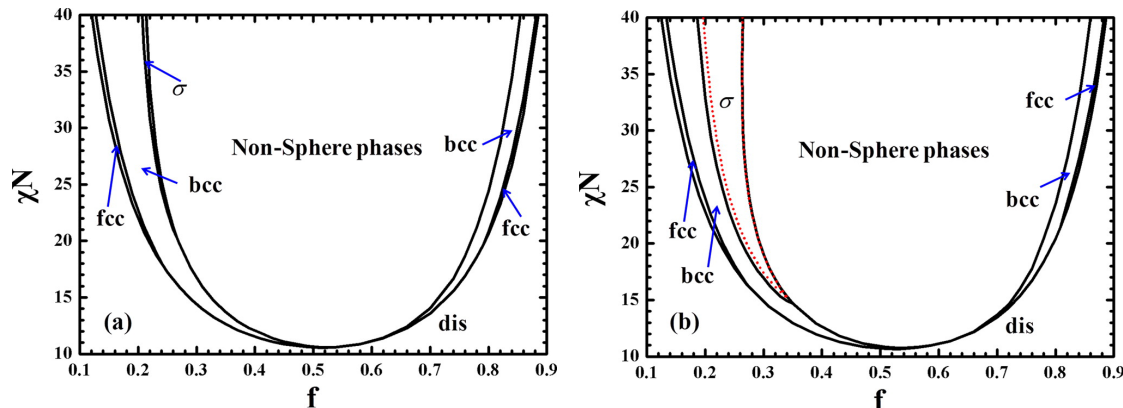
Figure 5.17 SCFT phase diagrams of conformationally asymmetric AB diblock copolymers. Phase diagrams for AB diblock copolymers with a ratio of statistical segment lengths of (a) 2.25 and (b) 4.0. Adapted with permission from Xie, N.; Li, W.; Qiu, F.; Shi, A. *ACS Macro Lett.* **2014**, *3*, 906–910. Copyright 2014 American Chemical Society.[43]

The IL system is estimated to have a modest value of ε of approximately 1.4 (estimated at 140 °C) yet exhibits a fairly broad window of stability of the σ phase. This modest value of ε is below the threshold at which the σ phase is predicted to be stable in the SCFT calculations of Figure 5.17.[43] Therefore, the SCFT calculations cannot be viewed as quantitatively predictive. In addition to fluctuation effects, additional asymmetries present in the IL diblock not captured by the SCFT calculations of Shi and co-workers (e.g., dispersity) may play a role in block polymer phase behavior near the σ phase. The SCFT calculations do, however, qualitatively suggest that conformational asymmetry plays an important role, with increases in ε stabilizing the σ phase. The appearance of the σ phase in IL diblock copolymers alone cannot prove or disprove this hypothesis. The σ phase does appear on the side of the phase diagram (i.e., in asymmetric diblocks rich in the component with the smaller statistical segment length) in region of the phase portrait between the HEX and BCC phases, as predicted by SCFT. These results are qualitatively consistent with the role of conformational asymmetry in diblock thermodynamics as it relates to the σ phase predicted by SCFT. A direct test of the SCFT prediction that increases in ε stabilizes the σ phase can be made by comparing the breadth in *f* of the window of stability of the σ phase in IL diblocks with that in other systems

with different values of ε. Such a comparison might involve, for example mapping the phase behavior of poly(ethylene-*alt*-propylene-*b*-DL-lactide) and poly(cyclohexyletheylene-*b*-DL-lactide) polymers that have lower and higher values of ε compared to the IL system, respectively.

The sphericity concept invoked to explain the stability of the σ phase at low temperature[88] (see Chapter 4) is perfectly consistent with the results of the SCFT calculations that suggest conformational asymmetry plays an important role in stabilizing the σ phase.[43] Increasing ε shifts the order–order phase boundaries to compositions richer in the block with the larger statistical segment length (to the right in Figure 5.17).[34,43] This increases the volume fraction of the core in the "sphere"-forming region of the phase diagram where the core is the block with the smaller statistical segment length (e.g., on the right side of Figure 5.17 and Figure 5.3). As the volume fraction of the particle cores is increased, the ability of the particle cores to "feel" the confining influence of the lattice site geometry is increased, enhancing the driving force to form the ordered phase with higher sphericity (i.e., the σ phase).

5.4.3 *Additional complex ordered phases*

A dodecagonal quasicrystalline (DQC) ordered phase was discovered to form as a long-lived metastable phase in IL diblock copolymers rapidly quenched well below T_{ODT} (i.e., to large values of χN). A detailed account of the formation of the DQC in IL-5.1 (IL-60-18) is presented in Chapter 4. Additional evidence of DQC formation was documented for the closely related sample IL-61-18 at short times following a rapid quench from the DIS phase to room temperature (Figure 5.5, 7 day anneal curve a). In IL-61-18, the relative peak intensities of the SAXS patterns collected after 122 days of annealing at room temperature also left open the possibility of formation of an additional Frank–Kasper phase, the cubic A15 structure, coexisting with the σ phase (Figure 5.6). Although, the observed IL-61-18 SAXS pattern can also be interpreted as arising from the σ phase with a preferred grain orientation without the presence of the A15 phase. As a whole, these results suggest the intriguing possibility that additional order phases may be lurking in the diblock copolymer phase diagram in the region where nearly spherical,

micelle-like point particles form ordered structures (i.e., BCC, σ phase, DQC). The DQC (and evidence of a possible A15 phase) was discovered by synthesizing series of IL diblocks with larger N_I relative to IL-15 (IL-47-22), leading to higher T_{ODT}s and enabling access to larger values of χN in quenching experiments before reaching $T_{g,L}$. An interesting avenue of inquiring would be to further increase N_I to access even larger values of χN, perhaps revealing additional phases or perhaps regions of stability of the DQC.

5.4.4 Role of molecular weight on thermodynamics and dynamics

The five homologous series' of IL diblock copolymers had N_I values of 44, 47, 49, 60, and 61. Changing N_I, and consequently N, at a given f_L influence phase behavior and ordering dynamics in several ways. Increasing N_I increases T_{ODT}. A higher T_{ODT} increases the range of temperatures between T_{ODT} and $T_{g,L}$, increases the range of χN values accessible in the ordered region of the phase portrait. This allows access to quenches deeper into the order phase at a fixed f_L or access to ordered phases at lower values of f_L. The increase in accessible χN values relative to the IL-47-xx series (of which IL-15 (IL-47-22) is a member) contributed to the discovery of the metastable DQC phase in IL-5.1 (IL-60-18). Decreasing N_I relative to the IL-47-xx series to 44 reduced T_{ODT} in the sample IL-44-17 below room temperature. The ODT of IL-44-17 could only be deduced during SAXS experiments in which a BCC phase began to nucleate and grow upon cooling to 6 °C. Presumably, ordering kinetics are significantly influenced by the proximity to $T_{g,L}$ (although $T_{g,L}$ was not detected in DSC experiments, based on results from all the other IL samples, it must be close to 0 °C). The true T_{ODT} is therefore probably at a higher temperature than that detected by SAXS, explaining the somewhat higher χN_{ODT} of IL-44-17 relative to other samples nearby in the phase portrait.

In addition, a higher T_{ODT} results in faster ordering dynamics of the BCC phase at temperature just below T_{ODT}. This is evident by comparing the time-temperature-transformation (TTT) diagrams of IL-15 (IL-47-22) and IL-5.1 (IL-60-18) presented in Lee et al.[88] and Chapter 4, respectively. The minimum ordering time at the "nose" of the TTT diagram occurs a shorter time in IL-5.1 (IL-60-18) than the lower N_I sample IL-15

(IL-47-22). The increase in the temperatures corresponding to the range of χN values in which BCC is the equilibrium phase increases the ordering dynamics (overwhelming any trivial slowing influence the increase in total molecular weight might be expected to have).

The increase in ordering dynamics of the BCC phase with increasing T_{ODT} could complicate future studies intending to target the DQC phase. If T_{ODT} is raised by increasing N_I, the nose of the TTT diagram may appear at such short times that it is challenging to cool samples rapidly enough to prevent nucleation and growth of a BCC structure during cooling. This is perhaps why only some IL-61-18 samples quenched to 25 °C for annealing showed evidence of the DQC while others showed coexistence of a primarily BCC structure with the nucleating σ phase. Although the detailed ordering kinetics were not measured in IL-61-18, the increased T_{ODT} of IL-61-18 relative to IL-5.1 (IL-60-18) presumably leads to the nose of the TTT diagram occurring at shorter times in IL-61-18. This combined with the less controlled and most likely slower cooling during quenching of the IL-61-18 samples encapsulated in DSC pans relative to the IL-5.1 (IL-60-18) samples prepared in capillary tubes may have resulted in nucleation and partial growth of a BCC structure during quenching of the IL-61-18 samples, as illustrated in Figure 5.18. It has been shown in Chapter 4 that if a BCC structure grows prior to quenching to low temperatures, the DQC will not form and the BCC structure will transform directly into the equilibrium σ phase. This perhaps contributes to the appearance of the DQC phase in only certain IL-61-18 samples, emphasizing the importance of controlled and repeatable quenching protocol when attempting to form the metastable DQC phase.
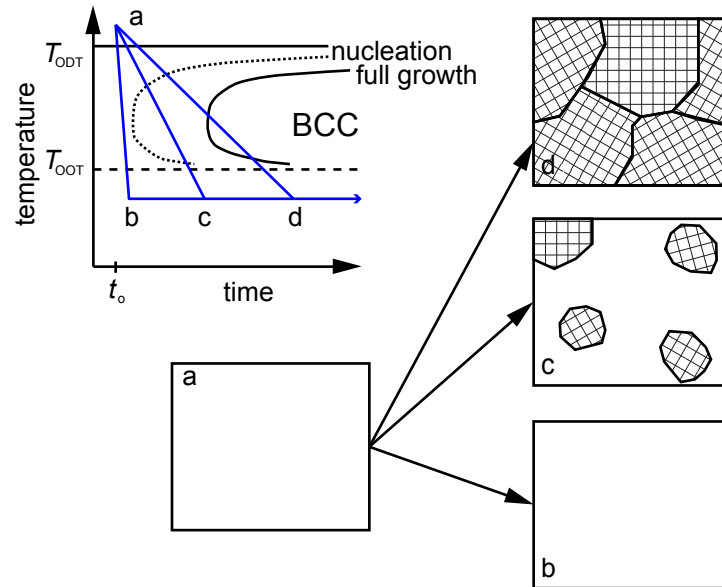
Figure 5.18 Illustration of the consequences of cooling at different rates relative to the nose of the TTT diagram. Fast quenching from an initial equilibrium disordered phase (a) results in a supercooled disordered phase (b). Slow quenching can result in partial nucleation of the BCC phase (c) where the hatched regions are meant to represent grains of the BCC phase. Even slower cooling leads to complete growth of the BCC phase (d) prior to reaching the target temperature.

One reason for the comparatively slow kinetics of ordering of the σ phase is that formation of the structure requires redistribution of chains between different particles in order to assume the five slightly different particles sizes on the various lattice sites of the low symmetry crystal. At a given temperature, the rate of individual chain exchange in the undiluted polymer melt is likely to depend very strongly on core block chain length, in analogy to the measured hypersensitivity of the individual chain exchange rate in block polymer micelles in a selective solvent.[180,189,190] This may be a contributing factor to the apparent chain length dependence of ordering times of the σ phase at room temperature and could present experimental challenges if chain length is increased further in future studies.

Chapter 6:

Determination of the Lamellae-to-Disorder Heat of Transition in a Short Diblock Copolymer by Relaxation Calorimetry [*,†]

6.1 Introduction

Block polymers have sustained the interest of researchers for decades as the preeminent uniquely tunable self-assembling soft materials.[1–4] Precise synthetic control of block chemical and physical properties, molecular architecture, morphology, characteristic length scale, and dynamics lend block polymers to fundamental investigations addressing a diverse array of scientific questions in condensed matter, while enabling applications in emerging technologies[6,8] such as next-generation lithographic materials,[10] batteries,[11] and drug delivery.[12] An understanding of block polymer self-assembly is a critical prerequisite for use in applications, and consequently

---

[*] This work was done in collaboration with Daniel Phelan and Chris Leighton.
[†] Reproduced with permission from Gillard, T. M.; Phelan, D.; Leighton, C.; Bates, F. S. *Macromolecules* **2015**, *48*, 4733–4741. Copyright 2015 American Chemical Society.

the thermodynamics of block polymer–based soft materials in the bulk, solutions, and blends have been the subject of continued intense study.[4,13,14] However, experimental investigations of the thermodynamics of block polymers have only rarely involved direct thermal measurements of the order–disorder phase transition (ODT).[15,31,80–86,191–194] Here we report measurements of the latent heat of the ODT, ΔH_{ODT}, of a model symmetric poly (1,4-isoprene-*b*-DL-lactide) (IL) diblock copolymer using relaxation calorimetry, a previously unused tool for thermal characterization of phase transitions in block polymers.

The dearth of thermal measurements of the ODT in block polymers is the result of two factors related to polymer molecular weight: (1) the sluggish ordering dynamics of block polymers with typical molecular weights are incommensurate with the relatively fast heating rates characteristic of routine polymer thermal analysis methods (i.e., differential scanning calorimetry (DSC)), and (2) the fact that the thermal signature of the weakly first-order ODT, ΔH_{ODT}, is small and decreases with increasing molecular weight. Recent interest in low molecular weight and highly incompatible (i.e., large segment–segment interaction parameter, χ) or "short" diblock copolymers for applications such as block polymer lithography[10,192,193] and as model systems to study the influence of fluctuations on block polymer thermodynamics[15] has made thermal measurements of the ODT more feasible. Our group recently reported a comprehensive experimental investigation of the thermodynamics of a series of IL diblock copolymers in which DSC measurements of ΔH_{ODT} for samples that span the diblock copolymer phase diagram were enabled by the fast molecular dynamics of these low molecular weight (2–5 kg/mol) and highly incompatible short diblock copolymers (Chapter 3).[15] The latent heat was found to be small and to depend strongly on the symmetry of the low temperature ordered phase, a result of strong non-mean-field composition fluctuations in the disordered state near the ODT.
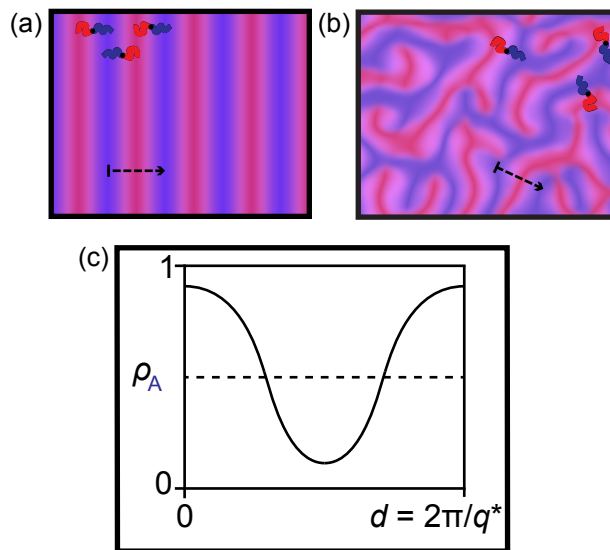
Figure 6.1 Illustration of the nature of the ODT in short diblock copolymers. Illustrations of (a) the ordered lamellar phase at temperatures just below T_{ODT}, (b) the fluctuating disordered phase at temperatures just above T_{ODT}, and (c) the equivalence of the local composition profile of a single domain period normal to an A/B interface in the ordered and disordered phases, as indicated by the dashed arrows in (a) and (b).

The values of ΔH_{ODT} measured by DSC were critical in supporting a principal conclusion of a recent study by Lee et al.—specifically that the ODT for block polymers of low molecular weight is a pattern transition, as depicted in Figure 6.1, and not a demixing transition.[15] The strongly fluctuating disordered phase near the ODT has significant microphase separation at the local level (i.e., distinct A- and B- rich domains separated by A/B interfaces) that is continuously rearranging due to thermally driven composition fluctuations. These fluctuations lead to a locally correlated, structured disordered phase that lacks long-range order but at any given instant has a structure that resembles a bicontinuous microemulsion[93] or the structure observed during spinodal decomposition[50] (Figure 6.1b). This fluctuating disordered phase transitions to the ordered lamellar morphology, represented in Figure 6.1a, with imperceptible changes in the degree of local microphase separation, evidenced by essentially no change in the small-angle X-ray scattering (SAXS) invariant or the average domain size d upon traversing the ODT.[15] As a result, the local composition profile normal to the A/B

interface is essentially unchanged in passing through the ODT, as depicted in Figure 6.1c. Apparently, the disordered to lamellae transition proceeds by rearrangement of the interfaces between the A- and B-rich domains and not by a demixing of the blocks as classically envisioned by mean-field theory. Consistent with this interpretation, nearly all of the latent heat of the ODT measured by Lee et al.[15] and in Chapter 3 (0.36–0.02 J/g depending on ordered phase symmetry) is attributable to the change in interfacial area per unit volume that accompanies the ODT.

This picture of the ODT as a pattern transition is reinforced by a series of coarse-grained simulation studies by Morse and co-workers, in which the similarity of the local composition profile in the ordered and disordered phase can be directly evaluated.[48,59] These simulations demonstrate that the amplitude of the (nearly sinusoidal) composition profile in the ordered phase at the ODT is quite high (ρ_A, the local volume fraction of A monomer units in the center of an A-rich domain is ≥ 0.8), even for relatively high molecular weights, and that there is little difference between the local correlations in composition in the ordered and disordered phases at the ODT. The amplitude of the composition profile in the ordered and disordered states shown schematically in Figure 6.1c was selected based on the universal values obtained in simulations with equivalent invariant degree of polymerization to the IL diblock copolymer studied in this work.[48] In addition, the latent heat of the ODT extracted from the simulations compares favorably with what we report here for an IL diblock copolymer.[48,90]

While we previously estimated the equilibrium value of ΔH_{ODT} by DSC, relatively fast heating rates and elaborate thermal profiles were required to ensure measurable signals and flat baselines, as required for extraction of the small latent heats. These experimental constraints of DSC led us to explore alternative calorimetric methods to corroborate and complement the DSC measurements and to expand the experimental toolkit for thermal characterization of block polymers. In particular, we sought to obtain more precise values of ΔH_{ODT} and to determine if pretransitional fluctuation effects would be evident in the temperature dependence of the heat capacity.

Of the commonly available thermal analysis methods, adiabatic scanning calorimetry (ASC) is perhaps the best technique for extracting high-resolution thermal information near weakly first-order phase transitions, where pretransitional fluctuation effects influence the heat capacity.[25] However, ASC presents considerable experimental challenges, including the requirement for custom instrumentation, large samples (0.1–10 g), and long experiment times. To the best of our knowledge, there has been only a single report of an ASC measurements of the ODT conducted with a poly(oxyethylene-*b*-oxybutylene) diblock copolymer.[82] To address the limitations of DSC and with the intent of obtaining similar information to that which can be obtained by ASC (i.e., pseudostatic measurement of the temperature dependence of heat capacity $C(T)$ near the ODT), we have adapted relaxation calorimetry,[195–197] a semiadiabatic thermal analysis technique popular in the hard materials community, to study phase transitions in block polymers.

6.2   Background: Relaxation Calorimetry

Relaxation calorimetry is an established semiadiabatic technique developed to measure the heat capacity of hard materials systems over broad temperature ranges using small sample sizes.[195] In addition, an automated, commercial instrument intended for hard materials applications is widely available and is used in this work: The heat capacity option for the Quantum Design Physical Property Measurement System (PPMS).[198] For details regarding the relaxation calorimetry method used by the PPMS, the reader is referred to [195–198] and references therein. The basics of the simplest implementation of a relaxation calorimetry experiment are summarized in the heat flow diagram in Figure 6.2. Briefly, a sample of unknown heat capacity C_{samp} is placed on a platform with heat capacity C_{plat}. This platform contains a resistive heater for adding heat to the system and a temperature sensor. The sample and platform are thermally isolated from their surroundings and connected to a heat bath with a large thermal mass maintained at temperature T_b by suspension in an atmosphere maintained at high vacuum ($\leq 10^{-4}$ Torr). The apparatus is designed to minimize radiative heat transfer between the heat bath and the suspended sample platform. This thermal isolation prevents conductive, convective,

and radiative heat transfer to and from the heat bath except through a weak thermal link of conductance K_w. This link exists almost entirely due to thermal conduction *via* the lead wires that serve both to provide electrical connections to the platform heater and temperature sensor, and to suspend the platform.
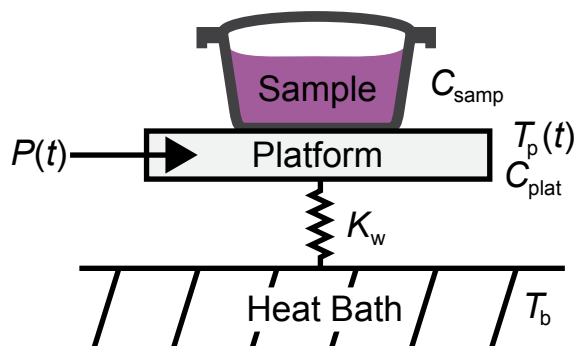
Figure 6.2 Heat flow schematic of the relaxation calorimetry experiment.

The raw data obtained during a relaxation calorimetry experiment is the time evolution of the platform temperature, T_p, during a pulse of constant heating power that leads to a temperature rise ΔT and the subsequent relaxation back to T_b when heating is ceased; see Figure 6.3 for an example of the raw data from a single heating pulse. To perform a measurement, the entire apparatus is first equilibrated at T_b. Then, a constant, small heating power $P(t) = P$ is applied to the platform beginning at time t_0, and $T_p(t)$ is measured. The apparatus and experiment are designed such that the time constant for equilibration of the sample and platform with the heat bath by conduction through the lead wires is much greater than any of the time constants for internal thermal equilibration within the sample and platform. Therefore, it is assumed that the temperature within the platform and sample are uniform throughout the experiment. At long times T_p will approach the saturation temperature at which the power supplied by the heater is equal to the heat lost to the heat bath by conduction through the lead wires (i.e., $\Delta T = P/K_w$). After a specified time, heating is stopped ($P(t) = 0$) and the relaxation of $T_p(t)$ back to T_b is measured.
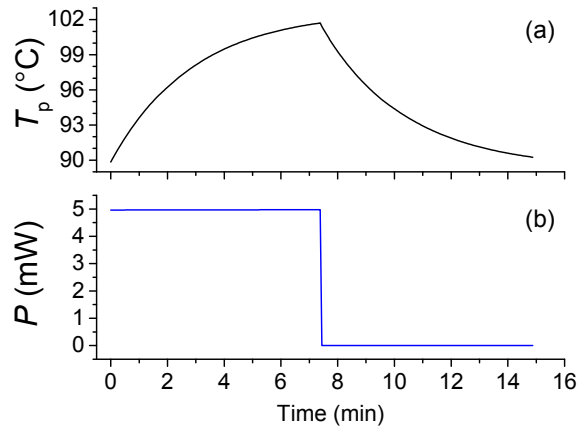
Figure 6.3 Example of raw relaxation calorimetry data. Raw (a) platform temperature T_p and (b) heater power P for a single temperature pulse. This large temperature pulse was used to extract the heat capacity data of Figure 6.9.

Extraction of heat capacity from the raw temperature pulse data requires a model. A heat balance on the sample and platform in Figure 6.2 yields the equation,

$$C_{Total}\frac{dT_p}{dt} = -K_w\left[T_p(t) - T_b\right] + P(t) \qquad\qquad 6.1$$

where $C_{Total} = C_{samp} + C_{plat}$. Two approaches can be used to extract the heat capacity of the sample from the raw data using eq 6.1; the most appropriate procedure depends on the details of the experiment. If the temperature dependence of the heat capacity is small over the temperature range ΔT such that the heat capacity can be assumed to be constant during the temperature pulse, eq 6.1 can be solved for $T_p(t)$ for each branch of the heating pulse (e.g., the heating and cooling portions). For example, the solution for the heating branch is

$$T_p(t) = \frac{P}{K_w}\left(1 - e^{t/\tau}\right) + T_b \qquad\qquad 6.2$$

where $\tau = C_{Total}/K_w$. If C_{plat} is known from calibration experiments conducted without a sample, C_{samp} and K_w at the average sample temperature $(T_b + \Delta T/2)$ can be determined by fitting the entire set of experimental $T_p(t)$ data to eq 6.2 and the analogous solution for the cooling branch. To establish the temperature dependence of C_{samp}, the temperature

pulse experiment is repeated at additional T_b values. This pseudostatic method works well when ΔT is small (i.e., $\Delta T/T \ll 1$) and the temperatures experienced during a temperature pulse are sufficiently far from a phase transition, ensuring that C_{samp} is approximately constant during the measurement; this represents the normal mode of operation for the PPMS relaxation calorimeter.[196]

A second method for extracting $C_{samp}(T)$ that can be used when C_{samp} is not constant over the temperature range of the temperature pulse is the scanning method.[196,197] In this approach, the raw $T_p(t)$ data are numerically differentiated to obtain dT_p/dt and C_{Total} is calculated directly at each temperature using eq 6.1. The scanning method trades the robustness of the fitting routine used in the pseudostatic method, which uses the entire temperature pulse to calculate a single value for C_{samp}, for the ability to measure $C_{samp}(T)$ near sharp features such as first-order phase transitions.[197,198] This method requires knowledge of $K_w(T)$, for example from sample platform calibration or previous measurements near but not overlapping the sharp feature of interest using the pseudostatic method described above.

Both the normal pseudostatic method and the scanning method described above can be extended to accommodate imperfect thermal contact between the sample and platform by inserting an additional thermal resistance between the sample and the platform. This results in a more complicated thermal model involving a set of coupled differential equations analogous to eq 6.1.[196–199] For pseudostatic experiments, this system of equations yields solutions that involve a sum of two exponentials with two relaxation times. In the experiments described here, the simple model is used for analysis of scanning method data while the more sophisticated, two relaxation time model is applied for pseudostatic measurements.

6.3 Experimental Section

6.3.1 *Materials*

Measurements reported here were performed on a volumetrically symmetric poly(1,4-isoprene-*b*-DL-lactide) (IL) diblock copolymer designated IL-1. The synthesis,

molecular characterization, and thermodynamic characterization of this material have been previously described.[15] Briefly, the number-average molecular weight M_n of 2750 g/mol is split between the poly(1,4-isoprene) (PI) (1130 g/mol) and poly(DL-lactide) (PLA) (1620 g/mol) blocks as determined by ^{1}H NMR, giving a volume fraction of PLA in IL-1 of 0.51 ± 0.01 based on published densities.[104,200] The molecular weight dispersity $Đ = 1.10$ was determined by size exclusion chromatography (SEC) using tetrahydrofuran as the mobile phase. A degree of polymerization $N = 39$ is calculated using a repeat unit reference volume $v_o = 110$ Å^3 with a reference temperature of 25 °C.

The glass transition temperatures, T_g, of the PI and PLA in IL-1 are −61 and 20 °C, respectively, as determined by DSC. The symmetric IL-1 diblock forms an ordered lamellar (LAM) phase at temperatures below the order–disorder transition temperature $T_{ODT} = 96 \pm 1$ °C, as detailed in a previous report.[15] The value of ΔH_{ODT} of IL-1 was measured by DSC to be in the range of 0.25–0.36 J/g, depending on the details of the measurement (e.g., dT/dt, and inclusion of an annealing step).

6.3.2 *Relaxation calorimetry*

Relaxation calorimetry measurements were conducted on a PPMS equipped with the heat capacity option.[198] Since the IL-1 polymer is a viscous liquid at temperatures above T_{ODT} and a soft viscoelastic solid below T_{ODT}, it was necessary to encapsulate the sample in a container prior to measurement to prevent the material from flowing off the measurement platform at elevated temperatures. Therefore, IL-1 samples (~15 mg) were hermetically sealed by mechanical crimping in PerkinElmer volatile aluminum sample pans (~24 mg; Part No. 02190062), similar to techniques previously used for powdered or air-sensitive samples.[201,202] These pans were chosen based on their low mass per internal volume relative to other comparable DSC pans, allowing the sample thermal mass to be a larger proportion of the total thermal mass. Using these pans (pan mass ≈ 24 mg), a polymer sample of approximately 15 mg accounts for ~55% of the total measured heat capacity signal (with ~30% due to the DSC pan, and the remaining ~15% due to the platform; see Figure 6.4). Hermetic sealing of the polymer sample within an aluminum

pan also prevents contamination of the high vacuum atmosphere within the PPMS calorimeter.
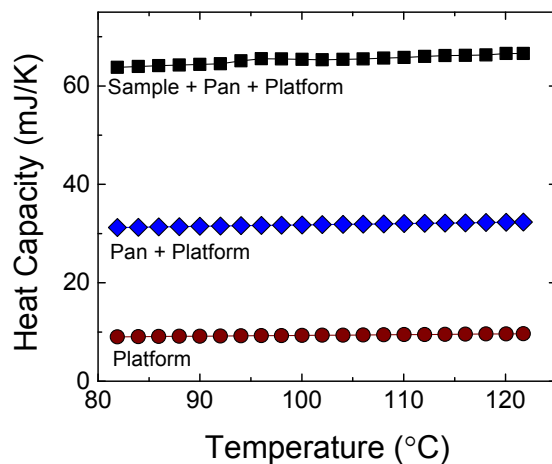
Figure 6.4 Relative contributions to total heat capacity in relaxation calorimetry experiments. Total heat capacity as a function of temperature from pseudo-static relaxation calorimetry measurements of the PPMS sample platform with a thin layer of grease (red circle markers); the sample platform and encapsulating aluminum DSC pan (blue diamond markers); and the sample platform, encapsulating aluminum DSC pan, and the IL-1 polymer (black square markers), demonstrating the relative contributions to the total measured heat capacity signal.

Adhesion and thermal contact between the sample platform and the sample pan were facilitated by application of a thin layer of Dow Corning high vacuum grease to the platform (applied as thin as possible using a minimal amount of grease). Appropriate choice of grease used for sample–platform adhesion is important as the grease must maintain adhesion and not exhibit any melting or other thermal transitions across the temperature range of interest. (Apiezon H grease is another suitable choice for the temperature range of the experiments described here while Apiezon N grease should be avoided for measurements at or above room temperature). The heat capacity of the platform including the thin layer of grease was measured over the temperature range of interest prior to placing the sample pan on the platform. These so-called addenda measurements are required to calculate the heat capacity of the sample by subtracting the

heat capacity of the platform and grease from the total measured heat capacity of the entire platform-sample system.

Normal pseudostatic mode relaxation calorimetry experiments were performed with various values of the temperature rise ΔT, ranging from 0.5 to 10 °C (~0.1–3% of the absolute temperature). Measurements on IL-1 were taken from the highest temperature of interest (~120 °C) in the disordered phase to the lowest temperature of interest in the lamellar phase. The temperature was equilibrated until it was stable within 1% of the temperature rise prior to initiating the temperature pulse. Processing of the normal mode raw data to extract sample heat capacity (including the encapsulating pan) for each pulse was done using the PPMS software that utilizes the more sophisticated two relaxation time model.[198,199]

Scanning mode measurements were performed using various pulse sizes ΔT and initial temperatures T_b. Prior to a temperature pulse, the sample was disordered by heating to 117 °C for 5 min, cooled at a controlled rate (1–10 °C/min) to T_b and then equilibrated until the temperature was stable within 0.3% of ΔT ($\geq$ 60 min). This temperature history leads to the formation of a well-ordered lamellar morphology.[15] Initial processing of the raw pulse data to extract $C_{samp}(T)$ was done using the PPMS software that utilizes the model of Figure 6.1 and eq 6.1, which calculates the slope of the noisy raw data at each temperature by fitting a line through a percentage of the measured data points surrounding the temperature of interest, as set by the user. We found 3% to be an optimal choice, reducing noise in the extracted slope to acceptable levels without noticeably smearing the sharp feature due to the ODT phase transition. This method uses K_w values determined during sample platform calibration measurements prior to mounting a sample. Latent heat was calculated as the step change in enthalpy at the ODT. The magnitude of the step change was determined by evaluating the difference between lines fit to the low- and high-temperature enthalpy data away from T_{ODT} at the center of the step change (i.e., at T_{ODT}).
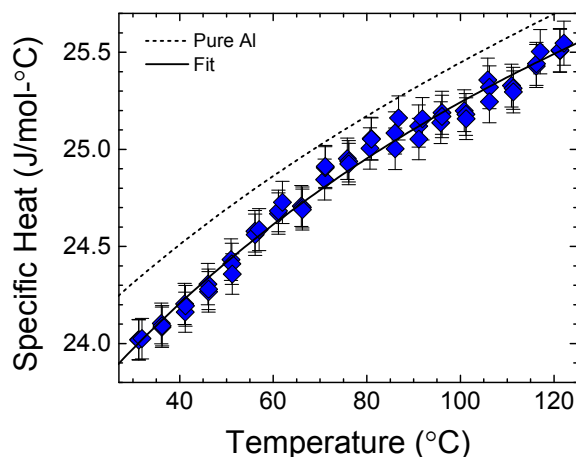
Figure 6.5 Specific heat measurement of an empty DSC pan. Specific heat of an empty aluminum DSC pan as a function of temperature from pseudo-static relaxation calorimetry measurements (blue symbols), fit to the data used to calculate contribution of encapsulation DSC pan to total heat capacity (solid black line), and literature values for the heat capacity of pure aluminum for comparison (dashed black line).[203] Error bars indicate estimated random error (see text).

For all PPMS measurements, the heat capacity of IL-1 was calculated by subtracting the contribution due to the aluminum sample pan from the total sample heat capacity, C_{samp}. The temperature dependence of the specific heat of the aluminum DSC pans was determined from pseudostatic relaxation calorimetry measurements of empty DSC pans over the temperature range of interest ($\Delta T = 10$ °C, see Figure 6.5); the heat capacity of the DSC pans was found to be 1–2% lower than that of literature values for pure aluminum, consistent with previous reports.[201,203] The contribution of the encapsulating DSC pan to the measured sample heat capacity at any temperature can then be determined by fitting a smooth function to the experimental pan heat capacity data and from the known pan mass measured prior to polymer sample loading. This approach is a simplified version of that recommended for volatile, powdered, or air sensitive samples described in Marriott et al.[201] In addition, polymer stability over the course of the PPMS experiments was confirmed by size exclusion chromatography, which revealed no change

in the molecular weight distribution over the period of a typical set of experiments (1–2 days).

6.3.3   Differential scanning calorimetry

DSC experiments were conducted using two instruments. A TA Instruments Q1000 DSC was employed to determine the breadth of the ODT; ~15 mg samples were encapsulated in TA hermetic aluminum DSC pans, heated to 150 °C then cooled to the maximum temperature of interest at 10 °C /min, and held in an isothermal state for 1 min prior to cooling and heating through T_{ODT} at a prescribed specified ramp rate. Heat capacity measurements were conducted using a TA Instruments Discovery DSC immediately after instrument calibration. Three IL-1 samples (10–20 mg) were encapsulated in TA aluminum Tzero hermetic DSC pans (~50 mg). All samples were heated to 180 °C, cooled at 20 °C /min to –20 °C, and held in an isothermal state at –20 °C for 2 minutes before measuring the heat capacity while heating to 180 °C at 20 °C /min. The measured heat capacities were binned and averaged at integer values of the temperature (°C). Measurements on each of the three samples were repeated three times (unloading the sample between each measurement), and the values for all nine experiments were averaged to give final values of heat capacity as a function of temperature. The random error in the measurement was approximated as the standard deviation of the measured values at each temperature.

6.4   Results

6.4.1   Pseudostatic heat capacity measurements

Pseudostatic measurements of the heat capacity of IL-1 were conducted over a range of temperatures near $T_{ODT} \approx 96$ °C, for various values of the temperature rise ΔT. Results using a value of ΔT of 10 °C are shown in Figure 6.6, which were obtained by averaging measured heat capacity data at each temperature for two sets of experiments (separated in time by approximately 1 day) on the same sample. A value of ΔT of 10 °C was found to be optimal, leading to estimated random errors of less than 1%, as also

shown in Figure 6.6. Estimates of random error include the estimated error calculated by the PPMS software (which accounts for errors in the fitting routine for both addenda and sample measurements),[198] the random error in measurements of pan mass and total sample mass (pan and polymer), and standard propagation of error for any background subtraction or measurement averaging conducted. Larger values of ΔT increase the measurement time, while smaller values increase random error as shown in Figure 6.7.
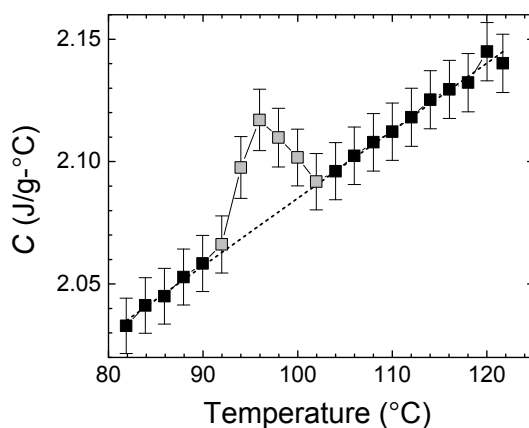
Figure 6.6 Specific heat of the IL-1 polymer as a function of temperature from pseudostatic relaxation calorimetry measurements. Gray markers indicate data points that were influenced by the latent heat of the ODT and are therefore not representative of the true heat capacity. Error bars indicate estimated random error (see text). The dashed line is C_{BG}, a linear fit to black data points.

For a ΔT that spans T_{ODT}, the assumption of constant heat capacity over the temperature range, a requirement for the pseudostatic data analysis method, is not satisfied, likely leading to erroneous heat capacity values near the transition. Data points where this was the case are indicated by gray points in Figure 6.6. Although the data in this region do not reflect the true heat capacity, a peak in the apparent heat capacity coincident with T_{ODT} is evident and this feature in the heat capacity is reduced in magnitude with increasing ΔT (see Figure 6.7).
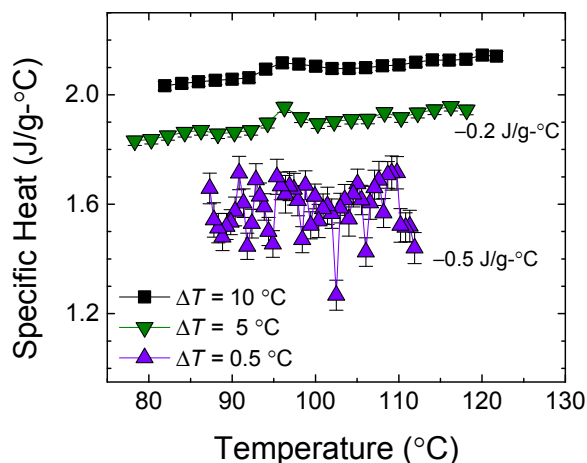
Figure 6.7 Comparison of temperature pulse amplitude in pseudostatic relaxation calorimetry experiments. Specific heat of the IL-1 polymer as a function of temperature from pseudo-static relaxation calorimetry measurements using different temperature pulse magnitudes. The $\Delta T = 5$ and 0.5 °C data sets have been shifted vertically for clarity. Error bars indicate estimated random error (see text).

The pseudostatic relaxation calorimetry heat capacity measurements were confirmed to be free from significant systematic errors, *at least within the constraints of the statements made above regarding points close to the ODT*, by comparing the measured specific heat to dynamic DSC measurements of the specific heat, as shown in Figure 6.8. The relaxation calorimetry measurements agree with the DSC measurements within the random error of repeated DSC measurements (~ 1%), and are well within both the accepted accuracy[204] of careful DSC measurements of specific heat of ± 5–10% and the ± 3% accuracy quoted by the manufacturer (TA Instruments) for the experimental protocol used.
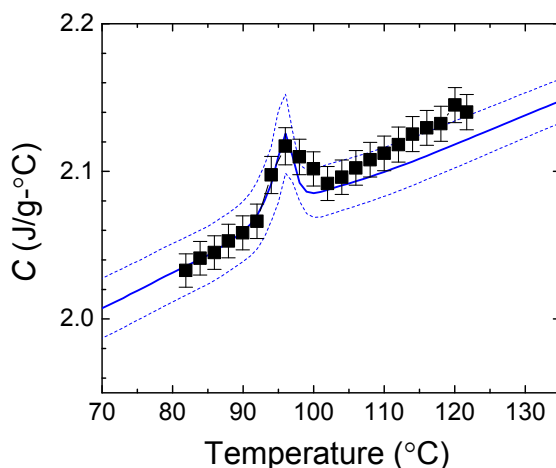
Figure 6.8 Comparison of relaxation calorimetry and DSC measurements. Comparison of the specific heat C of the IL-1 polymer as a function of temperature for pseudo-static relaxation calorimetry measurements reproduced from Figure 6.6 (black symbols) and for DSC measurements (solid blue line indicates average C obtained from several measurements; dotted blue lines indicates $\pm$ the standard deviation of the repeated measurements). Accuracy of the DSC measurements is $\pm \sim 3–10\%$ ($\pm 0.06–0.2$ J/g-°C).

These data thus provide a convenient measure of the true equilibrium heat capacity as a function of temperature away from T_{ODT} since the sample is allowed ample time to reach equilibrium during annealing prior to each pseudostatic heat capacity measurement. In addition, these measurements provide a method to extract a nonarbitrary baseline temperature dependence of the heat capacity that spans the first-order ODT, shown as the dotted curve in Figure 6.6. This baseline temperature dependence of the heat capacity can be used to accurately determine the heat capacity associated with the phase transition at T_{ODT} measured by scanning mode relaxation calorimetry.

6.4.2 Scanning mode heat capacity and latent heat measurements

Scanning mode relaxation calorimetry measurements were conducted beginning at several initial temperatures $T_b < T_{ODT}$ and using various values of ΔT to determine optimal conditions. Prior to each scanning mode measurement the sample was equilibrated in the disordered phase above T_{ODT} before being cooled to the desired T_b and annealed for at least 60 min, a process known to produce a well-ordered, equilibrium

lamellar morphology.[15] This ability to achieve equilibrium in the ordered phase prior to making a measurement at the phase transition temperature is a key advantage of relaxation calorimetry over DSC. A T_b of 90 °C and a ΔT of approximately 15 °C, measurement conditions that place T_{ODT} in the center of the temperature range probed, were found to give the best results. An example of such a measurement is shown in Figure 6.9a. The baseline subtracted specific heat near the ODT phase transition, $\Delta C(T)$, was calculated from the extracted $C(T)$ as

$$\Delta C(T) \equiv C(T) - C_{BG}(T) \qquad 6.3$$

where $C_{BG}(T)$ is the background temperature dependence of the specific heat of the IL-1 polymer that was interpolated from pseudostatic measurements for temperatures removed from but spanning the ODT (i.e., the dashed line in Figure 6.6).
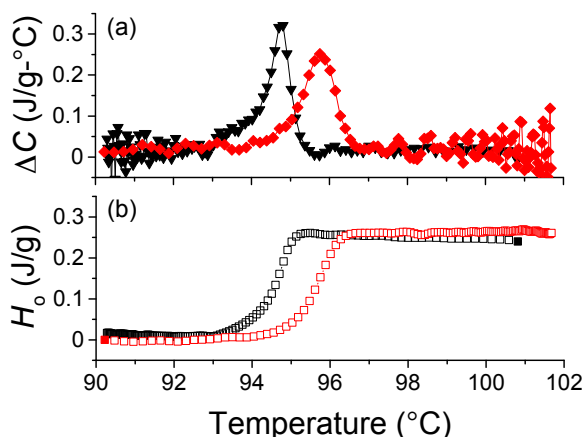
Figure 6.9 Representative scanning mode relaxation calorimetry data. (a) Baseline-subtracted specific heat, ΔC, and (b) corresponding enthalpy, H_o, of the IL-1 polymer near the ODT from scanning mode relaxation calorimetry measurements. Red and black data markers indicate data calculated from the heating and cooling branch of the temperature pulse, respectively. Filled data markers in (b) indicate $T = T_{ref}$ for each branch. The cooling portion enthalpy data (open black squares) have been shifted vertically by 0.24 J/g for comparison with the heating data.

The ODT is evident as a sharp peak in the $\Delta C(T)$ in the data extracted from both the heating (disordering) and subsequent cooling (ordering) branches of the heat pulse. There is a small (≤ 1.5°C) hysteresis in the local maxima of $\Delta C(T)$ evident on heating and

cooling, characteristic of first-order phase transitions, although the onset temperature on both cooling and heating is nearly identical at 95 °C. This value of the onset temperature differs slightly from the previously reported T_{ODT}s measured by DSC (96 °C) and dynamic mechanical spectroscopy (93 °C), perhaps owing to differences in experimental conditions (e.g., different dT/dt and possible temperature gradients in the sample), small systematic errors in thermometry, and differences in how T_{ODT} is defined in the various methods of determination.[15]

Although the specific heat away from T_{ODT} extracted from the scanning mode measurements generally agree quite well with pseudostatic measurements away from the ODT, values extracted from the scanning mode measurements were systematically approximately 1% higher than values from pseudostatic measurements (i.e., $C_{BG}(T)$). This can be seen in Figure 6.9a, as the data at high and low temperature away from T_{ODT} do not approach exactly zero. This small discrepancy was deemed acceptable given the noise level and general quality of the scanning mode data, and may be due to the use of the simpler thermal model in the analysis of the scanning mode data (though sample coupling, a measure of thermal contact between the sample and platform,[198] was $\geq 98\%$ in all cases for pseudostatic measurements, where a value of 100% would indicate perfect coupling and strict validity of the simpler model of Figure 6.2 and eq 6.1).

The latent heat of the ODT can be extracted from the $\Delta C(T)$ data by integration to give the contribution to the enthalpy of the sample due to the phase transition, $H_o(T)$, defined as

$$H_o(T) = \int_{T_{ref}}^{T} \Delta C(T)\, dT + H_o\big|_{T=T_{ref}} \qquad\qquad 6.4$$

where $H_o\big|_{T=T_{ref}}$ is the enthalpy at the reference temperature T_{ref}, which in practice is taken to be zero (see section 6.7 for a simple derivation of eq 6.4). The reference temperature is chosen as the initial temperature for a given heating or cooling branch of a temperature pulse. $H_o(T)$ calculated from the data of Figure 6.9a is given in Figure 6.9b. The latent heat ΔH_{ODT} is clearly evident as the magnitude of the step-like change in $H_o(T)$ at the ODT. A small, constant offset was subtracted from the $\Delta C(T)$ data prior to integration to

account for the lack of perfect agreement between $C_{BG}(T)$ and the $C(T)$ extracted from the scanning mode measurement away from the ODT. This correction has no influence on the extracted latent heat. In addition, we note that eq 6.4 assumes that the heat capacity measured in these experiments is C_p, the constant pressure heat capacity. While this is not precisely true (the polymer samples were hermetically sealed in the encapsulating DSC pans with some air at ambient pressure and temperature and then heated to the measurement temperature, resulting in a small change in pressure within the sample pan), the polymer liquids of interest are essentially incompressible and the changes in pressure are thus not significant.

The values of ΔH_{ODT} extracted from the data in Figure 6.9 on heating and cooling are both 0.25 J/g. A total of 10 separate scanning mode temperature pulse experiments were conducted to measure ΔH_{ODT} for the IL-1 polymer using the optimized conditions ($T_o = 90$ °C, $\Delta T \approx 15$ °C) for two separately prepared test samples. The temperature profile prior to initializing the pulse was varied, with different controlled cooling rates from the disordered state and annealing times tested. All experiments yielded similar results to those shown in Figure 6.9, with the value of ΔH_{ODT} being approximately the same on heating and cooling, 0.262 ± 0.008 and 0.26 ± 0.02 J/g, respectively, though there was more variability in the data extracted from the cooling branches (quoted errors are standard deviations of the data sets). Combining all the data yields an average value for the latent heat of $\Delta H_{ODT} = 0.26 \pm 0.02$ J/g.

6.5 Discussion

6.5.1 *Relaxation calorimetry as a polymer characterization tool*

We have shown that relaxation calorimetry using the PPMS instrument complements DSC as a convenient thermal analysis technique for measuring the equilibrium heat capacity and latent heat of phase transitions in block polymers. The ability to equilibrate a specimen at the initial experimental temperature arbitrarily close to T_{ODT} for any amount of time prior to initiating a temperature pulse measurement is a key advantage to the technique relative to DSC. In DSC experiments, transient behavior upon

changes in temperature ramp rate necessitate elaborate thermal profiles to ensure flat baselines, and equilibrium behavior can only be deduced by extrapolating to zero temperature ramp rate.[15] Relaxation calorimetry is thus an excellent technique for accurate measurements of the equilibrium values of heat capacity and ΔH_{ODT}.

While relaxation calorimetry can be an important experimental tool for thermal characterization of block polymers, there are a number of considerations and experimental constraints imposed by the currently marketed PPMS instrument, which is designed for studying hard materials at low (cryogenic) temperatures with a maximum operating temperature of approximately 130 °C (~400 K). The amplitude of the temperature pulse required to obtain high quality heat capacity data is proportional to absolute temperature (a typical value of the amplitude is 2% of the absolute temperature), necessitating the use of relatively large pulse amplitudes ($\Delta T = 10$–15 °C) to obtain data of sufficient quality to extract precise heat capacity and ΔH_{ODT} values in the experiments described here conducted near 100 °C. Furthermore, since the relaxation time τ is proportional to heat capacity, which generally increases with temperature, higher experimental temperatures necessitate longer experimental times. Therefore, this technique is most applicable to block polymers characterized by relatively low block T_gs (e.g., rubbery blocks at ambient conditions) and designed to have a low T_{ODT}. This would allow more accurate data to be collected more quickly, with access to a broader range of pulse amplitudes.

6.5.2 *The order–disorder transition*

The value $\Delta H_{ODT} = 0.26 \pm 0.02$ J/g for IL-1 is very small relative to the heat of transition associated with the melting (crystallization) of polymers (e.g., $\Delta H_{melt} = 93$ J/g for polylactide crystals)[121] and falls at the low end of the range of previously reported values of ΔH_{ODT} for this material as measured by DSC (0.25–0.36 J/g).[15] The fact that DSC measurements appear to slightly overestimate ΔH_{ODT} is unsurprising. Since heat capacity generally increases with increasing temperature but at a decreasing rate (see Figure 6.4), the heat flow curves in a DSC thermogram are typically concave toward zero heat flow. Extraction of ΔH_{ODT} from DSC data by integrating a weak peak in a heat flow

curve (a peak that is often smeared over a fairly large temperature range due to the relatively fast temperature ramp rates required in DSC) using an arbitrarily drawn linear baseline is subject to considerable error.

The general agreement of the more accurate relaxation calorimetry measurements with the previously reported DSC values[15] for the latent heat of the ODT strengthens the main conclusions of Lee et al. discussed above: that, as a result of strong thermally driven composition fluctuations in the disordered state, the ODT for block polymers of low molecular weight proceeds as a pattern transition, as depicted in Figure 6.1, and not as a demixing transition. In addition to corroborating and improving upon the accuracy of DSC measurements of ΔH_{ODT}, we were interested in attempting to measure any manifestation of pretransitional composition fluctuations on the heat capacity very near T_{ODT}. Specifically, we set out to document evidence of the underlying second-order-like character associated with the composition fluctuations similar to the behavior found in certain liquid crystal phase transitions.[25] However, the relaxation calorimetry data do not reveal any evidence of pretransitional composition fluctuations in the disordered (or ordered) state near T_{ODT}. We attribute this result to the broad range of temperatures in the disordered state over which fluctuations develop, beginning at least 50 °C above T_{ODT} in IL-1, as evidenced by curvature in the inverse SAXS peak intensity $I(q^*)$ with inverse temperature.[90] As a consequence, any signature of these fluctuations in the heat capacity will be spread over an equally broad range of temperature prior to the first-order transition at the ODT.

What is instead evident in the relaxation calorimetry data is a first-order phase transition with a small but nontrivial breadth in transition temperature, $\Delta T_{\text{ODT}} \approx 1.5$ °C. The effective temperature ramp rate of the scanning mode relaxation calorimetry measurements reported here was approximately 2 °C/min near T_{ODT} (see Figure 6.2). This modest temperature ramp rate perhaps contributed to the apparent transition breadth, although evidence of completion of the phase transition in a matter of seconds, as documented by SAXS measurements during heating and cooling of IL-1, argues against this interpretation.[15] In order to further explore this possibility, DSC measurements of

ΔT_{ODT} were conducted at various temperature ramp rates ranging from 10 to 0.1 °C/min as shown in Figure 6.10. Even at the slowest ramp rates, ΔT_{ODT} is never observed to be narrower than ~ 1 °C. The documented breadth of the ODT may be due to a variety of factors arising from both fundamental thermodynamics and experimental nonidealities, including dispersity in polymer molecular weight (leading to a two-phase window), a distribution of T_{ODT}s resulting from the distributions of grain sizes in the sample[205] (which would be sensitive to the details of the polycrystalline grain structure and therefore the precise thermal history during ordering), temperature gradients that may exist in the sample, and smearing effects resulting from data processing and analysis routines.
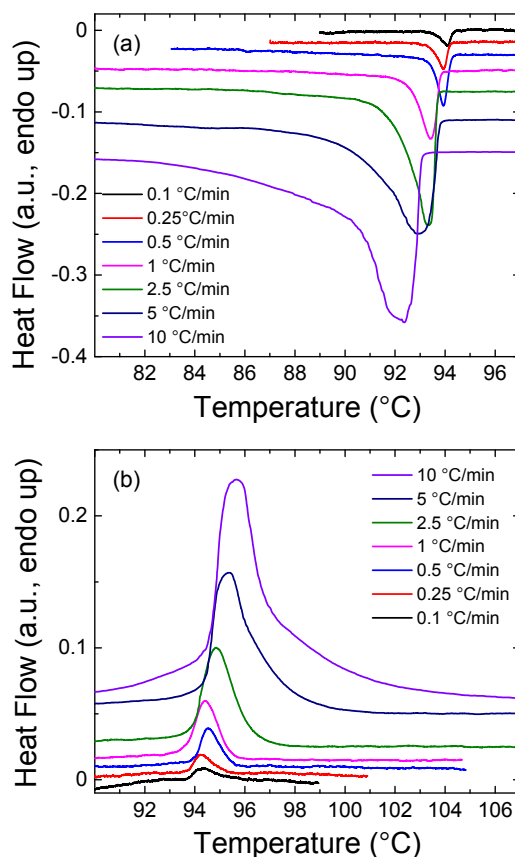
Figure 6.10 DSC measurements of the ODT breadth. Background-subtracted differential scanning calorimetry data collected on (a) cooling and (b) heating for the IL-1 polymer near the ODT for various temperature ramp rates. Curves have been shifted vertically for clarity.

While it is not possible to definitively sort out these possibilities, we can use the value of ΔH_{ODT} measured here to estimate the influence of polymer chain length dispersity on ΔT_{ODT}. For simplicity, we approximate the continuous molecular weight distribution of the IL-1 polymer as a simple binary mixture of two hypothetical diblock copolymers of different but exactly uniform molecular weights, M_1 and M_2. This approximation allows us to calculate the two-phase window at the ODT using established analytical theory commonly employed to model T–x–y phase diagrams for the melting of

a binary mixture that forms an ideal solution in both the solid and liquid phases.[206] Phase boundaries in the $T - x_1^{DIS} - x_1^{LAM}$ plane are given by

$$x_1^{DIS} = \frac{1 - \exp\left[\frac{\Delta\underline{H}_{m,2}}{RT}\left(1 - \frac{T}{T_{m,2}}\right)\right]}{\exp\left[\frac{\Delta\underline{H}_{m,1}}{RT}\left(1 - \frac{T}{T_{m,1}}\right)\right] - \exp\left[\frac{\Delta\underline{H}_{m,2}}{RT}\left(1 - \frac{T}{T_{m,2}}\right)\right]} \qquad 6.5$$

and

$$x_1^{LAM} = \frac{1 - \exp\left[-\frac{\Delta\underline{H}_{m,2}}{RT}\left(1 - \frac{T}{T_{m,2}}\right)\right]}{\exp\left[-\frac{\Delta\underline{H}_{m,1}}{RT}\left(1 - \frac{T}{T_{m,1}}\right)\right] - \exp\left[-\frac{\Delta\underline{H}_{m,2}}{RT}\left(1 - \frac{T}{T_{m,2}}\right)\right]} \qquad 6.6$$

where x_1^{DIS} and x_1^{LAM} are the mole fractions of the hypothetical polymer of molecular weight M_1 in the high temperature disordered phase (analogous to the liquid phase) and the low temperature ordered lamellar phases (analogous to the solid phase), respectively, $\Delta\underline{H}_{m,i}$ and $T_{m,i}$ are the estimated specific molar latent heat of the ODT and T_{ODT} of polymer of molecular weight M_i, and R is the gas constant. The width of the two-phase window ΔT_{ODT} is taken as the difference in temperature of x_1^{DIS} and x_1^{LAM} at a fixed composition x_1. This approach is enabled by the precise measurement of the latent heat of the ODT reported here, a key parameter in this simple model. On the basis of this approach, we have estimated the two-phase window ΔT_{ODT} for binary pairs of hypothetical IL polymers that when mixed with either (1) equal mole fraction or (2) equal mass fraction, yield a number-average molecular weight M_n = 2750 g/mol, the experimental M_n of IL-1, and dispersities $Đ$ that ranged from 1.0001 to 2 as summarized in Figure 6.11. The specific (mass) latent heat was taken as ΔH_{ODT} = 0.26 J/g for all polymers. T_{ODT}s for the hypothetical polymers were approximated by assuming $(\chi N)_{ODT}$ is the same for all polymers and equal to the experimentally observed value for IL-1 using the previously reported function for $\chi_{IL}(T)$ (i.e., $\chi_{IL}(T) = 230/T - 0.38$).[15] For values

of $Đ$ less than 1.01 ΔT_{ODT} is estimated to be a small fraction of 1 °C ($\Delta T_{ODT} \leq 0.1$ °C; see Figure 6.11d). However, as $Đ$ increases to 1.10, the value experimentally measured by SEC for IL-1, ΔT_{ODT} is estimated to be 1.3 °C as is shown in Figure 6.11c. This value is close to the experimentally observed breadth of the ODT of IL-1 of approximately 1.5 °C.

Dispersity is known to have an impact on the phase behavior of block polymers,[207] influencing properties such as the domain spacing, ODT location, and the ranges in block composition over which the various low temperature ordered phases are stable, often in ways that depend on the details of the particular materials being studied (e.g., segregation strength).[47,115,207–209] In addition, how dispersity influences phase behavior is not reducible simply to the value of $Đ$ but depends on the details of the molecular weight distributions of the polymers or individual blocks.[47] Recognizing that the hypothetical binary blend used to construct Figure 6.11 is a poor approximation of the unimodal continuous molecular weight distribution of IL-1 (see Figure 6.11a), these calculations are not meant to be quantitatively predictive. Notwithstanding the crude nature of this simple model, these results nevertheless suggest that dispersity plays a significant role in the observed finite breadth of the ODT phase transition in IL-1.
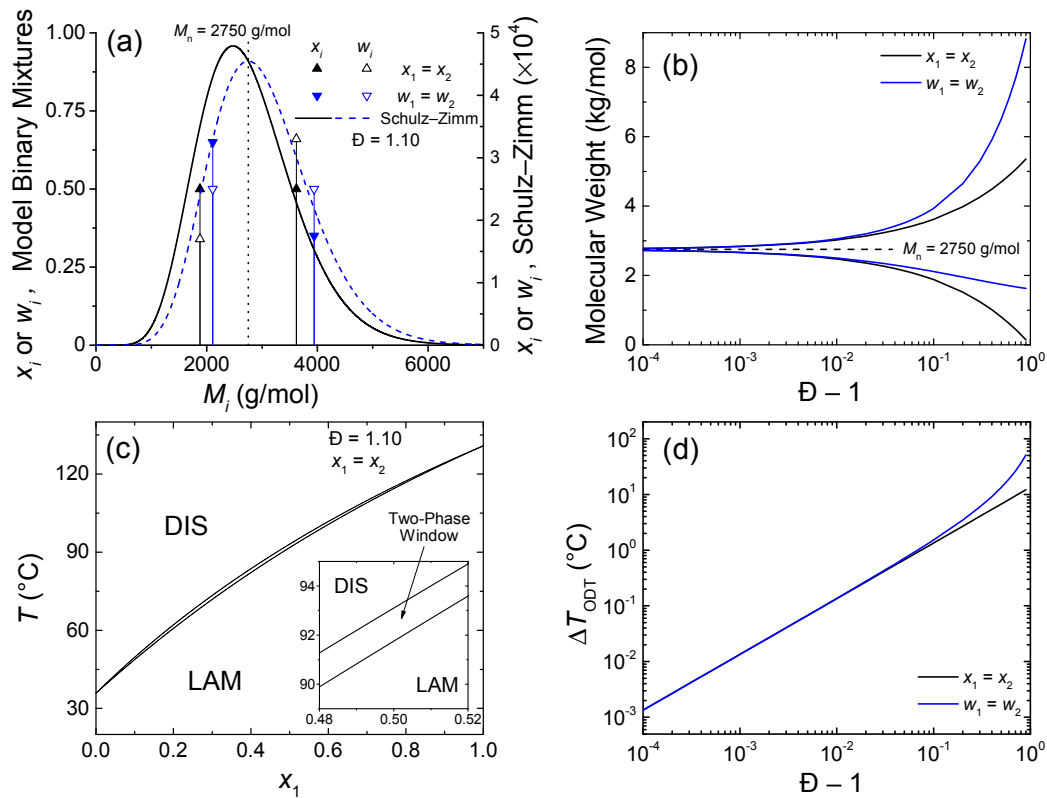
Figure 6.11 Calculation of ODT breadth. (a) Example of the hypothetical binary mixtures for the cases of equal mole x_i and weight fraction w_i that yield $M_n = 2750$ g/mol and a dispersity $Đ = 1.10$ equal to that measured for the IL-1 polymer compared with a continuous Schultz–Zimm distribution with and equivalent M_n and $Đ$. (b) Molecular weights of the constituents of hypothetical binary mixtures that yield $M_n = 2750$ g/mol for various values of $Đ$. (c) Computed $T - x_1^{DIS} - x_1^{LAM}$ phase diagram for the hypothetical binary mixture ($M_1 = 3620$ g/mol, $M_2 = 1880$ g/mol) that at $x_1 = x_2 = 0.5$ has $M_n = 2750$ g/mol and $Đ = 1.10$. The inset shows an expanded view of the two-phase window near $x_1 = x_2 = 0.5$ where $\Delta T_{ODT} = 1.3$ °C. (d) ΔT_{ODT} as a function of $Đ$ for the two series of hypothetical binary mixtures.

In principle, multiphase windows should separate all single-phase regions of the phase diagram for real block polymers (i.e., not strictly uniform molecular weight) as they are not true single-component systems. However, in practice two-phase windows are thought to be quite small and are rarely observed experimentally in neat block polymer systems of typical modest dispersities ($Đ \leq 1.1$). For larger values of $Đ$, sizable

dispersity-induced two-phase windows separating the various ordered phases are anticipated by self-consistent mean-field theory (SCFT).[36] However, SCFT is not accurate near the fluctuation-induced ODT of block polymers of finite molecular weight and therefore cannot provide insight into the influence of dispersity on the breadth of the ODT. Experimentally, binary blends of chemically similar diblock copolymer differing only in molecular weight, much like the hypothetical blends of Figure 6.11 but of higher average molecular weight and with $Đ \approx 1.3$, exhibit broad ODTs ($\Delta T_{ODT} \approx 10–20$ °C).[210] The observed breadth of the ODT in IL-1 ($\Delta T_{ODT} \approx 1.5$ °C), attributed here to dispersity, is consistent with relatively low dispersity (measured $Đ = 1.10$) and unimodal molecular weight distribution when compared to blends of Almdal et al.[210]

An additional intriguing feature of the ODT in IL-1 is the lack of any sizable hysteresis in the first-order ODT. This invites the interesting conjecture that there is no energy barrier to be overcome when transitioning between the lamellar and disordered state, perhaps signifying the existence of a stability limit very close to T_{ODT}.

6.6   Summary and Conclusions

Relaxation calorimetry using a commercial PPMS instrument was adapted to measure the temperature dependence of the heat capacity and the latent heat of the ODT ($\Delta H_{ODT} = 0.26 \pm 0.02$ J/g) for a symmetric poly(1,4-isoprene-b-D,L-lactide) diblock copolymer. The measured value of the latent heat agrees with previous measurements using DSC and reinforces the importance of fluctuations on the phase behavior of low molecular weight block polymers. In addition, these measurements demonstrate the utility of relaxation calorimetry as a thermal characterization tool for block polymers near phase transitions, particularly for material with low T_gs and T_{ODT}s.

6.7   Supplemental Information: Derivation of Equation 6.4

Constant pressure heat capacity is defined as

$$C_p = \left(\frac{\partial H}{\partial T} \right)_p \qquad\qquad 6.7$$

Therefore changes in enthalpy from a given reference state with enthalpy $H\big|_{T=T_{ref}}$ at T_{ref} can be given by

$$H(T) - H\big|_{T=T_{ref}} = \int_{T_{ref}}^{T} C_p(T) dT \qquad\qquad 6.8$$

Here we take the total heat capacity as the sum of the background temperature dependence of the IL-1 heat capacity $C_{p,BG}$ and the heat capacity due to the ODT phase transition ΔC_p given by

$$C_p(T) = C_{p,BG}(T) + \Delta C_p(T) \qquad\qquad 6.9$$

Combining eqs 6.8 and 6.9 gives

$$H(T) - H\big|_{T=T_{ref}} = \int_{T_{ref}}^{T} C_{p,BG}(T) dT + \int_{T_{ref}}^{T} \Delta C_p(T) dT \qquad\qquad 6.10$$

which can also be written as

$$H(T) - H\big|_{T=T_{ref}} = \left[H_{BG}(T) - H_{BG}\big|_{T=T_{ref}} \right] + \left[H_o(T) - H_o\big|_{T=T_{ref}} \right] \qquad\qquad 6.11$$

where H_{BG} is the contribution to the enthalpy due to the background temperature dependence of the heat capacity and H_o is the contribution to the enthalpy arising due to the additional heat capacity resulting from the ODT (the latent heat). Comparing eqs 6.10 and 6.11 yields eq 6.4

$$H_o(T) = \int_{T_{ref}}^{T} \Delta C(T) dT + H_o\big|_{T=T_{ref}} \qquad\qquad 6.12$$

Chapter 7:

Fluctuations, Phase Transitions, and Latent Heat in Short Diblock Copolymers: Comparison of Experiment, Simulation, and Theory[*,†]

7.1 Introduction

Short diblock copolymers currently occupy an interesting position at the intersection of exciting new technological applications (e.g., block copolymer lithography[10]) and interesting scientific questions regarding the physics of block polymer self-assembly. From a fundamental point of view, low molecular weight block polymers represent a large departure from the expected range of validity of the classical self-consistent-field theory (SCFT) and the Fredrickson–Helfand (FH) theory of block copolymer melts, which are expected to be accurate only in the limit of very long chains.[16,17,37] Short diblock copolymers thus provide a particularly stringent test case for

---

newer theories that aim to describe a wider range of parameters. Moreover, advances in computing power and analysis methods have now made it feasible to conduct and unambiguously interpret simulations with parameters similar to those of experimental systems.[48,59–61,211] This confluence of circumstances enables direct quantitative comparisons of experiments, simulations, and theory. Here, we report a comparison of results of small-angle X-ray and neutron scattering (SAXS and SANS) and calorimetry experiments on a low molecular weight poly(1,4-isoprene-*b*-DL-lactide) diblock copolymer to the results of coarse-grained simulations, and to predictions of the renormalized one-loop (ROL) theory developed by Morse and co-workers.[56,57]

In what follows, we compare experimental results to results of simulations of very simple bead–spring models and to theoretical predictions that are based on an even more simplified model of polymer chemistry.[48,56,57,59–61,211] Such comparisons can succeed only if the thermodynamic behavior of diblock copolymer melts is highly universal. Coarse-grained theories for block copolymers yield predictions that depend on only a small set of dimensionless state parameters. Specifically, SCFT yields predictions for diblock copolymers that depend only on composition (i.e., the volume fraction of one of the blocks), the ratio of the statistical segment lengths, and the product $\chi_e N$.[16,37] Here, χ_e is an effective segment–segment interaction parameter, and N is a corresponding volumetric degree of polymerization. More sophisticated post-self-consistent-field theories, including both the FH and ROL theories, yield predictions that depend on these parameters and on the invariant degree of polymerization $\bar{N}$.[17,56,57] The quantity $\bar{N}$ is a measure of the degree of overlap among polymers in a dense liquid and is defined as $\bar{N} \equiv N b^6 / v_o^2$, where b is the statistical segment length and v_o is the monomer reference volume.

One of the main challenges when attempting to make comparisons among any combination of experiments, simulation, and theory is the need to estimate χ_e for specific chemical systems or simulation models. Experimental or simulation data must generally be fit to some theoretical prediction to estimate how χ_e depends upon temperature in experiments or upon temperature or some other control parameter in simulations. The

quality of the resulting estimates of χ_e then, of course, depends on the accuracy of the theory used for this fit.

Recently, Morse and co-workers have made significant advances in the interpretation of coarse-grained simulations of symmetric diblock copolymers, which have allowed consistent results to be obtained from different simulation models.[5–8] A key element of their approach was to estimate the parameter dependence of χ_e for each simulation model of interest by fitting results for the structure factor $S(q)$ in the disordered phase to predictions of the ROL theory.[60] The ROL theory was found to provide an excellent simultaneous fit to results for $S(q)$ from several simulation models over a wide range of chain lengths and values of $\chi_e N$. A subsequent study of the order–disorder transition (ODT) then showed that consistent results could be obtained from several simulation models for a variety of thermodynamic properties, including the free energy per chain, the latent heat of transition, and $(\chi_e N)_{ODT}$, the value of $\chi_e N$ at the ODT, *if* all results were analyzed using estimates of χ_e that were obtained in the same manner (i.e., by fitting simulation results for $S(q)$ to the ROL theory).[48,59] Specifically, it was shown that estimated values of $(\chi_e N)_{ODT}$ from different simulation models and chain lengths collapse onto a common curve when plotted vs the invariant degree of polymerization $\bar{N}$, which is well approximated by

$$\left(\chi_e N\right)_{ODT} = 10.495 + 41.0\bar{N}^{-1/3} + 123.0\bar{N}^{-0.56} \tag{7.1}$$

The first two terms of this empirical relationship for the dependence of $(\chi_e N)_{ODT}$ upon $\bar{N}$ give the prediction of the FH theory. The difference between this expression and the FH prediction (i.e., the magnitude of the last term) is relatively small for $\bar{N} > 10^4$, but is significant for values of $\bar{N}$ typical of many experiments, including those presented here.

This chapter presents the first attempt to carefully compare experimental results to this body of simulation data, using closely analogous data analysis methods to analyze experimental and simulation results. Here, we analyze experimental scattering and thermal measurements of low molecular weight poly(1,4-isoprene-*b*-DL-lactide) (IL) diblock copolymers. The comparison takes advantage of an unusually comprehensive set

of measurements for one polymer, denoted IL-1, including a previously reported measurement of the latent heat associated with the ODT, ΔH_{ODT} (see Chapters 3 and 6 for details).[15] Results of SAXS and SANS experiments from IL-1 are compared to the ROL theory in order to estimate the dependence of $\chi_e(T)$ upon temperature T in IL copolymers in a manner analogous to that used by Morse and co-workers in their analysis of simulations (and which differs from the approach used to approximate $\chi_e(T)$ in Chapter 3. Results of scattering experiments from the same sample are combined in a manner that allows us to leverage the advantages of both techniques, specifically the availability of simple methods to calibrate the absolute scattering intensity in SANS experiments and the higher wavenumber resolution available in synchrotron SAXS experiments. The resulting estimate of $\chi_e(T)$ is then used to directly compare simulation results to experimental measurements of the latent heat of transition of this sample and to the value of $(\chi_e N)_{ODT}$ for this and several other IL diblock copolymers.

The remainder of this chapter is organized as follows: We first present details of experimental measurements. We then present our analysis of experimental results from the IL-1 polymer, including the comparison of scattering measurements to the ROL theory, and a comparison of simulation and experimental results for ΔH_{ODT} and $(\chi_e N)_{ODT}$. Finally, we compare simulation results to experimental results for $(\chi_e N)_{ODT}$ for several other nearly symmetric IL diblock copolymers of varying molecular weight and state our conclusions.

7.2 Experimental Section

7.2.1 Materials

Experiments described here were conducted on a poly(1,4-isoprene-*b*-DL-lactide) (IL) diblock copolymer designated IL-1. The synthesis, molecular characterization, and extensive thermodynamic characterization of this material have been previously described (see Chapters 2 and 3 for details).[15] Briefly, the total number-average molecular weight M_n of 2750 g/mol is divided between the poly(1,4-isoprene) (PI) (1130 g/mol) and poly(DL-lactide) (PLA) (1620 g/mol) blocks and was determined using [1]H

NMR experiments. The molecular weight dispersity $Đ$ = 1.10 was determined by size exclusion chromatography (SEC) using tetrahydrofuran as the mobile phase (this value is slightly smaller than reported previously, attributable to the use of a different SEC instrument and a different solvent).[15] The volume fraction of PLA in IL-1 is 0.51 ± 0.01 based on published densities[104,200] and the volumetric degree of polymerization N = 39, calculated using the reference temperature and repeat unit reference volume v_o of 140 °C and 118 Å^3, respectively, used throughout this chapter. We note that the reference volume and reference temperature used here differ from those used in our previously published study on the thermodynamic of IL block polymers and in Chapter 3.[15] In addition to extensive characterization of IL-1, comparisons are made based on the previously reported thermodynamic properties of additional nearly symmetric IL diblock copolymers, IL-2, -3, -7, and -10, that have volume fractions of 0.54, 0.54, 0.55, and 0.50 and N values of 50, 51, 63, and 58, respectively, calculated as described above for the reference volume and temperature used in this chpater.[15] All experimental values of N in this chapter are subject to an uncertainty of approximately ± 5% resulting from uncertainties involved with molecular characterization.

7.2.2 *Thermal measurements*

The glass transition temperatures, T_g, of the PI and PLA blocks of IL-1, measured by differential scanning calorimetry (DSC) experiments, are −61 and 20 °C, respectively. The symmetric IL-1 diblock forms an ordered lamellar (LAM) phase below the order–disorder transition temperature T_{ODT} = 96 ± 1 °C as determined by DSC. IL-2, -3, -7, and -10 have reported T_{ODT} values determined by DSC of 114, 157, 112, and 147 °C, respectively (see Chapter 3).[15] In Chapter 3, extensive thermal characterization using DSC of the ODT in IL-1 was detailed.[15] The equilibrium value of the latent heat (enthalpy) of the ODT (ΔH_{ODT}) for IL-1 was measured in the range of 0.25–0.36 J/g, depending on details of the measurement (e.g., dT/dt and application of an annealing step).[15] For reliable measurements of ΔH_{ODT}, the DSC experiments required relatively fast temperature ramp rates (dT/dt ≥ 5 °C/min) and elaborate thermal profiles to ensure suitable signal-to-noise levels and flat baselines near the transition. To overcome these

limitations and corroborate the DSC measurements of ΔH_{ODT}, a different type of calorimetric experiment, relaxation calorimetry,[197] was performed to measure ΔH_{ODT} of IL-1. The details of these experiments are summarized in Chapter 6. Here we simply report the main result that ΔH_{ODT} of IL-1 was measured to be 0.26 ± 0.02 J/g, in general agreement with the DSC measurements. This builds confidence that the true equilibrium value of ΔH_{ODT} is being measured by both techniques and is approximately 0.3 J/g.

7.2.3   *Small-angle neutron scattering (SANS)*

Neutron scattering experiments were performed on the NG7 30 m SANS instrument at the National Institute of Standards and Technology Center for Neutron Research (NCNR) using a neutron wavelength of $\lambda = 6$ Å, a wavelength spread $\Delta\lambda/\lambda = 0.115$, and a sample-to-detector distance of 2 m.[212] The SANS data were corrected for background and empty cell scattering, sample transmission, sample thickness, and detector efficiency. The 2D data were converted to an absolute intensity scale, differential scattering cross section per unit volume, using measurements of the direct beam flux then radially averaged to obtain 1D plots of intensity versus the magnitude of the scattering momentum transfer vector $q = 4\pi\lambda^{-1}sin(\theta/2)$, where θ is the scattering angle. Data correction and reduction were accomplished with the NCNR SANS software package used with WaveMetrics Igor Pro.[213] Polymer samples were loaded into custom fabricated quartz banjo-style cells with path lengths of approximately 1 mm; precise sample path lengths were determined by subtracting the measured window thicknesses from the overall cell dimension. The cells were sealed in an inert argon atmosphere glovebox using Permtex High-Temp Red RTV silicone gasket maker to prevent oxidative degradation of sample from occurring upon heating. The SANS patterns for IL-1 were collected on heating in a temperature control heating block at 105, 125, 165, and 185 °C. At each temperature, the sample was equilibrated for 5 min after the heating block had reached the desired set point before SANS patterns were recorded. The various calibration measurements (e.g., direct beam, background, empty cell, sample transmission, etc.) were collected at 105 °C. This temperature profile was designed to minimize the amount of time the sample experienced elevated temperatures to prevent

polymer degradation. IL-1 SANS patterns were corrected for incoherent scattering by subtracting the sum of the measured q-independent incoherent scattering from PI (M_n = 2640 g/mol, Đ = 1.06) and PLA (M_n = 9,200 g/mol, Đ = 1.46)[*] homopolymers weighted by their respective volume fractions in the IL-1 diblock copolymer. Incoherent scattering from the homopolymers was measured at 105 and 185 °C, and linear interpolation was used to estimate the values at intermediate temperatures.

7.2.4   *Small-angle X-ray scattering (SAXS)*

SAXS experiments were conducted on the DND-CAT 5-ID-D beamline at the Advanced Photon Source (Argonne National Laboratory).[160] Experiments utilized a sample-to-detector distance of 7495 mm and an X-ray wavelength of λ = 0.729 Å. 2D SAXS patterns were collected with a Rayonix area CCD detector. All SAXS patterns were azimuthally symmetric and were integrated to obtain 1D plots of intensity (in arbitrary units) versus q. The IL-1 sample was loaded in a 1.5 mm nominal diameter quartz capillary (Charles Supper Company), and the temperature was controlled during experiments with a modified Linkam HFS91 hot stage. Prior to data collection, the sample was heated to 125 °C, well above the order–disorder transition temperature (see below), to eliminate any effects due to processing history, then slowly cooled (ca. 1 °C/min) to 80 °C, a protocol known to produce a well-ordered equilibrium LAM phase.[15] The sample was then heated to 185 °C, while stopping at several temperatures to collect scattering patterns. The sample was equilibrated at each temperature for approximately 1 min prior to data collection. Changes in temperature between measurements were fast (> 20 °C/min). Data were similarly collected at several temperatures on cooling to 90 °C.

7.3   Results and Analysis

Most of our analysis is based on scattering measurements on the IL-1 polymer. We discuss how SAXS and SANS measurements were compared to ROL predictions in order to obtain estimates of the statistical segment lengths and of $\chi_e(T)$ and how these estimates were used to compare experimental results for the latent heat of transition and

---

[*] PLA homopolymer synthesized by Debbie Schneiderman.

T_{ODT} of this sample to corresponding simulation results. We then compare simulation results to experimental results for $(\chi_e N)_{\mathrm{ODT}}$ computed using the extracted estimate of $\chi_e(T)$ for several other nearly symmetric IL diblock copolymers of varying molecular weight.
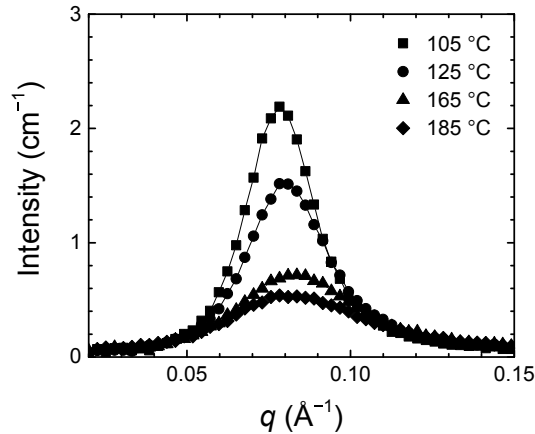
Figure 7.1 Experimental IL-1 SANS patterns.

7.3.1   Calibrating SAXS with SANS

To experimentally determine the peak position q^* and peak intensity $I(q^*)$ in the disordered (DIS) phase for IL-1 ($T_{\mathrm{ODT}} \approx 96$ °C, LAM at $T < T_{\mathrm{ODT}}$), we have used a combination of SANS and SAXS measurements that capitalizes on the advantages of both experimental methods. Specifically, a small number of SANS measurements were used to calibrate the intensity scale of a larger series of synchrotron SAXS measurements. This strategy overcomes instrument-smearing effects that lead to lower q resolution in SANS measurements by taking advantage of the excellent q resolution and much faster data collection of synchrotron SAXS. Using this strategy, it is possible to obtain high quality scattering data with an absolute intensity scale over a wide range of elevated temperatures quickly, avoiding the risk of degradation of the labile IL-1 material inherent in the longer experimental times required if SANS experiments alone were used.
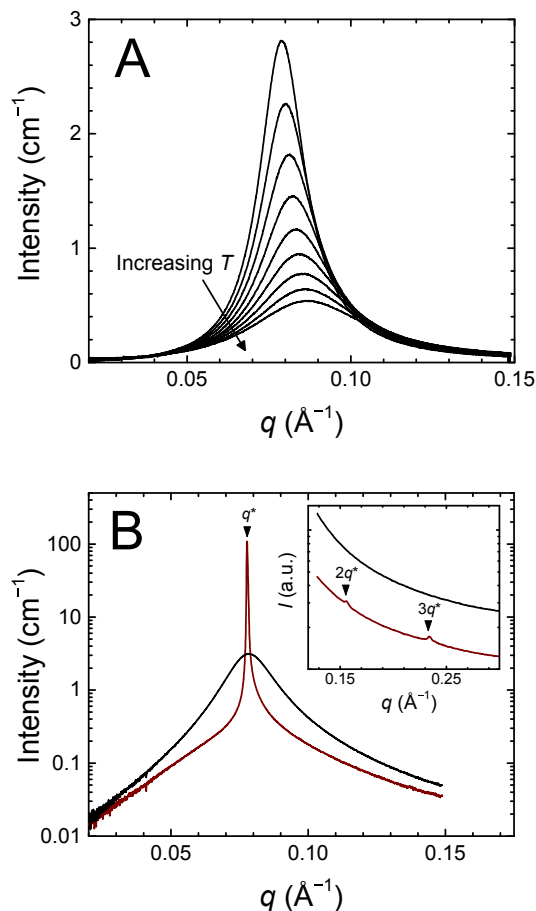
Figure 7.2 Experimental IL-1 SAXS patterns. (A) Selected patterns in the DIS phase collected at 105, 115, 125, 135, 145, 155, 165, 175, and 185 °C on heating. (B) A comparison of SAXS patterns in the DIS phase at 100 °C (black lines) and the ordered LAM phase at 90 °C (red lines). High q data collected on the MAXS detector are shown in the inset (note that the intensity scales of the MAXS and SAXS data are not equivalent). Data in the inset have been shifted vertically for clarity.

Isothermal SANS patterns for IL-1 collected at four temperatures while heating in the DIS phase (i.e., above T_{ODT}) are shown in Figure 7.1. Isothermal SAXS patterns were collected every 5–10 °C from a minimum temperature of 80 °C (LAM phase) to a maximum temperature of 185 °C in the DIS phase during heating and cooling. Selected SAXS patterns are shown in Figure 7.2. For all temperatures above T_{ODT}, a single broad peak characteristic of the DIS phase is observed in the SANS and SAXS patterns,[16,214]

becoming less intense at higher temperatures, as can be seen in Figure 7.1 and Figure 7.2.A. As shown in Figure 7.2.B, the SAXS patterns are dramatically different below T_{ODT}. A narrow, intense primary peak appears (note the log scale on the intensity axis in Figure 7.2.B) with higher order Bragg peaks at relative positions $q/q^* = 2$ and 3, consistent with an ordered LAM phase as previously reported for the IL-1 polymer (see Chapter 3).[15] In these experiments, the higher order Bragg reflections ($q/q^* = 2, 3$) were above the experimentally accessible maximum q of the SAXS detector but were captured on the so-called middle angle (MAXS) detector of the recently upgraded instrument at the DND-CAT 5-ID-D beamline, as shown in the inset of Figure 7.2.B.[160] We note that the background subtraction and calibration routine as described here for the SAXS data was not performed on the MAXS data. Therefore, the MAXS data in the inset of Figure 7.2.B are presented on arbitrary relative intensity scale that differs from the intensity scale of the SAXS data. For a comprehensive set of SAXS data in the LAM phase for IL-1, see Chapter 3 or Lee et al.[15]

The SAXS data presented here were collected on a relative intensity scale. To determine $S^{-1}(q^*)$, the quantity required for comparison to theory and simulation, it was necessary to convert the experimental SAXS data to an absolute intensity scale. This process was accomplished using the absolute calibrated SANS data with a method outlined in Figure 7.3. The SAXS patterns were smeared with the known instrument resolution function for the configuration used during SANS data collection as shown in Figure 7.3.A. The peak intensity $I(q^*)$ was then extracted from the smeared SAXS data and the (inherently smeared) SANS data at each experimental temperature. $I^{-1}(q^*)$ were plotted as a function of T^{-1}. The data set extracted from the smeared SAXS data was scaled by a single calibration factor adjusted to allow the SAXS data to overlay the absolute intensity SANS data on the $I^{-1}(q^*)$ versus T^{-1} plot, as shown in Figure 7.3.B. This procedure allows us to convert the SAXS data to the absolute intensity scale of the SANS measurements (i.e., the differential scattering cross section per unit volume based on the scattering length density contrast in neutron scattering measurements). To convert the unsmeared SAXS patterns to the intensity scale appropriate to the SANS experiment

(shown in Figure 7.2), the extracted calibration factor is then applied to the full SAXS data set. The temperature dependence of $q*$ and $\Gamma^{-1}(q*)$ was extracted from the resulting calibrated, unsmeared SAXS data. The results are plotted in Figure 7.4 and Figure 7.5, respectively.
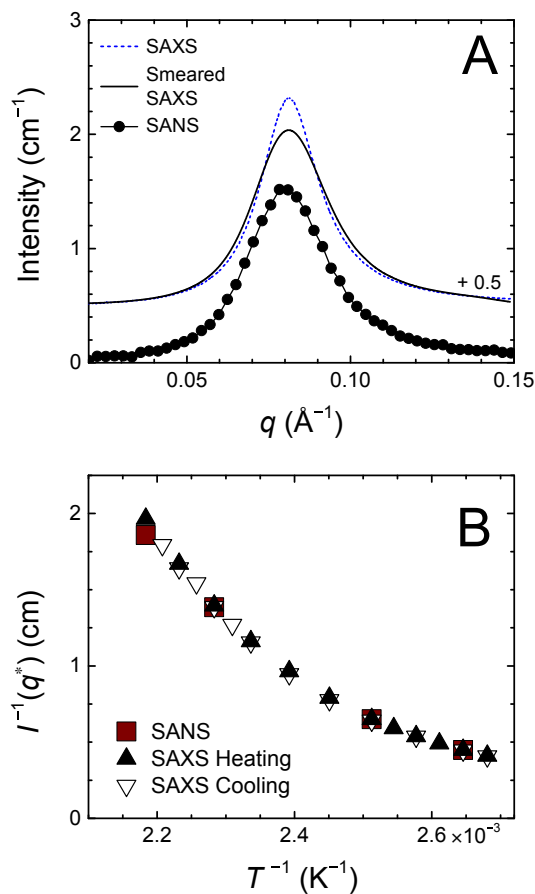
Figure 7.3 Routine used to convert SAXS patterns to the SANS absolute intensity scale. (A) SANS pattern, SAXS pattern, and SAXS pattern smeared with the SANS instrument resolution function, all collected at 125 °C. (B) $\Gamma^{-1}(q*)$ as a function of T^{-1} extracted from SANS (squares) and smeared SAXS measurements (triangles). The SAXS calibration factor of 5.13 is extracted by scaling the smeared SAXS data to overlay the SANS data.
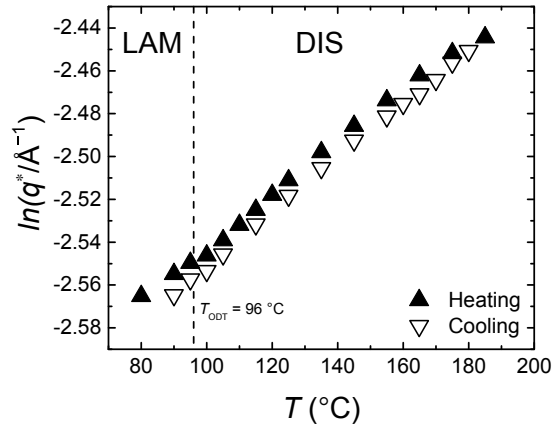
Figure 7.4 Temperature dependence of q^* extracted from SAXS measurements.

As shown in Figure 7.4, q^* changes continuously through the T_{ODT}, with no measurable discontinuity in q^* at the transition. The temperature dependence of q^* obtained here from isothermal SAXS measurements is consistent with that extracted previously from SAXS measurements collected for IL-1 during a dynamic heating ramp ($dT/dt = 10$ °C/min; see Chapter 3).[15]

The inverse peak intensity $\Gamma^1(q^*)$ shown in Figure 7.5 does exhibit a large discontinuous change at T_{ODT}. $I(q^*)$ for the primary Bragg peak in the LAM phase is orders of magnitude larger than that of the diffuse peak associated with the DIS phase, as seen in Figure 7.2.B. Departure from linearity in $\Gamma^1(q^*)$ on T^{-1} in Figure 7.5 is inconsistent with the prediction of the random phase approximation (RPA),[16,50,71,72] indicating that fluctuation effects are important throughout the experimentally accessible range of temperatures for this polymer. To convert the calibrated values of $\Gamma^1(q^*)$ of Figure 7.5 to the relevant quantities related to the structure factor for comparison to the ROL theory, the neutron scattering contrast factor must be taken into account. Specifically, using the notation used throughout this work and in Glaser et al.[60], $S(q^*) = I(q^*)/[v_o(\Delta SLD)]^2$, where (ΔSLD) is the difference in coherent neutron scattering length densities of the PI and PLA blocks (2.4×10^{-7} and 1.6×10^{-6} Å^{-2}, respectively, at 140 °C). We note that, as defined in Glaser et al.[60], $S(q)$ has the units of number concentration

of monomers and is related to the dimensionless structure factor common in the experimental literature, $S_{Exp}(q)$, through normalization by the monomer reference volume $S_{Exp}(q) = v_o S(q)$.
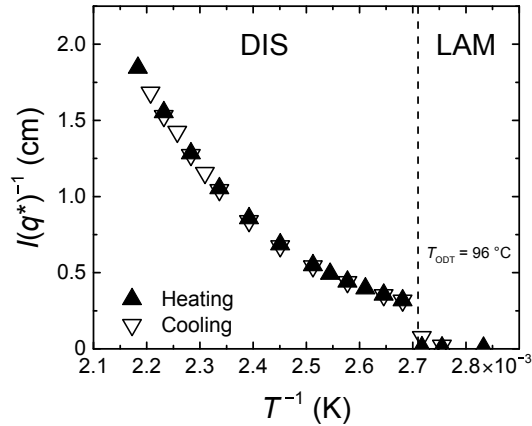
Figure 7.5 Temperature dependence of $I^{-1}(q^*)$ extracted from SAXS measurements.

7.3.2 Comparison of small-angle scattering to ROL theory

Here, we discuss the analysis required to estimate $\chi_e(T)$ by fitting ROL predictions to the scattering results discussed above. Before attempting such a fit, we must compute or estimate values for N and the monomer statistical lengths, which (along with χ_e) are required as inputs to the theory. In what follows, we define volumetric degrees of polymerization, statistical segment lengths, and an interaction parameter $\chi_e(T)$ using a fixed segment volume of $v_o = 118$ Å^3.

Volumetric degrees of polymerization for both blocks are calculated from the block molecular weights and densities of the pure materials. These are given by $N_I(T) = M_I/v_o N_A \rho_I(T)$ for PI and $N_L(T) = M_L/v_o N_A \rho_L(T)$ for PLA, where M_I and M_L are the number-average molecular weights of the two blocks, $\rho_I(T)$ and $\rho_L(T)$ are temperature-dependent densities of the two species, and N_A is Avogadro's number.[12,13] Because the densities of both pure materials vary with temperature, our use of a fixed monomer reference volume yields definitions for N_I and N_L that also vary slightly with temperature.

Values for the monomer statistical segment lengths b_I and b_L of the PI and PLA blocks can be assigned either by using literature values obtained from measurements on homopolymers of PI and PLA or by fitting the behavior of the peak wavenumber $q*$ obtained in our experiments to theoretical predictions. Below, we show comparisons of our experimental results for $q*$ to theoretical predictions using both methods. We focus on a comparison to predictions of the ROL theory because this theory was found to give accurate predictions for the behavior of $q*$ in simulations, thus allowing the ROL theory to be used a surrogate for the simulation results.[60]

Converting literature results to our chosen segment volume ($v_o = 118$ Å^3) yields statistical segment lengths $\ln[b_I(T)] = 1/2[0.0004T + 3.445]$ and $\ln[b_L(T)] = 1/2[0.00141T + 4.484]$ for PI and PLA, respectively, where $b_i(T)$ is given in Å.[116,117,215] This yields values of $b_I = 6.1$ Å, $b_L = 7.0$ Å and

$$\bar{N} = N(T)\frac{\left[f_I b_I^{\,2}(T) + f_L b_L^{\,2}(T)\right]^3}{v_o^{\,2}} = 231 \tag{7.2}$$

at a reference temperature of 140 °C.

A comparison of experimental results to various theoretical predictions for $q*$ is shown in Figure 7.6. There, we plot $q*$ vs a dimensionless quantity

$$\chi_a^* N \equiv 10.495 - cNS^{-1}(q*)/2 \tag{7.3}$$

as done in previous comparisons of simulation results to ROL theory where c is the number concentration of monomer units and equal to v_o^{-1}.[57,60,61,216] By definition, the quantity χ_a^*, known as the ''apparent'' interaction parameter, is the value of χ_e that would be inferred by fitting the measured inverse peak structure factor to the RPA prediction, $cNS^{-1}(q*) = 2(10.495 - \chi_e N)$. The advantage of plotting the data in this manner is that it allows a comparison of results for $q*$ to ROL predictions in a way that does not require us to first estimate how $\chi_e(T)$ depends on temperature.
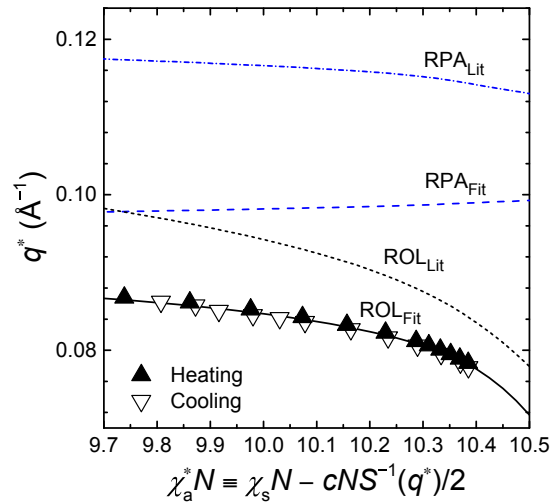
Figure 7.6 Fitting of the temperature dependence of q^* to the ROL theory. The predictions of the ROL and RPA theories in which the temperature dependence of the statistical segment length of IL-1 is approximated using reported literature values for the constituent homopolymers are the lines labeled "Lit". The ROL and RPA predictions in which the temperature dependence of the statistical segment length of IL-1 is fit using the ROL theory are the lines labeled "Fit". Experimental data are the symbols (triangles).

The simplest theoretical prediction is obtained from the RPA using literature values for the statistical segment lengths $b_I(T)$ and $b_L(T)$. This prediction, shown by the dashed line in Figure 7.6, (labeled RPA_{Lit}), is approximately 30% larger than the experimental values. Corresponding predictions of the ROL theory evaluated using these literature values for $b_I(T)$ and $b_L(T)$ are indicated by the line labeled ROL_{Lit}. Use of the ROL reduces the discrepancy, but yields predicted values of q^* that are still approximately 10% larger than experimental values.

Because the ROL theory has consistently yielded accurate predictions for the behavior of q^* in simulations,[60,61] we tentatively ascribe the remaining discrepancy between ROL predictions and experimental results to our use of statistical segment lengths that were obtained from experiments on homopolymers. Statistical segment lengths of polymers in a dense liquid are sensitive to changes in the environment of each block, which can cause changes in the probabilities of local conformational states (e.g.,

trans and gauche), and can thus be somewhat different in a polymer mixture than in a pure polymer melt. Any such sensitivity of the value of the statistical segment lengths to changes in local environment is conceptually distinct from the universal deviations from random walk behavior predicted by the ROL theory, which are the result of long wavelength correlations. If present, this effect can be incorporated into the ROL theory only via the introduction of composition-dependent statistical segment lengths.

To allow for this possibility, we have chosen to estimate the statistical segments lengths by fitting our results for $q*$ to ROL predictions. Because a fit of $q*$ does not allow us to estimate the statistical segment lengths of both blocks independently, we model the data by simply multiplying the literature values of $b_I(T)$ and $b_L(T)$ by a common "stretching" factor $s(T)$, giving revised segment lengths, $s(T)b_I(T)$ and $s(T)b_L(T)$. The factor $s(T)$ is assumed to be an exponential function of temperature $\exp(s_1 T + s_2)$ with two free parameters, s_1 and s_2, that were determined by fitting results for $q*$ vs $\chi_a^* N$ to ROL predictions. The ROL theory was evaluated using the different statistical segment lengths for the two blocks as well as the slightly different calculated values for the lengths of both blocks, thus attempting to take into account the effects of slight asymmetries that were not present in previous comparisons to simulations of completely symmetric diblock copolymers. The resulting fit is shown by the solid curve in Figure 7.6, marked by the label ROL_{Fit}. For completeness, we also show the predictions obtained by using these "stretched" statistical segment lengths in the RPA in Figure 7.6 as a dotted line labeled RPA_{Fit}. Note that this fitting procedure yields a modified RPA prediction with a weak, nearly linear dependence on the abscissa, which directly reflects the weak temperature dependence of the resulting estimates for $b_I(T)$ and $b_L(T)$, but that the ROL prediction very accurately captures the curvature of the experimental data near the ODT.

We were surprised to find, however, that this fitting procedure yields estimated statistical segment lengths that are almost 20% larger than the values reported for homopolymers, giving $b_I = 7.2$ Å and $b_L = 8.3$ Å at 140 °C. Moreover, because statistical segment lengths appear in the definition of $\bar{N}$ raised to the sixth power, this change

yields an estimated value of $\bar{N} = 611$ at 140 °C that is more than twice that obtained using homopolymer statistical segment lengths.

The final stage of our analysis of scattering data was to estimate the interaction parameter function $\chi_e(T)$ by fitting experimental results for inverse peak structure factor $S^{-1}(q^*)$ vs temperature. This data was fit to predictions of the ROL theory for $S^{-1}(q^*)$ vs $\chi_e N$ using the statistical segment lengths that we estimated by fitting q^* to ROL predictions and assuming a temperature dependence of the form $\chi_e(T) = A/T + B$. Figure 7.7 illustrates the excellent quality of the fit, which yields $\chi_e(T) = 381T^{-1} - 0.48$.
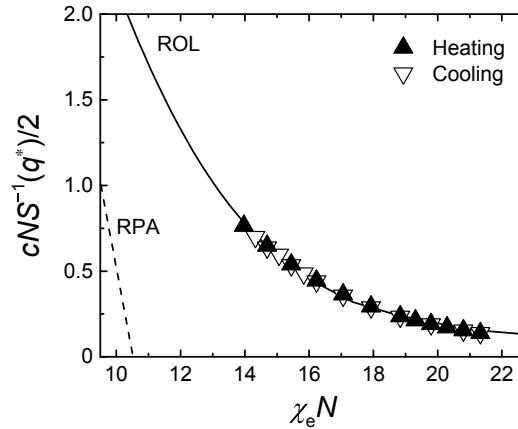
Figure 7.7 Extraction of $\chi_e(T)$ using the ROL theory. The temperature dependence of $\Gamma^{-1}(q^*)$ fit to the ROL theory predictions with $\bar{N} = 611$ (solid line). The dashed line is the RPA prediction.

7.3.3 Latent heat

A recent simulation study of symmetric diblock copolymers has yielded consistent results for the change in the interaction energy at the ODT in a form that can be compared to the latent heat observed in recent calorimetry experiments on IL-1.[15,48] Analysis of the simulations was based upon a scaling relation that we also apply here to experimental results.

The simulations to which we compare showed that the normalized excess free energy per chain $g = \underline{G}/RT$ for symmetric diblock copolymers can be well

approximated as a universal function of the state variables $\chi_e N$ and $\bar{N}$. Here, $\underline{G}$ is a molar excess free energy of a copolymer liquid, defined relative to an appropriately weighted sum of homopolymer standard states, and R is the ideal gas constant. This implies that the free energy derivative

$$g' \equiv \frac{\partial g}{\partial(\chi_e N)} = \frac{1}{R}\frac{\partial(\underline{G}/T)}{\partial(\chi_e N)} \tag{7.4}$$

is also a universal function of $\chi_e N$ and $\bar{N}$. By applying the chain rule to eq 7.4 and using the Gibbs–Helmholtz identity, we find that

$$g' = \frac{1}{R}\frac{\partial(\underline{G}/T)}{\partial(\chi_e N)} = \frac{1}{RN}\frac{\partial(\underline{G}/T)/\partial(1/T)}{\partial(\chi_e(T))/\partial(1/T)} = \frac{1}{RN}\frac{\underline{H}}{A} \tag{7.5}$$

where $\underline{H}$ is a corresponding excess molar enthalpy. In the last expression, we have taken $\partial(\chi_e(T))/\partial(1/T) = A$ based on the approximation $\chi_e(T) = A/T + B$.

Let $\Delta(g')_{ODT}$ denote the discontinuity in the value of g' across the ODT (i.e., the difference between the values of g' in the disordered phase and in the ordered phase at the ODT). It was shown that values of the dimensionless quantity $\Delta(g')_{ODT}$ for a variety of simulation models fall on a common curve when plotted as a function of $\bar{N}$ and that these values exhibit a very weak $\bar{N}$ dependence. The quantity $\Delta(g')_{ODT}$ can be related to the (molar) latent enthalpy of transition $\Delta\underline{H}_{ODT}$ by using eq 7.5 to evaluate difference between values of g' in the disordered and ordered phase at the ODT, giving

$$\Delta(g')_{ODT} = \frac{1}{RN}\frac{\Delta\underline{H}_{ODT}}{A} \tag{7.6}$$

Note that this relationship involves the coefficient A that controls the temperature dependence of $\chi_e(T)$, which we have estimated independently by analyzing scattering in the disordered phase

Equation 7.6 allows us to compare results for the latent heat from experiments and simulations. According to the simulation results, $\Delta(g')_{ODT} \approx 0.008 \pm 0.0005$ at $\bar{N} = 611$, where the uncertainty is an estimate of the scatter of results obtained from different

simulation models. Using eq 7.6, and the estimated value of A = 381 K obtained from our analysis of scattering data, this yields a predicted molar latent heat of $\Delta \underline{H}_{\text{ODT}}$ = 988 J/mol or, equivalently, ΔH_{ODT} = 0.36 J/g based on the molecular weight of IL-1 (2750 g/mol). This agrees with the range of the measured values ΔH_{ODT} = 0.25–0.36 J/g determined by DSC, as reported in Chapter 3 and Lee et al.[15], and is slightly greater than the more precise value of ΔH_{ODT} = 0.26 ± 0.02 determined independently by relaxation calorimetry in Chapter 6.

7.3.4 *Order–disorder transition*

We also compare ODT measurements of IL-1 ($\bar{N}$ = 611) to simulation results for the ODT. The simulation study reported Glaser et al.[59] showed that results of several simulation models yield a master curve for $(\chi_e N)_{\text{ODT}}$ vs $\bar{N}$ (eq 7.1) when χ_e is estimated for each model by a procedure similar to that used here. Using the estimate of $\chi_e(T)$ described above, we obtain $(\chi_e N)_{\text{ODT}}$. In Figure 7.8, we show this experimental result on the same plot as the simulation results, along with SCFT and FH predictions for the ODT. The estimated value of $(\chi_e N)_{\text{ODT}}$ is much closer to the simulation results than to either FH or (particularly) SCFT predictions but is about 10% greater than the simulation results.
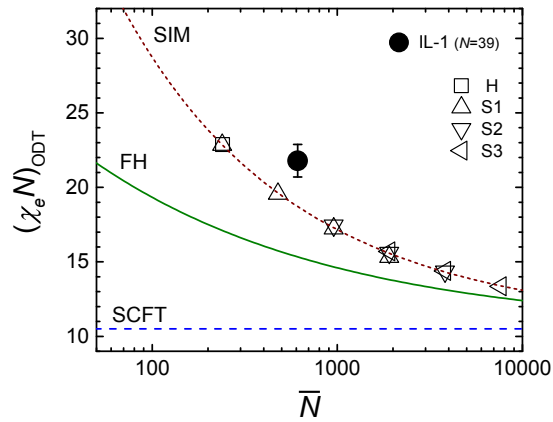
Figure 7.8 Comparison of values of $\chi_e N$ at the ODT. $\chi_e N$ at the ODT predicted by theory (SCFT: dashed blue line; FH: solid green line), observed in simulations (open symbols; the dotted red line is a phenomenological fit to the simulation data given by eq 7.1), and observed experimentally in IL-1 (filled symbol). Error bars indicate ± 5% uncertainty in N. The identifiers H, S1, S2, and S3 that appear in the legend are labels that were used by Morse and co-workers[48,59] to identify different simulation models.

7.3.5   *Dependence of ODT on molecular weight*

To this point, our analysis has exclusively considered experimental data for the IL-1 polymer. However, values for the T_{ODT}s of 5 nearly symmetric IL diblock copolymers of varying molecular weight were also reported in Chapter 3 and Lee et al.,[15] of which IL-1 was the lowest in molecular weight. These additional data points allow an extension of our analysis to the chain length dependence of $(\chi_e N)_{ODT}$ based on our estimate of $\chi_e(T)$ as well as providing a test of the robustness of various methods used to extract $\chi_e(T)$ in describing the experimental scattering data and T_{ODT}s. It is important to note that the only polymer for which disordered phase scattering data were collected and analyzed in the fashion described above was IL-1. T_{ODT}s for all polymers were determined by DSC.[15]
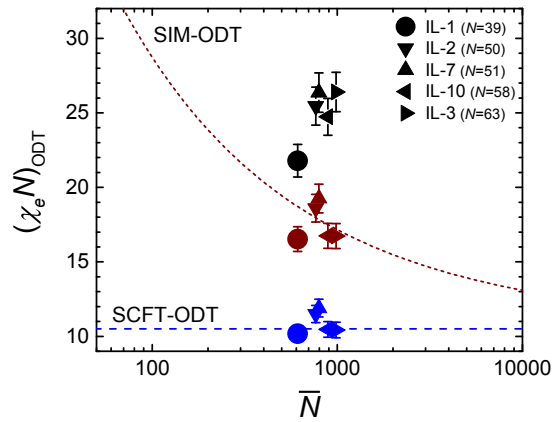
Figure 7.9 Comparison of experimental results for $(\chi_e N)_{ODT}$ as a function of N calculated using the three different $\chi_e(T)$ functions shown in Figure 7.10. (ROL: black symbols; SIM-ODT: red symbols; SCFT-ODT: blue symbols). The universal N dependence of $(\chi_e N)_{ODT}$ predicted by mean-field theory and simulations are shown as the dashed blue and dotted red lines, respectively. Error bars indicate $\pm 5\%$ uncertainty in N.

Figure 7.9 shows experimental results for $(\chi_e N)_{ODT}$ for this series of IL polymers plotted vs $\overline{N}$ calculated using several different methods of estimating $\chi_e(T)$. The most stringent comparison of experiment and simulations, shown by black symbols, uses the estimate of $\chi_e(T)$ and statistical segment lengths that were obtained by analyzing scattering from IL-1 to plot values of $(\chi_e N)_{ODT}$ as a function $\overline{N}$ for all five samples. The results are less encouraging than those obtained by analyzing experiments on IL-1 alone (Figure 7.8): The values of $(\chi_e N)_{ODT}$ for the other four samples are all greater, and further from the simulation results, than those obtained for IL-1. The values for $(\chi_e N)_{ODT}$ for the longer four polymers do not seem to show a clear trend with molecular weight. The only clear trend is that the result from sample IL-1 (the sample which we used to extract $\chi_e(T)$, and the shortest polymer) lies noticeably closer to the simulation results than the others.

For comparison, we also show results for $(\chi_e N)_{ODT}$ obtained using two methods of fitting the measured ODTs to simulation results or theory in Figure 7.9. The red symbols show the results obtained when $\chi_e(T)$ was estimated by fitting the measured ODTs to eq 7.1 (i.e., to the curve SIM-ODT in Figure 7.9). The blue symbols show the previously

reported results of a fit to the SCFT prediction (i.e., $(\chi_e N)_{ODT} = 10.5$; see Chapter 3).[15] Both fits assumed a function of the form $\chi_e(T) = A/T + B$.
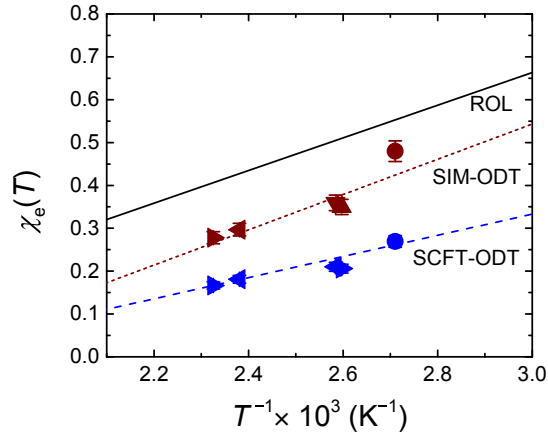
Figure 7.10 Comparison of $\chi_e(T)$ functions obtained from three different fitting procedures. (1) ROL (solid black line): obtained from experimental peak scattering intensity data using ROL theory. (2) SIM-ODT (dotted red line, red symbols): obtained from measured T_{ODT}s and the prediction of eq 7.1. (3) SCFT-ODT (dashed blue line, blue symbols): obtained from measured T_{ODT}s and the mean field prediction of $(\chi_e N)_{ODT}$. The three functions are $\chi_e^{ROL}(T) = 381/T - 0.48$, $\chi_e^{SIM}(T) = 411/T - 0.69$, and $\chi_e^{SCFT}(T) = 247/T - 0.41$. Error bars indicate ±5% uncertainty in N.

Figure 7.10 shows the estimates $\chi_e(T)$ obtained by all three methods, which differ substantially. The difference between the estimates obtained by fitting ODTs to SCFT and from other methods is neither disturbing nor surprising: It is known that SCFT cannot quantitatively describe ODTs for such short polymers. The discrepancy between the estimate obtained from fitting the ROL theory to scattering from IL-1 and that obtained from fitting ODTs from several chain lengths to eq 7.1 is more significant, however, because it indicates a substantial difference between the behavior of this sequence of polymers and that of the simulation models studied by Morse and co-workers[48,59–61,211]. We emphasize that this difference is not a result of differences in how data were analyzed, since we have taken care to use analogous methods to estimate $\chi_e(T)$ in our analysis of simulations and experiments.
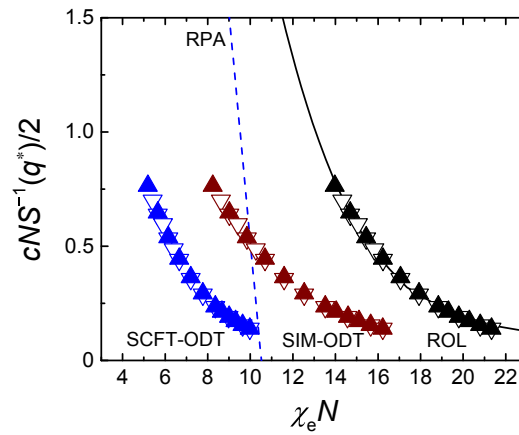
Figure 7.11 Comparison of experimental scattering data calculated using the three different $\chi_e(T)$ functions shown in Figure 7.9. Experimental data (ROL: black symbols; SIM-ODT: red symbols; SCFT-ODT: blue symbols) compared to ROL (solid black line) and RPA (dashed blue line) predictions. In all cases, filled and open symbols indicate data measured upon heating and cooling, respectively.

In Figure 7.11, as an alternate way of quantifying the inconsistency between different ways of estimating $\chi_e(T)$, we show results for the inverse scattering intensity vs $\chi_e N$, plotted using the three different ways of estimating $\chi_e(T)$ that are shown in Figure 7.10. The results make it particularly clear that the expression for $\chi_e(T)$ that was obtained by attempting to match experimental and simulation results (eq 7.1) for the ODTs (red symbols) yields estimated values of $\chi_e(T)$ that are too low to be consistent with the scattering intensity measured from IL-1. It is also clear from Figure 7.10, and from the values of the coefficients in expressions of the form $\chi_e(T) = A/T + B$, that the difference between estimates of $\chi_e(T)$ obtained by these two methods is primarily the result of a difference in the coefficient B, which represents an entropic contribution, rather than a difference in the A coefficient, which controls the heat of mixing.

7.4 Discussion and Conclusions

We have analyzed experimental measurements from low molecular weight poly(1,4-isoprene-*b*-DL-lactide) diblock copolymers with respect to theoretical predictions and coarse-grained simulations. The comparison takes advantage of an

unusually comprehensive set of measurements of a single polymer, IL-1, that includes both SANS and SAXS scattering experiments and measurements of the latent heat of the ODT, as well as more limited data for the T_{ODT} of other symmetric IL diblock copolymers.

Our comparison of experiments and simulations also relied on the availability of an unusually comprehensive analysis of the simulation data to which we compare. It was shown by Glaser et al.[61] that results from several simulation models for the structure factor $S(q)$ in the disordered phase could all be fit by the ROL theory over a range of chain lengths using a single estimate of how the effective interaction parameter χ_e for each simulation model depends on a corresponding simulation parameter. Subsequent work showed that, by using the resulting estimate of χ_e to analyze other properties, it was possible to obtain consistent results for $(\chi_e N)_{ODT}$ and for the scaled latent heat $\Delta(g')_{ODT}$ from different simulation models.[48] To allow as direct as possible a comparison of experiments to simulations, our experimental results for the T_{ODT} and latent heat for IL-1 were converted to values for $(\chi_e N)_{ODT}$ and $\Delta(g')_{ODT}$ by the same procedure, using an estimate of $\chi_e(T)$, that was obtained by fitting experimental results for $S(q)$ in the disordered phase to the ROL theory.

To compare scattering results to the ROL theory, one must estimate values for the temperature dependence of the monomer statistical segment lengths and the effective interaction parameter. We focused first on estimating values for the statistical segment lengths, which can be estimated independently of $\chi_e(T)$ by analyzing the relationship between the peak wavenumber q^* and the peak intensity. Previous analysis of simulation results for q^* by this method had shown good agreement with predictions of the ROL theory, using a value of the statistical segment length that was obtained from independent simulations of homopolymer melts.[60] Experimental results for q^* for IL-1 did not, however, agree with ROL predictions obtained using literature values for the statistical segment lengths of PLA and PI homopolymers as functions of temperature. To bring the theory into agreement with experimental results, we found that it was necessary to apply a correction of almost 20% to these literature values. We chose to allow for such

correction because it is known that the statistical segment length of a polymer depends somewhat upon its chemical environment, and can thus be somewhat different in an environment that contains a mixture of two blocks than in a homopolymer. The magnitude of the required correction is surprisingly large, however, on the basis of what is known about the sensitivity of statistical segment lengths to changes in chemical environment.[217] Specifically, the required correction is larger than the differences between values of statistical segment lengths measured in a homopolymer melt and in theta solvent for most (though not all) common polymers, as summarized in Table 7.1, p 268 of Graessley.[217] In the absence of a fundamental reason to reject this analysis, however, we chose to use the larger "corrected" statistical segment lengths in the analysis of other properties.

By assuming a function of the form $\chi_e(T) = A/T + B$, we were able to fit the measured temperature dependence of the peak intensity $S(q^*)$ for IL-1 to predictions of the ROL theory. This sort of a fit of data from a single polymer is, by itself, not a particularly stringent test of the theory and simply provides a way of calibrating $\chi_e(T)$ in a manner consistent with the earlier analysis of simulation results.

One particularly striking success of our comparison of experiment and simulation results was the rough agreement between experimental results for IL-1 and corresponding simulation results for the normalized latent heat of transition.[15,48] The success of this comparison is particularly gratifying in light of the fact that accurate experimental and simulation results for the latent heat both became available only recently, so that this is the first attempt to compare them. The level of agreement is also encouraging in light of the fact that the analysis required to compare simulation and experimental results for latent heat depends sensitively on how we estimate χ_e.

For the location of the ODT, we obtained $(\chi_e N)_{ODT} = 21.8$ for IL-1 ($\bar{N} = 611$), using the estimate of $\chi_e(T)$ obtained from fitting scattering in the disordered phase to the ROL. For comparison, SCFT predicts of $(\chi_e N)_{ODT} = 10.5$, the FH theory predicts $(\chi_e N)_{ODT} = 10.495 + 41.0\bar{N}^{-1/3} = 15.3$ at the value of $\bar{N} = 611$ obtained using the statistical segment lengths required to fit q^*. For the same value of $\bar{N}$, the empirical

correlation obtained from simulations, eq 7.1, yields 18.7. The fact that the experimental value is more than twice the SCFT prediction reinforces the overwhelming importance of fluctuations. The fact that it is also significantly greater than the FH prediction confirms the inadequacy of this theory for quantitative predictions for such short polymers. The predicted value of 18.7 obtained from simulations is significantly closer to the experimental result than is either theoretical prediction. The remaining discrepancy of approximately 15% is, however, larger than estimated experimental uncertainties, the largest of which is the approximately 5% uncertainty in molecular weight. We note in passing that using literature values for the statistical segment lengths to calculate $\bar{N}$ and then using the resulting smaller value of $\bar{N} = 231$ in eq 7.1 would yield a higher value of $(\chi_e N)_{ODT}$ that agrees well with the simulation results, at the cost of destroying the agreement between ROL predictions or simulation results and experimental results for q^*. The combination of the ROL theory for $S(q)$ and simulation results for other quantities thus provides an almost (but not quite) consistent description of data for polymer IL-1, which appears to be a substantial improvement over either the RPA/SCFT theory or the FH theory.

This near-agreement between simulation and experiment broke down, however, when we compared simulation results both to scattering experiments on IL-1 and to measurements of the T_{ODT} of a series of nearly symmetric IL diblock copolymers of varying (greater) molecular weight. The estimate of $\chi_e(T)$ that we obtained by comparing simulation and experimental results for the ODT was found to be significantly lower than the estimate obtained by analyzing scattering from the shortest polymer, IL-1.

At this point, we can only speculate about possible causes of this disagreement. The consistency of the results obtained from simulations of different coarse-grained models by Morse and co-workers[48,59–61,211] leads us to believe that these simulation results represent a close approximation to the behavior of the idealized "standard model" of dense polymer liquids as Gaussian random walks with short-range interactions. The identification of statistically significant differences between experimental and simulation results imply that there are physical differences between real IL copolymers and the

simple bead–spring models used in these simulations that cannot be adequately described by the standard model. Physical effects that could lead to such differences include (1) breakdown of the random walk description of chain statistics for sufficiently short chains, (2) breakdown of the assumption that repulsive interactions can be adequately described by a wavenumber-independent interaction parameter, due to the nonzero range of effective interactions, and (3) end-group contributions to the free energy of mixing, due to the fact that chemical structure and environment of a chain end group is always somewhat different from that of any monomer.

In addition to the fundamental physical differences outlined above between the standard model and real IL polymers, there exist a variety of possible sources of experimental error that, while present, are difficult to quantify and may contribute to the lack of perfect agreement between experiments, simulations, and theory in our analysis. A partial list of such factors include (1) the use of literature values for polymer densities that originate from high molecular weight materials (i.e., uncorrected for any molecular weight dependence of density), (2) dispersity in both molecular weight and composition, and (3) systematic errors possibly introduced during various utilized fitting and interpolation routines.

For the IL systems here, it is perhaps most relevant that the PLA-terminal end-segment of the block polymer contains a hydroxyl group. This hydroxyl group can interact with the PLA backbone carbonyl groups through a hydrogen-bonding interaction. Frielinghaus et al. have studied the effect of a hydroxyl end group on the thermodynamics of poly(styrene)-b-poly(ethylene oxide) (PS–PEO) diblock copolymers by synthesizing otherwise similar polymers in which the PEO block is terminated by either a polar hydroxyl or nonpolar methoxy group.[218] They found that the presence of a hydroxyl end-group increased the ODT temperature in PS–PEO copolymers with M_n of approximately 20 kg/mol, relative to analogous systems with a methoxy end group, by approximately 45 K. For IL-1 (M_n = 2750 g/mol), there are only, on average, 22 PLA repeat units per chain, making the terminal PLA unit a non-negligible fraction of the total number of PLA repeat units. The expected effect of this end-group is to lead to an

estimate of $\chi_e(T)$ somewhat larger than the hypothetical "bulk" parameter that would be obtained in the absence of this end-group. Because the relative effect of the end-group upon scattering and thermodynamics is expected to become stronger with decreasing chain length, this could plausibly lead to an overestimate of $\chi_e(T)$ when the value extracted from the shortest IL polymer, IL-1, is applied to longer chains, for which the terminal PLA unit is a smaller fraction of the total PLA block. It appears to us that the documented effect of a hydroxyl end-group on PS–PEO polymers[218] is more than enough to explain the discrepancies that we observe when comparing data from chains of different length.

The fact that the best agreement between experimental and simulation results for $(\chi_e N)_{ODT}$ is obtained when we compared scattering and ODT measurements from a single polymer could be explained if we assume that the ODT in a system with some specified invariant degree of polymerization occurs at some critical value of the invariant peak intensity $S(q^*)/cN$. To explain the near-consistency of $S(q)$ and ODT data obtained from a single polymer, we would need to assume that this critical value is not strongly effected by nonidealities (such as end-group effects) that can modify how the magnitude of fluctuations at wavenumbers near q^* depends on temperature and molecular weight in a particular chemical system. We note that this seemingly *ad hoc* conjecture is consistent with both the phenomenology of crystallization in simple liquids[219] and FH theory, both of which predict a universal value at the crystallization transition for an appropriate measure of the scattering amplitude $S(q^*)$ at the critical wavenumber q^*.

The analysis presented here was based on comparisons of experimental data to a theory (the ROL theory) and to simulations of strictly monodisperse polymers and thus did not account for dispersity in the block lengths. It is known, however, that introduction of even modest levels of dispersity into the RPA theory can cause a significant decrease in the predicted value of q^* and an increase in the peak intensity.[220,221] As a direct result of the low degrees of polymerizations, the dispersities of the IL diblocks studied here ($Đ = 1.10$ for IL-1) are slightly greater than that typical for other anionically polymerized model polymers of higher molecular weight. Our treatment of the discrepancy between

the measured value of $q*$ and the value predicted using homopolymer statistical segments (by adjusting the statistical segment lengths) was motivated by the observation that statistical segment lengths in a mixture can depend somewhat on composition. An alternative hypothesis, which we have not tested here, is that this discrepancy could be primarily a result of dispersity. In the future, we plan to modify the theory to allow explicitly for the effects of dispersity.

The lack of perfect consistency between our experimental and simulation results is notable when compared to the consistency obtained in recent simulations[48] but less surprising when viewed in the context of the existing experimental literature. Relatively few experimental studies have been designed to test the ability of specific theories (or any theory) to consistently describe polymer liquids of widely varying chain length or architecture. The results of such studies have included both some striking successes and equally striking failures. Studies of polymer mixtures have shown that the combination of Flory–Huggins and RPA theories, generalized to allow for the possibility of a composition-dependent interaction parameter, provides a consistent description of scattering and phase behavior in several binary homopolymer mixtures[222–225] and in mixtures of homopolymers and diblock copolymers that are susceptible to macroscopic phase separation rather than ordering.[226,227] A recent study of a polymer blend system that was chosen specifically to allow the theory to be tested over a much broader range of molecular weights found, however, that the data for this system could be fit only by allowing for a molecular-weight-dependent effective interaction parameter.[228,229] It has long been understood that SCFT cannot quantitatively describe the vicinity of the ODT for block copolymers. Encouraging results were obtained from the initial comparison of data from comparatively high molecular weight nearly symmetric polyolefin diblock copolymer melts to the FH theory that included a comparison of ODT temperatures from copolymers of varying molecular weight to disordered phase scattering data, as also done here.[50,72] Subsequent attempts to compare results obtained from diblock copolymers and homopolymer blends using several different systems have shown that that the

relationship between the blend and diblock copolymer is qualitatively different in different chemical systems, for reasons that remain unexplained.[230–234]

The results presented here provide encouraging evidence of the ability of coarse-grained simulations to describe the dominant effect of strong composition fluctuations in measurements on short diblock copolymers near the ODT, in a manner that improves upon the FH theory. These include the first comparison of simulation and experimental measurements for the latent heat associated with the order–disorder transition. Our findings also, however, make clear the need to compare chains of differing length in order to adequately test the relationships among experiments, simulations and theory, and the need for attention to possible chemically specific nonidealities, such as end-group effects, when comparing very generic simulations to experimental data on very short chains.

References

(1)   Lodge, T. P. *Macromol. Chem. Phys.* **2003**, *204*, 265–273.

(2)   Bates, F. S.; Fredrickson, G. H. *Phys. Today* **1999**, *52*, 32–38.

(3)   Bates, F. S.; Hillmyer, M. A.; Lodge, T. P.; Bates, C. M.; Delaney, K. T.; Fredrickson, G. H. *Science* **2012**, *336*, 434–440.

(4)   Mai, Y.; Eisenberg, A. *Chem. Soc. Rev.* **2012**, *41*, 5969–5985.

(5)   Hamley, I. W. *The Physics of Block Copolymers*; Oxford University Press: Oxford, 1998.

(6)   Ruzette, A.-V.; Leibler, L. *Nat. Mater.* **2005**, *4*, 19–31.

(7)   Hadjichristidis, N.; Pispas, S.; Floudas, G. *Block Copolymer: Synthetic Strategies, Physical Properties, and Applications*; John Wiley & Sons, 2002.

(8)   Hu, H.; Gopinadhan, M.; Osuji, C. O. *Soft Matter* **2014**, *10*, 3867–3889.

(9)   Schacher, F. H.; Rupar, P. A.; Manners, I. *Angew. Chemie - Int. Ed.* **2012**, *51*, 7898–7921.

(10)   Bates, C. M.; Maher, M. J.; Janes, D. W.; Ellison, C. J.; Willson, C. G. *Macromolecules* **2014**, *47*, 2–12.

(11)   Hallinan Jr., D. T.; Balsara, N. P. *Annu. Rev. Mater. Res.* **2013**, *43*, 503–525.

(12)   Duncan, R. *Nat. Rev. Drug Discov.* **2003**, *2*, 347–360.

(13)   Fredrickson, G. H.; Bates, F. S. *Annu. Rev. Mater. Sci.* **1996**, *26*, 501–550.

(14)   Bates, F. S.; Fredrickson, G. H. *Annu. Rev. Phys. Chem.* **1990**, *41*, 525–557.

(15)   Lee, S.; Gillard, T. M.; Bates, F. S. *AIChE J.* **2013**, *59*, 3502–3513.

(16)   Leibler, L. *Macromolecules* **1980**, *13*, 1602–1617.

(17)   Fredrickson, G. H.; Helfand, E. *J. Chem. Phys.* **1987**, *87*, 697–705.

(18)   Stoykovich, M. P.; Nealey, P. F. *Mater. Today* **2006**, *9*, 20–29.

(19)   *Handbook of Liquid Crystals*; Demus, D., Goodby, J., Gray, G. W., Spiess, H.-W.,
       Vill, V., Eds.; Wiley-VCH Verlag GmbH: Weinheim, Germany, 1998.

(20)   Laughlin, R. G. *The Aqueous Phase Behavior of Surfactants*; Academic Press Inc.:
       San Diego, CA, 1994.

(21)   Gruner, S. M. *J. Phys. Chem.* **1989**, *93*, 7562–7570.

(22)   Gandini, A. *Macromolecules* **2008**, *41*, 9491–9504.

(23)   Coates, G. W.; Hillmyer, M. A. *Macromolecules* **2009**, *42*, 7987–7989.

(24)   Miller, S. A. *ACS Macro Lett.* **2013**, *2*, 550–554.

(25)   Thoen, J.; Cordoyiannis, G.; Glorieux, C. *Liq. Cryst.* **2009**, *36*, 669–684.

(26)   Bates, F. S. *Science* **1991**, *251*, 898–905.

(27)   Hiemenz, P. C.; Lodge, T. P. *Polymer Chemistry*, 2nd ed.; CRC Press: New York,
       2007.

(28)   Bates, F. S.; Rosedale, J. H.; Stepanek, P.; Lodge, T. P.; Wiltzius, P.; Fredrickson,
       G. H.; Hjelm, R. P. *Phys. Rev. Lett.* **1990**, *65*, 1893–1896.

(29)   Hückstädt, H.; Göpfert, A.; Abetz, V. *Macromol. Chem. Phys.* **2000**, *201*, 296–
       307.

(30)   *Polymer Handbook*, 4th ed.; Brandrup, J., Immergut, E. H., Grulke, E. A., Abe, A., Bloch, D. R., Eds.; John Wiley & Sons, 2005.

(31)   Schmidt, S. C.; Hillmyer, M. A. *J. Polym. Sci. Part B Polym. Phys.* **2002**, *40*, 2364–2376.

(32)   Schwahn, D.; Mortensen, K.; Yee-Madeira, H. *Phys. Rev. Lett.* **1987**, *58*, 1544–1546.

(33)   Khandpur, A. K.; Foerster, S.; Bates, F. S.; Hamley, I. W.; Ryan, A. J.; Bras, W.; Almdal, K.; Mortensen, K. *Macromolecules* **1995**, *28*, 8796–8806.

(34)   Matsen, M. W.; Bates, F. S. *J. Polym. Sci. Part B Polym. Phys.* **1997**, *35*, 945–952.

(35)   Lynd, N. A.; Hillmyer, M. A. *Macromolecules* **2005**, *38*, 8803–8810.

(36)   Matsen, M. W. *Phys. Rev. Lett.* **2007**, *99*, 148304.

(37)   Matsen, M. W. *J. Phys. Condens. Matter* **2002**, *14*, R21–R47.

(38)   Fredrickson, G. H. *The Equilibrium Theory of Inhomogeneous Polymers*; Oxford University Press, 2005.

(39)   Matsen, M. W.; Schick, M. *Phys. Rev. Lett.* **1994**, *72*, 2660–2663.

(40)   Matsen, M. W.; Bates, F. S. *Macromolecules* **1996**, *29*, 7641–7644.

(41)   Matsen, M. W.; Bates, F. S. *Macromolecules* **1996**, *29*, 1091–1098.

(42)   Tyler, C. A.; Morse, D. C. *Phys. Rev. Lett.* **2005**, *94*, 1–4.

(43)   Xie, N.; Li, W.; Qiu, F.; Shi, A. *ACS Macro Lett.* **2014**, *3*, 906–910.

(44)   Bates, F. S.; Cohen, R. E.; Berney, C. V. *Macromolecules* **1982**, *15*, 589–592.

(45)   Meuler, A. J.; Hillmyer, M. A.; Bates, F. S. *Macromolecules* **2009**, *42*, 7221–7250.

(46)   Takenaka, M.; Wakada, T.; Akasaka, S.; Nishitsuji, S.; Saijo, K.; Shimizu, H.; Kim, M. I.; Hasegawa, H. *Macromolecules* **2007**, *40*, 4399–4402.

(47)   Lynd, N. A.; Hillmyer, M. A.; Matsen, M. W. *Macromolecules* **2008**, *41*, 4531–4533.

(48)   Medapuram, P.; Glaser, J.; Morse, D. C. *Macromolecules* **2015**, *48*, 819–839.

(49)   Brazovskii, S. A. *Sov. Phys JETP* **1975**, *41*, 85–89.

(50)   Bates, F. S.; Rosedale, J. H.; Fredrickson, G. H. *J. Chem. Phys.* **1990**, *92*, 6255–6270.

(51)   Hamley, I. W.; Podneks, V. E. *Macromolecules* **1997**, *30*, 3701–3703.

(52)   Barrat, J.-L.; Fredrickson, G. H. *J. Chem. Phys.* **1991**, *95*, 1281–1289.

(53)   Olvera de la Cruz, M. *Phys. Rev. Lett.* **1991**, *67*, 85–88.

(54)   Mayes, A. M.; de la Cruz, M. O. *J. Chem. Phys.* **1991**, *95*, 4670–4677.

(55)   Beckrich, P.; Johner, A.; Semenov, A. N.; Obukhov, S. P.; Benoît, H.; Wittmer, J. P. *Macromolecules* **2007**, *40*, 3805–3814.

(56)   Grzywacz, P.; Qin, J.; Morse, D. C. *Phys. Rev. E* **2007**, *76*, 061802.

(57)   Qin, J.; Grzywacz, P.; Morse, D. C. *J. Chem. Phys.* **2011**, *135*, 084902.

(58)   Morse, D. C.; Qin, J. *J. Chem. Phys.* **2011**, *134*, 084902.

(59)   Glaser, J.; Medapuram, P.; Beardsley, T. M.; Matsen, M. W.; Morse, D. C. *Phys. Rev. Lett.* **2014**, *113*, 068302.

(60)   Glaser, J.; Qin, J.; Medapuram, P.; Morse, D. C. *Macromolecules* **2014**, *47*, 851–869.

(61)   Glaser, J.; Qin, J.; Medapuram, P.; Müller, M.; Morse, D. C. *Soft Matter* **2012**, *8*, 11310–11317.

(62)   Dalvi, M. C.; Eastman, C. E.; Lodge, T. P. *Phys. Rev. Lett.* **1993**, *71*, 2591–2594.

(63)   Dalvi, M. C.; Lodge, T. P. *Macromolecules* **1994**, *27*, 3487–3492.

(64)   Kannan, R. M.; Su, J.; Lodge, T. P. *J. Chem. Phys.* **1998**, *108*, 4634.

(65)   Stepanek, P.; Lodge, T. P. *Macromolecules* **1996**, *29*, 1244–1251.

(66)   Stühn, B.; Stickel, F. *Macromolecules* **1992**, *25*, 5306–5312.

(67) Patel, A. J.; Narayanan, S.; Sandy, A.; Mochrie, S. G. J.; Garetz, B. A.; Watanabe, H.; Balsara, N. P. *Phys. Rev. Lett.* **2006**, *96*, 257801.

(68) Zhao, Y.; Sivaniah, E.; Hashimoto, T. *Macromolecules* **2008**, *41*, 9948–9951.

(69) Roe, R.-J.; Fishkis, M.; Chang, J. C. *Macromolecules* **1981**, *14*, 1091–1103.

(70) Hashimoto, T.; Shibayama, M.; Hiromichi, K. *Macromolecules* **1983**, *16*, 1093–1101.

(71) Sakamoto, N.; Hashimoto, T. *Macromolecules* **1995**, *28*, 6825–6834.

(72) Bates, F. S.; Rosedale, J. H.; Fredrickson, G. H.; Glinka, C. J. *Phys. Rev. Lett.* **1988**, *61*, 2229–2232.

(73) Rosedale, J. H.; Bates, F. S.; Almdal, K.; Mortensen, K.; Wignall, G. D. *Macromolecules* **1995**, *28*, 1429–1443.

(74) Hashimoto, T.; Sakamoto, N. *Macromolecules* **1995**, *28*, 4779–4781.

(75) Hashimoto, T.; Sakamoto, N.; Koga, T. *Phys. Rev. E* **1996**, *54*, 5832–5835.

(76) Sakamoto, N.; Hashimoto, T. *Macromolecules* **1998**, *31*, 3815–3823.

(77) Bates, F. S. *Macromolecules* **1984**, *17*, 2607–2613.

(78) Rosedale, J. H.; Bates, F. S. *Macromolecules* **1990**, *23*, 2329–2338.

(79) Kennemur, J. G.; Hillmyer, M. A.; Bates, F. S. *ACS Macro Lett.* **2013**, *2*, 496–500.

(80) Stuhn, B. *J. Polym. Sci. Part B Polym. Phys.* **1992**, *30*, 1013–1019.

(81) Kasten, H.; Stuhn, B. *Macromolecules* **1995**, *28*, 4777–4778.

(82) Voronov, V. P.; Buleiko, V. M.; Podneks, V. E.; Hamley, I. W.; Fairclough, J. P. A.; Ryan, A. J.; Mai, S.-M.; Liao, B.-X.; Booth, C. *Macromolecules* **1997**, *30,* 6674–6676.

(83) Hajduk, D. A.; Gruner, S. M.; Erramilli, S.; Register, R. A.; Fetters, L. J. *Macromolecules* **1996**, *29*, 1473–1481.

(84) Floudas, G.; Hadjichristidis, N.; Stamm, M.; Likhtman, A. E.; Semenov, A. N. *J. Chem. Phys.* **1997**, *106*, 3318–3328.

(85)   Hillmyer, M. A.; Bates, F. S. *Macromol. Symp.* **1997**, *117*, 121–130.

(86)   Kim, J. K.; Lee, H. H.; Gu, Q.-J.; Chang, T.; Jeong, Y. H. *Macromolecules* **1998**, *31*, 4045–4048.

(87)   Lee, S.; Bluemle, M. J.; Bates, F. S. *Science* **2010**, *330*, 349–353.

(88)   Lee, S.; Leighton, C.; Bates, F. S. *Proc. Natl. Acad. Sci. U. S. A.* **2014**, *111*, 17723–17731.

(89)   Gillard, T. M.; Phelan, D.; Leighton, C.; Bates, F. S. *Macromolecules* **2015**, *48*, 4733–4741.

(90)   Gillard, T. M.; Medapuram, P.; Morse, D. C.; Bates, F. S. *Macromolecules* **2015**, *48*, 2801–2811.

(91)   Habersberger, B. M.; Gillard, T. M.; Hickey, R. J.; Lodge, T. P.; Bates, F. S. *ACS Macro Lett.* **2014**, *3*, 1041–1045.

(92)   Hickey, R. J.; Gillard, T. M.; Lodge, T. P.; Bates, F. S. *ACS Macro Lett.* **2015**, *4*, 260–265.

(93)   Bates, F. S.; Maurer, W. W.; Lipic, P. M.; Hillmyer, M. A.; Almdal, K.; Mortensen, K.; Fredrickson, G. H.; Lodge, T. P. *Phys. Rev. Lett.* **1997**, *79*, 849–852.

(94)   Szwarc, M. *Nature* **1956**, *178*, 1168–1169.

(95)   Schmidt, S. C.; Hillmyer, M. A. *Macromolecules* **1999**, *32*, 4794–4801.

(96)   Wang, Y.; Hillmyer, M. A. *Macromolecules* **2000**, *33*, 7395–7403.

(97)   Hsieh, H. L.; Quirk, R. P. *Anionic Polymerization: Principles and Practical Applications*; Marcel Dekker, Inc.: New York, NY, 1996.

(98)   Pangborn, A. B.; Giardello, M. A.; Grubbs, R. H.; Rosen, R. K.; Timmers, F. J. *Organometallics* **1996**, *15*, 1518–1520.

(99)   Williams, C. K.; Hillmyer, M. A. *Polym. Rev.* **2008**, *48*, 1–10.

(100)   Roe, R.-J. *Methods of X-Ray and Neutron Scattering in Polymer Science*; Oxford University Press: New York, 2000.

(101) Higgins, J. S.; Benoît, H. *Polymers and Neutron Scattering*; Clarendon Press, 1994.

(102) Glatter, O.; Kratky, O. *Small Angle X-ray Scattering*; Academic Press Inc., 1982.

(103) Epps, T. H.; Cochran, E. W.; Bailey, T. S.; Waletzko, R. S.; Hardy, C. M.; Bates, F. S. *Macromolecules* **2004**, *37*, 8325–8341.

(104) Fetters, L. J.; Lohse, D. J.; Richter, D.; Witten, T. A.; Zirkel, A. *Macromolecules* **1994**, *27*, 4639–4647.

(105) Schwab, M.; Stühn, B. *Phys. Rev. Lett.* **1996**, *76*, 924–927.

(106) Wang, X.; Dormidontova, E. E.; Lodge, T. P. *Macromolecules* **2002**, *35*, 9687–9697.

(107) Abuzaina, F. M.; Patel, A. J.; Mochrie, S.; Narayanan, S.; Sandy, A.; Garetz, B. A.; Balsara, N. P. *Macromolecules* **2005**, *38*, 7090–7097.

(108) Han, C. D.; Vaidya, N. Y.; Kim, D.; Shin, G.; Yamaguchi, D.; Hashimoto, T. *Macromolecules* **2000**, *33*, 3767–3780.

(109) Cochran, E. W.; Garcia-Cervera, C. J.; Fredrickson, G. H. *Macromolecules* **2006**, *39*, 4264–4264.

(110) Vassiliev, O. N.; Matsen, M. W. *J. Chem. Phys.* **2003**, *118*, 7700.

(111) Cochran, E. W.; Bates, F. S. *Macromolecules* **2002**, *35*, 7368–7374.

(112) Barton, A. F. M. *CRC Handbool of Polymer-Liquid Interaction Parameters*; CRC Press, 1995.

(113) Schulz, M. F.; Khandpur, A. K.; Bates, F. S.; Almdal, K.; Mortensen, K.; Hajduk, D. A.; Gruner, S. M. *Macromolecules* **1996**, *29*, 2857–2867.

(114) Mai, S.; Fairclough, J. P. A.; Terrill, N. J.; Turner, S. C.; Hamley, I. W.; Matsen, M. W.; Ryan, A. J.; Booth, C. *Macromolecules* **1998**, *31*, 8110–8116.

(115) Lynd, N. A.; Hillmyer, M. A. *Macromolecules* **2007**, *40*, 8050–8055.

(116) Shefelbine, T. A.; Vigild, M. E.; Matsen, M. W.; Hajduk, D. A.; Hillmyer, M. A.; Cussler, E. L.; Bates, F. S. *J. Am. Chem. Soc.* **1999**, *121*, 8457–8465.

(117) Anderson, K. S.; Hillmyer, M. A. *Macromolecules* **2004**, *37*, 1857–1862.

(118) Ungar, G.; Liu, Y.; Zeng, X.; Percec, V.; Cho, W.-D. *Science* **2003**, *299*, 1208–1211.

(119) Ungar, G.; Zeng, X. *Soft Matter* **2005**, *1*, 95.

(120) Chaikin, P. M.; Lubensky, T. C. *Principles of Condensed Matter Physics*; Cambridge University Press, 2000.

(121) Fischer, E. W.; Sterzel, H. J.; Wegner, G. *Colloid Polym. Sci.* **1973**, *251*, 980–990.

(122) Helfand, E.; Tagami, Y. *J. Polym. Sci. Part B Polym. Lett.* **1971**, *9*, 741–746.

(123) Jinnai, H.; Koga, T.; Nishikawa, Y.; Hashimoto, T.; Hyde, S. T. *Phys. Rev. Lett.* **1997**, *78*, 2248–2251.

(124) Porod, G. *Kolloid-Zeitschrift* **1951**, *124*, 83–114.

(125) Semenov, A. N. *Sov. Phys JETP* **1985**, *61*, 733–742.

(126) Dormidontova, E. E.; Lodge, T. P. *Macromolecules* **2001**, *34*, 9143–9155.

(127) Wang, J.; Wang, Z.-G.; Yang, Y. *Macromolecules* **2005**, *38*, 1979–1988.

(128) Binder, K. *Reports Prog. Phys.* **1999**, *50*, 783–859.

(129) Van Roie, B.; Leys, J.; Denolf, K.; Glorieux, C.; Pitsi, G.; Thoen, J. *Phys. Rev. E* **2005**, *72*, 1–8.

(130) Martínez-Miranda, L. J.; Kortan, A. R.; Birgeneau, R. J. *Phys. Rev. Lett.* **1986**, *56*, 2264–2267.

(131) Anisimov, M. A.; Cladis, P. E.; Gorodetskii, E. E.; Huse, D. a.; Podneks, V. E.; Taratuta, V. G.; Van Saarloos, W.; Voronov, V. P. *Phys. Rev. A* **1990**, *41*, 6749–6762.

(132) Dalidovich, D.; Yang, K. *Phys. Rev. Lett.* **2004**, *93*, 247002.

(133) Janoschek, M.; Garst, M.; Bauer, A.; Krautscheid, P.; Georgii, R.; Böni, P.; Pfleiderer, C. *Phys. Rev. B* **2013**, *87*, 134407.

(134) Gopalakrishnan, S.; Lev, B. L.; Goldbart, P. M. *Nat. Phys.* **2009**, *5*, 8.

(135) Beardsley, T. M.; Matsen, M. W. *Eur. Phys. J. E. Soft Matter* **2010**, *32*, 255–264.

(136) Levine, D.; Steinhardt, P. J. *Phys. Rev. Lett.* **1984**, *53*, 2477–2480.

(137) Shechtman, D.; Blech, I.; Gratias, D.; Cahn, J. W. *Phys. Rev. Lett.* **1984**, *53*, 1951–1953.

(138) *Acta Crystallogr.* **1992**, *A48*, 928.

(139) Steurer, W. *Zeitschrift fur Krist.* **2004**, *219*, 391–446.

(140) Hayashida, K.; Dotera, T.; Takano, A.; Matsushita, Y. *Phys. Rev. Lett.* **2007**, *98*, 1–4.

(141) Percec, V.; Imam, M. R.; Peterca, M.; Wilson, D. A.; Graf, R.; Spiess, H. W.; Balagurusamy, V. S. K.; Heiney, P. A. *J. Am. Chem. Soc.* **2009**, *131*, 7662–7677.

(142) Fischer, S.; Exner, A.; Zielske, K.; Perlich, J.; Deloudi, S.; Steurer, W.; Lindner, P.; Förster, S. *Proc. Natl. Acad. Sci.* **2011**, *108*, 1810–1814.

(143) Zeng, X.; Ungar, G.; Liu, Y.; Percec, V.; Dulcey, A. E.; Hobbs, J. K. *Nature* **2004**, *428*, 157–160.

(144) Zhang, J.; Bates, F. S. *J. Am. Chem. Soc.* **2012**, *134*, 7636–7639.

(145) Xiao, C.; Fujita, N.; Miyasaka, K.; Sakamoto, Y.; Terasaki, O. *Nature* **2012**, *487*, 349–353.

(146) Talapin, D. V; Shevchenko, E. V; Bodnarchuk, M. I.; Ye, X.; Chen, J.; Murray, C. B. *Nature* **2009**, *461*, 964–967.

(147) Rosen, B. M.; Wilson, D. A.; Wilson, C. J.; Peterca, M.; Won, B. C.; Huang, C.; Lipski, L. R.; Zeng, X.; Ungar, G.; Heiney, P. A.; Percec, V. *J. Am. Chem. Soc.* **2009**, *131*, 17500–17521.

(148) Bindi, L.; Steinhardt, P. J.; Yao, N.; Lu, P. J. *Science* **2009**, *324*, 1306–1309.

(149) Bindi, L.; Yao, N.; Lin, C.; Hollister, L. S.; Andronicos, C. L.; Distler, V. V.; Eddy, M. P.; Kostin, A.; Kryachko, V.; MacPherson, G. J.; Steinhardt, W. M.; Yudovskaya, M.; Steinhardt, P. J. *Sci. Rep.* **2015**, *5*, 9111.

(150) Bindi, L.; Eiler, J. M.; Guan, Y.; Hollister, L. S.; MacPherson, G.; Steinhardt, P. J.; Yao, N. *Proc. Natl. Acad. Sci.* **2012**, *109*, 1396–1401.

(151) Frank, F. C.; Kasper, J. S. *Acta Crystallogr.* **1958**, *11*, 184–190.

(152) Frank, F. C.; Kasper, J. S. *Acta Crystallogr.* **1959**, *12*, 483–499.

(153) Alexandridis, P. *Macromolecules* **1998**, *31*, 6935–6942.

(154) Vargas, R.; Mariani, P.; Gulik, A.; Luzzati, V. *J. Mol. Biol.* **1992**, *225*, 137–145.

(155) Sakya, P.; Seddon, J. M.; Templer, R. H.; Mirkin, R. J.; Tiddy, G. J. T. *Langmuir* **1997**, *13*, 3706–3714.

(156) Balagurusamy, V. S. K.; Ungar, G.; Percec, V.; Johansson, G. *J. Am. Chem. Soc.* **1997**, *119*, 1539–1555.

(157) Perroni, D. V; Mahanthappa, M. K. *Soft Matter* **2013**, *9*, 7919–7922.

(158) Huang, M.; Hsu, C.; Wang, J.; Mei, S.; Dong, X.; Li, Y.; Li, M.; Liu, H.; Zhang, W.; Aida, T.; Zhang, W.-B.; Yue, K.; Cheng, S. Z. D. *Science* **2015**, *348*, 424–428.

(159) Förster, S.; Khandpur, A. K.; Zhao, J.; Bates, F. S.; Hamley, I. W.; Ryan, A. J.; Bras, W. *Macromolecules* **1994**, *27*, 6922–6935.

(160) Weigand, S. J.; Keane, D. T. *Nucl. Instruments Methods Phys. Res. Sect. A Accel. Spectrometers, Detect. Assoc. Equip.* **2011**, *649*, 61–63.

(161) Ferree, D. S.; van der Woerd, M. J. *Cryst. Growth Des.* **2003**, *3*, 193–196.

(162) Lee, S. "Structure and Dynamics of Block Copolymer Based Soft Materials," Ph.D. Dissertation, University of Minnesota, 2011.

(163) Janot, C. *Quasicrystals: A Primer*, 2nd ed.; Oxford University Press, 2012.

(164) Iwami, S.; Ishimasa, T. *Philos. Mag. Lett.* **2015**, 1–8.

(165) Bluemle, M. J.; Zhang, J.; Lodge, T. P.; Bates, F. S. *Macromolecules* **2010**, *43*, 4449–4452.

(166) Zhang, J.; Sides, S.; Bates, F. S. *Macromolecules* **2012**, *45*, 256–265.

(167) Zhang, J. "Phase Behaviors of ABAC Tetrablock Terpolymers," Ph.D. Dissertation, University of Minnesota, 2012.

(168) Dotera, T. *J. Polym. Sci. Part B Polym. Phys.* **2012**, *50*, 155–167.

(169) Levine, D.; Steinhardt, P. *Phys. Rev. Lett.* **1984**, *53*, 2477–2480.

(170) *Quasicrystals: The State of the Art*, 2nd ed.; DiVincenzo, D. P., Steinhardt, P. J., Eds.; World Scientific, 1999.

(171) Jain, S.; Bates, F. S. *Science* **2003**, *300*, 460–464.

(172) Damasceno, P. F.; Engel, M.; Glotzer, S. C. *Science* **2012**, *337*, 453–457.

(173) Iacovella, C. R.; Keys, A. S.; Glotzer, S. C. *Proc. Natl. Acad. Sci.* **2011**, *108*, 20935–20940.

(174) Xie, N.; Liu, M.; Deng, H.; Li, W.; Qiu, F.; Shi, A. C. *J. Am. Chem. Soc.* **2014**, *136*, 2974–2977.

(175) Dzugutov, M. *Phys. Rev. Lett.* **1993**, *70*, 2924–2927.

(176) Roth, J.; Denton, A. R. *Phys. Rev. E* **2000**, *61*, 6845–6857.

(177) Keys, A. S.; Glotzer, S. C. *Phys. Rev. Lett.* **2007**, *99*, 235503.

(178) Cavicchi, K. A.; Lodge, T. P. *Macromolecules* **2003**, *36*, 7158–7164.

(179) Cavicchi, K. A.; Lodge, T. P. *J. Polym. Sci. Part B Polym. Phys.* **2003**, *41*, 715–724.

(180) Choi, S. H.; Lodge, T. P.; Bates, F. S. *Phys. Rev. Lett.* **2010**, *104*, 1–4.

(181) Liu, A. J.; Nagel, S. R. *Nature* **1998**, *396*, 21–22.

(182) Trappe, V.; Prasad, V.; Cipelletti, L.; Segre, P. N.; Weitz, D. A. *Nature* **2001**, *411*, 772–775.

(183) Ediger, M. D.; Angell, C. A.; Nagel, S. R. *J. Phys. Chem.* **1996**, *100*, 13200–13212.

(184) Debenedetti, P. G.; Stillinger, F. H. *Nature* **2001**, *410*, 259–267.

(185) Zhang, C. Z.; Wang, Z. G. *Phys. Rev. E* **2006**, *73*, 1–16.

(186) Frank, F. C. *Proc. R. Soc. London* **1952**, *215*, 43–46.

(187) Royall, C. P.; Williams, S. R. *Phys. Rep.* **2015**, *560*, 1–75.

(188) Ma, E. *Nat. Mater.* **2015**, *14*, 547–552.

(189) Choi, S. H.; Bates, F. S.; Lodge, T. P. *Macromolecules* **2011**, *44*, 3594–3604.

(190) Lu, J.; Bates, F. S.; Lodge, T. P. *ACS Macro Lett.* **2013**, *2*, 451–455.

(191) Martello, M. T.; Schneiderman, D. K.; Hillmyer, M. A. *ACS Sustain. Chem. Eng* **2014**, *2*, 2519–2526.

(192) Sweat, D. P.; Kim, M.; Larson, S. R.; Choi, J. W.; Choo, Y.; Osuji, C. O.; Gopalan, P. *Macromolecules* **2014**, *47*, 6687–6696.

(193) Kennemur, J. G.; Yao, L.; Bates, F. S.; Hillmyer, M. A. *Macromolecules* **2014**, *47*, 1411–1418.

(194) Lee, D. H.; Lee, H.; Lee, Y.; Kim, Y.; Ryu, D. Y. *Macromolecules* **2014**, *47*, 2169–2173.

(195) Bachmann, R.; DiSalvo, F. J.; Geballe, T. H.; Greene, R. L.; Howard, R. E.; King, C. N.; Kirsch, H. C.; Lee, K. N.; Schwall, R. E.; Thomas, H. U.; Zubeck, R. B. *Rev. Sci. Instrum.* **1972**, *43*, 205–214.

(196) Lashley, J. C.; Hundley, M. F.; Migliori, A.; Sarrao, J. L.; Pagliuso, P. G.; Darling, T. W.; Jaime, M.; Cooley, J. C.; Hults, W. L.; Morales, L.; Thoma, D. J.; Smith, J. L.; Boerio-Goates, J.; Woodfield, B. F.; Stewart, G. R.; Fisher, R. A.; Phillips, N. E. *Cryogenics* **2003**, *43*, 369–378.

(197) Suzuki, H.; Inaba, A.; Meingast, C. *Cryogenics* **2010**, *50*, 693–699.

(198) Physical Property Measurement System: Heat Capacity Option. Quantum Design, Inc. 6325 Lusk Boulevard, Sand Diego, CA 92121. <http://www.qdusa.com>.

(199) Hwang, J. S.; Lin, K. J.; Tien, C. *Rev. Sci. Instrum.* **1997**, *68*, 94–101.

(200) Witzke, D. R.; Narayan, R.; Kolstad, J. J. *Macromolecules* **1997**, *30*, 7075–7085.

(201) Marriott, R. A.; Stancescu, M.; Kennedy, C. A.; White, M. A. *Rev. Sci. Instrum.* **2006**, *77*, 096108.

(202) Dachs, E.; Benisek, A. *Cryogenics* **2011**, *51*, 460–464.

(203) Chase Jr., M. W. *J. Phys. Chem. Ref. Data, Monogr. No. 9* **1998**, 1–1951.

(204) ASTM Standard E1269 2011. *Standard Test Method for Determining Specific Heat Capacity by Differential Scanning*; ASTM International: West Conshohocken, PA, 2011.

(205) Floudas, G.; Pakula, T.; Velis, G.; Sioula, S.; Hadjichristidis, N. *J. Chem. Phys.* **1998**, *108*, 6498–6501.

(206) Sandler, S. I. *Chemical, Biochemical, and Engineering Thermodynamics*, 4th ed.; John Wiley & Sons, 2006.

(207) Lynd, N. A.; Meuler, A. J.; Hillmyer, M. A. *Prog. Polym. Sci.* **2008**, *33*, 875–893.

(208) Beardsley, T. M.; Matsen, M. W. *Macromolecules* **2011**, *44*, 6209–6219.

(209) Schmitt, A. K.; Mahanthappa, M. K. *Macromolecules* **2014**, *47*, 4346–4356.

(210) Almdal, K.; Rosedale, J. H.; Bates, F. S. *Macromolecules* **1990**, *23*, 4336–4338.

(211) Qin, J.; Morse, D. C. *Phys. Rev. Lett.* **2012**, *108*, 11–14.

(212) Glinka, C. J.; Barker, J. G.; Hammouda, B.; Krueger, S.; Moyer, J. J.; Orts, W. J. *J. Appl. Crystallogr.* **1998**, *31*, 430–445.

(213) Kline, S. R. *J. Appl. Crystallogr.* **2006**, *39*, 895–900.

(214) Bates, F. S. *Macromolecules* **1985**, *18*, 525–528.

(215) Krishnamoorti, R.; Graessley, W. W.; Zirkel, A.; Richter, D.; Hadjichristidis, N.; Fetters, L. J.; Lohse, D. J. *J. Polym. Sci. Part B Polym. Phys.* **2002**, *40*, 1768–1776.

(216) Qin, J. "Studies of Block Copolymer Melts by Field Theory and Molecular Simulation," Ph.D. Dissertation, University of Minnesota, 2009.

(217) Graessley, W. W. *Polymer Liquids & Networks: Structure and Properties*; Garland Science, 2004.

(218) Frielinghaus, H.; Pedersen, W. B.; Larsen, P. S.; Almdal, K.; Mortensen, K. *Macromolecules* **2001**, *34*, 1096–1104.

(219) Hansen, J. P.; Verlet, L. *Phys. Rev.* **1969**, *184*, 151–161.

(220) Leibler, L.; Benoit, H. *Polymer* **1981**, *22*, 195–201.

(221) Bates, F. S.; Hartney, M. A. *Macromolecules* **1985**, *18*, 2478–2486.

(222) Roe, R.-J.; Zin, W.-C. *Macromolecules* **1980**, *13*, 1221–1228.

(223) Han, C. C.; Bauer, B. J.; Clark, J. C.; Muroga, Y.; Matsushita, Y.; Okada, M.;
       Tran-cong, Q.; Chang, T.; Sanchez, I. C. *Polymer* **1988**, *29*, 2002–2014.

(224) Bates, F. S.; Muthukumar, M.; Wignall, G. D.; Fetters, L. J. *J. Chem. Phys.* **1988**,
       89, 535–544.

(225) Krishnamoorti, R.; Graessley, W. W.; Balsara, N. P.; Lohse, D. J. *J. Chem. Phys.*
       1994, *100*, 3894–3904.

(226) Balsara, N. P.; Jonnalagadda, S. V; Lin, C. C.; Han, C. C.; Krishnamoorti, R. *J.
       Chem. Phys.* **1993**, *99*, 10011–10020.

(227) Lin, C. C.; Jonnalagadda, S. V; Balsara, N. P.; Han, C. C.; Krishnamoorti, R.
       Macromolecules **1996**, *29*, 661–669.

(228) Nedoma, A. J.; Robertson, M. L.; Wanakule, N. S.; Balsara, N. P. *Macromolecules*
       2008, *41*, 5773–5779.

(229) Nedoma, A. J.; Lai, P.; Jackson, A.; Robertson, M. L.; Wanakule, N. S.; Balsara,
       N. P. *Macromolecules* **2011**, *44*, 3077–3084.

(230) Maurer, W. W.; Bates, F. S.; Lodge, T. P.; Almdal, K.; Mortensen, K.;
       Fredrickson, G. H. *J. Chem. Phys.* **1998**, *108*, 2989–3000.

(231) Jeon, H. S.; Lee, J. H.; Balsara, N. P. *Macromolecules* **1998**, *31*, 3328–3339.

(232) Bartels, V. T.; Abetz, V.; Mortensen, K.; Stamm, M. *Europhys. Lett.* **1994**, *27*,
       371–376.

(233) Frielinghaus, H.; Abbas, B.; Schwahn, D.; Willner, L. *Europhys. Lett.* **1998**, *44*,
       606–612.

(234) Frielinghaus, H.; Mortensen, K.; Almdal, K. *Macromol. Symp.* **2000**, *149*, 63–68.

(235) Sethna, J. P. *Statistical Mechanics: Entropy, Order Parameters, and Complexity*;
       Oxford University Press, 2010.

(236) Stanley, H. E. *Rev. Mod. Phys.* **1999**, *71*, S358–S366.

(237) Thelen, J. L.; Teran, A. A.; Wang, X.; Garetz, B. A.; Nakamura, I.; Wang, Z.-G.;
       Balsara, N. P. *Macromolecules* **2014**, *47*, 2666–2673.

(238) Steinhardt, P. J. *Rend. Lincei* **2013**, *24*, S85–S91.

Appendix A

Fluctuation Effects in Symmetric Diblock Copolymer–Homopolymer Ternary Mixtures Near the Lamellar–Disorder Transition[*],[†]

ABSTRACT: We have systematically mapped the phase behavior of a series of symmetric CE/C/E ternary copolymer/homopolymer mixtures, where C is poly(cyclohexylethylene) and E is poly(ethylene), identifying the location in composition of the technologically important bicontinuous microemulsion (BμE) channel as a function of diblock molecular weight. The lamellar-to-disorder transition, characterized by dynamic mechanical spectroscopy, small-angle X-ray scattering and optical transmission measurements, exhibits increasingly second-order behavior as the BμE state is approached with increasing homopolymer content. Real-space transmission electron microscopy images obtained from rapidly frozen specimens evidence the development of large-scale fluctuating smectic correlations in the disordered state as the order–disorder transition is approached. This discovery provides fresh insights into the unexplained role of fluctuations in the formation of the BμE in ternary mixtures formed from binary blends of homopolymers that display an Ising-like critical point, and a symmetric diblock copolymer governed by a weak, fluctuation-induced, first-order phase transition.

Ternary mixtures of an AB diblock copolymer and the constituent A- and B-type homopolymers, high molecular weight analogues of oil/water/surfactant systems, have been the subject of intense scientific interest due to a combination of practical

---

applications for the materials and interesting problems in fundamental physics encountered in these systems.[1-7] Of primary practical interest is the polymeric bicontinuous microemulsion (BμE). This thermodynamically stable isotropic cocontinuous morphology with tunable domain sizes (50–250 nm) has been exploited as a template to create a variety of other nanoporous functional materials that are of interest for an array of potential applications.[1, 2] On a fundamental level, synthetic polymers in general offer remarkable control over the symmetry, length scale, dynamics, and dimensionality of various types of phase transitions making them ideal model systems for studying universal phenomena in condensed matter.[8, 9] Specifically, AB/A/B ternary blends display rich phase behavior connecting the self-assembly of pure diblock copolymers into nanoscopically ordered mesophases to macrophase separation of binary homopolymer blends.[5, 10]

Symmetric AB diblock copolymers exhibit a fluctuation-induced weakly first-order phase transition of the Brazovskii class between ordered striped (lamellar) and disordered states, where the degree of polymerization (N_{AB}) dictates the fundamental periodic length scale d.[11-15] The domain spacing, $d = 2\pi/q*$ can be measured by scattering experiments where $q*$ is the principal (first-order) Bragg reflection. Adding equal amounts of A and B homopolymers ($N_A \approx N_B$) to a symmetric AB diblock copolymer dilates (swells) the lamellae.[2] Within the context of mean-field theory $d \to \infty$ as $\phi_H \to \phi_{H,U}$, where ϕ_H is the total volume fraction of homopolymers and $\phi_{H,U}$ is the unbinding composition, roughly coincident with a predicted higher-order multicritical Lifshitz (L) point (i.e., $\phi_{H,U} \approx \phi_{H,L} = 1/(1 + 2N_A N_B/N_{AB}^2)$).[2, 3, 10] Experiments have shown that this divergence in periodicity is interrupted by the formation of a finite scale and technologically important BμE in a small window of blend composition.[2] A different universality class, macroscopic phase separation and Ising-like critical behavior characteristic of binary blends, is accessed at higher homopolymer content, $\phi_{H,L} < \phi_H \leq 1$.[3, 16] Fluctuations impact each region of this ternary phase diagram differently.[2, 4, 5, 11, 16-20] To date, most research on this topic has focused on understanding and exploiting the BμE morphology and characterizing the critical behavior on the homopolymer-rich side

of the BµE channel. Less well studied is the lamellar-to-disordered transition on the diblock-rich side of the phase diagram, which is generally assumed to belong to the Brazovskii class analogous to pure diblocks.[3-5, 16, 21] Application of the Gibbs phase rule anticipates that, in general, a two-phase window should separate the ordered and disordered states with varying temperature,[2] although this does not preclude the possibility of a line of continuous (second-order) transitions as a function of ϕ_H as predicted by mean-field theory.[10] In this Letter, we explore the effect of fluctuations on the lamellar-to-disorder (LAM–DIS) phase transition in AB/A/B ternary polymer blends at compositions between the pure diblock copolymer and the onset of the BµE channel.
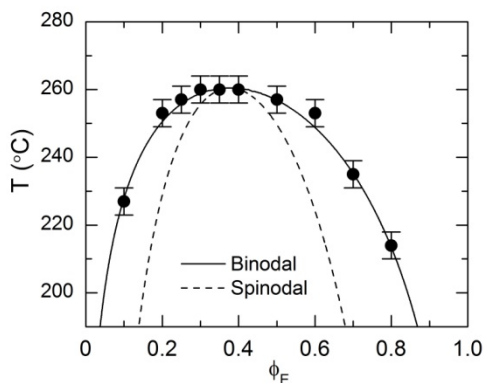
Figure A.1 Binary phase diagram for C/E homopolymer blends. Experimentally determined cloud point measurements are represented as black symbols. The binodal and spinodal curves are results of a fit to the data using Flory–Huggins theory with a composition-dependent c parameter.

We have investigated the volumetrically symmetric isopleths of ternary blends that bridge the divide in parameter space between lamellar forming symmetric diblocks and binary homopolymer blends that display upper critical solution temperature behavior. These blends were studied in mixtures of nearly equal amounts by volume of poly(cyclohexylethylene) (C) and polyethylene (E) homopolymers ($N_C = 40$ and $N_E = 37$ are the number-average degrees of polymerization based on a 118 Å^3 reference volume) and volumetrically symmetric poly(cyclohexylethylene-*b*-ethylene) (CE) diblock copolymers ($f_c = 0.51 \pm 0.1$; where f_c is the volume fraction of the C block) of various

N_{CE}, corresponding to number average-molecular weights M_n = 13, 14, 19, and 38 kg/mol (N_{CE} values of 220, 230, 310, and 630, respectively). These samples are referred to as 13CE, 14CE, 19CE, and 38CE, respectively. All polymers were synthesized and characterized using established methods resulting in narrow molecular weight distributions ($Đ$ < 1.1 in all cases).[22] Experimental and molecular characterization details are summarized in the Supporting Information.

The phase diagram for binary blends of C and E is shown in Figure A.1. The boundary between a single-phase and a two-phase region, the binodal curve, was determined from cloud point measurements on slow cooling. This phase diagram has been modeled using Flory–Huggins theory with a composition-dependent segment–segment interaction parameter, $\chi(T, \phi_E) = (\alpha/T - \beta)(1+c(1 - \phi_E)$, where α, β, and c are constants, resulting in a critical temperature and composition of 260 °C and $\phi_{E,c}$ = 0.37, respectively.[7, 23]

In all CE/C/E ternary blends studied here, the volume ratio between the C and E homopolymers was kept constant (ϕ_C / ϕ_E = 1) and the overall total homopolymer volume fraction ($\phi_H = \phi_C + \phi_E$) was varied. Due to the slight asymmetry of the C/E binary system, the ϕ_E = 0.5 blend at the pure homopolymer end of this isopleth (binodal temperature of 257 °C) is not precisely at the critical composition; this has a trivial impact on the phase behavior as $\phi_H \rightarrow \phi_{H,B\mu E}$. Each blend is referred to as xxCEyy, where xxCE is the CE diblock used in the blend and yy is the total homopolymer volume percent.
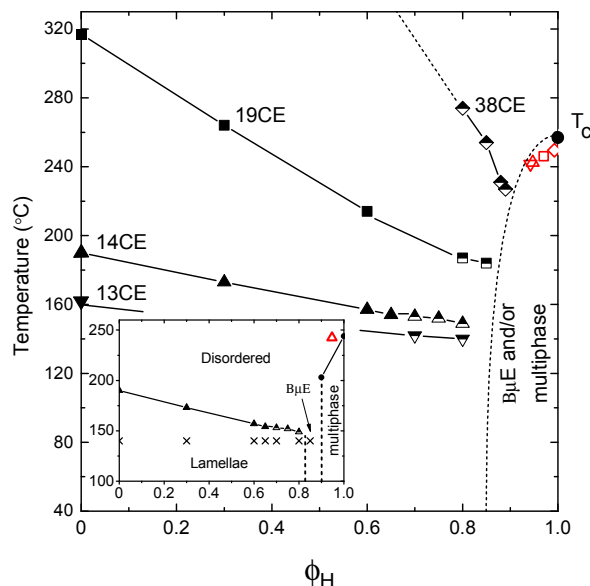
Figure A.2 Phase diagrams showing the LAM–DIS transitions along the volumetrically symmetric isopleths for ternary CE/C/E blends with several CE diblocks. ϕ_H represents the total volume fraction of homopolymer. Half-filled symbols indicate blends for which a local minimum of optical transmission was observed at the ODT. T_C is the experimentally determined cloud point for the $\phi_E = 0.5$ binary blend from Figure A.1. The inset graph is a detailed ternary phase diagram for 14CE containing blends. The cross mark symbols indicate points where SAXS data were collected to determine phase symmetry (See Figure S1). Empty red symbols indicate predicted Lifshitz composition and temperature. All lines connecting data points are to guide the eye.

The ternary CE/C/E phase diagrams along the volumetrically symmetric isopleth are summarized in Figure A.2. These were experimentally determined using a combination of optical transmission and dynamic mechanical spectroscopy (DMS) to locate order–disorder transition temperatures (T_{ODT}) and both small-angle X-ray scattering (SAXS) and TEM to determine phase symmetries. In all cases, the low temperature ordered phase is lamellar (LAM). See Figure S1 in Supporting Information for detailed SAXS patterns. When the C and E homopolymers are blended with the CE diblocks, the homopolymers swell the LAM domains, and the T_{ODT} of the LAM–DIS transition decreases as ϕ_H increases. At high ϕ_H the line of order–disorder transitions (ODT) terminates at the narrow BµE channel, while a multi-phase region characterizes

still higher homopolymer contents as ϕ_H approaches 1. As the diblock molecular weight (N_{CE}) increases, larger quantities of homopolymer are needed to reach the BμE channel, following the trend predicted by the theoretical Lifshitz points (calculated to occur at values of $\phi_{H,L}$ of 0.94, 0.95, 0.97, and 0.99 for the 13CE, 14CE, 19CE, and 38CE systems, respectively). However, the onset of the BμE always occurs at values of ϕ_H lower than the predicted Lifshitz points, consistent with previous observations.[2]

The inset of Figure A.2 shows a detailed ternary phase diagram for the blends containing the 14CE diblock copolymer. SAXS measurements confirm that the lamellar morphology persists up to $\phi_H = 0.80$, and the BμE forms at $\phi_H = 0.85$. For $\phi_H \geq 0.90$, macroscopic phase separation occurs below the envelope of upper critical solution temperatures (UCSTs) identified by cloud points in optical transmission measurements (see Supporting Information).

In addition to simple cloud points that evidence macroscopic phase separation, two other light scattering phenomena were recorded in optical transmission experiments while heating and cooling the ternary blends through the T_{ODT} of the LAM-DIS transition, as shown in Figure A.3. We attribute changes in relative transmission in this temperature range to variations in the fraction of incident light scattered to wider angles than collected at the detector in our experimental measurements.[24-26] For blends with low homopolymer content $\phi_H \leq 0.65$, a small discontinuous increase in the transmission occurs in some samples at the T_{ODT} upon heating through the LAM–DIS transition (or reduction upon cooling through the DIS–LAM transition). This behavior is shown for the 14CE60 blend and the pure 14CE diblock ("blend" 14CE0) in Figure A.3. This change in transmission coincides with the T_{ODT} measured with DMS, indicated in Figure A.3 by an abrupt decline in the storage modulus (G') as the soft solid response of the LAM phase gives way upon heating to liquid-like behavior. Scattering of visible light from the LAM state has been shown to originate from randomly oriented grains of the locally anisotropic and birefringent striped phase.[24-26] When the material disorders, this source of scattering is extinguished, and an increase in transmission occurs.

For blends with higher homopolymer content, a second, unexpected light scattering phenomenon was discovered as the BμE channel was approached. In these blends, a local minimum in the transmission (corresponding to a maximum in scattered intensity) appears at a temperature that is coincident with the T_{ODT} measured with DMS. This is illustrated for the blends 14CE80 and 19CE85 in Figure A.3. All blends in which this local minimum in transmission was recorded are shown with half-filled symbols in the phase diagrams in Figure A.2. The depth of the local minimum increases with increasing homopolymer content, beginning at approximately $\phi_H \approx 0.70$, where this feature first becomes evident, and becoming most pronounced at values of ϕ_H nearest the BμE channel. In addition, the breadth in temperature of the local minimum of transmission increases with increasing diblock molecular weight. The local transmission minimum is fully reversible upon heating and cooling through the ODT. The location, depth, and breadth of the local minimum of transmission are essentially independent of the rate of change in temperature; only a small hysteresis in the location in temperature of the minimum transmission, T_{min}, was documented at the highest temperature ramp rates ($\Delta T_{min} \approx 3$ °C for a rate of 1 °C/min). Moreover, near the local minimum, ceasing heating or cooling and holding the temperature constant for extended periods of time does not influence the transmission value. For example, the inset in Figure A.3 shows the stability of the transmission near the local minimum at T_{ODT} for the 14CE80 blend. Similarly, the reduced transmission at temperatures near T_{ODT} is essentially independent of thermal history. These results confirm that the reduced transmission at temperatures near T_{ODT} is not a transient phenomenon but a manifestation of equilibrium states near the LAM–DIS transition in these ternary blends.
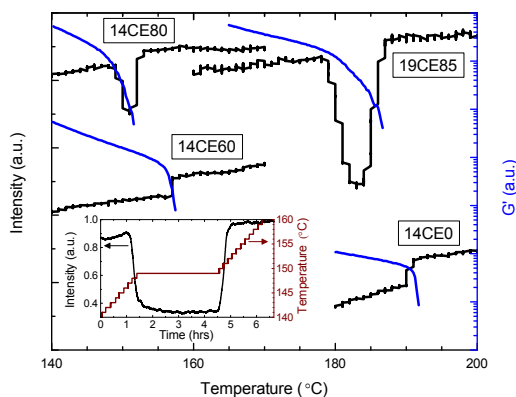
Figure A.3 Representative optical transmission and DMS determination of ODT for blends containing 14CE and 19CE polymers. The black and blue lines represent optical transmission and DMS data, respectively. Data were collected while heating at a rate of 1 °C/min. The inset plot shows the time-dependent stability of the transmission for the 14CE80 blend when the heating ramp (at a rate of 0.1 °C/min) was halted at 149 °C, the temperature approximately at the local minimum in transmission. The black and red lines represent the optical transmission and temperature, respectively. Data have been shifted vertically for clarity.

Direct real space imaging by TEM was employed to probe the structure of these materials near the LAM–DIS transition. Because the mixtures solidify near 100 °C (the glass transition for C and the melting transition for E), we were able to freeze and image the morphology at specific temperatures by rapidly immersing the specimen in a dry ice and 2-propanol bath ($T = -78$ °C), which fixes the polymers in less than 5 seconds. Representative TEM images of the 38CE88 blend near the LAM–DIS transition for samples quenched after annealing for 16 hours from temperatures below (Figure A.4a), at (Figure A.4b), and above (Figure A.4c) the local minimum in transmission are shown in Figure A.4. These TEM images reveal a well-ordered LAM phase at low temperature (Figure A.4a) and an isotropic but microphase separated disordered phase that resembles the BµE at high temperatures at and above the transmission minimum. At 230 °C (Figure A.4b), i.e., coincident with the minimum in the optical transmission, the morphology is disordered at large length scales (*ca.* > 1 mm) but characterized by local lamellar (smectic-like) correlations that extend over several hundred nanometers. This strongly

fluctuating morphology explains the origins of the loss in light transmission, i.e., a smectic fluctuation correlation length commensurate with the wavelength of visible light. At 238 °C (Figure A.4c) the smectic fluctuation correlation length is considerably smaller, consistent with the increase in transmission.
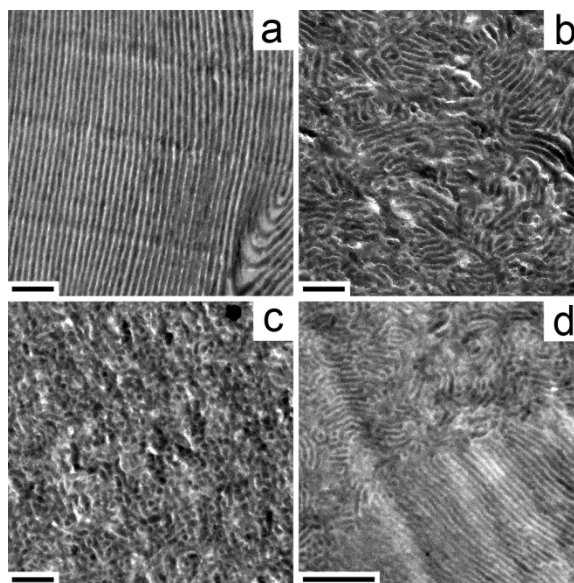
Figure A.4 Transmission electron microscopy images depicting the morphology of ternary blends during the LAM–DIS transition. Images represent quenched states after 16 hours of annealing (a) below (170 °C), (b) at (230 °C), and (c) above (238 °C) the ODT for sample 38CE88. (d) A coexistence between fluctuating disordered and ordered lamellar phases for sample 19CE85 quenched at 177 °C upon the observation of a reduction in optical transmission during a heating ramp. All scale bars are 500 nm and samples have been stained with ruthenium tetroxide.

The sharp increase in light scattering near the ODT for homopolymer-rich blends (Figure A.3) and the fluctuating morphology evident in Figure A.4 lead us to hypothesize that the nature of the LAM-DIS phase transition changes as the BµE channel (and the mean-field predicted Lifshitz point) is approached with increasing homopolymer content. At low homopolymer content ($\phi_H \leq 0.65$), a weakly first-order transition is observed, which we interpret as an extension of the behavior at $\phi_H = 0$ (i.e., pure diblock copolymer) where fluctuations in the local composition at finite q induce the ODT. For

$0.65 < \phi_H \leq \phi_{H,B\mu E}$, the LAM–DIS transition is qualitatively different. Here, fluctuations in a second quantity (perhaps related to the interfacial curvature between domain spaces, see below) give rise to the documented smectic correlations of which the characteristic length scale grows as the transition is approached, eventually spanning the sample in the ordered phase. This diverging length scale suggests the system is at or near a continuous second-order LAM–DIS transition. In addition, the reported local minimum in transmission is reminiscent of critical opalescence near a second-order transition.[27] The reported change in character of the LAM–DIS transition for $\phi_{H,L} \leq \phi_H$ may reflect a crossover effect analogous to the crossover between Ising and Lifshitz behavior near the line of critical points in the homopolymer-rich region of the phase diagram ($\phi_{H,L} < \phi_H \leq 1$).[16]

Other experiments at temperatures coincident with the minimum in light transmission suggest that the mixtures reported in Figure A.3 may not be located precisely along a line of continuous second-order transitions. For example, Figure A.4d shows a TEM image obtained from blend 19CE85 after quenching (during heating at 1 °C/min) from the temperature where the local minimum in transmission occurs. This micrograph shows coexistence between the LAM and disordered phases; smectic-like fluctuations in the disordered state closely resemble those found in Figure A.4b. In this case, development of large-scale smectic fluctuations (which should diverge in length scale at a true second-order transition) appears to be cut off by a first-order transition. In practice, verifying the existence of a line of critical points as the BμE is approached requires finely tuning the ratio ϕ_C / ϕ_E at constant ϕ_{CE}, which will be undertaken in future experiments.

The transition from first- to second-order-like behavior in the work presented here is reminiscent of the seminal work by McMillan, in which, using a mean-field treatment, a change from a second- to a first-order transition was predicted for the smectic-A-to-nematic transition in liquid-crystalline molecules with increasing alkyl-chain length due to a coupling of the nematic and smectic order parameters.[28] Here we note that these one-component liquid crystals lack the thermodynamic degrees of freedom necessary to

produce multiple phase windows as a function of temperature. The behavior of the CE/C/E ternary blends described in this Letter raises the intriguing possibility of the existence of an additional order parameter, perhaps relating to curvature of the interface dividing the C- and E-rich domains, even in the limit $\phi_H \to 0$. In pure (single component) symmetric diblock copolymers the fluctuating disordered state has been shown to transition to the LAM phase without changing either d or the local composition profile.[12] Attaining constant negative Gauss and zero mean curvature at the interface dividing the fluctuating domain spaces in the disordered bicontinuous morphology (a general driving force in self-assembled soft materials governed by constant density)[29] requires twisting the saddle-shaped interfacial surface, introducing the possibility of local chirality in the system (similar geometric arguments result in the familiar gyroid phase).[30, 31] Adding homopolymer alleviates such packing constraints (since the homopolymers are not pinned to the interface), perhaps altering this hypothetical order parameter and facilitating the development of smectic fluctuations with arbitrary correlation length without the need to twist the local interfacial surface topology.

In the $\phi_H \to 0$ (and $\phi_H \to 1$) limit, as $N_{AB} \to \infty$ ($N_A = N_B \to \infty$) and $d \to \infty$ (and the correlation length $\xi \to \infty$),[32, 33] the effects of fluctuations disappear leading to the recovery of a (mean-field) second-order ODT (and mean-field *versus* Ising-like critical scaling exponents). By analogy, as $\phi_H \to \phi_{H,U}$ and $d \to \infty$ we might expect the symmetric ternary mixture to become more mean-field-like. Theory anticipates that a (mean-field) multicritical Lifshitz point occurs when $N_{AB} \to \infty$ and $N_A = N_B \to \infty$ at finite N_{AB}/N_A. However, the greater upper and lower critical dimensions associated with the Lifshitz point[34] make the symmetric ternary mixture more susceptible to fluctuation effects than the binary homopolymer blend; the upper critical dimension for the undiluted symmetric diblock copolymer appears to be infinite.[35] The added degrees of freedom associated with 3 components, and the mixing of universality classes, leads to the formation of an entirely different phase state, a bicontinuous microemulsion as $d \to \infty$. We believe the experimental evidence presented here offers clues regarding the underlying competition between fluctuation effects in the LAM and DIS phases and the transition to the

fascinating bicontinuous microemulsion, which has not yet been described by fundamental theory.

The ability to precisely tune the molecular (e.g., N_{AB}, $N_A = N_B$) and thermodynamic (T_{ODT}, T_c, and ϕ_H) parameters, along with access to quantitative real-space and reciprocal-space structural probes, makes AB/A/B mixtures especially attractive as model systems for studying the universal behavior of condensed matter systems, in particular one-dimensionally ordered lamellar or striped phases.[36-38] Striped phases govern the physical properties of a host of condensed matter systems including high-temperature superconductors,[39-41] magnetic alloys,[42] and liquid crystals.[43] For example, the fluctuating smectic correlations reported here are perhaps analogous to recent work where fluctuating charge stripes were observed near the charge order temperature for high-temperature superconducting cuprates.[40] Understanding the universal phase behavior that governs this form of one-dimensional order is complicated by difficulties associated with precisely tuning the interactions that give rise to striped phases, along with visualizing fluctuations, which generally dominate the transition from disorder to a state of one-dimensional order. Ternary blends of symmetric AB diblock copolymers and the associated A and B homopolymers provide an ideal remedy to these problems.

ASSOCIATED CONTENT

Supporting Information

Detailed experimental procedures, polymer characterization, X-ray scattering data, optical transmission schematic, and additional TEM images. This material is available free of charge via the Internet at http://pubs.acs.org.

AUTHOR INFORMATION

Corresponding Author

*E-mail: (FSB) bates001@umn.edu

Notes

The authors declare no competing financial interest.

REFERENCES

(1)   Jones, B. H.; Lodge, T. P. *Polym. J.* **2012,** *44*, 131-146.

(2)   Bates, F. S.; Maurer, W. W.; Lipic, P. M.; Hillmyer, M. A.; Almdal, K.; Mortensen, K.; Fredrickson, G. H.; Lodge, T. P. *Phys. Rev. Lett.* **1997,** *79*, 849-852.

(3)   Schwahn, D.; Mortensen, K.; Frielinghaus, H.; Almdal, K. *Phys. Rev. Lett.* **1999,** *82*, 5056-5059.

(4)   Schwahn, D.; Mortensen, K.; Frielinghaus, H.; Almdal, K.; Kielhorn, L. *J. Chem. Phys.* **2000,** *112*, 5454-5472.

(5)   Pipich, V.; Schwahn, D.; Willner, L. *J. Chem. Phys.* **2005,** *123*, 124904.

(6)   Hillmyer, M. A.; Maurer, W. W.; Lodge, T. P.; Bates, F. S.; Almdal, K. *J. Phys. Chem. B* **1999,** *103*, 4814-4824.

(7)   Washburn, N. R.; Lodge, T. P.; Bates, F. S. *J. Phys. Chem. B* **2000,** *104*, 6987-6997.

(8)   Bates, F. S. *Science* **1991,** *251*, 898-905.

(9)   Chaikin, P. M.; Lubensky, T. C., *Principles of Condensed Matter Physics*. Cambridge University Press: Cambridge, England, 2000.

(10)   Broseta, D.; Fredrickson, G. H. *J. Chem. Phys.* **1990,** *93*, 2927-2938.

(11)   Fredrickson, G. H.; Helfand, E. *J. Chem. Phys.* **1987,** *87*, 697-705.

(12)   Lee, S.; Gillard, T. M.; Bates, F. S. *AIChE J.* **2013,** *59*, 3502-3513.

(13)   Voronov, V. P.; Buleiko, V. M.; Podneks, V. E.; Hamley, I. W.; Fairclough, J. P. A.; Ryan, A. J.; Mai, S. M.; Liao, B. X.; Booth, C. *Macromolecules* **1997,** *30*, 6674-6676.

(14)   Rosedale, J. H.; Bates, F. S.; Almdal, K.; Mortensen, K.; Wignall, G. D. *Macromolecules* **1995,** *28*, 1429-1443.

(15)   Brazovskii, S. A. *Sov. Phys. JETP* **1975,** *41*, 85-89.

(16)   Schwahn, D. *Adv. Polym. Sci.* **2005,** *183*, 1-61.

(17)   Bates, F. S.; Rosedale, J. H.; Fredrickson, G. H. *J. Chem. Phys.* **1990,** *92*, 6255-6270.

(18)   de Gennes, P. G. *J. Chem. Phys.* **1980,** *72*, 4756-4763.

(19)   Düchs, D.; Ganesan, V.; Fredrickson, G. H.; Schmid, F. *Macromolecules* **2003,** *36*, 9237-9248.

(20)   Bates, F. S.; Rosedale, J. H.; Stepanek, P.; Lodge, T. P.; Wiltzius, P.; Fredrickson, G. H.; Hjelm, R. P. *Phys. Rev. Lett.* **1990,** *65*, 1893-1896.

(21)   Pandav, G.; Ganesan, V. *Macromolecules* **2013,** *46*, 8334-8344.

(22)   Cochran, E. W.; Bates, F. S. *Macromolecules* **2002,** *35*, 7368-7374.

(23)   Qian, C.; Mumby, S. J.; Eichinger, B. E. *Macromolecules* **1991,** *24*, 1655-1661.

(24)   Balsara, N. P.; Garetz, B. A.; Dai, H. J. *Macromolecules* **1992,** *25*, 6072-6074.

(25)   Balsara, N. P.; Perahia, D.; Safinya, C. R.; Tirrell, M.; Lodge, T. P. *Macromolecules* **1992,** *25*, 3896-3901.

(26)   Garetz, B. A.; Newstein, M. C.; Dai, H. J.; Jonnalagadda, S. V.; Balsara, N. P. *Macromolecules* **1993,** *26*, 3151-3155.

(27)   Stanley, H. E., *Introduction to Phase Transitions and Critical Phenomena*. Oxford University Press: New York, 1971.

(28)   McMillan, W. L. *Phys. Rev. A* **1971,** *4*, 1238-1246.

(29)   Seddon, J. M. *Biochim. Biophys. Acta* **1990,** *1031*, 1-69.

(30)   Fogden, A.; Hyde, S. T. *Eur. Phys. J. B* **1999,** *7*, 91-104.

(31)   Matsen, M. W.; Bates, F. S. *J. Chem. Phys.* **1997,** *106*, 2436-2448.

(32)   Leibler, L. *Macromolecules* **1980,** *13*, 1602-1617.

(33)   de Gennes, P. G., *Scaling Concepts in Polymer Physics*. Cornell University Press: Ithica, New York, 1979.

(34)   Bates, F. S.; Maurer, W.; Lodge, T. P.; Schulz, M. F.; Matsen, M. W.; Almdal, K.; Mortensen, K. *Phys. Rev. Lett.* **1995,** *75*, 4429-4432.

(35)   Glenn Fredrickson, personal communication.

(36)   Seul, M.; Monar, L. R.; O'Gorman, L.; Wolfe, R. *Science* **1991,** *254*, 1616-1618.

(37)   Seul, M.; Andelman, D. *Science* **1995,** *267*, 476-483.

(38)   Malescio, G.; Pellicane, G. *Nat. Mater.* **2003,** *2*, 97-100.

(39)   Kivelson, S. A.; Bindloss, I. P.; Fradkin, E.; Oganesyan, V.; Tranquada, J. M.; Kapitulnik, A.; Howald, C. *Rev. Mod. Phys.* **2003,** *75*, 1201-1241.

(40)   Abeykoon, A. M. M.; Božin, E. S.; Yin, W.-G.; Gu, G.; Hill, J. P.; Tranquada, J. M.; Billinge, S. J. L. *Phys. Rev. Lett.* **2013,** *111*, 096404.

(41)   Valla, T.; Fedorov, A. V.; Lee, J.; Davis, J. C.; Gu, G. D. *Science* **2006,** *314*, 1914-1916.

(42)   Zhao, J.; Shen, Y.; Birgeneau, R. J.; Gao, M.; Lu, Z.-Y.; Lee, D. H.; Lu, X. Z.; Xiang, H. J.; Abernathy, D. L.; Zhao, Y. *Phys. Rev. Lett.* **2014,** *112*, 177002.

(43)   Link, D. R.; Natale, G.; Shao, R.; Maclennan, J. E.; Clark, N. A.; Körblova, E.; Walba, D. M. *Science* **1997,** *278*, 1924-1927.

Appendix B

Influence of Composition Fluctuations on the Linear Viscoelastic Properties of Symmetric Diblock Copolymers near the Order–Disorder Transition [*],[†]

ABSTRACT: Rheological evidence of composition fluctuations in disordered diblock copolymers near the order–disorder transition (ODT) has been documented in the literature over the past three decades, characterized by a failure of time–temperature superposition (tTS) to reduce linear dynamic mechanical spectroscopy (DMS) data in the terminal viscoelastic regime to a temperature independent form. However, for some materials, most notably poly(styrene-b-isoprene) (PS-PI), no signature of these rheological features has been found. We present small-angle X-ray scattering (SAXS) results on symmetric poly(cyclohexylethylene-b-ethylene) (PCHE-PE) diblock copolymers that confirm the presence of fluctuations in the disordered state, and DMS measurements that also show no sign of the features ascribed to composition fluctuations. Assessment of DMS results published on five different diblock copolymer systems leads us to conclude that the effects of composition fluctuations can be masked by highly asymmetric block dynamics, thereby resolving a long-standing disagreement in the literature and reinforcing the importance of mechanical contrast in understanding the dynamics of ordered and disordered block polymers.

Materials with nanoscale features are being incorporated into emerging technologies with applications in energy,[1] electronics,[2] and medicine.[3] Block polymers are a class of materials for which synthetic methods offer precise control over chemical architecture, morphology, dynamics, and morphological length scale.[4] As a consequence, they are an active area of research with potential uses in a diverse array of products, including batteries,[5] lithographic materials,[6] and drug delivery.[7] A fundamental understanding of block polymer phase transitions, nanoscale morphologies, and processing is an essential prerequisite to integration into future commercial products.[8,9] It is well established that volumetrically symmetric AB diblock copolymers ($f = \frac{1}{2}$) of finite molecular weight undergo an order–disorder phase transition (ODT) characteristic of the Brazovskii class, for which the change from an ordered lamellar phase (LAM) to an isotropic disordered phase (DIS) is weakly first-order.[10-13] Thermally driven fluctuations in local composition profoundly influence block copolymer phase behavior near this fluctuation-induced phase transition, destroying the second-order ODT anticipated by mean-field theory (i.e., infinite molecular weight limit).[10,14] Here, we present dynamic mechanical spectroscopy (DMS) results that help elucidate how differences in the individual A- and B-block relaxation times of an AB diblock copolymer are manifested in linear oscillatory viscoelastic measurements.

A host of experimental techniques, including small-angle X-ray scattering (SAXS),[15-18] small-angle neutron scattering (SANS),[11,12,19] differential scanning calorimetry (DSC),[13] transmission electron microscopy (TEM),[20-22] rheology,[23-25] and others,[26-32] have confirmed the presence of composition fluctuations in the disordered phase of block polymers near the ODT. Schematic illustrations of the morphology around the LAM–DIS transition for a symmetric diblock copolymer are presented in Figure B.1. Below the order–disorder transition temperature (T_{ODT}), a static microphase-separated state with coherent, long-range lamellar order is obtained. In the absence of an aligning field (e.g., hydrodynamic,[33] electric,[34] magnetic[35]), a polycrystalline structure with many randomly arranged LAM grains occurs, where the material is isotropic on long length scales (Figure B.1a). Above T_{ODT}, composition fluctuations produce a structured but

globally isotropic disordered state characterized by transient microphase-separation at the local level, i.e., with short-range correlations but no long-range order (Figure B.1b). This fluctuating equilibrium disordered state resembles both a bicontinuous microemulsion and the nonequilibrium structure observed during spinodal decomposition of a binary blend of immiscible liquids.[13,36] While there are obvious differences in the microstructure of the LAM and DIS phases on large length scales (i.e., greater than the periodicity d, where the interfacial curvature is characterized by zero and negative Gauss curvature, respectively), locally (i.e., on the molecular scale) they are quite similar: both contain an AB interface with zero mean curvature separating A- and B-rich domains. Indeed, the local composition profile normal to the AB interface has been shown to be nearly identical in the LAM and DIS phases at the ODT and of relatively high amplitude for experimental molecular weights.[13,37]

Although the first reported experimental evidence of composition fluctuations in block polymers was a rheological feature in the disordered state near the ODT,[23] a comprehensive understanding of the influence of fluctuations on rheology has remained elusive. The rheological feature attributed to composition fluctuations, which we refer to as the "rheological fingerprint", manifests as additional elasticity in the low frequency ($\omega \ll \tau^{-1}$, where τ is the single chain relaxation time) linear dynamic elastic (G') modulus near the ODT. The associated temperature dependent onset of terminal relaxation ($G' \sim \omega^2$; $G'' \sim \omega^1$) is clearly evident in master plots prepared using the time–temperature superposition (tTS) principle (i.e., a lack of superposition of G' at low frequencies as the ODT is approached)[38] in certain systems; see Rosedale et al.[25] and Kennemur et al.[24] for clear examples obtained with symmetric poly(ethylene-*alt*-propylene-*b*-ethylethylene) (PEP-PEE) and poly(*t*-butylstyrene-*b*-methyl methacrylate) (PtBS-PMMA) diblock copolymer melts, respectively. In apparent disagreement with these reports, the rheological fingerprint of fluctuations is absent in publications dealing with several other diblock copolymer systems,[39,40] most notably poly(styrene-*b*-isoprene) (PS-PI), leading to skepticism regarding the fluctuation-based interpretation of this dynamical feature.[39] One hypothesis for explaining this relaxation mode implicates polymer chain

entanglements.[29,38] However, a recent report dealing with the rheology of unentangled PtBS-PMMA, a system governed by essentially a single glass transition temperature (T_g ≈ 130 °C), unambiguously shows the rheological fingerprint of composition fluctuations,[24] dispelling this notion.
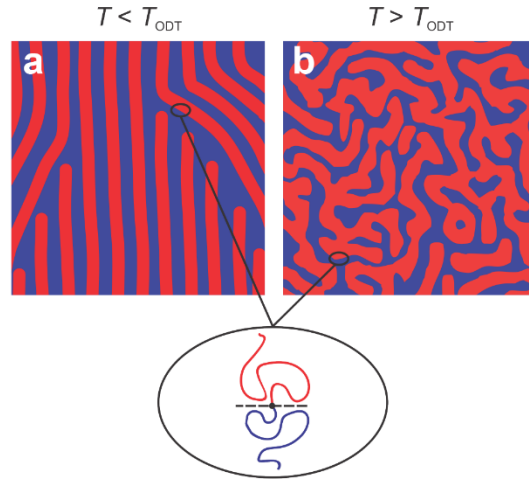
Figure B.1 Illustration of structure near the ODT. Morphology of the (a) ordered ($T < T_{ODT}$) and (b) fluctuating disordered ($T > T_{ODT}$) states of a diblock copolymer melt.

Here, we present results that connect the rheological fingerprint of composition fluctuations to the ratio of the individual A- and B-block relaxation times of an AB diblock copolymer, a parameter previously referred to as "mechanical contrast".[38] We investigated the rheological response near the ODT of a symmetric poly(cyclohexylethylene-b-ethylene) (PCHE-PE) diblock copolymer and compare the data to previously published results, including a reanalysis of the data from the PtBS-PMMA polymer.[24] These samples are referred to as PCHE-PE-14 and PtBS-PMMA-236; synthesis and characterization of these materials is detailed in previously published works.[41,42] These two polymers were chosen because they have similar molecular weights (M_n), 13.6 and 17.6 kg/mol, T_{ODT} values, 189 ± 1 and 193 ± 1 °C, and block volume fractions, f_{PCHE} = 0.52 and f_{PtBS} = 0.53, respectively. We find that when the single-chain relaxation times (τ) for the individual blocks differ by orders of magnitude (ratio > 10^4) the rheological fingerprint indicative of fluctuations is not found in $G'(\omega)$. This work

resolves a long-unanswered question pertaining to the ability to measure rheologically the effects of composition fluctuations and aids in understanding low-frequency scaling for both the dynamic elastic and loss moduli in block copolymers in general.

The presence of fluctuations in disordered PCHE-PE-14 near the ODT ($T > T_{ODT}$ = 189 ± 1 °C) was conclusively established using SAXS experiments. Below T_{ODT}, this material forms an ordered LAM phase with a domain spacing $d = 2\pi/q^* = 17$ nm, where q^* is the scattering wave vector associated with the first-order Bragg reflection ($q = 4\pi\lambda^{-1}\sin(\theta/2)$; λ is the X-ray wavelength; and θ is the scattering angle) (see Supporting Information). In Figure B.2, the inverse primary peak intensity, $\Gamma^{-1}(q^*)$, is plotted as a function of inverse temperature, T^{-1}. When the sample is heated through the ODT, there is a discontinuous increase in $\Gamma^{-1}(q^*)$ and broadening of the primary scattering peak (see Supporting Information), which signifies the transition from an ordered to a disordered state. The concave upward curvature of $\Gamma^{-1}(q^*)$ with T^{-1}, which persists to at least 50 °C above T_{ODT}, is indicative of the presence of composition fluctuations in the disordered phase.[11]
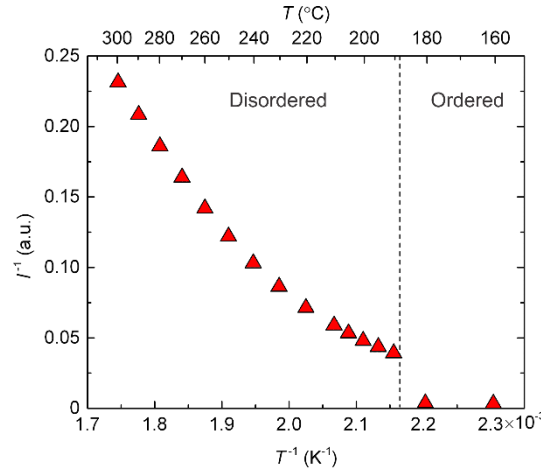
Figure B.2 Inverse SAXS primary peak intensity, I^{-1} (q^*), versus inverse temperature, T^{-1}. Data obtained while heating sample PCHE-PE-14 from the ordered lamellar phase to temperatures above the order–disorder transition at 189 ± 1 °C (dashed line). Curvature in I^{-1} (q^*) in the disordered state results from composition fluctuations.

The linear dynamic elastic (G') and loss (G'') moduli were measured for PCHE-PE-14 (and PCHE-PE-19; M_n =18.9 kg/mol and f_{PCHE} = 0.51; T_{ODT} = 317 °C)[41] using a Rheometrics Scientific ARES strain-controlled rheometer with a 25 mm diameter parallel plate geometry over the frequency range $0.01 \leq \omega \leq 100$ rad/s and $140 \leq T \leq 260$ °C. Time–temperature shift factors (a_T) were obtained by constructing a master plot for PCHE-PE-19 and application of the Williams–Landel–Ferry (WLF) equation, $\log(a_T) = -c_1(T - T_{ref}) / (c_2 + T - T_{ref})$; c_1 = 5.16 and c_2 = 104.25 °C, based on the reference temperature T_{ref} = 180 °C (see Supporting Information). These shift factors were used to construct a master plot for PCHE-PE-14, without any adjustable parameters, as shown in Figure B.3. Two distinct branches are evident in G' (ω) and G''(ω) for $\omega < \omega_c$, where ω_c marks the point of transition from single chain ($\omega > \omega_c$) to collective (domain) dominated ($\omega < \omega_c$) dynamics.[38] For $T > T_{ODT}$ all the data collapse onto common, temperature-independent, terminal response curves, $G' \sim \omega^2$ and $G'' \sim \omega^1$, while for $T < T_{ODT}$ non-terminal behavior ($G' \sim G'' \sim \omega^\delta$ with $\delta < 1$)[38] is obvious. Significantly, there is no evidence of the composition fluctuations (documented by SAXS, Figure B.2) in these results. This result duplicates previous work with another hydrogenated polyolefin

diblock copolymer, poly(cyclohexylethylene-*b*-ethylene propylene) (PCHE-PEP), which showed similar tTS master plots in which the rheological fingerprint of fluctuations was not observed.[40]
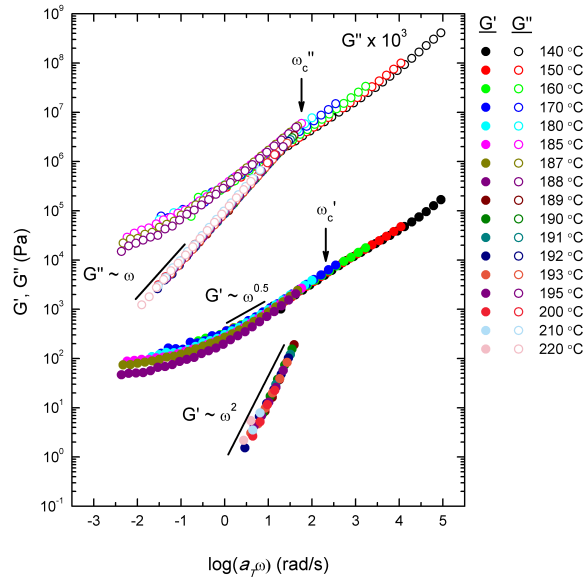
Figure B.3 Master plot for the linear dynamic elastic (*G*') and loss (*G*") moduli for PCHE-PE-14 near the order–disorder transition (T_{ODT} = 189 ± 1 °C). Time–temperature shift factors (a_T) were obtained from ordered (lamellae) sample PCHE-PE-19 and applied to PCHE-PE-14 using the reference temperature T_{ref} = 180 °C. The G" data have been shifted vertically by the factor 10^3 for clarity.

Although often applied with success to block polymers, the assumptions underlying tTS do not strictly apply to thermorheologically complex systems that have more than one fundamental time constant, e.g., diblock copolymers with two distinct glass transition temperatures (T_g).[38,39] Therefore, plots of log *G*' vs log *G*" (a type of Cole–Cole or Nyquist diagram also referred to by some authors as a Han plot[43]) have been used to display block polymer dynamics and determine T_{ODT} in block copolymer systems; this procedure eliminates the need to apply arbitrary shift factors.[38,43] In Figure B.4 the data from Figure B.2 (PCHE-PE-14) and the results reported by Kennemur, et al.[24] for PtBS-PMMA-236 are replotted in the Cole–Cole format. There are striking similarities between the tTS master plots and the Cole–Cole plots for PCHE-PE and

PtBS-PMMA-236.[24] In both depictions, the low modulus regime ($\omega < \omega_c$) shows two branches corresponding to the disordered ($T > T_{ODT}$) and ordered ($T < T_{ODT}$) phases. The disordered state branch in the Cole–Cole construction for both polymers shows behavior analogous to the low-frequency branches in the tTS master plots. Specifically, near perfect overlay of the data is obtained for all temperatures in PCHE-PE-14, while the rheological fingerprint of fluctuations is plainly evident in both the tTS and Cole-Cole constructions for PtBS-PMMA-236. These comparisons validate the use of the tTS procedure for both specimens.
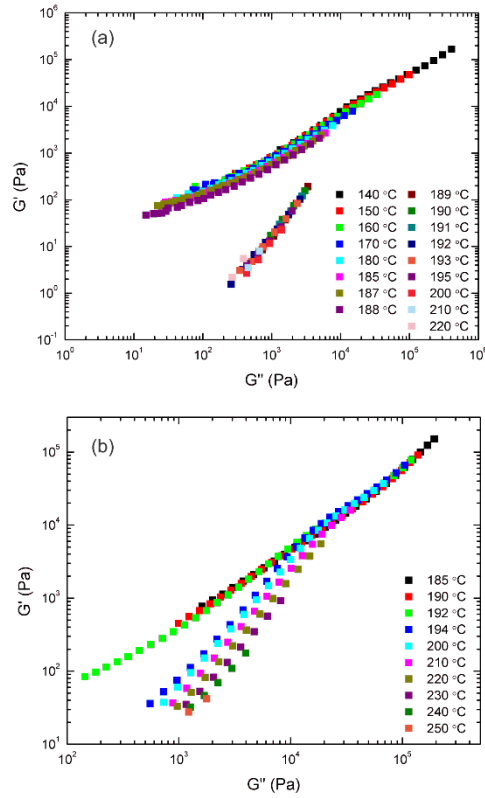
Figure B.4 Modified Cole–Cole plots for (a) PCHE-PE-14 and (b) PtBS-PMMA-236. The order–disorder transition for these materials occurs at 189 ± 1 °C and 193 ± 1 °C, respectively. The temperature dependence of the low-frequency response in G' in panel (b) is attributed to composition fluctuations. Absence of this feature in (a) is associated with highly asymmetric block relaxation times.

These results raise an intriguing question: Why do PCHE-PE-14 and PtBS-PMMA-236, which exhibit comparable fluctuating disordered states (as confirmed by SAXS) and have similar physical properties (M_n and T_{ODT}), exhibit qualitatively different viscoelastic responses just above the T_{ODT}? We propose that this difference can be traced to the relative relaxation times for the individual blocks of the diblock copolymers, which is controlled primarily by differences in the glass transition temperatures and to a lesser extent by the relative extents of entanglement. For the PCHE-PE system $T_{g,PCHE} = 140$ °C and $T_{g,PE} = -120$ °C ($\Delta T_g = T_{g,PCHE} - T_{g,PE} \approx 260$ °C). The PCHE block is unentangled ($M_e \cong 40$ kg/mol),[44] while the PE block is entangled ($M_e \cong 0.8$ kg/mol).[44] For PtBS-PMMA neither block is entangled and $T_{g,PtBS} = 141$ °C and $T_{g,PMMA} = 110$ °C ($\Delta T_g \approx 20$ °C).

However, based on DSC measurements near T_{ODT}, PtBS-PMMA-236 exhibits essentially a single glass transition temperature $T_g \approx 130\ °C$.[24]

Table B.1 Calculated ratio of relative block relaxation times.

Diblock Copolymer	Chain M_w (kg/mol)[a]	$\tau_r = \tau_A/\tau_B$	rheological fingerprint[b]
PCHE-PE $T = 190\ °C$	PCHE (7.6)[45] PE (6.0)[46]	3×10^4	no
PtBS-PMMA $T = 180\ °C$	PtBS (8.4) PMMA (9.3)	$\approx 1^c$	yes[24]
PS-PI $T = 180\ °C$	PS (10.7)[47] PI (10.3)[48]	4×10^4	no[39]
1,2-PBD-1,4-PBD $T = 100\ °C$	1,2-PBD (50.4)[49] 1,4-PBD (30.9)[50]	30^d	yes[23]
PEP-PEE $T = 96\ °C$	PEP (28.0)[25] PEE (22.0)[25]	4	yes[25]

(a) References indicate where longest relaxation times were determined for the respective homopolymers. (b) References indicate publications where diblock copolymer rheology exhibited the rheological fingerprint. (c) The ratio τ_r was assumed to be approximately 1 since both blocks are unentangled and exhibit an identical T_g. (d) $\tau_r \approx 3$ using measured ΔT_g for the block polymer versus homopolymer T_gs (See Supporting Information).

The ratio of relative block relaxation times, $\tau_r = \tau_A/\tau_B > 1$, for five AB diblock copolymer systems investigated using DMS has been estimated based on the corresponding homopolymer single-chain longest relaxation times, evaluated at temperatures near the reported T_{ODT} values based on published tTS shift factors.[25,45-50] Rouse ($\tau_1 \sim M_n^2$) or reptation ($\tau_{rep} \sim M_n^{3.4}$) single-chain relaxation times were estimated

for the unentangled or entangled homopolymer chains, respectively, using the crossover point, $G'(\omega) = G''(\omega)$, in DMS spectra. As shown in Table 1, the three diblock copolymer systems that exhibit the rheological fingerprint of fluctuations, poly(1,2-butadiene-b-1,4-butadiene) (1,2-PBD-1,4-PBD),[23] PEP-PEE,[25] and PtBS-PMMA,[24] have estimated τ_r values near unity,[23-25] which we categorize as relatively low mechanical contrast. Conversely, the diblock copolymer systems that do not exhibit the rheological fingerprint of fluctuations, PS-PI and PCHE-PE, exhibit $\tau_r > 10^4$, which we associate with large mechanical contrast.[39,40] When calculating the 1,2-PBD-1,4-PBD and PEP-PEE single-chain relaxation times, we have used homopolymer T_g values, which likely overestimates the true ΔT_g resulting in a somewhat inflated τ_r (See Supporting Information for an estimate on the magnitude of this effect for 1,2-PBD-1,4-PBD). For example, Kennemur et al.[42] showed using a DSC measurement that $\Delta T_g \cong 0$ for PtBS-PMMA-236 due to mixing of the blocks across the domain interfaces; similar effects occur with the other systems near T_{ODT}.[51, 52] Also, we have assumed that the different blocks of the diblock copolymers relax independently and ignore the fact that they are tethered to the interface. While these idealizations are not strictly valid, especially in the case of entangled blocks, we believe the ratio τ_r, based on the estimated values for τ_A and τ_B, provide valuable insight into the influence of chain dynamics on the viscoelastic response in block polymers.
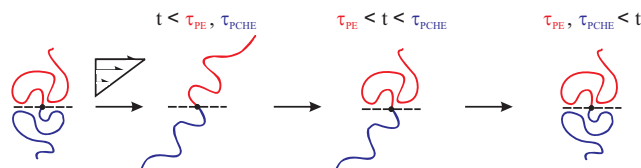
Figure B.5 Scheme depicting single-chain stress relaxation for dynamically asymmetric PCHE-PE-14 in the ordered or fluctuating disordered state. The relaxation time (τ) for the PE block (red) is orders of magnitude smaller than for the PCHE block (blue) primarily due to the large disparity in glass transition temperatures (see Table 1).

How the single-chain relaxation time for the individual blocks influences expression of composition fluctuations in the disordered state is not directly obvious. We

first consider hypothetical modes of relaxation as the frequency is swept from high ($\omega \gg \omega_c$) to low ($\omega \ll \omega_c$) values in the ordered LAM state. Figure B.5 depicts the configurational changes that occur during stress relaxation after an applied step shear strain. In the initial state, prior to any applied strain, the polymer blocks have random walk configurations (subject to the constraints imposed by localizing the junction at the interface). In response to the imposition of an instantaneous step shear strain (parallel to the interface) both blocks deform affinely. For a dynamically symmetric system the blocks will relax simultaneously leading to recovery of the initial random walk configuration. However, a dynamically asymmetric system, e.g., $\tau_r \gg 1$, will behave quite differently. Using PCHE-PE as the example, after time $\tau_{PE} \ll t \ll \tau_{PCHE} < \omega_c^{-1}$ the PE block will be fully relaxed, and the stress supported by the material will be essentially entirely borne by the PCHE blocks. (Here we note that the disparity in relaxation times for PCHE-PE, $\tau_r > 10^4$, is dominated by ΔT_g, which overwhelms the effects due to differences in M_e). At longer times, $\tau_{PE} \ll \tau_{PCHE} < t$, the entire diblock copolymer molecule is relaxed. At long times ($t > \omega_c^{-1}$) $G'(\omega)$ and $G''(\omega)$ reflect interfacial dynamics mediated by interfacial tension and diffusion of diblock copolymers parallel and perpendicular to the interface.[38] The longest-time dynamical modes ($\omega \rightarrow 0$) are sensitive to the detailed state of order, including the domain geometry (e.g., lamellae versus cylinders), correlation length, and polycrystalline grain structure.[38]

This picture is helpful when interpreting differences in the low-frequency response of dynamically symmetric and asymmetric block polymers. When $\omega \gg \omega_c$, single-chain dynamics dominate, and $G'(\omega)$ and $G''(\omega)$ are insensitive to the morphology. For $\omega < \omega_c$ the detailed morphology directly influences the viscoelastic behavior.[38] A single lamellar crystal will have a viscoelastic response that depends on its orientation relative to the flow field. When the lamellae are arranged parallel to the shear plane we anticipate Maxwell-like behavior,[53] where the two domains are coupled in series. In the case of dynamically asymmetric block polymers, the mechanical response is dominated by the dynamically faster blocks. In the perpendicular orientation (shear direction parallel to the lamellar normal) parallel coupling of the domains will produce a Voigt-like

mechanical response that is instead dominated by the slower relaxing blocks for dynamically asymmetric block polymers.[53] A polycrystalline morphology averages these effects over all orientations, which produces the documented $G' \sim G'' \sim \omega^{1/2}$ scaling observed experimentally for $\omega << \omega_c$ for both dynamically symmetric and asymmetric block polymers (although at the lowest frequencies ($\omega \to 0$), a polycrystalline lamellar morphology may exhibit solid-like behavior ($G' \sim \omega^0$) due to the presence of grain boundaries).[38] Several theories have been developed to describe this low-frequency power law behavior,[38,54,55] for example based on mode coupling,[54] entanglement,[55] and excess chain density equilibration concepts.[55]

At the lowest frequencies ($\omega << \omega_c$) the fluctuating disordered phase is a fluid exhibiting terminal scaling ($G' \sim \omega^2$ and $G'' \sim \omega^1$) implying that the bicontinuous composition pattern (Figure B.1, $T > T_{ODT}$) can be reorganized to remain isotropic in response to an applied strain. Apparently, mechanical contrast plays a significant role in setting the temperature-dependent time constant for relaxing composition fluctuations. We believe this result can be explained using the concepts associated with the orientation dependence of stress relaxation in ordered lamellae. As the ODT is approached in the disordered state the spatial range of correlations between locally segregated domains increases; i.e., at a local level the morphology is increasingly lamellar-like. Due to the isotropic nature of the fluctuating regions and the absence of fixed boundaries (i.e., grain boundaries as in the polycrystalline state) there will always be regions with a parallel orientation within a few periods of a correlated set of fluctuating domains with perpendicular alignment. Stress relaxation will be controlled by slip in these parallel regions as the ODT is approached. In systems with large mechanical contrast slip occurs in the dynamically fast domains, masking the consequences of the structural heterogeneities, analogous to the linear viscoelastic response of a suspension of solid particles dispersed in a simple fluid. In the absence of mechanical contrast the restrictions to molecular motion imposed by localization of the block copolymer chains at the domain interfaces lead to an additional mode of relaxation, which emerges at $\omega \leq \omega_c$.

Over the past 30 years, contradictory dynamic mechanical spectroscopy results concerning composition fluctuations in diblock copolymer systems have led to questions regarding the validity of experimentally probing the character of the ODT with rheology. This work demonstrates that highly asymmetric block dynamics, i.e., characterized by large mechanical contrast, eliminates the rheological fingerprint of fluctuations found in dynamically symmetric diblock copolymers. This finding has the potential to impact the theory of stress-relaxation mechanisms for ordered and disordered phases and shear-induced alignment of block polymers.[9,33,38,56-59]

ASSOCIATED CONTENT

Supporting Information.[*] Detailed DMS and SAXS experimental procedures. This material is available free of charge via the Internet at http://pubs.acs.org.

AUTHOR INFORMATION

Corresponding Author

Email: (FSB) bates001@umn.edu, (TPL) lodge@umn.edu

Author Contributions

RJH and TMG contributed equally.

Notes

The authors declare no competing financial interest.

ACKNOWLEDGMENT

---

[*] Two typographical errors appear in the Supporting Information. In Table S3, the τ for 1,4 PBD should be 7.6×10^{-5}. In the first sentence in the first paragraph on page 7, the single-chain relaxation time should be 0.009 s, as is stated in following text and in Table S3.

REFERENCES

(1)   Orilall, M. C.; Wiesner, U. *Chem. Soc. Rev.* **2011,** *40*, 520-535.

(2)   Sanchez, C.; Belleville, P.; Popall, M.; Nicole, L. *Chem. Soc. Rev.* **2011,** *40*, 696-753.

(3)   Shi, J.; Votruba, A. R.; Farokhzad, O. C.; Langer, R. *Nano Lett.* **2010,** *10*, 3223-3230.

(4)   Bates, F. S.; Hillmyer, M. A.; Lodge, T. P.; Bates, C. M.; Delaney, K. T.; Fredrickson, G. H. *Science* **2012,** *336*, 434-440.

(5)   Hallinan, D. T.; Balsara, N. P. *Annu. Rev. Mater. Res.* **2013,** *43*, 503-525.

(6)   Bates, C. M.; Maher, M. J.; Janes, D. W.; Ellison, C. J.; Willson, C. G. *Macromolecules* **2013,** *47*, 2-12.

(7)   Duncan, R. *Nat. Rev. Drug. Discovery* **2003,** *2*, 347-360.

(8)   Lodge, T. P. *Macromol. Chem. Phys.* **2003,** *204*, 265-273.

(9)   Chen, Z.-R.; Kornfield, J. A.; Smith, S. D.; Grothaus, J. T.; Satkowski, M. M. *Science* **1997,** *277*, 1248-1253.

(10)   Fredrickson, G. H.; Helfand, E. *J. Chem. Phys.* **1987,** *87*, 697-705.

(11)   Bates, F.; Rosedale, J.; Fredrickson, G.; Glinka, C. *Phys. Rev. Lett.* **1988,** *61*, 2229-2232.

(12)   Bates, F. S.; Rosedale, J. H.; Fredrickson, G. H. *J. Chem. Phys.* **1990,** *92*, 6255-6270.

(13)   Lee, S.; Gillard, T. M.; Bates, F. S. *AIChE J.* **2013,** *59*, 3502-3513.

(14)   Leibler, L. *Macromolecules* **1980,** *13*, 1602-1617.

(15)   Hashimoto, T.; Shibayama, M.; Kawai, H. *Macromolecules* **1983,** *16*, 1093-1101.

(16)   Roe, R.-J.; Fishkis, M.; Chang, J. C. *Macromolecules* **1981,** *14*, 1091-1103.

(17)   Sakamoto, N.; Hashimoto, T. *Macromolecules* **1995,** *28*, 6825-6834.

(18)   Zhao, Y.; Sivaniah, E.; Hashimoto, T. *Macromolecules* **2008,** *41*, 9948-9951.

(19)   Rosedale, J. H.; Bates, F. S.; Almdal, K.; Mortensen, K.; Wignall, G. D. *Macromolecules* **1995,** *28*, 1429-1443.

(20)   Hashimoto, T.; Sakamoto, N. *Macromolecules* **1995,** *28*, 4779-4781.

(21)   Hashimoto, T.; Sakamoto, N.; Koga, T. *Phys. Rev. E* **1996,** *54*, 5832-5835.

(22)   Sakamoto, N.; Hashimoto, T. *Macromolecules* **1998,** *31*, 3815-3823.

(23)   Bates, F. S. *Macromolecules* **1984,** *17*, 2607-2613.

(24)   Kennemur, J. G.; Hillmyer, M. A.; Bates, F. S. *ACS Macro Lett.* **2013,** *2*, 496-500.

(25)   Rosedale, J. H.; Bates, F. S. *Macromolecules* **1990,** *23*, 2329-2338.

(26)   Dalvi, M.; Eastman, C.; Lodge, T. *Phys. Rev. Lett.* **1993,** *71*, 2591-2594.

(27)   Dalvi, M. C.; Lodge, T. P. *Macromolecules* **1994,** *27*, 3487-3492.

(28)   Jian, T.; Anastasiadis, S. H.; Semenov, A. N.; Fytas, G.; Adachi, K.; Kotaka, T. *Macromolecules* **1994,** *27*, 4762-4773.

(29)   Jin, X.; Lodge, T. *Rheol. Acta* **1997,** *36*, 229-238.

(30)   Kannan, R. M.; Su, J.; Lodge, T. P. *J. Chem. Phys.* **1998,** *108*, 4634-4639.

(31)   Stepanek, P.; Lodge, T. P. *Macromolecules* **1996,** *29*, 1244-1251.

(32)   Stuehn, B.; Stickel, F. *Macromolecules* **1992,** *25*, 5306-5312.

(33)   Chen, Z.-R.; Kornfield, J. A. *Polymer* **1998,** *39*, 4679-4699.

(34)   Xu, T.; Zhu, Y.; Gido, S. P.; Russell, T. P. *Macromolecules* **2004,** *37*, 2625-2629.

(35)   Tran, H.; Gopinadhan, M.; Majewski, P. W.; Shade, R.; Steffes, V.; Osuji, C. O.; Campos, L. M. *ACS Nano* **2013,** *7*, 5514-5521.

(36)   Jones, B. H.; Lodge, T. P. *Polym. J.* **2012,** *44*, 131-146.

(37)   Glaser, J.; Medapuram, P.; Beardsley, T. M.; Matsen, M. W.; Morse, D. C. *Phys. Rev. Lett.* **2014,** *113*, 068302.

(38)   Fredrickson, G. H.; Bates, F. S. *Annu. Rev. Mater. Sci.* **1996,** *26*, 501-550.

(39)   Choi, S.; Han, C. D. *Macromolecules* **2004,** *37*, 215-225.

(40)   Gehlsen, M. D.; Bates, F. S. *Macromolecules* **1993,** *26*, 4122-4127.

(41)   Habersberger, B. M.; Gillard, T. M.; Hickey, R. J.; Lodge, T. P.; Bates, F. S. *ACS Macro Lett.* **2014,** *3*, 1041-1045.

(42)   Kennemur, J. G.; Hillmyer, M. A.; Bates, F. S. *Macromolecules* **2012,** *45*, 7228-7236.

(43)   Han, C. D.; Kim, J. *J. Polym. Sci., Part B* **1987,** *25*, 1741-1764.

(44)   Fetters, L. J.; Lohse, D. J.; Richter, D.; Witten, T. A.; Zirkel, A. *Macromolecules* **1994,** *27*, 4639-4647.

(45)   Zhao, J.; Hahn, S. F.; Hucul, D. A.; Meunier, D. M. *Macromolecules* **2001,** *34*, 1737-1741.

(46)   Vega, J. F.; Aguilar, M.; Martínez-Salazar, J. *J. Rheol.* **2003,** *47*, 1505-1521.

(47)   Baumgaertel, M.; Schausberger, A.; Winter, H. H. *Rheol. Acta* **1990,** *29*, 400-408.

(48)   Abdel-Goad, M.; Pyckhout-Hintzen, W.; Kahle, S.; Allgaier, J.; Richter, D.; Fetters, L. J. *Macromolecules* **2004,** *37*, 8135-8144.

(49)   Roovers, J.; Toporowski, P. M. *Macromolecules* **1992,** *25*, 3454-3461.

(50)   Baurngaertel, M.; De Rosa, M. E.; Machado, J.; Masse, M.; Winter, H. H. *Rheol. Acta* **1992,** *31*, 75-82.

(51)   Bates, F. S.; Bair, H. E.; Hartney, M. A. *Macromolecules* **1984,** *17*, 1987-1993.

(52)   Bates, F. S.; Rosedale, J. H.; Bair, H. E.; Russell, T. P. *Macromolecules* **1989,** *22*, 2557-2564.

(53)   Hiemenz, P. C.; Lodge, T. P., *Polymer Chemistry*. 2nd ed.; CRC Press: Boca Raton, FL, 2007.

(54)   Kawasaki, K.; Onuki, A. *Phys. Rev. A* **1990,** *42*, 3664-3666.

(55)   Rubinstein, M.; Obukhov, S. P. *Macromolecules* **1993,** *26*, 1740-1750.

(56)   Hermel, T. J.; Wu, L.; Hahn, S. F.; Lodge, T. P.; Bates, F. S. *Macromolecules* **2002,** *35*, 4685-4689.

(57)   Vigild, M. E.; Chu, C.; Sugiyama, M.; Chaffin, K. A.; Bates, F. S. *Macromolecules* **2001,** *34*, 951-964.

(58)   Koppi, K. A.; Tirrell, M.; Bates, F. S.; Almdal, K.; Colby, R. H. *J. Phys. II* **1992,** *2*, 1941-1959.

(59)   Wiesner, U. *Macromol. Chem. Phys.* **1997,** *198*, 3319-3352.

Appendix C

Structure, Viscoelasticity, and Interfacial Dynamics of a Model Polymeric Bicontinuous Microemulsion [*],[†]

ABSTRACT: We have systematically studied the equilibrium structure and dynamics of a polymeric bicontinuous microemulsion (BµE) composed of poly(cyclohexylethylene) (PCHE), poly(ethylene) (PE), and a volumetrically symmetric PCHE-PE diblock copolymer, using dynamic mechanical spectroscopy, small-angle X-ray and neutron scattering, and transmission electron microscopy. The BµE was investigated over an 80 °C temperature range, revealing a structural evolution and a rheological response not previously recognized in such systems. As the temperature is reduced below the point associated with the lamellar-disorder transition at compositions adjacent to the microemulsion channel, the interfacial area per chain of the BµE approaches that of the neat (undiluted) lamellar diblock copolymer. With increasing temperature, the diblock-rich interface swells through homopolymer infiltration. Time-temperature-superposed linear dynamic data obtained as a function of frequency show that the viscoelastic response of the BµE is strikingly similar to that of the fluctuating pure diblock copolymer in the disordered state, which we associate with membrane undulations and the breaking and reforming of interfaces. This work provides new insights into the structure and dynamics that characterize thermodynamically stable BµEs in the limits of relatively weak and strong segregation.

Introduction

Materials containing bicontinuous morphologies, characterized by discrete phases that percolate in three dimensions forming interpenetrating networks with a large surface area to volume ratio, are desirable for many applications including catalysis, filtration, and energy technologies.[1-7] To date, a host of ingredients (metals,[8] oxides,[9,10] surfactants,[6] and polymers[3]) and processing strategies (both kinetic[11,12] and thermodynamic[3,6]) have been exploited to control the characteristic length scale and physical properties of such co-continuous structures. Polymers are particularly attractive for this purpose.[13,14] A variety of approaches afford access to characteristic length scales in co-continuous polymeric systems that range from nanometers to millimeters.[3,4,12,15-21] For example, recent work has shown that a kinetically controlled co-continuous structure with nanometer scale features can be trapped by *in situ* cross-linking through a process called polymerization-induced microphase separation.[12,20,22] In contrast, coarsening of a two-phase morphology generated by spinodal decomposition of polymer/solvent blends can lead to bicontinuous structures with micrometer, and even millimeter size domains.[4,18,21,23,24] Immiscible liquid blends stabilized with surfactants or block polymers enable the formation of thermodynamically stable bicontinuous phases with feature sizes intermediate to these two length scales.[3,25]

Ternary systems composed of two immiscible liquids and a corresponding amphiphile (e.g., blends of either oil/water/surfactant or A- and B-type homopolymers stabilized with the corresponding AB diblock copolymer) are characterized by rich phase diagrams containing numerous morphologies and exhibiting an extraordinary range of structural dynamics.[25-33] Under appropriate conditions such three-component mixtures will self-assemble into a thermodynamically stable bicontinuous microemulsion (BμE) with structural dimensions ranging from 10 to 500 nm.[3,25,27] The BμE is globally isotropic, but contains locally correlated domains of either oil/water or A/B homopolymers mediated respectively by surfactants or AB diblock copolymers at the interface (Figure C.1).[25,27] The interfacial curvature in a perfectly balanced mixture is characterized by zero mean curvature, $H = [R_1 + R_2]/2 = 0$, and negative Gaussian

curvature, $K = R_1R_2 < 0$, where R_1 and R_2 are the principal curvatures of the interface (see Figure C.1).[27] The detailed structure of a BμE can be quantitatively characterized using either small-angle neutron or small-angle X-ray scattering (SANS or SAXS) aided by the Teubner–Strey (T-S) model, derived from an order parameter expansion of the free energy density.[34] The domain spacing (d), correlation length (ξ), and amphiphilicity factor (f_a) of the BμE can be extracted by fitting the T-S model to experimental scattering data.[34,35] This fascinating state of molecular organization forms through a combination of complex interactions involving interfacial dynamics, bending modulus, preferred curvature, and surface tension. Although a variety of theoretical descriptions have been advanced, a complete theory that fully captures the thermodynamic and dynamic features of the BμE remains elusive.[36-42]
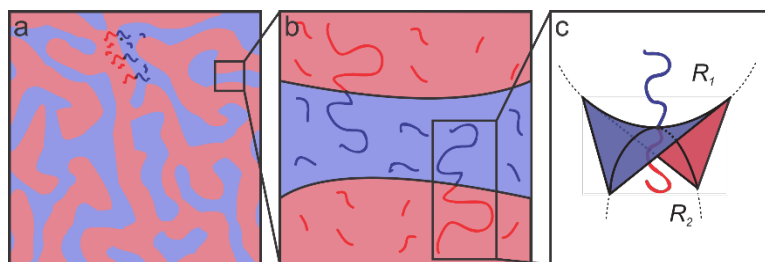

Figure C.1 Schematic illustrations representing the varying length scales of the BμE. (a) The BμE morphology is globally disordered with (b) domains separated by diblock copolymers at the interface and swollen with homopolymer. (c) The interfacial curvature of a perfectly structured BμE is characterized by zero mean curvature ($H = [R_1 + R_2]/2 = 0$) and negative Gaussian curvature ($K = R_1R_2 < 0$).

Polymeric systems are very well suited for studying the fundamental nature of the BμE state. An especially enabling and simplifying attribute is the identical chemistry associated with the A and B homopolymers and the individual blocks in an A-B diblock copolymer, which provides powerful flexibility in designing such mixtures with near perfect structural symmetry. By controlling the composition and molecular weight of the diblock, and molecular weight of the individual homopolymers, the location of the BμE in the three-dimensional phase space (volume fraction of each component and temperature at constant pressure) can be precisely specified. Moreover, the dynamics of a

BμE are intimately connected to the viscoelastic properties of the ingredients, which also can be tuned by regulating the molecular weight and glass transition temperature of each component. Judicious choice of the A and B polymers provides additional advantages, including access to isotopic labeling (essential for SANS) and the ability to fix the morphology for investigation by transmission electron microscopy (TEM) through rapid quenching below the glass transition (or melting) temperature. We developed the saturated hydrocarbon system comprised of poly(cyclohexylethylene) (PCHE) and poly(ethylene) (PE) homopolymers, and the corresponding PCHE-PE diblock copolymer, in order to capitalize on these advantages.[32] This report describes an in-depth investigation of the structure and dynamics of the BμE created by mixing these three materials.

Equilibrium and non-equilibrium structure and dynamics of the polymeric BμE morphology have been studied using a variety of techniques, with a majority of the experimental work involving rheological, scattering, and real-space imaging methods.[43-51] Linear viscoelastic studies have shown that the BμE morphology has "excess" viscosity and elasticity arising from the structured nature of the fluid, similar to the behavior of sponge phases,[52,53] liquid crystal based blue phases,[54,55] and worm-like micelles.[56-59] The "excess" linear viscoelasticity has been well described by the Pätzold–Dawson model, which anticipates certain general features of polymeric BμEs, but there are discrepancies in the viscosity and the relaxation times.[43,44,60] Specifically, the Pätzold–Dawson model contains a single relaxation time, but dynamic light scattering (DLS) and X-ray photon correlation spectroscopy (XPCS) studies of polymeric BμEs have revealed multiple relaxation mechanisms that are hypothesized to arise from domain diffusion, copolymer dynamics, and undulating interfaces.[43,46,47] Interestingly, bicontinuous morphologies and membrane structures derived from surfactants also exhibit multiple relaxation times, similar to polymeric systems.[61-64]

Here, we report an extensive experimental study of a PCHE-PE/PCHE/PE BμE across a broad range of the structural parameters (including d, ξ, and particularly f_a) by investigating this system over a large (80 °C) temperature interval. This work builds upon

previous reports related to other BµE systems.[43-48] The structural and dynamical features of the BµE were probed using SANS, SAXS, dynamic mechanical spectroscopy (DMS), and transmission electron microscopy (TEM). We have discovered that at low temperatures, the diblock copolymer located at the interface in the BµE experiences a molecular environment (interfacial packing) similar to that encountered in the undiluted, neat diblock in the lamellar (LAM) morphology at equivalent temperatures. With increasing temperatures, the homopolymers intermix with the diblock copolymers and swell the BµE interface, leading to a reduction in domain spacing and increase in the interfacial area per diblock chain. We associate the terminal relaxation response with membrane undulations and the breaking and reforming of interfaces, and draw analogies to the rheological response of worm-like micelles and sponge phases.[65-69] Previous reports have involved more limited temperature windows that did not capture in a single sample the full progression of structures reported here. This work highlights the intricate interplay between structure and dynamics in BµE systems, and provides a better understanding of the underlying mechanisms that drive the fascinating behavior of thermodynamically stable co-continuous morphologies in which the interface controls the properties.

Experimental

Materials and molecular characterization Detailed synthetic procedures and molecular characterization methods employed in this work are described elsewhere.[32] Briefly, polyethylene (PE, M_n = 2.1 kg/mol,) and polycylohexylethylene (PCHE, M_n = 2.6 kg/mol) homopolymers and a symmetric poly(cylohexylethylene-*b*-ethylene) (PCHE-PE-14, M_n = 13.6 kg/mol, volume fraction of the PCHE block f_c = 0.52 ± 0.01) diblock copolymer were prepared by catalytic hydrogenation of the corresponding unsaturated precursors (poly(1,4-butadiene), poly(styrene), and poly(styrene-*b*-1,4-butadiene), respectively) synthesized by anionic polymerization. See Table C.1 for additional molecular details. For neutron scattering experiments, the poly(styrene) precursor was saturated using deuterium gas, resulting on average in 4.5 deuterium atoms per repeat

unit of the d-PCHE homopolymer, determined gravimetrically; full deuteration (i.e., 6 deuterons per repeat unit) was not obtained due to hydrogen-deuterium solvent-polymer exchange.[70]

Table C.1 Molecular characterization of homopolymers and diblock copolymer.

Polymer	M_n (kg/mol)[a]	N[b]	$Đ = M_w/M_n$[c]	f_{PCHE}[d]	T_{ODT} (°C)[e]
PCHE	2.6	39	1.06	–	–
PE	2.1	38	1.05	–	–
PCHE-PE-14[14]	13.6	230	1.08	0.52	189[71]

a) Number average molecular weight, determined from SEC performed on unsaturated precursors. b) Volumetric degree of polymerization, based on 118 Å^3 reference volume and published densities at 140 °C.[72] c) Molecular weight dispersity measured for unsaturated precursors by size exclusion chromatography (SEC) in tetrahydrofuran at 25 °C (no evidence of broadening was evident in SEC of the fully saturated polymers. However, SEC of polyethylene containing polymers was done at elevated temperatures in a separate instrument with significant instrument smearing. Therefore, we believe the dispersities measured for the unsaturated precursors more accurately reflect the true dispersity.) d) Volume fraction PCHE calculated from ^{1}H-NMR spectroscopy on the unsaturated precursors and based on melt densities at 140 °C. e) Order–disorder transition temperatures, measured by DMS. f) PCHE-PE-14 contained a small amount (≤ 3 vol. %) of residual PCHE homopolymer.

Blend preparation The BμE-forming blend was prepared by co-dissolving the appropriate quantity of each polymer in hot benzene (just below the boiling temperature ~80 °C), followed by quenching the solution in liquid nitrogen and freeze-drying under dynamic vacuum for 24 h to remove the solvent. The total homopolymer volume fraction (ϕ_H) for the ternary blend studied was $\phi_H = 0.86$, with the volume ratio between the PCHE and PE homopolymers $\phi_{PCHE}/\phi_{PE} = 1$.

Dynamic mechanical spectroscopy (DMS) Most DMS measurements were conducted using the 25 mm diameter stainless steel parallel plate geometry on a Rheometrics Scientific ARES strain-controlled rheometer equipped with a forced convection oven (inert nitrogen atmosphere). For increased torque on selected samples, we employed 40

mm diameter stainless steel plates on a TA Instruments Discovery Hybrid Rheometer with a forced convection oven (inert nitrogen atmosphere). All polymer samples were loaded to give a gap of approximately 1 mm, heated above any thermal transitions (e.g., glass, melting, or order–disorder transitions), cooled at 1 °C/min to specific temperatures and held for 1 h before collecting data as a function of frequency over the range $0.01 \leq \omega \leq 100$ rad/s. Strains were chosen to maximize torque while remaining in the linear viscoelastic regime. Steady shear experiments were conducted between 0.001 and 100 s^{-1} in the temperature range 120 – 220 °C. Zero-shear viscosity was determined in the limit of low shear rate.

Small-angle X-ray scattering (SAXS) Synchrotron SAXS experiments were conducted at the DND-CAT 5-ID-D beamline at the Advanced Photon Source (Argonne National Laboratory, Argonne, IL USA) using the triple-detector system, which simultaneously records small-, middle-, and wide-angle X-ray scattering (SAXS/MAXS/WAXS).[73] An X-ray wavelength of 1.24 Å was used with SAXS, MAXS, and WAXS sample-to-detector distances of approximately 8.5, 1 and 0.2 m, respectively. 2D data were collected with Rayonix area CCD detectors; for brevity we will refer to all such experiments simply as SAXS. All scattering patterns were nearly azimuthally isotropic and were azimuthally integrated to obtain 1D plots of scattered intensity (in arbitrary units) versus scattering wave vector $q = 4\pi\lambda^{-1}\sin(\theta/2)$. The BμE ($\phi_H = 0.86$) sample was contained in a 1.5 mm nominal diameter quartz capillary (Charles Supper Company) and the temperature was controlled during scattering experiments with a modified Linkam HFS91 heating stage. Prior to the SAXS experiments, the sample was heated to 200 °C to facilitate equilibration and to remove any processing history, slowly cooled (*ca.* 1 °C/min) to 120 °C, annealed at 120 °C under vacuum for 15 h, and then rapidly quenched to room temperature by immersion in a water bath to kinetically trap the equilibrium structure. At the beamline, the sample was quickly (*ca.* ~ 10 seconds) reheated to 120 °C to record the structure at this temperature. The sample was then heated to 200 °C and cooled back to 120 °C, pausing at several temperatures to collect scattering patterns. The sample was equilibrated at each temperature for approximately 2 min prior to data

collection while changes in temperature between measurements were rapid (> 20 °C/min).

Small-angle neutron scattering (SANS) SANS experiments were performed at the National Institute of Standards and Technology (NIST), Gaithersburg, Maryland, on the 30 m NG-7 (University of Minnesota/ExxonMobil/NIST) beam line using a neutron wavelength of $\lambda = 8.09$ nm and $\Delta\lambda/\lambda = 0.115$. Three different configurations were used with sample-to-detector distances of 15.3 m (lenses inserted), 4 m, and 1 m. PE, deuterated PCHE, and BµE samples were loaded into custom quartz banjo cells with 1.0 mm nominal path length (precise path length was determined by subtracting known quartz window thickness from the measured total cell thickness). The 2D scattering data were corrected for background and empty cell scattering, sample transmission, sample thickness, and detector sensitivity and converted to an absolute intensity scale using measurements of the direct beam flux. All measured scattering patterns were essentially azimuthally isotropic and were averaged to produce 1D plots of scattered intensity vs. q. Incoherent scattering, estimated based on the volume fraction weighted average scattering intensity at high-q from pure homopolymer samples (PE and d-PCHE), was subtracted from the BµE scattering data. Data reduction was performed using the NCNR software package for Igor Pro provided by NIST.[74] Isotope effects are ignored in this study, as these are insignificant at the molecular weights employed.[75]

Transmission electron microscopy (TEM) TEM specimens were prepared by heating the sample to 200 °C for 30 min, then cooling to the temperature of interest (120 °C, 150 °C, and 180 °C) at 1 °C/min and annealing for a minimum of 16 h. Samples were then plunged into a mixture of dry ice and 2-propanol to rapidly cool and solidify the material ($T_{g,PCHE} \cong T_{m,PE} \cong 100$ °C), fixing the blend morphology present at the annealing temperature. We estimate that the specimens are cooled below the solidification temperature in roughly 5 s.[32] All samples were stained with ruthenium tetroxide vapor for 4 h to enhance contrast between microphases. Microtoming was performed at room temperature using a Leica EM UC6 ultramicrotome and a MicroStar diamond knife. BµE sample sections were microtomed to a thickness of approximately 70 nm, and collected

on a tabbed copper grid (PELCO, 300 mesh) and imaged using a FEI Tecnai G^2 Spirit BioTWIN transmission electron microscope operating at a 120 kV accelerating voltage.

Results

This ternary polyolefin blend contains a mixture of PCHE and PE homopolymers with nearly equal molecular volumes (N_{PCHE} = 39 and N_{PE} = 38 are the number average degrees of polymerization based on a 118 Å^3 reference volume and published densities) and a volumetrically symmetric PCHE-PE-14 diblock copolymer (f_{PCHE} = 0.52 ± 0.01, $N_{PCHE-PE}$ = 230).[32] Figure C.2 summarizes the PCHE-PE/PCHE/PE phase diagram for the volumetrically symmetric isopleth (ϕ_H = ϕ_{PCHE} + ϕ_{PE} versus T, where ϕ_{PCHE} /ϕ_{PE} = 1) for this system. A BμE channel splits the isopleth into two distinctly different regions: (1) a diblock-rich portion of the phase diagram characterized by microphase separation into ordered lamellae (LAM) at low temperature, and (2) a homopolymer-rich region of the phase diagram characterized by macrophase separation at temperatures below a line of second-order phase transitions (Figure C.2).[32]
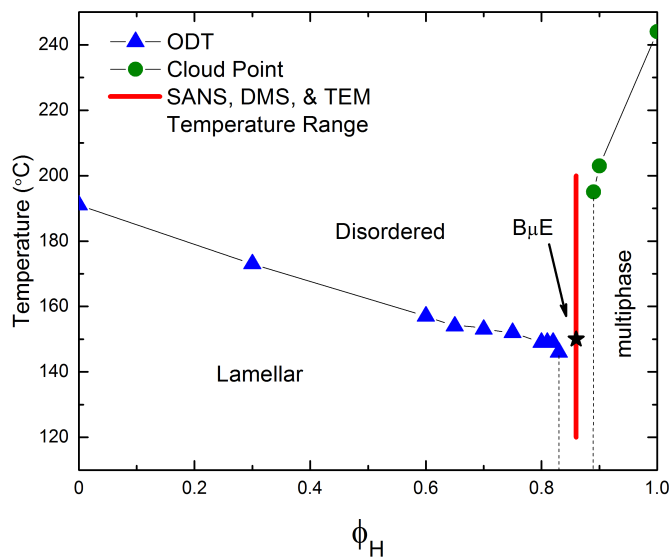
Figure C.2 Phase diagram of the volumetrically symmetric isopleth for the ternary PCHE-PE-14/PCHE/PE blend. ϕ_H represents the total fraction of homopolymer. Blue triangles and green circles identify T_{ODT} and phase separation temperatures, respectively. The red line indicates the experimental temperature range (120 – 200 °C) and composition ($\phi_H = 0.86$) for SANS, DMS, and TEM experiments on the BµE. The black star corresponds to $T_x = 150$ °C, which is associated with the crossover from intermediate to strong segregation. All lines connecting data points are to guide the eye.

In the LAM region of phase space, DMS and SAXS were used to determine the line of order–disorder transition temperatures (T_{ODT}) and to assign the morphology, respectively.[32] As previously reported, addition of PCHE and PE homopolymers to PCHE-PE-14 swells the LAM domains and results in a small concomitant decrease in T_{ODT}.[32] The line of order–disorder transitions (ODT) terminates at the BµE channel. (The character of the line of ODTs associated with the LAM-disorder transition will be the subject of a future report). In this system, the BµE channel occurs in the homopolymer range $0.85 \leq \phi_H \leq 0.88$, somewhat below the theoretical Lifshitz composition ($\phi_{H,L} = 0.95$) and the associated line of unbinding transitions predicted by mean-field theory.[32] Macroscopic phase separation occurs, at temperatures below the envelope of upper critical solution temperatures (UCSTs) located at homopolymer contents greater than those for the BµE channel ($\phi_H \geq 0.89$), as confirmed by cloud point measurements.[32] The experiments were conducted on a ternary mixture with $\phi_H = 0.86$ (and $\phi_{PCHE} / \phi_{PE} = 1$) as

identified by the red vertical line in Figure C.2. This places the material within (or above) the BμE channel at all measurement temperatures.

Structure Real space TEM imaging was performed at room temperature on specimens quenched after annealing at various temperatures between 120 and 180 °C, as shown in Figure C.3. The combined effects of PCHE vitrification and PE crystallization fixes the morphology present in the melt state and renders a material suitable for microtoming into thin (*ca.* 70 nm thick) sections. The PE domains in the images shown in Figure C.3 appear lighter since semicrystalline polymers such as PE do not stain as heavily as amorphous polymers like PCHE.[76] These micrographs show no evidence of LAM and BμE coexistence; the BμE morphology is disordered and globally isotropic, with well-defined domains and a local periodicity of about 30 to 60 nm.
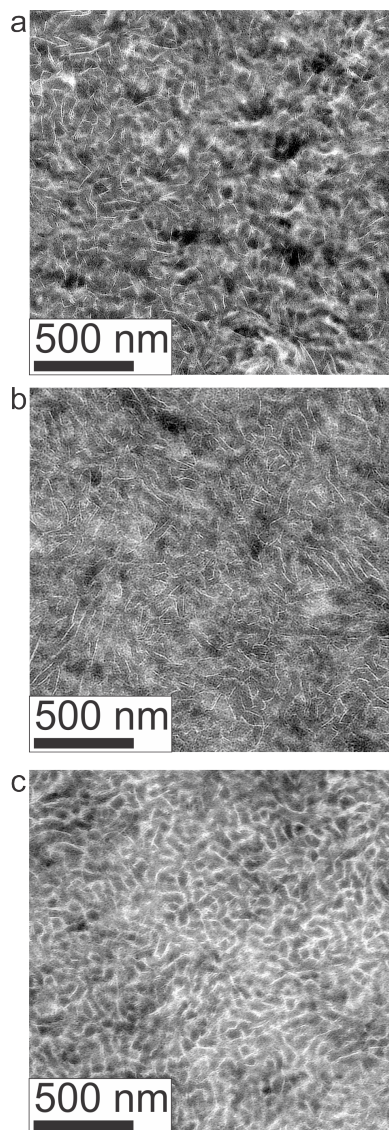
Figure C.3 Transmission electron micrographs confirming a bicontinuous morphology for temperatures (a) 120 °C, (b) 150 °C, and 180 °C. All samples were annealed for at least 16 h at the indicated temperature, quenched to room temperature, stained with ruthenium tetroxide vapors and microtomed to a thickness of approximately 70 nm.

The static structure of the BμE was evaluated over the temperature range 125–200 °C using SANS. As seen in Figure C.4, the mixture produces a single prominent peak at all temperatures, which changes in intensity by two orders of magnitude and broadens between the highest and lowest temperatures. A nearly flat incoherent background intensity, estimated based on the weighted average of the scattering obtained from the pure homopolymers (see Figure C.4), was subtracted from these data, which are re-plotted in Figure C.5. The background corrected scattering patterns were fit with the Teubner–Strey (T-S) structure factor,

$$I(q) = \frac{1}{a_2 + c_1 q^2 + c_2 q^4} \, ,$$

(C.1)

where $q = 4\pi\lambda^{-1}\sin(q/2)$ (λ is the wavelength, and q is the scattering angle), and a_2, c_1, and c_2 are fitting coefficients.[34] We obtained good agreement between the SANS results and the T-S model over a large q-range, as seen in Figure C.5. The model fails to quantitatively reproduce the coherent scattering intensity for $q > 0.04$ Å^{-1}, which is attributed to Gaussian coil scattering ($I(q) \sim q^{-2}$) from the h-PCHE blocks of PCHE-PE-14, a consequence of the lack of contrast matching with the d-PCHE homopolymer.[43,47]
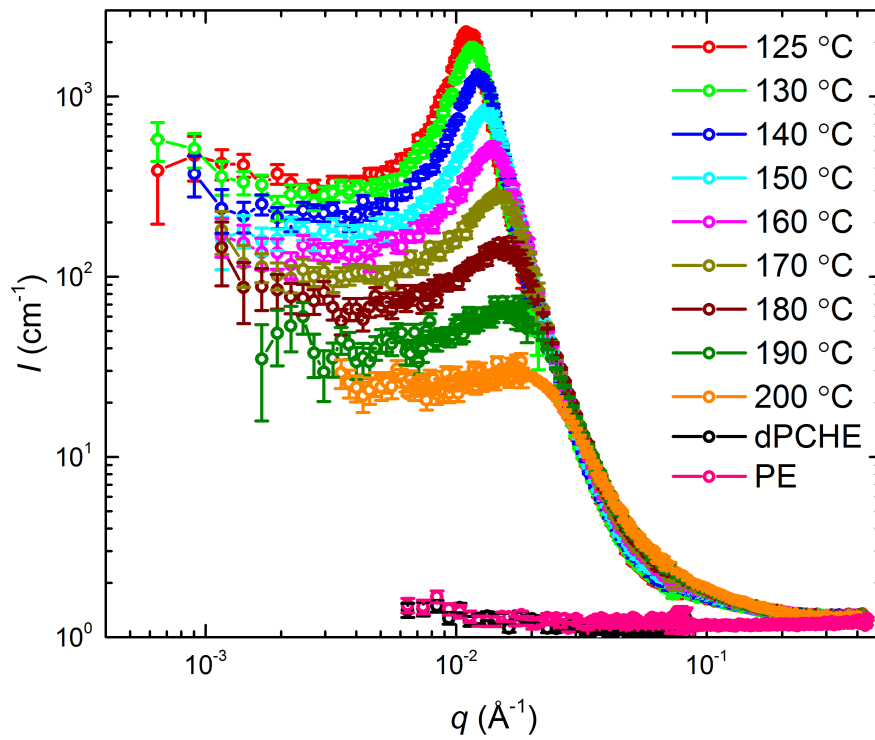
Figure C.4 SANS data in units of absolute intensity. Data acquired as a function of temperature for the BμE; dPCHE (black) and PS (red) homopolymer data were obtained at 140 °C.
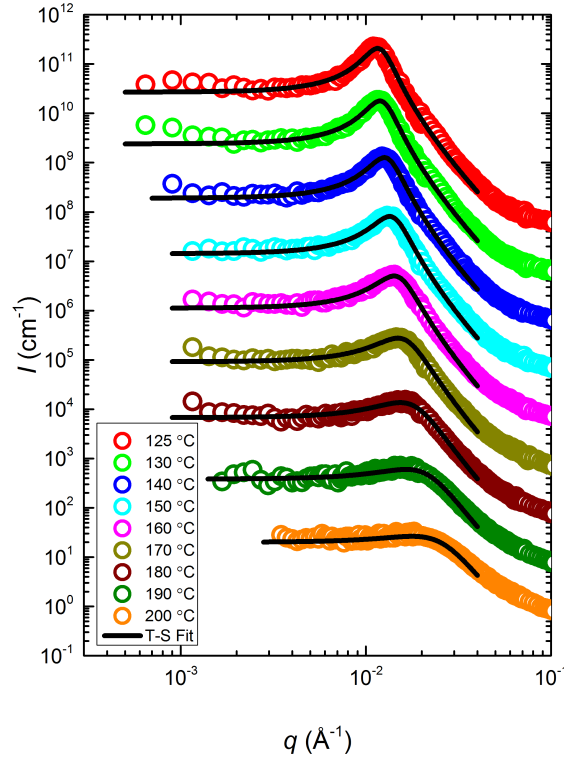
Figure C.5 SANS data (corrected for incoherent background scattering) with optimized fits to the 3-parameter Teubner–Strey model (solid curves). The data at 200 °C is in absolute units. The other scattering patterns (190−125 °C) have been vertically shifted successively by factors of 10.

Two structural length scales are associated with the fitting coefficients of the T-S model, the domain spacing (d) and the correlation length (ξ),

$$d = 2\pi \left[\frac{1}{2} \left(\frac{a_2}{c_2} \right)^{\frac{1}{2}} - \frac{1}{4} \left(\frac{c_1}{c_2} \right) \right]^{-\frac{1}{2}} ,$$

(C.2)

and

$$\xi = \left[\frac{1}{2} \left(\frac{a_2}{c_2} \right)^{\frac{1}{2}} + \frac{1}{4} \left(\frac{c_1}{c_2} \right) \right]^{-\frac{1}{2}} ,$$

(C.3)

where d describes the periodicity ($d/2$ is the average distance between adjacent PCHE or PE domains), and ξ is the correlation length, a measure of the spatial coherence of the interfaces between domains.[34] The third parameter, the amphiphilicity factor (f_a),

$$f_a = \frac{c_1}{\sqrt{4a_2c_2}} \ ,$$

(C.4)

characterizes the strength of the diblock copolymer as an interfacial agent; when $f_a = -1$, the structure is an ordered lamellar morphology, while $-1 < f_a \leq 0$ corresponds to a well-structured microemulsion.[35] Over the experimental temperature range of the SANS measurements (125–200 °C), d and ξ decrease with increasing temperature (Figure C.6). Two limiting behaviors are found for the amphiphilicity factor, also shown in Figure C.6. Above 160 °C f_a increases linearly with temperature, while below about 150 °C this parameter asymptotically approaches the strongly structured and well-segregated limit ($f_a = -1$).
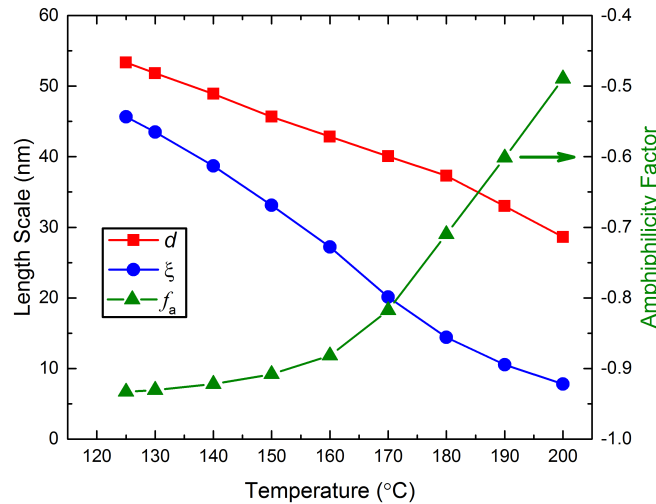

Figure C.6 Domain spacing (d), correlation length (ξ), and amphiphilicity factor (f_a) as a function of temperature associated with the best fits of the Teubner–Strey model (Equation C.1) to the SANS data shown in Figure C.5.

Dynamics The viscoelastic properties associated with the structural features documented above were studied using DMS. Dynamic frequency sweeps ($0.01 \leq \omega \leq 100$ rad/s) were

acquired over the temperature range $120 \leq T \leq 180$ °C in the linear viscoelastic regime. Recognizing the likelihood of thermorheological complexity (three different polymer components and a complex temperature dependent mesostructure), we first plotted the temperature dependent frequency data in a modified Cole-Cole format (Figure C.7). This treatment of the data, which involves no arbitrary shifting factors, results in a surprisingly effective collapse of the rheological data onto a mostly temperature independent master curve, particularly at high modulus (i.e., low temperature or high frequency). This motivated us to apply the time-temperature superposition (tTS) principle in order to extract additional insight into the underlying dynamical processes through comparison of the responses of the BμE and the individual components on a common basis (i.e., a single master plot). Figure C.8 shows a tTS master plot for the BμE constructed by placing an emphasis on the high modulus (i.e., high frequency) data using a reference temperature of $T_{ref} = 140$ °C. The corresponding shift factors (a_T) were fit to the Williams-Landel-Ferry (WLF) equation, $\log(a_T) = -C_1(T - T_{ref}) / (C_2 + T - T_{ref})$, where $C_1 = 16.09$, and $C_2 = 164.13$ °C, based on $T_{ref} = 140$ °C (Table C.2). As seen in Figure C.8, there is good superposition of the data for the BμE over a majority of the frequency and temperature ranges. Non-terminal behavior for the storage (G') and loss (G'') moduli ($G' \sim G'' \sim \omega^{1/2}$) is apparent at high frequencies ($a_T\omega > 1$ rad/s), while for $a_T\omega < 0.1$ rad/s a terminal response is evident ($G' \sim \omega^2$ and $G'' \sim \omega^1$). Below about 160 °C there is a subtle but systematic failure of superposability in G' with decreasing temperature (inset of Figure C.8), similar to what has been reported in dynamically symmetric disordered diblock copolymer melts and attributed to composition fluctuations.[71,77] Unfortunately, we could not fully establish this trend due to an inability to access the terminal regime below 145 °C at manageable frequencies ($\omega \geq 0.01$ rad/s).
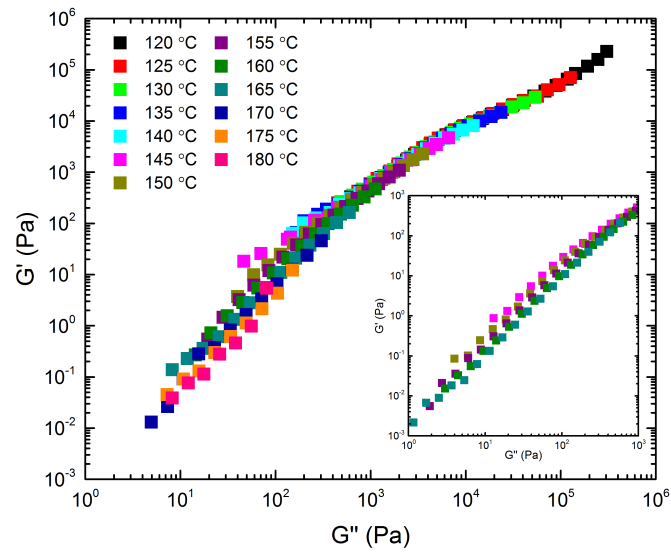
Figure C.7 Cole–Cole plot. Dynamic elastic (*G'*) and loss (*G''*) moduli obtained from the BµE over the range of frequencies $0.01 \leq \omega \leq 100$ rad/s and indicated temperatures plotted in modified Cole–Cole format. The inset highlights failure of the data to superpose at the lowest moduli values.
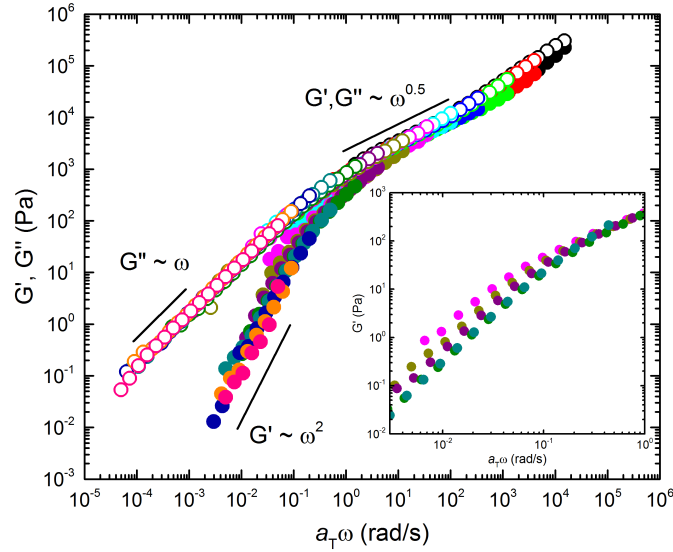
Figure C.8 Master plot of the linear dynamic elastic (G') and loss (G'') moduli for the BμE. Time-temperature shift factors (a_T) were obtained by shifting on G'' with T_{ref} = 140 °C giving WLF parameters of C_1 = 16.09 and C_2 = 164.13 ºC. The inset reveals a failure to superpose G' in the terminal regime. The inset data were obtained by extending the frequency region using a stress controlled TA Instruments Discovery Hybrid Rheometer. G' and G'' are indicated with closed and open symbols, respectively. Color of symbols represent temperatures indicated in Figure C.7.

WLF parameters also were determined for pure PCHE-PE, and the PCHE and PE homopolymers, and these values are listed in Table C.2. In order to avoid ambiguities associated with the ODT we have assigned the shift factors for PCHE-PE-14 diblock copolymer based on values obtained from another symmetric, ordered sample, PCHE-PE-18 (M_n =18.9 kg/mol, f_{PCHE} = 0.51, and T_{ODT} = 317 °C);[71] previous reports demonstrate the validity of this approach with symmetric diblock copolymers of similar molecular weight.[77,78] Interestingly, the WLF parameters calculated for the BμE differ significantly from both the PCHE and PE homopolymers and the diblock copolymer (Table C.2). Naively, one might expect the WLF parameters for the BμE to be close to those for the diblock and the PCHE homopolymer, since $T_{g,PCHE} \gg T_{g,PE}$, i.e. PCHE should dominate the temperature dependence of all three systems. However, neither set of C_1 and C_2 parameters adequately superposes the BμE DMS data. We return to this point in the Discussion Section.

Table C.2 WLF parameters for the BμE, PCHE-PE-14, PCHE, and PE.

Sample	T_{ref} (°C)	C_1	C_2 (°C)
BμE	140	16.1	164
PCHE-PE-14[a]	140	8.37	64.3
PCHE[a]	140	8.82	90.4
PE	140	2.43	295

a) PCHE-PE-14 and PCHE WLF parameters for T_{ref} = 140 °C were calculated using the relationships $C_{1,140} = C_{1,ref} C_{2,ref} / (C_{2,ref} + T_{140} - T_{ref})$ and $C_{2,140} = C_{2,ref} + T_{140} - T_{ref}$.

Temperature-independent master plots of G' and G'' for the BμE and PCHE-PE-14 based on T_{ref} = 140 °C and the shift factors listed in Table C.2 are presented in Figure C.9. There is remarkable similarity between the reduced viscoelastic properties of the BμE and disordered PCHE-PE-14 exposed by this master plot. (The low frequency response of the ordered branch of the PCHE-PE-14 data reflects a solid-like response due to the polycrystalline long-range ordered LAM morphology).[79] To a close approximation, both sets of G' and G'' data can be superimposed by vertically shifting the BμE results upward by about two orders of magnitude. Most strikingly, the reduced relaxation time τ_c = $(a_T\omega)_c^{-1}$ of the pure PCHE-PE-14 is essentially identical to that of the BμE, which contains 86% by volume homopolymer, where $(a_T\omega)_c$ represents the reduced frequency associated with the transition to terminal behavior. The molecular relaxation time constants for the homopolymers are smaller by three or more orders of magnitude than τ_c for the diblock copolymer and microemulsion. These results unambiguously demonstrate that the dynamical behavior of the disordered state is controlled by sheets of diblock copolymers that constitute the interfaces separating PE and PCHE in both the fluctuating pure diblock and bicontinuous microemulsion. We expand on this finding in the following section.
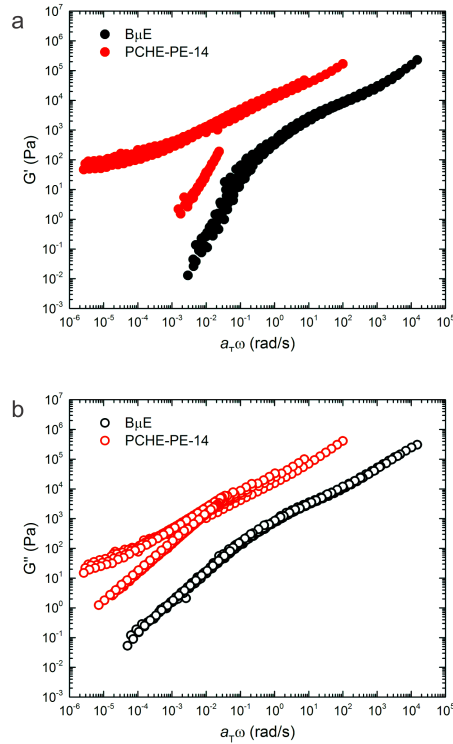
Figure C.9 Master plots of the (a) storage (G') and (b) loss (G'') moduli for the BµE and PCHE-PE-14 with T_{ref} = 140 °C. Time-temperature shift factors (a_T) for the BµE were obtained from shifting on G'' with T_{ref} = 140 °C. PCHE-PE-14 data were shifted using WLF parameters acquired from another symmetric PCHE-PE diblock copolymer and corrected to T_{ref} = 140 °C.

The temperature dependence of the zero shear viscosity (η_0) for the BµE, PCHE-PE-14, and the PCHE and PE homopolymers, are presented in Figure C.10. This property was determined using two procedures: linear oscillatory shear ($\eta_{0} = \eta'(\omega \rightarrow 0) = G''/\omega$, filled symbols) and steady shear (open symbols) experiments. Within experimental uncertainly both methods yield identical results. The temperature dependence of the viscosity of the BµE is clearly different from those of both the diblock and the homopolymers, consistent with the results listed in Table C.2.
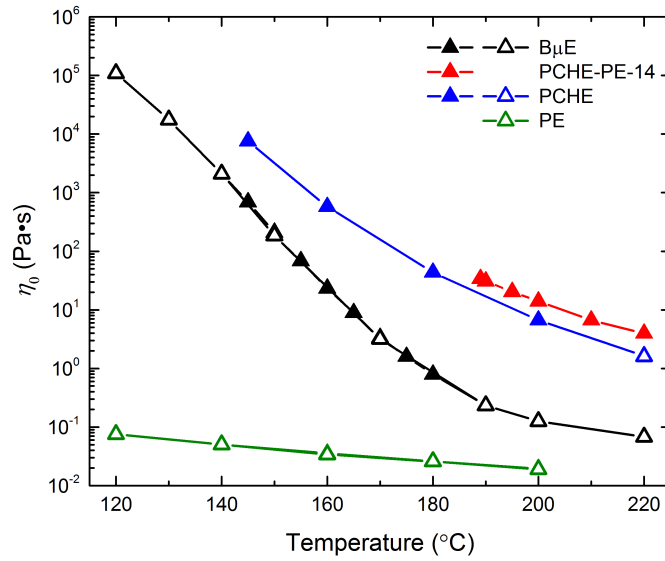
Figure C.10 Temperature dependence of the zero shear viscosity (η_0) for the BµE, PCHE-PE-14, and PCHE and PE homopolymers. The zero shear viscosity was determined using linear dynamic ($\eta_{0 =} \eta' = G''/\omega$ in the limit of $\omega \rightarrow 0$; closed triangles) and steady shear (opened triangles) experiments.

Discussion

The experimental results presented in the previous section reveal the structural and dynamical features that govern this fascinating state of condensed matter. Figure C.11 summarizes schematically what we have deduced regarding the equilibrium structure that emerges as the ternary mixture is cooled from a mean-field homogeneous state at high temperatures, to a fluctuating, highly structured, bicontinuous morphology at temperatures below approximately 150 °C. The transition temperature, T_x = 150 °C, identified by a black star in Figure C.2, coincides with two seemingly independent features: (1) as the temperature within the BµE channel extrapolated from the line of LAM-disorder transitions at lower homopolymer concentrations, and (2) the point that defines the low temperature behavior of f_a (Figure C.6). This section describes the rationale behind the illustrations in Figure C.11 and the associated dynamic consequences.
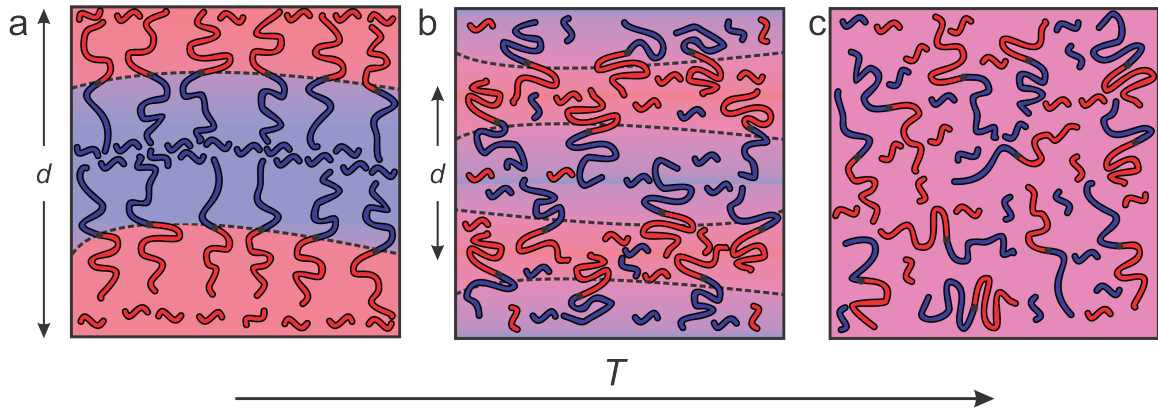
Figure C.11 Scheme representing the change in the interfacial area per chain, domain spacing (*d*), and degree of polymer intermixing with respect to temperature (*T*) for the BµE sample. (a) At low temperatures ($T \ll T_x$), the PCHE-PE-14 diblock copolymer packs at the interface with the same crowded areal density as the neat LAM forming diblock copolymer. In this temperature regime, homopolymers are largely excluded from the interfacial region. (b) At intermediate temperatures ($T \approx T_x$) homopolymers penetrate into the interfacial region, leading to an increase in the surface area per diblock chain and a reduction in *d*. (c) At significantly increased temperatures ($T \gg T_x$), the system reaches a mean-field homogeneously mixed state.

Structure We first estimate the interfacial area per diblock copolymer chain (A_c) from estimates of the interfacial area per unit volume (*S*) of the BµE. A_c is related to *S* for the BµE (and the LAM and DIS states in PCHE-PE-14) by

$$A_c = \frac{SM_n}{(1-\phi_H)\rho N_{av}} \, ,$$ (C.5)

where N_{av} is Avogadro's number, ρ is the density and M_n is the molecular weight of the block copolymer chain.[47] In principle, *S* can be extracted from any 2-phase system using Porod's law[80]

$$S = q^4 I(q \to \infty) / 2\pi (\Delta\rho)^2$$ (C.6)

where $\Delta\rho$ is the difference in scattering length density. We can eliminate $\Delta\rho$ by invoking the scattering invariant, Q_I, given by[80]

$$Q_I = \int_0^\infty q^2 I(q)\,dq = 2\pi^2 (\Delta\rho)^2 \phi_{PCHE}(1-\phi_{PCHE}) \, ,$$ (C.7)

where ϕ_{PCHE} is the total volume fraction of PCHE (0.5 for the BμE). Combining equations C.6 and C.7 yields

$$S = q^4 I(q) \, \pi \, \phi_{PCHE} \, (1 - \phi_{PCHE})/Q_I \; . \tag{C.8}$$

Here we note that equations C.6, C.7 and C.8 are based on the assumption of an ideal two-phase structure in which compositionally uniform domains are separated by sharp interfaces, i.e., the scattering length density profile normal to an interface is a step function. This condition is not strictly satisfied for the BμE studied here. At temperatures around T_x the true scattering length density profile varies smoothly, with a finite interfacial width that approaches the domain dimension d with increasing temperature. This also reduces the average magnitude of $\Delta\rho$ below what would be calculated for the pure homopolymers. Both of these effects impact the quantitative application of Porod's law. Nevertheless, the qualitative trends that result from changing the temperature of the BμE are captured by this simple analysis.

The experimental SANS data at high q (Figure C.5) are dominated by contributions from the incoherent background and scattering arising from the h-PCHE blocks within the d-PCHE homopolymer domains. This precludes reliable extraction of S using a direct application of Porod's law. Therefore, we have taken advantage of the excellent quality of the T-S fits to the SANS data and used these fitted functions to estimate Q_I and calculate S and A_c, assuming these functions apply over all values of q. As seen in Figure C.12, A_c thus calculated increases from 4.1 nm^2 at 125 °C to 24.7 nm^2 at 200 °C. A similar trend was reported previously for another polymeric BμE.[47]

We have estimated A_c for the neat PCHE-PE-14 diblock copolymer in the LAM and DIS states for comparison with the BμE, using $S_{LAM} = q^*/\pi$ and $S_{DIS} = 0.5q^*$.[81,82] The relationship $S_{DIS} = 0.5q^*$ is an approximation drawn by analogy with the structure of the bicontinuous morphology that results from spinodal decomposition of a mixture of two immiscible liquids.[81-83] Values of q^* were determined from SAXS data obtained from previously reported work[71] and the associated S values were converted to A_c using equation C.5 and are plotted in Figure C.12. (The jump in A_c with disordering, at virtually constant q^*, reflects an increase in the interfacial area associated with the transition from

lamellae to a fluctuating bicontinuous state, as discussed elsewhere.[81]) Remarkably, the area per block copolymer chain for the BµE asymptotically approaches that of the PCHE-PE-14 chains in the undiluted LAM morphology in the low temperature limit. Hence, we conclude that cooling the ternary mixture deep into the bicontinuous channel, $T \ll T_x$, leads to the expulsion of homopolymer from the interfacial region as illustrated in Figure C.11a.

The T-S fits to the SANS data also allow an estimate of the extent of segregation between PCHE and PE (proportional to $\Delta\rho$) as a function of temperature based on the invariant Q_I (equation C.7). The relative amplitude of the composition profile can be expressed as,

$$\Delta\rho / \Delta\rho_{cal} = \sqrt{\left[Q_I / 2\pi^2 \phi_{PCHE}(1-\phi_{PCHE}) \right]} / \Delta\rho_{cal} , \qquad (C.9)$$

where $\Delta\rho_{cal} = 2.7 \times 10^{-6}$ Å^{-2} represents the maximum scattering contrast that would be obtained from pure d-PCHE and PE domains. The results of this analysis, plotted in Figure C.13, reveal that the average amplitude of the composition profile changes by a factor of 2 as the mixture is cooled from 200 °C to 125°C. We have illustrated this feature schematically in Figure C.11 by separating the purple background color evident at the highest temperature (Figure C.11c) into a continuously graded background at intermediate temperature (Figure C.11b) and the constituent red and blue domains in the low temperature limit (Figure C.11a).
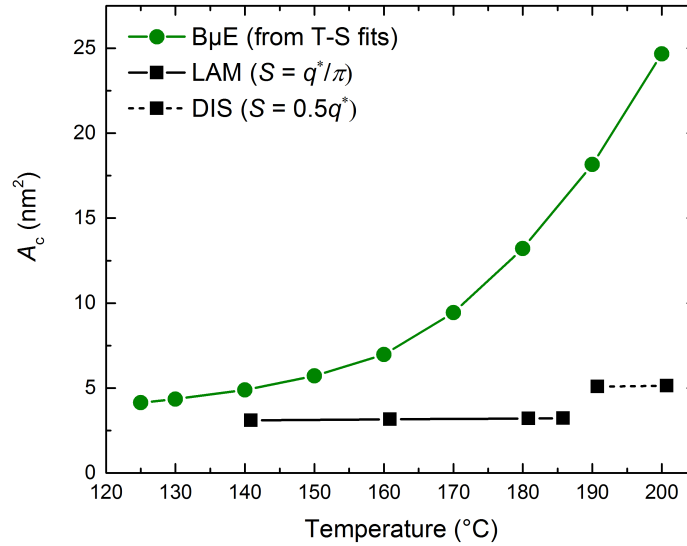
Figure C.12 Temperature dependence of the interfacial area per PCHE-PE-14 chain (A_c) for the BµE and neat PCHE-PE-14 samples. A_c was calculated for the BµE sample from the Teubner–Strey functions shown in Figure C.5. A_c was calculated for the neat PCHE-PE-14 sample using the relationships $S_{LAM} = q^*/\pi$ and $S_{DIS} = 0.5q^*$ for the LAM and DIS states, respectively. S is the interfacial area per volume and q^* was determined from previously reported SAXS data.[32,71]
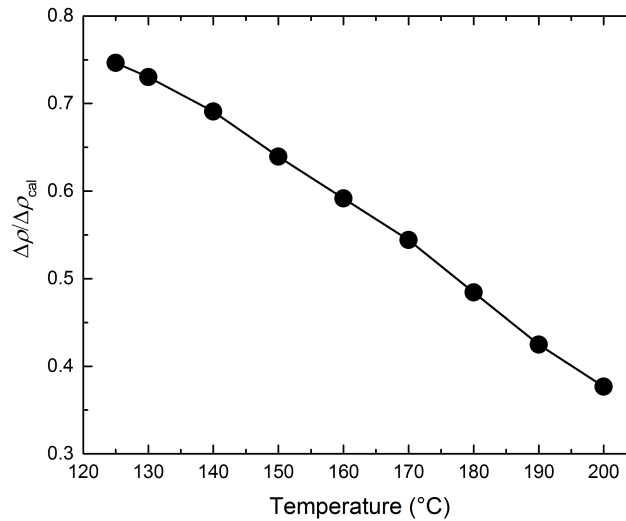

Figure C.13 The ratio of the scattering length density ($\Delta\rho$) and the calculated maximum possible scattering length density ($\Delta\rho_{cal}$) with respect to temperature for the BµE sample. The ratio is determined from the invariant (Q_I) using the Teubner–Strey fits to the SANS data.

Notwithstanding the assumptions involved in generating Figures 12 and 13, these results offer new insights regarding the local properties of the interface and the extent of polymer intermixing in the BµE, as summarized in Figure C.11. Although the BµE is globally disordered at all levels of segregation, the molecular environment of the interface resembles that of the neat PCHE-PE-14 in the LAM morphology at lower temperatures. As T is reduced below T_x, the interface becomes "saturated" ("crowded") with block copolymer, largely excluding the PCHE and PE homopolymers from the interfacial region, creating a situation analogous to the "dry-brush" regime encountered when a dense array of polymer chains are anchored to a surface in contact with an athermal melt of polymers. This exclusion of homopolymer leads to stiffening of the interface and an increase in the correlation length. Interestingly, as the BµE interface becomes saturated with diblock copolymer and A_c approaches that of neat PCHE-PE-14, the lamellar ordering anticipated by mean-field theory does not occur.[84] Apparently, fluctuation effects, associated with a finite diblock copolymer molecular weight, overwhelm the tendency to order at reduced temperatures as opposing diblock copolymer rich interfaces become decoupled through the expulsion of homopolymer. Obviously, diblock decoupling cannot happen when $\phi_H \rightarrow 0$, nor at the lamellar unbinding transition in the mean-field limit (coincident with the Lifshitz composition)[84] when $N_{AB} \rightarrow \infty$.

Dynamics The temperature dependence of the zero shear viscosity of the BµE reinforces the structural interpretations discussed in the previous section. As is evident in Figure C.10, the temperature dependence of the viscosity of the BµE differs significantly from PCHE-PE-14 and the two homopolymers. At low temperatures, the behavior of the BµE approaches that of the diblock (and PCHE homopolymer), consistent with a morphology of two 3-dimensional interpenetrating networks of well-segregated domains enriched with each homopolymer (Figure C.11a). However, with increasing temperature the opposite trend is evident, where at the highest measurement temperatures the viscosity of the BµE more closely resembles that of the PE homopolymer. This behavior conforms to expectation for an increased state of mixing (Figure C.11c) where the flow behavior is

most dominated by the low viscosity component. Between these two limits, the viscosity of the BμE is more strongly dependent on temperature than either homopolymer or the pure diblock (which is relatively strongly segregated over the entire temperature range), as reflected in the WLF parameters listed in Table C.2. These dynamic phenomena are a direct consequence of the substantial differences in the viscoelastic behavior (also referred to as mechanical contrast) between PCHE and PE, due primarily to the large difference in T_g ($\Delta T_g \approx 260$ °C). To the best of our knowledge this aspect of bicontinuous microemulsion dynamics has not been recognized in previous studies.[43-45,48]

Similarities in the frequency dependence of the linear viscoelastic properties of the BμE and the pure disordered PCHE-PE-14 diblock, evident in the time-temperature superposed master plots (Figure C.9), also supports this interpretation. At low temperatures, the diblock copolymer molecules in the BμE morphology experience a local (crowded) environment similar to that encountered in the pure, fluctuating diblock copolymer melt above T_{ODT}. In both cases, we expect G' and G'' at reduced frequencies, $a_T\omega \geq (a_T\omega)_c$, to be dominated by interfacial dynamics, where $\tau_c^{-1} = (a_T\omega)_c$ defines the time constant associated with terminal behavior. Apparently, the presence of PCHE and PE homopolymer in the BμE serves only to dilute the amount of interface, which has the effect of reducing the absolute magnitude of the measured moduli, but without significantly influencing τ_c or the frequency dependence of G' and G'' for $a_T\omega \geq \tau_c^{-1}$. Clearly, the 2-dimensional sheets of diblocks control the magnitude of G' and G'' in pure PCHE-PE-14 and the BμE; the terminal time constants for the homopolymers are orders of magnitude smaller than τ_c for the microstructured materials. However, more quantitative comparison of the homopolymer and diblock-based materials is not warranted since partial mixing of PE and PCHE greatly influences the quantitative values of the moduli in the structured materials.

Upon ordering, the low frequency ($a_T\omega < \tau_c^{-1}$) behavior of PCHE-PE-14 changes dramatically, reflecting the correlated response of periodically stacked flat interfaces ($G' \sim G'' \sim \omega^{1/2}$) as described in numerous earlier studies.[71,77] This mode of viscoelastic

response is not accessed by the BµE, which remains disordered and liquid-like ($G' \sim \omega^2$ and $G'' \sim \omega^1$) at $a_T\omega < \tau_c^{-1}$ and all measurement temperatures.

In the terminal regime of the master plot for the BµE (Figure C.8), the G' data fail to superpose precisely, resembling previously reported work in which rheological evidence of composition fluctuations are evident in dynamically symmetric disordered diblock copolymer melts.[71,77] Curiously, we did not find this behavior with pure PE-PCHE diblock copolymer in the vicinity of T_{ODT}, a result which was attributed to a large mechanical contrast.[71] As rationalized in the previous paragraphs, we infer that the terminal regime of the BµE reflects purely interfacial dynamics. At low temperatures ($T \ll T_x$), the system is relatively well-segregated, with saturated interfaces, and increased correlation lengths (i.e., the structure is stiffer). With increasing temperature, the homopolymers mix into and "soften" the interfaces, with a concomitant reduction in the correlation length. These changes in the interfacial properties with temperature are reflected in τ_c, which increases as the temperature is reduced, leading to a reduction in $(a_T\omega)_c$ and the apparent failure of tTS. Because both homopolymers have terminal relaxation times that are orders of magnitude shorter than the bicontinuous blend, the system is essentially mechanically "contrast matched", which explains the similarity with the behavior of dynamically symmetric diblocks[71] such as PtBS-PMMA[77] and PEP-PEE.[85]

General Remarks We have characterized the structural evolution of the BµE from the high temperature regime ($T \gg T_x$), where the system approaches the homogeneously mixed mean-field state, to low temperatures ($T \ll T_x$) where the components segregate into well-correlated domains enriched in PCHE and PE homopolymer, separated by an interface crowded with diblock copolymer. In this section we draw connections to related soft material systems, specifically, worm-like micelles and sponge phases.

Previous investigations involving BµE systems have shown that there are multiple diffusion modes related to domain structure, amphiphile dynamics, and undulating interfaces.[43,46,47] An X-ray photon correlation spectroscopy (XPCS) study on a polymeric

BμE demonstrated that a stretched-exponential function was required to model autocorrelation functions, indicating that a single structural relaxation time is not adequate to describe the equilibrium dynamics.[43] The stretched exponent values for the BμE were found to be similar to those predicted theoretically and determined experimentally for membrane systems such as sponge phases, lamellae, and vesicles.[61-64,86] Similarly, worm-like micelles subjected to shear deformation exhibit stretched exponential relaxation behavior, where reptation is the major mode of stress relaxation.[59,65,66,87] Additionally, worm-like micelles exhibit a relaxation spectrum that is dependent on the relative ratio between the reptation (τ_{rep}) and cylinder breaking and reforming (τ_{break}) time constants.[65,66] In the $\tau_{rep} \ll \tau_{break}$ regime, an 'entanglement plateau' is present[65,66] and relaxation occurs by diffusion of the micelles in the entanglement network accompanied by 'Rouse modes' that occur along the contour of the worm-like micelle.[59,65,66,87] This behavior is similar to stress relaxation via reptation of linear entangled polymer melts as described by Doi and Edwards.[88] Conversely, there is no entanglement plateau when $\tau_{rep} \gg \tau_{break}$.[65,66] In real systems, worm-like micelles display a combination of these two relaxation mechanisms.[59,87,89]

With lyotropic sponge phases, the topological relaxation time, or the time required for breaking and reforming of the bilayer structure, has been found experimentally to occur on fast time scales ($\sim$ 0.01 s).[68,69] For the BμE addressed in this study, we expect that breaking and reforming of the bicontinuous domains is thwarted at low temperatures as a result of increased segregation and rigid lamellar-like interfaces. Similar behavior is seen during the shear alignment of lamellar diblock copolymers: it is more difficult to align block copolymers well below the ODT because of slower chain relaxation dynamics and higher energy barriers.[90-93] As homopolymers intermix with the diblock copolymer at higher temperatures, the BμE interface becomes more flexible, and the energetic barrier for breaking and reforming of interfaces should diminish. Therefore, we expect the BμE to have a strongly temperature dependent interfacial relaxation spectrum, as observed experimentally. The mode of stress relaxation at high frequencies in Figure C.8 appears to be Rouse-like with no 'entanglement plateau'. Yet the BμE

contains a sheet-like diblock copolymer rich interface that is folded into an interpenetrating manifold that spans the entire volume. It is hard to imagine a mechanism analogous to reptation with this topology. Breaking and reforming the bicontinuous morphology likely involves multiple processes, including membrane undulations[94] and out-of-plane fluctuations that are common in fluid membranes formed by lipids and surfactants.[67,95-98] For these reasons, we speculate that at time scales longer than the longest relaxation time, τ_c, the interfacial dynamics of the BµE reflect a competition between interfacial undulations and the breaking and reforming of the interfaces, as depicted schematically in Figure C.14. Further insight into this fascinating aspect of BµEs awaits additional theory and simulation.
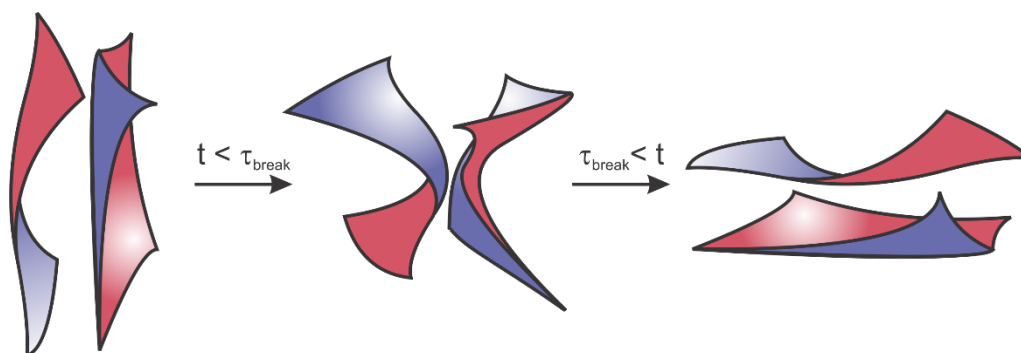

Figure C.14 Scheme illustrating a proposed mechanism for the interfacial dynamics of the BµE undergoing shear deformation. The BµE interface is continually breaking (τ_{break}) and reforming, and is therefore fluid-like at long time scales.

This work helps to elucidate the fundamental thermodynamic driving forces for the formation of the BµE morphology. Adding homopolymer to diblock lamellae swells the domains non-linearly, as predicted by mean-field theory and established experimentally.[25,84] Mean-field theory anticipates that the lamellar domain spacing diverges at an unbinding transition coincident with the Lifshitz composition ($\phi_{H,L}$).[84] This prediction is not realized experimentally because thermally driven composition fluctuations preempt the unbinding transition, giving rise to the BµE channel.[25] The BµE displays structural relaxation mechanisms including interfacial undulations and the breaking and reforming of interfaces. The magnitude of membrane undulations, to a first

approximation, is related to the interlayer spacing of the interfaces. If layers of membranes have a sufficiently small interlayer spacing, steric hindrance will drive the membranes to order into a lamellar morphology as a result of repulsive forces.[67,95-98] As the interlayer spacing increases, and the interfaces decouple, the effects of steric hindrance will be reduced and permit the formation of a microemulsion phase, as predicted by de Gennes and Taupin.[37] We hypothesize that adding homopolymer to the diblock copolymer, which increases the domain spacing, amplifies interfacial dynamics. Exactly how this stabilizes the BμE is an open question. We have shown in this study that interfacial dynamics are temperature dependent, and that the interface becomes stiffer at lower temperatures while simultaneously decoupling from neighboring sheets by expulsion of homopolymer. Application of simultaneous SANS and neutron spin echo scattering, as employed by Holderer *et al.*[99,100] to characterize the bending rigidity of surfactant based BμEs, might provide additional insights into this aspect of the dynamics.

These considerations raise the question: Will an ordered LAM structure form as $T \rightarrow 0$? Fortunately, this pivotal question can be addressed using cleverly designed AB/A/B polymeric BμEs. This will require precisely tuning the ratio ϕ_A / ϕ_B, and perhaps f_A, to account for the effects of conformational asymmetry, along with the establishment of efficient experimental methods to identify the exact composition that perfectly balances the mean (H) and Gauss (K) interfacial curvature. Perfect balance in real polymer systems will not occur in general at $\phi_A / \phi_B = 1$ and $f_A = \frac{1}{2}$, and significant deviation from ideal interfacial symmetry will likely lead to multiphase behavior as $T \rightarrow 0$. These issues are currently under investigation.

Finally, we comment briefly on how this work relates to the large literature on surfactant/water/oil microemulsions. In the case of non-ionic surfactant systems, the BμE window is narrow in both composition and temperature, appearing at the tip of what is referred to as the 'fish cut' in the phase prism.[27] Increasing or decreasing temperature by just a few degrees at the optimal composition leads to macroscopic phase separation. This complex phase behavior is intrinsically tied to the dual upper and lower critical solution temperature behaviors (UCST and LCST, respectively) of the hydrophobic and

hydrophilic constituents of the amphiphile. Moreover, such systems are inherently structurally asymmetric due to the nature of the interactions of oil, and especially water, with the surfactant, making it difficult if not impossible to perfectly tune the overall bicontinuous morphology. These deficiencies are fully overcome with properly designed ternary AB/A/B polymeric systems as outlined in the previous paragraph.

Summary

We have presented the results and an analysis of a comprehensive study of a bicontinuous microemulsion (BµE) formed from equal volumes of poly(cyclohexylethylene) (PCHE), poly(ethylene) (PE) and 14% by volume of the corresponding PCHE-PE diblock copolymer. Small-angle neutron and X-rays scattering (SANS and SAXS) measurements, obtained over an 80 °C temperature range, were modeled using the Teubner–Strey structure factor. These experiments provide detailed information regarding the extent of segregation and the interfacial area per block copolymer molecule (A_c) well above and below the temperature extrapolated from the line of lamellar-disorder transition temperatures established at lower homopolymer concentrations denoted T_x. As the system is cooled deep into the BµE channel ($T \ll T_x$) A_c decreases, asymptotically approaching the value that characterizes undiluted PCHE-PE in the lamellar state. This interfacial crowding of diblock copolymer and expulsion of homopolymer from the interfacial region results in a stronger state of segregation, accompanied by increases in the domain spacing and correlation length. Mechanical spectroscopy experiments reinforce this picture. Vastly different homopolymer relaxation times, attributable to disparate glass transition temperatures ($\Delta T_g \approx 260$ °C), lead to zero-shear viscosities that reflect enhanced mixing at high temperatures and stronger segregation at low temperatures. Remarkably, the time constant associated with the transition to terminal (liquid-like) behavior in the BµE, determined by linear dynamic mechanical spectroscopy, coincides with the behavior of the pure disordered diblock copolymer at a common reduced temperature. These results indicate that the rheological properties of the BµE are controlled by the same interfacial dynamics that govern the

behavior of undiluted fluctuating disordered diblock copolymer melts near the order–disorder transition. These findings offer fresh insights into the thermodynamic driving forces responsible for the formation of BµEs and the resulting properties, and highlight opportunities to better understand this fascinating state of self-assembly.

References

(1)   H. Zhang and A. I. Cooper, *Soft Matter*, 2005, **1**, 107-113.

(2)   E. A. Jackson and M. A. Hillmyer, *ACS Nano*, 2010, **4**, 3548-3553.

(3)   B. H. Jones and T. P. Lodge, *Polym. J.*, 2012, **44**, 131-146.

(4)   R. M. Dorin, H. Sai and U. Wiesner, *Chem. Mater.*, 2014, **26**, 339-347.

(5)   H. Pernot, M. Baumert, F. Court and L. Leibler, *Nat. Mater.*, 2002, **1**, 54-58.

(6)   M.-J. Schwuger, K. Stickdorn and R. Schomaecker, *Chem. Rev.*, 1995, **95**, 849-864.

(7)   D. Kipp, O. Wodo, B. Ganapathysubramanian and V. Ganesan, *ACS Macro Lett.*, 2015, **4**, 266-270.

(8)   J. Erlebacher, M. J. Aziz, A. Karma, N. Dimitrov and K. Sieradzki, *Nature*, 2001, **410**, 450-453.

(9)   P. Levitz, G. Ehret, S. K. Sinha and J. M. Drake, *J. Chem. Phys.*, 1991, **95**, 6151-6161.

(10)   X. Lang, A. Hirata, T. Fujita and M. Chen, *Nat. Nano.*, 2011, **6**, 232-236.

(11)   L. Li, C. Miesch, P. K. Sudeep, A. C. Balazs, T. Emrick, T. P. Russell and R. C. Hayward, *Nano Lett.*, 2011, **11**, 1997-2003.

(12)   M. Seo and M. A. Hillmyer, *Science*, 2012, **336**, 1422-1425.

(13)   C. J. Hawker and K. L. Wooley, *Science*, 2005, **309**, 1200-1205.

(14)   F. S. Bates, M. A. Hillmyer, T. P. Lodge, C. M. Bates, K. T. Delaney and G. H. Fredrickson, *Science*, 2012, **336**, 434-440.

(15)   M. Seo, S. Kim, J. Oh, S.-J. Kim and M. A. Hillmyer, *J. Am. Chem. Soc.*, 2015, **137**, 600-603.

(16)   M. Seo, C. J. Murphy and M. A. Hillmyer, *ACS Macro Lett.*, 2013, **2**, 617-620.

(17)   C. H. Chew, T. D. Li, L. H. Gan, C. H. Quek and L. M. Gan, *Langmuir*, 1998, **14**, 6068-6076.

(18)   A.-L. Esquirol, P. Sarazin and N. Virgilio, *Macromolecules*, 2014, **47**, 3068-3075.

(19)   W. Lu, D. Yuan, D. Zhao, C. I. Schilling, O. Plietzsch, T. Muller, S. Bräse, J. Guenther, J. Blümel, R. Krishna, Z. Li and H.-C. Zhou, *Chem. Mater.*, 2010, **22**, 5964-5972.

(20)   L. D. McIntosh, M. W. Schulze, M. T. Irwin, M. A. Hillmyer and T. P. Lodge, *Macromolecules*, 2015, **48**, 1418-1428.

(21)   H. Sai, K. W. Tan, K. Hur, E. Asenath-Smith, R. Hovden, Y. Jiang, M. Riccio, D. A. Muller, V. Elser, L. A. Estroff, S. M. Gruner and U. Wiesner, *Science*, 2013, **341**, 530-534.

(22)   M. W. Schulze, L. D. McIntosh, M. A. Hillmyer and T. P. Lodge, *Nano Lett.*, 2014, **14**, 122-126.

(23)   H. Jinnai, Y. Nishikawa, T. Koga and T. Hashimoto, *Macromolecules*, 1995, **28**, 4782-4784.

(24)   P. Sarazin, X. Roy and B. D. Favis, *Biomaterials*, 2004, **25**, 5965-5978.

(25)   F. S. Bates, W. W. Maurer, P. M. Lipic, M. A. Hillmyer, K. Almdal, K. Mortensen, G. H. Fredrickson and T. P. Lodge, *Phys. Rev. Lett.*, 1997, **79**, 849-852.

(26)   S. E. Friberg and P. OBothorel, eds., *Microemulsions: Structure and Dynamics*, CRC Press, Boca Raton, FL, 1987.

(27)   R. Strey, *Colloid Polym. Sci.*, 1994, **272**, 1005-1019.

(28)   L. Kielhorn and M. Muthukumar, *J. Chem. Phys.*, 1997, **107**, 5588-5608.

(29)   D. Düchs, V. Ganesan, G. H. Fredrickson and F. Schmid, *Macromolecules*, 2003, **36**, 9237-9248.

(30)   J. H. Lee, M. L. Ruegg, N. P. Balsara, Y. Zhu, S. P. Gido, R. Krishnamoorti and M.-H. Kim, *Macromolecules*, 2003, **36**, 6537-6548.

(31)   M. A. Hillmyer, W. W. Maurer, T. P. Lodge, F. S. Bates and K. Almdal, *J. Phys. Chem. B*, 1999, **103**, 4814-4824.

(32)   B. M. Habersberger, T. M. Gillard, R. J. Hickey, T. P. Lodge and F. S. Bates, *ACS Macro Lett.*, 2014, **3**, 1041-1045.

(33)   G. Pandav and V. Ganesan, *Macromolecules*, 2013, **46**, 8334-8344.

(34)   M. Teubner and R. Strey, *J. Chem. Phys.*, 1987, **87**, 3195-3200.

(35)   K. V. Schubert, R. Strey, S. R. Kline and E. W. Kaler, *J. Chem. Phys.*, 1994, **101**, 5343-5355.

(36)   M. E. Cates, D. Andelman, S. A. Safran and D. Roux, *Langmuir*, 1988, **4**, 802-806.

(37)   P. G. De Gennes and C. Taupin, *J. Phys. Chem.*, 1982, **86**, 2294-2304.

(38)   D. C. Morse, *Phys. Rev. E*, 1994, **50**, R2423-R2426.

(39)   D. C. Morse, *Curr. Opin. Colloid Interface Sci.*, 1997, **2**, 365-372.

(40)   Y. Talmon and S. Prager, *J. Chem. Phys.*, 1978, **69**, 2984-2991.

(41)   Y. Talmon and S. Prager, *J. Chem. Phys.*, 1982, **76**, 1535-1538.

(42)   Z. G. Wang and S. A. Safran, *J. Phys.*, 1990, **51**, 185-200.

(43)   K. L. Brinker, S. G. J. Mochrie and W. R. Burghardt, *Macromolecules*, 2007, **40**, 5150-5160.

(44)   W. R. Burghardt, K. Krishnan, F. S. Bates and T. P. Lodge, *Macromolecules*, 2002, **35**, 4210-4215.

(45)   K. Krishnan, B. Chapman, F. S. Bates, T. P. Lodge, K. Almdal and W. R. Burghardt, *J. Rheol.*, 2002, **46**, 529-554.

(46)   T. L. Morkved, B. R. Chapman, F. S. Bates, T. P. Lodge, P. Stepanek and K. Almdal, *Faraday Discuss.*, 1999, **112**, 335-350.

(47)   T. L. Morkved, P. Stepanek, K. Krishnan, F. S. Bates and T. P. Lodge, *J. Chem. Phys.*, 2001, **114**, 7247-7259.

(48)   N. Zhou, F. S. Bates, T. P. Lodge and W. R. Burghardt, *J. Rheol.*, 2007, **51**, 1027-1046.

(49)   K. Krishnan, K. Almdal, W. R. Burghardt, T. P. Lodge and F. S. Bates, *Phys. Rev. Lett.*, 2001, **87**, 098301.

(50)   K. Krishnan, W. R. Burghardt, T. P. Lodge and F. S. Bates, *Langmuir*, 2002, **18**, 9676-9686.

(51)   B. Narayanan, V. Pryamitsyn and V. Ganesan, *Phys. Rev. Lett.*, 2006, **96**, 028302.

(52)   G. Porte, *Curr. Opin. Colloid Interface Sci.*, 1996, **1**, 345-349.

(53)   P. Snabre and G. Porte, *Europhys. Lett.*, 1990, **13**, 641.

(54)   R. Mezzenga, C. Meyer, C. Servais, A. I. Romoscanu, L. Sagalowicz and R. C. Hayward, *Langmuir*, 2005, **21**, 3322-3333.

(55)   R. N. Kleiman, D. J. Bishop, R. Pindak and P. Taborek, *Phys. Rev. Lett.*, 1984, **53**, 2137-2140.

(56)   T. M. Clausen, P. K. Vinson, J. R. Minter, H. T. Davis, Y. Talmon and W. G. Miller, *J. Phys. Chem.*, 1992, **96**, 474-484.

(57)   C. A. Dreiss, *Soft Matter*, 2007, **3**, 956-970.

(58)   S. A. Rogers, M. A. Calabrese and N. J. Wagner, *Curr. Opin. Colloid Interface Sci.*, 2014, **19**, 530-535.

(59)   L. M. Walker, *Curr. Opin. Colloid Interface Sci.*, 2001, **6**, 451-456.

(60)   G. Pätzold and K. Dawson, *Phys. Rev. E*, 1996, **54**, 1669-1682.

(61)   P. Falus, M. A. Borthwick, S. Narayanan, A. R. Sandy and S. G. J. Mochrie, *Phys. Rev. Lett.*, 2006, **97**, 066102.

(62)   E. Freyssingeas and D. Roux, *J. Phys. II*, 1997, **7**, 913-929.

(63)   S. Komura, T. Takeda, Y. Kawabata, S. K. Ghosh, H. Seto and M. Nagao, *Phys. Rev. E*, 2001, **63**, 041402.

(64)   M. Maugey and A. M. Bellocq, *Langmuir*, 2001, **17**, 6740-6742.

(65)   M. E. Cates and S. J. Candau, *J. Phys. Condens. Matter*, 1990, **2**, 6869.

(66)   H. Rehage and H. Hoffmann, *Mol. Phys.*, 1991, **74**, 933-973.

(67)   R. Granek, *J. Phys. II*, 1997, **7**, 1761-1788.

(68)   L. Porcar, W. A. Hamilton, P. D. Butler and G. G. Warr, *Langmuir*, 2003, **19**, 10779-10794.

(69)   L. Porcar, W. A. Hamilton, P. D. Butler and G. G. Warr, *Phys. Rev. Lett.*, 2004, **93**, 198301.

(70)   B. M. Habersberger, T. P. Lodge and F. S. Bates, *Macromolecules*, 2012, **45**, 7778-7782.

(71)   R. J. Hickey, T. M. Gillard, T. P. Lodge and F. S. Bates, *ACS Macro Lett.*, 2015, **4**, 260-265.

(72)   L. J. Fetters, D. J. Lohse, D. Richter, T. A. Witten and A. Zirkel, *Macromolecules*, 1994, **27**, 4639-4647.

(73)   S. J. Weigand and D. T. Keane, *Nucl. Instr. Meth. Phys. Res.*, 2011, **649**, 61-63.

(74)   S. Kline, *J. Appl. Cryst.*, 2006, **39**, 895-900.

(75)   M. D. Gehlsen, J. H. Rosedale, F. S. Bates, G. D. Wignall, L. Hansen and K. Almdal, *Phys. Rev. Lett.*, 1992, **68**, 2452-2455.

(76)   G. M. Brown and J. H. Butler, *Polymer*, 1997, **38**, 3937-3945.

(77)   J. G. Kennemur, M. A. Hillmyer and F. S. Bates, *ACS Macro Lett.*, 2013, **2**, 496-500.

(78)   J. G. Kennemur, M. A. Hillmyer and F. S. Bates, *Macromolecules*, 2012, **45**, 7228-7236.

(79)   G. H. Fredrickson and F. S. Bates, *Annu. Rev. Mater. Sci.*, 1996, **26**, 501-550.

(80)   O. Glatter and O. Kratky, eds., *Small Angle X-ray Scattering*, Academic Press, New York, 1982.

(81)   S. Lee, T. M. Gillard and F. S. Bates, *AIChE J.*, 2013, **59**, 3502-3513.

(82)   H. Jinnai, T. Koga, Y. Nishikawa, T. Hashimoto and S. T. Hyde, *Phys. Rev. Lett.*, 1997, **78**, 2248-2251.

(83)   F. S. Bates, J. H. Rosedale and G. H. Fredrickson, *J. Chem. Phys.*, 1990, **92**, 6255-6270.

(84)   D. Broseta and G. H. Fredrickson, *J. Chem. Phys.*, 1990, **93**, 2927-2938.

(85)   J. H. Rosedale and F. S. Bates, *Macromolecules*, 1990, **23**, 2329-2338.

(86) P. Falus, M. A. Borthwick and S. G. J. Mochrie, *Phys. Rev. Lett.*, 2005, **94**, 016105.

(87) K. Esumi and M. Ueno, eds., *Structure-Performance Relationships in Surfactants*, Marcel Dekker, New York, 1997.

(88) M. Doi and S. F. Edwards, *The Theory of Polymer Dynamics*, Oxford University Press, Oxford, 1990.

(89) J. F. Berret, J. Appell and G. Porte, *Langmuir*, 1993, **9**, 2851-2854.

(90) V. K. Gupta, R. Krishnamoorti, Z. R. Chen, J. A. Kornfield, S. D. Smith, M. M. Satkowski and J. T. Grothaus, *Macromolecules*, 1996, **29**, 875-884.

(91) R. M. Kannan and J. A. Kornfield, *Macromolecules*, 1994, **27**, 1177-1186.

(92) K. A. Koppi, M. Tirrell, F. S. Bates, K. Almdal and R. H. Colby, *J. Phys. II*, 1992, **2**, 1941-1959.

(93) S. S. Patel, R. G. Larson, K. I. Winey and H. Watanabe, *Macromolecules*, 1995, **28**, 4313-4318.

(94) A. J. Levine and F. C. MacKintosh, *Phys. Rev. E*, 2002, **66**, 061606.

(95) W. Helfrich, *Z. Naturforsch. C*, 1973, **28**, 693-703.

(96) W. Helfrich, *Z. Naturforsch.* 1978, **33a**, 305-315.

(97) W. Helfrich and R. M. Servuss, *Il Nuovo Cimento D*, 1984, **3**, 137-151.

(98) A. G. Zilman and R. Granek, *Phys. Rev. Lett.*, 1996, **77**, 4788-4791.

(99) O. Holderer, H. Frielinghaus, D. Byelov, M. Monkenbusch, J. Allgaier and D. Richter, *J. Chem. Phys.*, 2005, **122**, 094908.

(100) O. Holderer, H. Frielinghaus, M. Monkenbusch, M. Klostermann, T. Sottmann and D. Richter, *Soft Matter*, 2013, **9**, 2308-2313.